Tumour-Stromal Interactions in Cancer Progression and Drug Resistance



Noemi Picco

St Cross College

University of Oxford

A thesis submitted for the degree of

Doctor of Philosophy

Michaelmas 2016

Abstract

The typical response of cancer patients to treatment is only temporary, and is often followed by relapse. The failure of various therapeutic strategies is commonly attributed to the emergence of drug resistance. The response patterns for patients under such treatments indicate that complex dynamics regulate the response of the tumour to the therapy. The environment in which the tumour lives (the stroma) is known to be a modulator of multiple mechanisms that lead to drug resistance and seems to be a likely candidate for explaining some of this complexity. Understanding the role of stromal cells in the promotion of drug resistance is critical for the design of optimal treatment strategies, and for the development of novel therapies that selectively target both the tumour and the stroma. In this thesis we design two novel mathematical models that describe cancer growth within its environment and the evolution of drug resistance within spatially complex and temporally dynamic tumours. A compartment model captures clinically observed dynamics and allows direct comparison with experimental data, facilitating model parametrisation and the understanding of inter-tumour heterogeneity. An individual cell-based model highlights the key role of local interactions, determining heterogeneity at the tissue scale, that will eventually determine treatment outcome. A non-spatial approximation of this second model allows us to find analytic guidelines for the design of effective therapy. These tools allow the simulation of a range of treatment strategies (including combination of different drugs and variation of schedule) as well as the investigation of therapy response based on patient- or organ-specific parameters. The work developed in this dissertation is based on the paradigmatic biology of melanoma and non-small-cell lung cancer. Its results are therefore applicable to a variety of cancer treatments that target similar processes, and whose therapeutic failure can be attributed to environment-mediated drug resistance.

Acknowledgements

I would like to thank Professor Philip Maini and Dr. Alexander Anderson for their precious mentorship and supervision during the past four years. They have been the best two mentors one could ask for. Thank you to Philip for a great deal of ideas and patience. I am grateful to Sandy for making this possible from the very beginning, guiding me in the discovery of mathematical oncology, and providing moral and financial support.

I would like to acknowledge the H. Lee Moffitt Cancer Center and Research Institute in Tampa for hosting me over a considerable amount of time of my DPhil research work. A special thanks to all of the members of the Integrated Mathematical Oncology for the continuous help throughout the years.

I would like to give thanks to the experimental group of Dr. Sahai at the Francis Crick Institute in London for providing the experimental data and for valuable discussion on the mechanisms of environment-mediated drug resistance in melanoma. Thank you to Ross Johnstone for ideas and discussion on Bayesian inference and parameter estimation. Thank you to Professor Ruth Baker and Dr. Jonathan Whiteley for valuable discussion and suggestions following the confirmation viva.

Further, I would like to acknowledge the SABS-IDC Centre for Doctoral Training, the EPSRC, which partially funded this research, and St Cross College and the Mathematical Institute for the travel scholarships that made the numerous trips between Oxford and Tampa possible.

A huge thank you to all of the old friends and the ones that I met along the way. You made me feel at home and welcome every time that I moved city. Thank you for the fun times and laughters that made this DPhil journey much brighter.

Finally, to the ones that did not wait for me to come back, but flew wherever I was, because "that's what family does". To Mamma, Papà, Yaya and Alessandro, thank you for showing me what selfless love is. You have been my rock throughout the years, and I could never thank you enough for your endless support that keeps me going every day.

Contents

Glossary of Acronyms **1**

1 Introduction **3**

2 The Biology of Molecularly Targeted Cancers **5**
2.1 Targeting Proliferation and Survival Mechanisms 8
2.2 The Tumour Microenvironment 11
2.3 Environment Mediated Drug Resistance 13
2.3.1 Cell Adhesion-Mediated Drug Resistance 14
2.3.2 Soluble Factor-Mediated Drug Resistance 14
2.4 Experimental Evidence for EMDR in Melanoma 15

3 Mathematical Modelling of Cancer Growth and Treatment **17**
3.1 Cancer Cell Population Growth 18
3.2 Cancer Cell-Environment Interactions 20
3.3 Modelling Drug Administration and Resistance 21
3.4 Modelling Tumour-Stroma Interactions and Treatment 23
3.4.1 Results and Critique 25

4 Modelling Tumour-Stroma Dynamics in BRAF-wildtype Melanoma Growth and Treatment: Parameter Estimation **27**
4.1 Treating BRAF Wild-type Melanoma with AKT Inhibitor and Chemotherapy 28
4.2 The Experimental Model for BRAF-wildtype Melanoma 29
4.3 Modelling Tumour-Stroma Interactions and Emergence of Drug Resistance 29
4.4 The ODE Model of AKTi and Chemotherapy 31
4.5 Parametrisation of the Decoupled System 34
4.5.1 Parameter Estimation with Matlab *fmincon* 35
4.5.2 Parameter Estimation with Approximate Bayesian Computation . 38
4.5.3 Parameter Estimation with Markov Chain Monte Carlo 44

4.6 Coupled Model System Behaviour 48
4.7 Simulating the Standard of Care 49
4.8 Simulating the Flare Response 51
4.9 Simulating a Disease Management Strategy 52
4.10 Conclusion 54

5 Dual Targeting of Tumour and Stroma in BRAF-mutated Melanoma: Bridging Scales 56
5.1 The Experimental Model for BRAF-mutated Melanoma 57
5.2 The ODE Model of BRAFi and FAKi 57
5.3 Model Parametrisation with Experimental Data 60
5.4 Treatment Strategies for BRAF-wildtype Melanomas 68
5.5 Discussion and Conclusion 75

6 The Hybrid Discrete Continuum Model 78
6.1 The Modelling Setup and the HDC Coupling 81
6.2 The Proliferation Signal 83
6.3 The Continuum Model of Environmental Signals 85
6.4 The Numerical Solution of the System of PDEs 86
6.5 The Cell-based Rules 88
6.6 The Vessel Distribution 92
6.7 Homeostasis of Normal Tissue 92
6.8 Tumour Metastasis 94
6.9 Conclusion 95

7 Exploration of Treatment Strategies and Mechanisms of EMDR 97
7.1 Treatment with Targeted Therapy 99
7.2 Drug Holiday Limits Stromal Activation 102
7.3 Pulsed Drug Treatment to Control Growth 104
7.4 A Multi-model Approach to Treatment Optimisation 107
7.4.1 Cancer and Reactive Stroma Monotonicity Regimes under Drug Administration 110
7.4.2 Cancer and Reactive Stroma Monotonicity Regimes under Drug Holiday 113
7.4.3 Treatment Schedule Guidelines for the Well Mixed System 114
7.5 Mechanisms of Stromal Activation and Renormalisation 117
7.6 Systemic Treatment of Multiple Metastases. Addressing Inter-site Heterogeneity 121

7.7 Combination of Targeted Inhibitors 125
7.8 Conclusions 127

8 Conclusion **130**
8.1 Future Directions 134

A Minimisation Problem **136**

B Analysis of the ODE system (4.1) **138**
B.1 No Treatment 139
B.2 Chemotherapy 139
B.3 Targeted Therapy 140
B.4 Chemotherapy and Targeted Therapy Combination 141
B.5 After Targeted Therapy is Removed 142

Bibliography **144**

Glossary of Acronyms

AKTi AKT inhibitor

BRAFi B-Raf inhibitor

CAF Cancer Associated Fibroblasts

CAM-DR Cell Adhesion-Mediated Drug Resistance

ECM Extracellular Matrix

EMDR Environment-Mediated Drug Resistance

FAKi Focal Adhesion Kinase inhibitor

HDC Hybrid Discrete Continuum

MAPK Mitogen-Activated Protein Kinase

NSCLC Non-Small-Cell Lung Cancer

ODE Ordinary Differential Equation

PDE Partial Differential Equation

SFM-DR Soluble Factor-Mediated Drug Resistance

Chapter 1

Introduction

Metastatic melanoma is the deadliest form of skin cancer. Non-small-cell lung cancer is one of the most common types of cancer, second only to breast cancer (statistics of National Cancer Institute). These two cancer types share a key hallmark of cancer: mutations that lead to the upregulation of proliferative cues, and the downregulation of growth-control signalling. These mutations are termed driver mutations, defined as abnormalities found in the cancer cells genome that have been involved in the development of the cancer. Identifying such driver mutations for a cancer type allows the design of a drug that targets the mutated cells with high specificity (see Chapter 2). However, for these cancers the typical response to treatment is only temporary, and is followed by relapse. The failure of various therapeutic strategies is commonly attributed to the emergence of drug resistance. The presence of dormant, aggressive phenotypes in the tumour cell population, and the context-driven emergence of new resistant strains, are the main causes attributed to treatment failure. Non-malignant cells and other factors, constituting the microenvironment in which the tumour lives (the tumour *stroma*), play a crucial role in the response to anti-cancer therapies. Specifically, the dialogue between the tumour and the stroma has been shown to modulate the response to treatment, through proliferative and survival signalling. The goal of this thesis is to investigate the interactions between the tumour and its environment driving the emergence of drug resistance.

We initially present key biological details about non-small-cell lung cancer and melanoma, then discuss how they are currently treated and highlight the known mechanisms of resistance with an emphasis on tumour-stromal interactions in Chapter 2. Understanding this complex interplay between tumour and host cells undergoing drug treatment is ideally suited for mathematical and computational models. A vast literature already exists for mathematical models of cancer growth, progression and response to treatment, however, models that integrate the role of the stroma are less well developed. We briefly discuss the

literature modelling cancer growth and treatment, specifically relevant to tumour-stroma dynamics and treatment resistance in Chapter 3.

We present a first minimal model of tumour-stromal interactions, which aims to reproduce *in vitro* cell culture results, within the framework of ordinary differential equations (ODEs). The model, based on available experimental evidence, will initially characterise the effects of combination therapy through the application of drugs targeting different cellular and stromal processes. Additionally, through the model, we will explain the variability across experimental replicates. We will present two applications, where the ODE model is adapted to the description of growth and treatment-response dynamics for two main classes of melanomas. A detailed description of the experimental data and ODE model, as well as numerically simulated results, are presented in Chapters 4 and 5.

In Chapter 6 we describe a different modelling approach, the Hybrid Discrete-Continuum (HDC) framework that allows for spatial variation, and coupling of individual cell-based processes with environmental continuum fields. Finally in Chapter 7 we develop a framework that links the HDC model to its approximation formulated as an ODE model. The latter, more amenable to analytical studies, and being easier to parametrise, will inform a method for treatment schedule refinement, together with the relevant experimental evidence that will guide model refinement and validation.

The final goal of this study is to develop a suite of models describing the baseline growth dynamics (from the ODE model) and the relevant tumour-stromal cell interactions determining the heterogeneous dynamics of growth and response to treatment (emerging from the HDC model). Modelling the spatially-dependent properties of the biological system, typically characterised by key local interactions and tissue scale variation, leads to a more realistic mathematical description. Introducing an additional degree of variation, namely across metastatic sites, will facilitate the more realistic description of the dynamics of response to a treatment for patients with metastatic disease characterised by high variability in the environmental component. This, in turn, will allow a fuller understanding of the role of stroma cells in the promotion of drug resistance which, we propose, is critical for the design of optimal treatment strategies.

Chapter 2

The Biology of Molecularly Targeted Cancers

The mechanisms of context-driven resistance that we will investigate are shared across a variety of solid tumours characterised by aberrations in growth-control signalling and a high level of interaction with the surrounding microenvironment. We will introduce two types of cancers that are highly representative of this category: lung and skin cancers.

According to the National Cancer Institute, lung cancer is the second most common type of cancer in the United States, after breast cancer, and the most deadly one. More than 224,000 new cases are expected to be diagnosed in 2016, accounting for 13% of all new cancer cases in the country (estimates from the National Cancer Institute, [100]). Non-small-cell lung cancer (NSCLC) is the most common type of lung cancer, often characterised by driving mutations. Approximately 25% of NSCLCs harbour the Epidermal Growth Factor Receptor (EGFR) gene mutation, while mutant KRAS (a protein with a major role in cell growth regulation) accounts for 25% of NSCLC diagnoses. Because of the low sensitivity of NSCLCs to standard treatment such as radiation and chemotherapy, the presence of such mutations can be a positive prognostic factor, extending the treatment options to tumour-targeted therapies. Other options for patients not displaying these mutations are surgery and treatment with a combination of chemotherapy and anti-angiogenesis agents.

Skin cancers account for the large majority of diagnosed tumours. According to the American Cancer Society about 3.5 million Americans are diagnosed with basal and squamous cell cancer each year. Melanoma is the deadliest, though least common, form of skin cancer. About 76,000 cases of melanoma are expected to be diagnosed in the United States during 2016 [100]. The 5-year survival rate for melanoma, based on the 2008 American Joint Committee on Cancer Melanoma Staging Database[1], varies with the stage at which the patient is diagnosed, from 97% for Stage IA, down to 15% for

[1] www.cancerstaging.org



Figure 2.1: *An example of initial response to targeted therapy followed by relapse in a metastatic melanoma patient. A: Before therapy, B: After 15 weeks of continuous therapy, C: After 23 weeks of continuous therapy. Image reproduced with permission from Wagle et al., 2011.*

Stage IV. A total of about 10,100 people in the US are expected to die of melanoma in 2016.

Early stage melanomas are typically treated with surgery, followed by biopsy analysis to verify that the outer rim of the removed mass does not include malignant cells. In some cases a second surgery or adjuvant therapy is required if malignant cells are found. Treatments for advanced stage, such as metastatic melanoma, include single agent and combination chemotherapy, combination of chemotherapy and targeted therapy or immunotherapy, radiation therapy, and isolated limb perfusion[2] techniques.

Despite some recent encouraging improvements in the treatment of advanced stage melanoma, responses to most therapies are only temporary and eventually show relapse (see Figure 2.1, for example). Treatment failure can be indicative of a number of underlying biological processes, including the emergence of a pre-existing dormant clone following

[2] *Isolated limb perfusion* is a technique that allows the localisation of the action of a toxic chemotherapeutic agent to the area of interest (a single leg, for example), in order to minimise toxicity in the rest of the body.

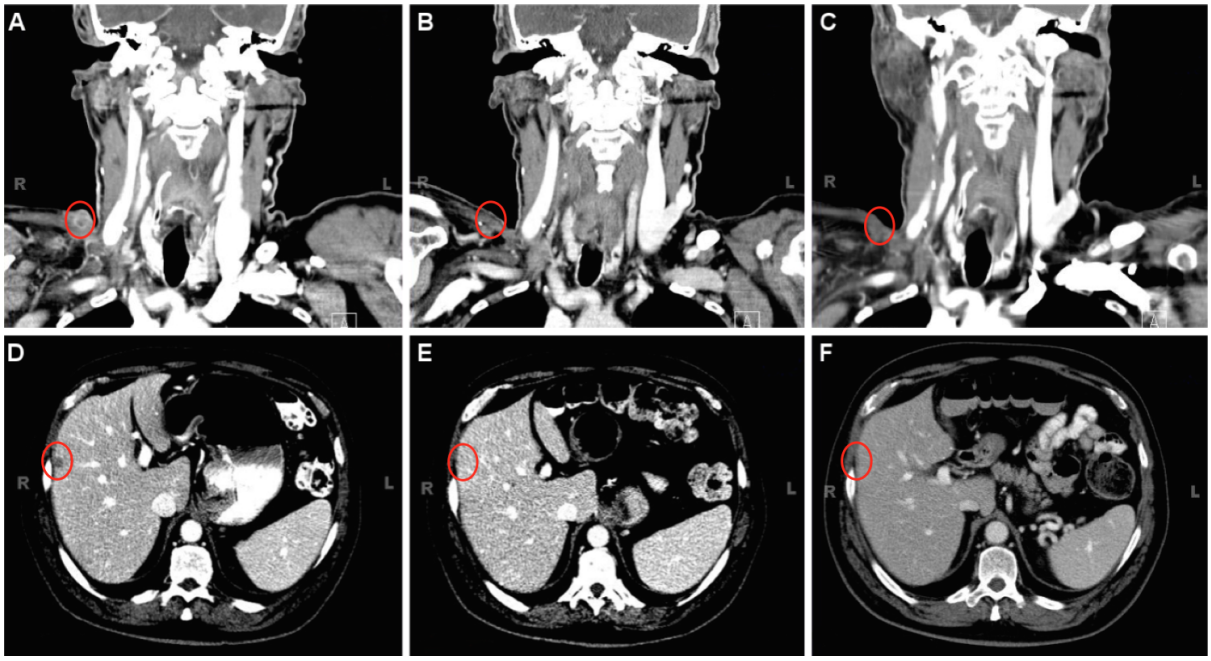


Figure 2.2: *An example of partial response to combination therapy in a metastatic melanoma patient. Images from a phase I clinical trial at the Moffitt Cancer Center of escalating doses of MK-2206 (AKT inhibitor) in combination with carboplatin (chemotherapy). Upper three panels show a metastasis at the right trapezius (frontal CT scan), lower three panels show a liver metastasis (cross-sectional CT scan). A and D: Baseline before therapy. B and E: After 3 months of therapy. C and F: After 15 months. After 16 months of response under continuous MK-2206 treatment, the patient relapsed (images not available). Image reproduced with permission from Rebecca et al., 2014.*

a switch to favourable environmental conditions, or the acquisition of additional mutations not targeted by the therapy.

The current paradigm for the treatment of metastatic melanoma includes a combination of chemotherapy and targeted therapy. The former indiscriminately attacks all cell types, both cancer and non-cancer, damaging the DNA and triggering mechanisms of controlled cell death. The latter specifically blocks a molecular pathway on which the cancer cells are strongly dependent, resulting in reduced toxicity for the whole body and increased specificity for the tumour. This combined therapeutic strategy is commonly adopted in a variety of cancers, including NSCLC and typically leads to a good initial response, including partial and complete disease regression. Nevertheless, in most cases the success of the therapy is only temporary and relapse seems to be inevitable (Palmieri et al., 2013, Sosman et al., 2012, Van Allen et al., 2014). Figures 2.1 and 2.2 show two examples of successfully treated cases of metastatic melanoma, followed by relapse.

Figure 2.3 shows a typical response curve for NSCLC patients undergoing such therapy. The initial response to a targeted treatment is followed by progression, indicative of the emergence of resistance, which suggests treatment failure. Upon removal of the

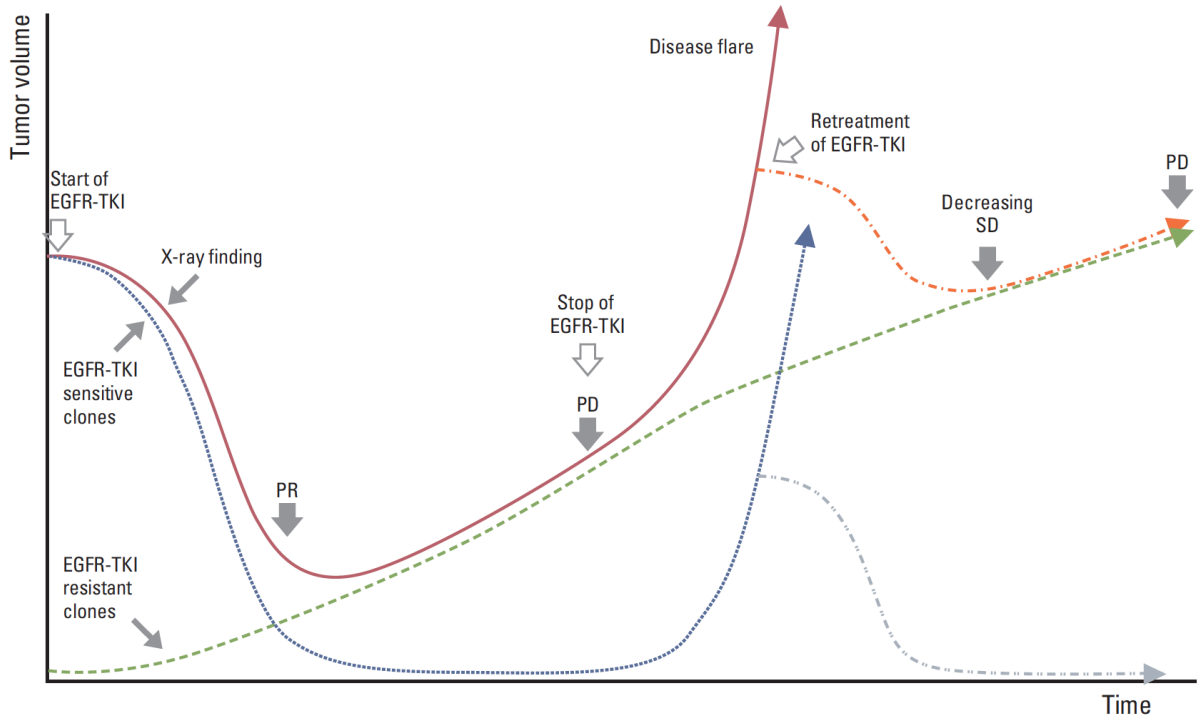


Figure 2.3: *Schematic of tumour volume evolution in time following the current therapeutic paradigm with targeted therapy (in this example EGFR-TKI: Epidermal Growth Factor Receptor Tyrosine Kinase Inhibitor, for non-small-cell lung cancer). The red line represents the tumour burden, as measured with X-rays. Partial Remission (PR) is initially observed. When progressive disease (PD) follows, the patient is removed from the therapy. Disease flare follows. If treatment is reintroduced (dashed orange line) a stable disease state (SD) can be achieved. Blue and green lines represent the sensitive and resistant components of the total tumour burden, respectively. Figure from Lee et al., 2013, reproduced under CC BY-NC 3.0.*

targeted drug, a typical *disease flare* is observed (Chaft et al., 2011 and Lee et al., 2013), suggesting that the treatment has somehow selected for a more aggressive clonal population from the tumour. However, a second treatment with the same inhibitor often leads to additional response (Figure 2.3, orange dashed line), suggesting that selection of resistant clones alone cannot explain the disease progression under treatment.

Following the description of the molecular pathways on which targeted therapies act, we will investigate possible mechanisms in the tumour microenvironment that can explain the response and relapse dynamics observed in patients with molecularly targeted tumours.

2.1 Targeting Proliferation and Survival Mechanisms

In malignancies highly dependent on a specific pathway, such as many melanomas, lung and breast cancers, the emergence of resistance is a non-trivial and multi-factorial process.

Therapies that aim at blocking the constitutive activation of a specific pathway, thought to confer resistance, often result in treatment failure. Such pathways often control proliferation, survival, or cell death, are extremely robust and can have many alternative routes that allow constitutive reactivation.

Metastatic melanoma offers a good paradigm for the investigation of drug resistance in tumours characterised by a high degree of molecular heterogeneity. Moreover, the signalling pathways controlling cell proliferation and cell death in this disease are similarly deregulated across a variety of other tumours (Porta et al., 2014). Therefore, understanding the mechanisms of therapeutic failure when using therapies that target such constitutively activated pathways is of broad interest.

The mitogen-activated protein kinase (MAPK) pathway consists of a chain of proteins starting from cell-surface receptors and ending in the nucleus, where changes in protein expression are elicited, leading to regulation in cell division and death events. The pathway involves a cascade of phosphorylation events, creating an on/off switch in key regulators of the cell cycle. When one of these regulators is mutated, a constitutive activation of the pathway leads to oncogenic cell proliferation and escape from apoptosis, hence uncontrolled malignant growth (Weinberg, 2006). In the MAPK pathway the RAS protein represents the interface between the cell and the environment. RAS is tethered to the cell surface and is characterised by an effector loop that can bind several proteins, known as *RAS effectors* (Figure 2.4).

The majority of cutaneous (skin focussed) melanoma (at least 70%) harbour a mutation in the MAPK pathway, specifically in genes encoding for one of the RAS effectors. BRAF mutations account for up to 60% of melanomas, and lead to constitutive activation of the MEK-ERK pathway, a signalling cascade that leads to enhanced proliferation, angiogenesis, cancer cell differentiation and survival (Mc Cubrey et al., 2007). Almost all of BRAF mutated melanomas (approximately 90%) harbour a point mutation consisting of a substitution of valine to glutamine at the 600th amino acid position (V600E). The overwhelming majority of melanoma patients present aberrant activation of the MAPK pathway. However, the high rates of BRAF mutations found in benign *nevi* (moles) suggest activation of the MAPK pathway alone is not enough to explain the pathogenesis of melanoma.

It is becoming increasingly clear that other signalling pathways may be equally as important. Other predominant mutations affect another RAS effector, PI3K, and the corresponding downstream signalling pathway, known as the PI3K-AKT-mTOR pathway (Figure 2.4). Activated AKT can phosphorylate a number of different substrates, determining:

- anti-apoptotic signalling, by inhibition of proteins involved in apoptotic programs;

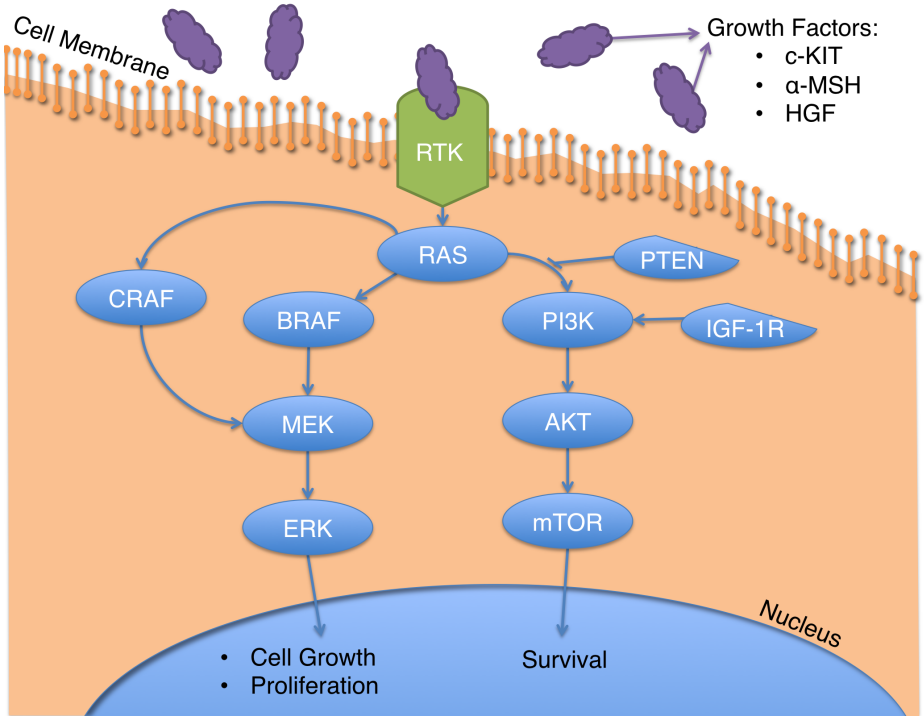


Figure 2.4: *The RAS effectors and corresponding pathways regulate cell proliferation and survival.*

- proliferative signalling, via regulation of proteins related to the cell cycle advance;
- growth, controlling synthesis of proteins related to the accumulation of cellular components necessary for cell growth.

Deregulation of this pathway usually involves either PI3K hyperactivation or PTEN inactivation (Paraiso et al., 2011). The latter is more frequently observed: PTEN activity loss accounts for 30% to 40% of human cancers. High AKT activity in patients correlates with far worse overall survival compared to patients with low AKT activity. Moreover, the percentage of high AKT activity has been observed to increase with the progression of melanoma, accounting for approximately 77% of the cases of metastatic disease.

Constitutive activation of the RAF-MEK-ERK and PI3K-AKT-mTOR pathways determines a shift in the mechanisms of control of cell growth and survival, leading to a competitive growth advantage to clones harbouring these mutations. It is therefore necessary to develop a strategy that reverses the activation of these pathways. Recently a new type of treatment, less aggressive than chemotherapy and effective on cancers that are strongly dependent on the signalling of one oncogene, is gaining preference. So-called *targeted therapies* aim at suppressing the key driver mutations found in a given type of cancer, as opposed to chemotherapy, which kills indiscriminately all cells in the division phase of their life cycle, eventually damaging the whole tissue and bringing severe toxicity

to the patient's body. Since the majority of melanoma cells present aberrant activation of the MAPK pathway and the inhibition of RAS has proven difficult with currently available approaches (Keeton et al., 2017), strategies have focused upon targeting RAF and MEK and, most recently, even ERK, the downstream effector of the pathway. Although much success has been achieved with the use of BRAF inhibition in melanomas with activating BRAF mutations, these BRAF inhibitors cannot be used in BRAF wild-type cells with constitutive MAPK activity. Indeed it has been observed that BRAF inhibitor treatment in BRAF wild-type melanoma patients results in the induction of paradoxical BRAF/CRAF signalling, which leads to hyperactivation of ERK (Poulikakos et al., 2010). In the following we will focus our study on the emergence of drug resistance both in BRAF wild-type melanomas treated with AKT inhibitors, and BRAF mutated melanomas treated with BRAF inhibitors.

We will review the role of the tumour microenvironment (the tumour *stroma*) in the modulation of the response to treatments and the emergence of resistance. Treatment strategies molecularly targeting the stromal components are currently under investigation (Viale et al., 2013). The development of such strategies presents a number of challenges, mainly because such a therapy would target a normal cell type, present in all connective tissues throughout the body. A more promising target is the tumour-stroma dialogue (Mc Millin et al., 2013, Hirata et al., 2015). This type of treatment will aim at modulating the interactions between the tumour and its microenvironment, affecting sensitivity to anticancer strategies directed at cancer cells (such as AKT or BRAF inhibitors).

2.2 The Tumour Microenvironment

In the last few decades the crucial role of the microenvironment as a key modulator of tumour progression and therapeutic response has been recognised. The tumour microenvironment is composed of the extracellular matrix (ECM), and a number of soluble factors and insoluble components (Tlsty and Coussens, 2006). Growth factors, nutrients and chemokines are examples of these factors. The ECM provides the structural scaffolding and contextual information to the cancer cells. It supports cell adhesion and allows the transmission of signals between cells. However, the main active components in the interaction with the tumour are the other cell types, which can be classified as normal, or *stromal*, cells. Fibroblasts, immune cells, endothelial cells, epithelial cells, and cells lining blood and lymphatic vessels have been shown to play an active role during cancer development.

Fibroblasts are the main component of the connective tissue. They are responsible for the production and regulation of ECM remodelling components, as well as a number

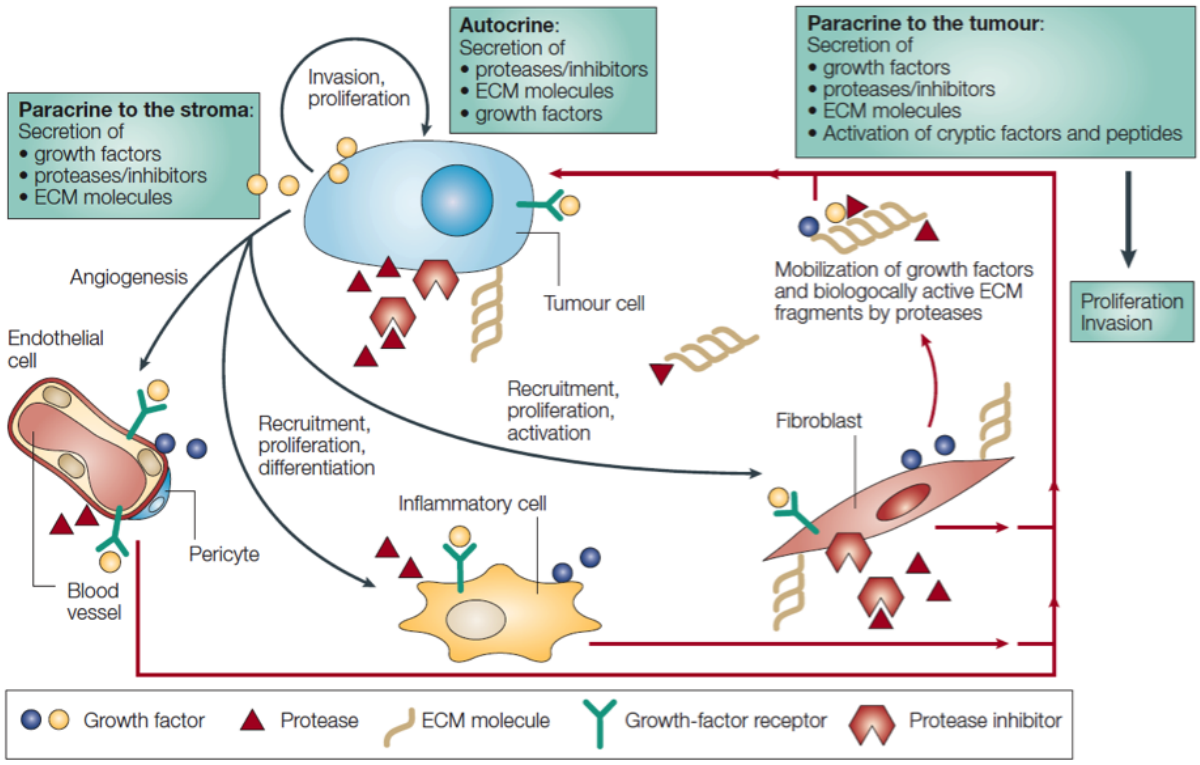


Figure 2.5: *The cross-talk between tumour cells and the activated stroma, reproduced with permission from Mueller and Fusenig, 2004. This schematic highlights the complicated feedback interactions between the tumour and its microenvironment. Paracrine signallling, originating from the cancer and directed to the stroma, induces recruitment of stromal cells (fibroblasts, endothelial and immune cells). Recruited stromal cells (also defined as "reactive") increase production of growth factors and remodelling of the ECM, offering survival and protecting stimuli to the cancer cells, and reinforcing the paracrine signalling with the tumour.*

of growth factors modulating signalling of cell proliferation and survival (Mueller and Fusenig, 2011).

Cells of the immune system also play a major role in the development of tumours. Activated inflammatory cells represent a *promoting* factor that, following initiation, can directly facilitate tumour progression. Specifically, this mechanism consists of tumour exposure to immune cell-derived soluble factors regulating proliferation, migration and genomic integrity (Holzel et al., 2013).

The cross-talk between the cancer cells and the stroma was meticulously analysed and schematically described in a review paper by Mueller and Fusenig, 2004 (reproduced in Figure 2.5). It is believed that tumour cells have the ability to actively modify their surrounding environment, inducing the stromal cells to form a permissive and supportive environment. Cancer cells can activate stromal cells, releasing a number of growth factors, pro-migratory ECM components, and proteolytic enzymes, together with their inhibitors, to modulate the remodelling of the matrix. These secreted factors initiate

a cascade of activating and proliferating signals, which act in both an autocrine and paracrine manner, establishing positive feedback loops that ultimately allow the formation of a permissive and supporting environment. Given their modified nature, with enhanced motility, proliferation and expression of key growth factors and their receptors, fibroblasts and stromal cells found in tumours are often referred to as *cancer associated fibroblasts* (CAFs) and *reactive stromal cells*, respectively (Mueller and Fusenig, 2011). Their role in melanoma has previously been investigated by Flach and colleagues, with an integrated mathematical and experimental approach (Flach et al., 2011). Their work will be described in detail in Section 3.4.

This microenvironment modulated perspective of tumour development has three main implications. First, the cancer cell population is not simply the passive target of accumulated random mutations. Indeed it plays an active role in tumourigenesis, recruiting a reactive stroma that facilitates progression to a malignant and invasive stage. Second, the tumour and the stroma have to be considered together as an evolving system, where subpopulations with a phenotypic advantage arise, as a consequence of the selective pressure of the microenvironment. We believe that evolution selects, upon both cancer and stromal cells, for those phenotypes more fit to survive in the dynamic microenvironment. Therefore, in line with the Mueller and Fusenig perspective, cooperation and possible co-evolution between the most fit subpopulations of the tumour and stromal components of the system seems to be a valid working hypothesis. Third, in relation to cancer therapy, the key implication of the dynamic cross-talk between the tumour and its stromal surroundings is environment-mediated drug resistance (EMDR).

2.3 Environment Mediated Drug Resistance

Tumour-stroma interactions have been recognised to be crucial in the modulation of factors that allow therapeutic escape and post-therapy relapse. The population of surviving cells following treatment is known as *minimal residual disease* (Meads et al., 2009). Such a population can be the result of the transient protective action of the tumour microenvironment, established as a result of the dialogue between tumour and stromal cells. Indeed the initial, rapidly developed, resistance to therapy is mainly attributed to EMDR (Meads et al., 2009).

Microenvironmental factors driving this type of drug resistance can include induction of gene transcription or non-transcriptional mechanisms, respectively, cell adhesion-mediated drug resistance (CAM-DR) and soluble factor-mediated drug resistance (SFM-DR). Both types of EMDR protect tumour cells from immunological mediators of cell

death and chemotoxics by modulation of molecules that control apoptosis and proliferation.

Once EMDR is established, selective pressure from the therapy can drive the so-called *acquired resistance*, involving the emergence of a population of highly resistant phenotypes that are not dependent on the environment.

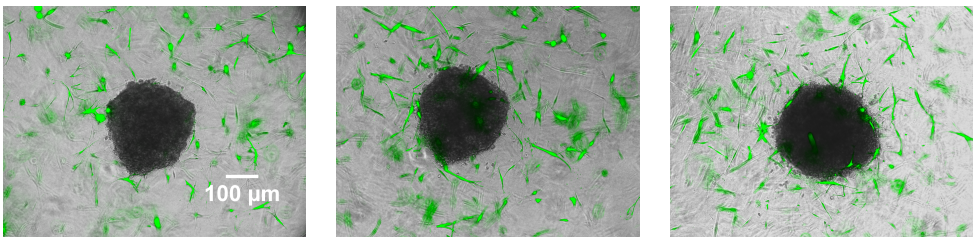
2.3.1 Cell Adhesion-Mediated Drug Resistance

Adhesion of integrins displayed at the tumour cell surface with ECM components (fibronectin, collagen, laminin), or ligands expressed on stromal cells, triggers mechanisms leading to drug resistance. These mechanisms are non-transcriptional: they involve cellular redistribution of regulators of proliferation and apoptosis, or proteosomal degradation of pro-apoptotic proteins. For example, $\beta 1$ integrin-mediated adhesion induces resistance to FAS (a surface receptor that induces apoptosis) shifting the anti-apoptotic protein CASP8 from the cytoplasm to the cell membrane (Shain et al., 2002). Additionally $\beta 1$ integrin adhesion induces degradation of BIM, a pro-apoptotic mediator (Hazlehurst et al., 2007). Finally, adhesion of metastatic epithelial tumour cells has been shown to trigger mechanisms of dormancy that allow transient resistance to cytotoxics (White et al., 2006).

2.3.2 Soluble Factor-Mediated Drug Resistance

The second type of EMDR involves modulation in the expression of chemokines and cytokines, resulting in upregulation in the expression of pro-survival factors. As a result of a dynamic cross-talk between tumour and stromal cells, which provides paracrine amplification, resistance-inducing factors are consistently produced. For example, interleukin 6 (IL-6) and stromal cell-derived factor 1 (SDF1) have been observed to be highly expressed across a variety of liquid and solid tumours (Castells et al., 2012).

The current understanding of the way in which all of these mechanisms come together to allow initial transient resistance, survival and eventually emergence of acquired, long term resistance is poor. This complex system is composed of tumour and stromal cells, soluble factors and local cell-cell interactions. CAM-DR and SFM-DR are strongly interconnected. For instance, soluble factors can increase expression of integrins or the affinity for ligands on tumour cells, contributing to CAM-DR (Hartmann et al., 2005 and Sanz-Rodriguez et al., 2001). It is therefore hard to establish a causal representation of the steps that lead to the emergence of resistance. The current hypothesis is that a pool of dormant cells, positioned in a protective microenvironment, survive treatment and later



(a) 1 day (b) 4 days (c) 7 days

Figure 2.6: *Fibroblast recruitment by melanoma cells and consecutive infiltration of fibroblasts in the melanoma spheroid (dark region). Fibroblasts are tagged with a green fluorescent protein. Images courtesy of the Smalley laboratory, Moffitt Cancer Center, Tampa.*

on proliferate acquiring more permanent resistance mechanisms and remodelling the very same environment (Meads et al., 2009).

2.4 Experimental Evidence for EMDR in Melanoma

The disrupted regulation of key signalling molecules and redundancy in proliferative and anti-apoptotic pathways in melanoma is one face of the resistance to anti-cancer therapies. In Section 2.3 we discussed the importance of the environmental component in the response to the treatment. A particular instance of EMDR in melanoma is represented by the production of fibronectin and growth factors by CAFs which allows for adhesion-mediated drug resistance.

A group of experimentalists at the Moffitt Cancer Center (the Keiran Smalley laboratory) have experimentally shown the adherence and infiltration of cancer-recruited CAFs into melanoma spheroids, as illustrated in Figure 2.6. The presence of recruited CAFs, "activated" by melanoma cells, induces an increased ECM deposition, as shown in Figure

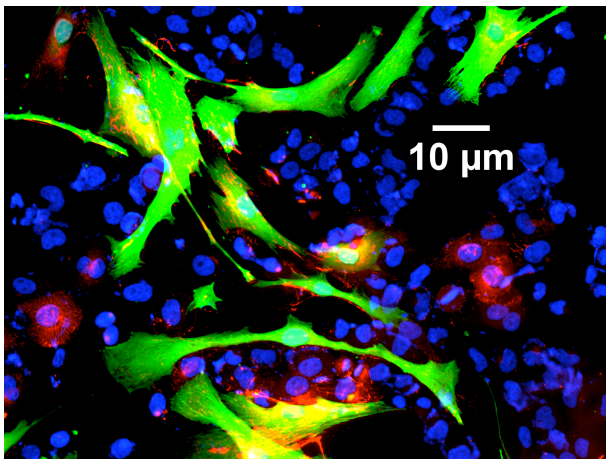


Figure 2.7: *ECM deposition (red) by activated fibroblasts (green), recruited by melanoma cells (blue). Yellow and purple stains correspond to superposition of colours. Image courtesy of the Smalley laboratory, Moffitt Cancer Center, Tampa.*

2.7. Finally it was shown that melanoma cells alone do not produce fibronectin, proving the key role of the interaction between cancer and host cells in the structural stabilisation of the tumour mass (Flach et al., 2011).

The complex biological system that we propose to study includes the presence of targetable mutations in the cancer cells, the environmental modulation of the response to treatment and the emergence of resistance.

Having briefly reviewed the relevant biological background, in Chapter 3 we will present a review of relevant mathematical models.

Chapter 3

Mathematical Modelling of Cancer Growth and Treatment

The biological system that we intend to study is composed of heterogeneous populations of both tumour and stromal cells, and non-cellular components such as the ECM and soluble factors. We wish to analyse the effect of various treatment regimes, including three types of drugs: a cytotoxic chemotherapeutic agent, a cytostatic targeted agent, and a stromal-targeted agent. The failure of such therapeutic strategies, especially after initial response, suggests the presence of intricate mechanisms of resistance (see Sections 2.3 and 2.4). The interaction with the tumour microenvironment appears to be crucial in the regulation of such mechanisms.

A vast literature of mathematical models for nearly every stage of cancer growth and progression is available (Altrock et al., 2015, Anderson and Quaranta, 2008, Byrne, 2010). Here, we restrict our literature review to only the relevant areas of our current study. Our modelling will focus on the interactions between cancer cells and their environment, and, in particular, on those interactions which facilitate the emergence of resistance to treatment. In the context of malignant melanoma, a very limited portion of the literature is dedicated to these aspects. Most of the previous mathematical models have focussed on the interactions with the immune system, which constitutes only part of the tumour microenvironment. For example, in the work by Pennisi (2012), an ordinary differential equation (ODE) model of immunotherapy describes the dynamics of the immune response driven by the competition between melanoma cells and injected antibodies. De Pillis and colleagues model the mechanisms of tumour surveillance (De Pillis et al., 2005). Using a system of nonlinear ODEs they model the interactions between two types of immune cells ($CD8^+$ T cells and natural killer cells) and tumour cells and validate their findings against data from metastatic melanoma patients treated with immunotherapy. A similar model, including tumour and immune cells, explores the combination of chemotherapy and immunotherapy (interferon-α treatment) in different sequence strategies (Isaeva et

al., 2009). A spatial description of the tumour-immune dynamics in recurrence is proposed by Eikenberry and colleagues (Eikenberry et al., 2009). Their reaction-diffusion framework includes a detailed description of angiogenic-mediated invasion and immunosuppression. However, it considers treatment by surgical excision only. Since the relevant literature is limited, specifically for melanoma, we present a broader review of modelling in different cancer applications but continue to restrict our interest to only relevant areas.

3.1 Cancer Cell Population Growth

Depending on the type of application, the description of tumour growth can be approached at the macroscopic length scale or at the microscopic cell scale. The former approach consists of a spatially averaged description of the events happening at the cell scale resulting in the observed growth of the tumour mass. Models following this approach are classified as *continuum* mathematical models. At their simplest they describe the variation in time of quantities such as tumour volume or size and take the form of ODEs. Various paradigms have been used to describe the evolution of the size of the tumour in time. A widely used model, mostly for its simplicity and ability to capture the behaviour of early stage, unconstrained tumour growth, is the *exponential growth* model:

$$\frac{dV}{dt} = \rho V. \tag{3.1}$$

This ODE describes the tumour volume as a function of time, $V(t)$. The assumption of constant growth rate ρ implies a constant doubling time: $t_D = (\log 2)/\rho$, a quantity that can be easily estimated from experimental measurements.

A more general model is: $dV/dt = \rho V^k$, with $k \in \mathbb{R}$. An approximate value for the power $k \approx 2/3$ was obtained by fitting growth curves for animal tumours (Dethlefsen et al., 1968). The physical interpretation of this value involves the proposal that growth is proportional to the size of the surface area $V^{2/3}$, through which the tumour receives resources necessary for proliferation.

Alternative descriptions of tumour growth account for limiting factors such as space and nutrient constraints. The ones predominantly used are the *logistic*,

$$\frac{dV}{dt} = \rho V \left(1 - \frac{V}{K}\right), \tag{3.2}$$

where K is the carrying capacity, and the *Gomperzian*,

$$\frac{dV}{dt} = \rho V \ln\left(\frac{K}{V}\right). \tag{3.3}$$

Both equations have solutions with sigmoid shape and saturation to an asymptotic value. The Gomperzian growth model is the more commonly adopted, given the ease of fit to

growth curves for experimental data (e.g. Iwata et al., 2000). Alternative models are derived from phenomenological observations. For example, if we consider surface area-limited growth and a death process occurring proportional to the volume, at constant rate δ, we obtain the *Bertalanffy* equation (Bertalanffy, 1949):

$$\frac{dV}{dt} = \rho V^{2/3} - \delta V. \tag{3.4}$$

The advantage of this approach is that, unlike the Gomperzian law, it is based on the biology of the system. This confers predictive power to the model, and allows for the exploration of mechanisms and dynamics underpinning the observed phenomenon. As remarked in a recent review by Gerlee (2013), the choice of the growth model should not be driven by the ease of its fit to data. A model has to include an appropriate description of the possible mechanisms that drive the observed biology, in order to serve as a prediction tool for other biological applications, instead of merely describing the observed system.

From an experimental perspective, tumour growth is best observed using tumour spheroids or cell culture assays as these allow one to gain a deeper understanding of the mechanisms underlying the observed growth dynamics. The models presented above can be extended to include a spatial description of the tumour density $u(\mathbf{x}, t)$ (where $\mathbf{x} \in \Omega \subset \mathbb{R}^d$ is the space vector in a $d-$dimensional space domain Ω), in the framework of partial differential equations (PDEs). Adding a diffusion term to the nonlinear ODEs of the models previously described, results in the *Fisher-Kolmogorov* equation (Fisher, 1937 and Kolmogorov et al., 1937):

$$\frac{\partial u}{\partial t} = \alpha u(1 - \beta u) + D\nabla^2 u, \tag{3.5}$$

where α is the proliferation rate, β is the carrying capacity, and D the diffusion coefficient. This is a nonlinear reaction-diffusion equation, whose solution can be explored in the form of a travelling wave with constant speed. Other examples of spatial continuum models, accounting for more than just the growth of the tumour mass, will be presented in Section 3.2.

Most widely used continuum models are deterministic. However, to account explicitly for phenomena causing noise or fluctuations in the described quantities (e.g. variations in the cell metabolism or cell cycle), stochastic continuum models can be used. Moreover, if in the biological system of interest stochasticity involves processes occurring at the single cell scale, thus including cell-cell interactions, the continuum approach is not suitable. Drasdo and colleagues proposed an individual-based model of birth and death in cancer (Drasdo et al., 2003). Their approach not only accounts for the stochasticity of events at the cell scale, it also explains, with a single mechanism, the two regimes of growth

experimentally observed in early stage tumours: the initial exponential regime, followed by slower growth with proliferation limited to the outer rim of the spheroid. This description involves an energy function, resulting from the balance between the adhesion forces between cells and the repulsion due to a limit of compression that a cell can withstand from its neighbours.

3.2 Cancer Cell-Environment Interactions

Relevant to our application is the modelling of tumour growth dynamics in the context of interactions with the environment. A prominent example of a phenomenological approach to the spatial modelling of tumour growth within its environment is given by Gatenby and Gawlinski (1996). Their model describes acid-mediated cancer invasion, in the framework of nonlinear reaction-diffusion equations, with carrying capacity-limited growth and density dependent diffusion:

$$\begin{aligned}
\frac{\partial u}{\partial t} &= \rho_u u\left(1-\frac{u}{K_u}-\alpha_u\frac{v}{K_v}\right)-\delta_u w u+\nabla\cdot(D_u(v)\nabla u),\\
\frac{\partial v}{\partial t} &= \rho_v v\left(1-\frac{v}{K_v}-\alpha_v\frac{u}{K_u}\right)+\nabla\cdot(D_v(u)\nabla v),\\
\frac{\partial w}{\partial t} &= \rho_w v-\delta_w w+D_w\nabla^2 w
\end{aligned} \tag{3.6}$$

where u and v are normal tissue and tumour densities, respectively, ρ_u and ρ_v are proliferation rates, K_u and K_v are carrying capacities, $D_u(v)$ and $D_v(u)$ are density dependent diffusion coefficients, α_u and α_v are competition parameters. w represents the concentration of excess acid toxic to normal tissue (resulting in death at a rate δ_u). It is assumed to be produced by tumour cells at rate ρ_w, cleared out at rate δ_w, and diffuses with diffusion coefficient D_w. This phenomenological model led to the formulation of important predictions that were subsequently tested and validated against *in vitro* and *in vivo* experimental findings.

An extension to the Gatenby and Gawlinski model was proposed by Martin et al. (2010). With a similar system of PDEs they investigated the role of competition and cooperation between the tumour and normal tissue, including normal cells, the ECM, and its degrading enzymes. The ECM is explicitly accounted for as a limiting factor in the tumour diffusion term: $\nabla\cdot\left[D_v(1-u/K_u)(1-m/K_m)\nabla v\right]$, where m is the ECM density, and K_m its carrying capacity. The model was solved on a one-dimensional domain, assuming there are no normal cells inside the tumour boundary and normal cells are at carrying capacity outside the tumour. Travelling wave solutions predicted an interesting behaviour. With increased acid production, the gap formed at the interface

between tumour and normal tissue is increased. The lack of contact between normal and cancer cells reduces the production of matrix degrading enzymes. Therefore the poorly degraded ECM at the invading front encapsulates the mass, limiting the expansion of the tumour. Similar mechanisms of invasion were modelled in Perumpanani et al. (1996) and Anderson et al. (2000) within the same framework (systems of coupled PDEs).

An alternative modelling approach involves the description of dynamics and interactions at the single cell scale, while incorporating environmental components, such as nutrients and soluble factors, that are better characterised in the continuum. This class of models, known as *hybrid discrete-continuum* (HDC), allows us to consider heterogeneity across scales: from the tumour cell behaviour, its environmental context, up to the tissue level. Anderson and colleagues explored the potential of this modelling approach, and other individual-based approaches such as the *immersed boundary cell* model, in the investigation of tumour morphologies emerging from environmental-driven invasion (Anderson et al., 2009). Recent work by Kim et al. (2013) represents the most relevant example of a HDC description of tumour-stromal interactions and their role in melanoma initiation and progression. The enhancing action of senescent fibroblasts on early-stage melanoma cell growth and invasion is investigated with an integrated experimental-theoretical approach. This model recapitulates *in silico* counterparts of experimentally observed phenomena such as wound healing and senescent fibroblast-induced invasion. The HDC modelling framework, together with the relevant literature, will be described in detail in Chapters 6 and 7, where it will be applied to the study of EMDR.

3.3 Modelling Drug Administration and Resistance

The extension of the continuum models to include the effects of cytotoxic therapies is straightforward. Chemotherapy administration can be modelled by including a death term in any of the systems of equations (presented earlier) that describe the evolution in time and space of the tumour mass. The implementation of specific targeted therapies, however, requires that the relevant environmental factors are included in the model. For example, Hinow and colleagues proposed a model of tumour-host interactions including oxygen concentrations and vascularisation (see Hinow et al., 2009). This set up allowed the investigation of the effects of chemotherapy and anti-angiogenic treatment. Specifically, they modelled the concentration of a cytotoxic drug c (normalised to 1) with the reaction-diffusion equation:

$$\frac{\partial c}{\partial t} = D_c \nabla^2 c + \alpha(t) m(1-c) - \gamma c - \kappa n c, \tag{3.7}$$

where m is the density of endothelial cells (i.e. the vasculature: the entry point for the drug), n is the density of normoxic tumour cells, which are the target of the chemotherapeutic drug. $\alpha(t)$ is a time-dependent drug production rate (allowing simulation of any given treatment schedule), γ is the rate of decay, and κ is the rate of consumption corresponding to kill of normoxic cells. The term $\alpha(t)m(1-c)$ assumes that flow into the tumour is down a concentration gradient (where the concentration in the blood is normalised to 1) and proportional to the vasculature density (taken to be proportional to the number of endothelial cells). For a complete description of the model, including equations for n and m, we refer to the original paper (Hinow et al., 2009).

Including resistance in the model is necessary for a systematic study of therapeutic strategies aimed at the optimisation of treatment. When it comes to scheduling design for cytotoxic agents it is necessary to account for toxicity effects of prolonged drug administration. Additionally, in the context of resistance, a trade-off for the treatment window must be considered. Too long an exposure will facilitate emergence of resistance, while too short an exposure increases the chances of the therapeutic escape of a bigger portion of the tumour cells. Resistance and treatment optimisation have been investigated with a variety of approaches and with specific applications. Coldman et al. (1983), for example, modelled resistance as the accumulation of single mutational events following a Poisson process. The mutation probabilities were related to dose of the drug, and multi-drug treatments were considered. They aimed at maximising the probability of cure (by eradication of the resistant strain) and proved that alternating doses of non cross-resistant drugs are to be preferred to pulses of a single chemotherapeutic agent. The latter favours the emergence of resistance during the drug holiday.

A mathematically elegant approach to a similar optimisation problem was proposed by Hahnfeldt et al. (2002). Using two sensitivity compartments, and assuming exponential growth and linear log-kill, they analytically described the two tumour populations and their modulation by different treatment strategies. They make the case for maintenance through growth suppression to be preferred to tumour eradication with maximum tolerated dose.

The use of control theory for therapeutic optimisation was proposed by Ledzewicz et al. (2013). They used this approach to investigate a cell cycle specific model of cancer treatment but limited this optimization to the application of a single chemotherapeutic agent. Unlike Coldman et al., the description of resistance does not involve mutational events. Instead, they model resistance through the cell distribution in the various cell cycle phases, to justify the fractional kill by the drug.

In certain situations the eradication of cancer has become an unrealistic endpoint: given the heterogeneous and plastic nature of tumours, evidence of residual disease is

commonly found even after treatment with the maximum tolerated dose (Baldi et al., 2000). Alternatively the clinical situation can suggest that disease control is preferable to eradication through toxic and painful treatments. This is the case of palliative or failed cure, which has been modelled by Monro and Gaffney (2009). With a nonlinear system of ODEs they model the competition dynamics between sensitive and resistant tumour populations, predicting longer survival with reduced chemotherapy protocols.

Other modelling approaches to the problem of treatment optimisation in the context of resistance are presented in a recent review by Lavi et al. (2012). They remark on the importance of creating models that include different types of resistance, since relapse can be caused not only by mutations, but also by cells surviving in favourable microenvironmental conditions.

3.4 Modelling Tumour-Stroma Interactions and Treatment

As previously stated, the mathematical literature for tumour-stroma interactions in the context of resistance is sparse, and mainly focused on specific dynamics involving the immune system. The most relevant model exploring the role of the stroma in the tumour growth dynamics and response to therapy was proposed by Flach et al. (2011). This model is formulated in terms of ODEs and describes the interactions between fibroblasts and cancer cells, including recruitment of specialised stromal cells that create a protective niche for the tumour leading to therapeutic escape. We discuss this approach in more detail, as it will constitute the starting point for the formulation of our model.

The model includes the dynamics depicted in Figure 3.1, in an attempt to describe the behaviour experimentally observed (tumour-recruited stroma cells enhancing treatment escape, see Section 2.4). Four cell populations are considered: "free" cancer cells, "fixed" cancer cells, "blocked" cancer cells and activated fibroblasts. This classification corresponds to the spatial position and proliferative state of cells. At the leading edge of the tumour mass, "free" cells stimulate the activation of fibroblasts, which in turn promote cancer cell stabilization: "free" cancer cells become "fixed", i.e. protected by the action of the stroma. Fixed cells divide, inheriting the protected state, and the tumour grows, and as cells accumulate, a portion of them, close to the inner core, become non-proliferative: these are classified as "blocked" cancer cells. It has to be noted that the fibroblast compartment represents the population of CAFs only, and it does not include all the non-activated fibroblasts present in the stroma. Therefore the growth term in the model corresponds to an actual recruitment, instead of cell division. This model does not

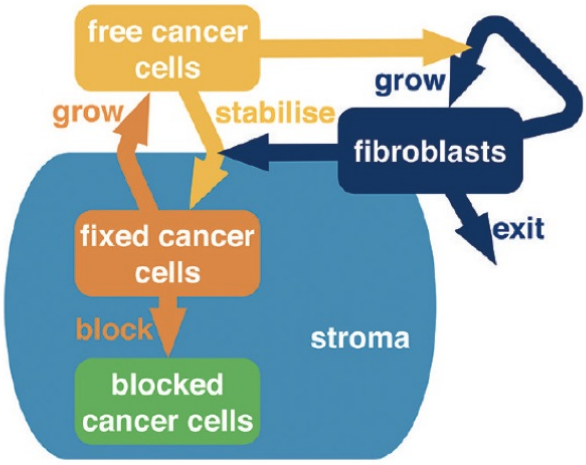


Figure 3.1: *Schematic of the Flach model, reproduced with permission from Flach et al. (2011). The tumour is divided into three compartments: "free", "fixed" and "blocked". The stroma is represented by one compartment only, composed of the cancer associated firbroblasts (CAFs). Cancer cells at the leading edge of the tum our ("free" cancer cells) stimulate the activation of stroma, resulting in growth of the CAF population. CAFs provide stabilisation by allowing the transition from free to "fixed" (i.e. protected) cancer cells . The accumulation of the latter will create an inner core of non-proliferative, "blocked" cancer cells.*

include a spatial component but rather assumes a well mixed system, and is defined as follows:

$$\begin{cases} \dfrac{dc}{dt} = \vartheta s - \sigma c \bar{f}; \\ \dfrac{ds}{dt} = \sigma c \bar{f} - \beta s; \\ \dfrac{db}{dt} = \beta s; \\ \dfrac{df}{dt} = \varphi f \bar{c} - \delta f; \end{cases} \tag{3.8}$$

where c, s, b, f are the free cell, fixed cell, blocked cell and fibroblast populations, respectively. The positive parameters $\vartheta, \varphi, \sigma, \beta, \delta$ are cancer cell division, fibroblast growth, cancer cell stabilisation, cancer cell self-blocking, and fibroblast activation rates, respectively. The interaction terms, i.e. stabilisation and activation, are scaled by the total population size: $n = c+s+b+f$, so that $\bar{f} = f/n$, and $\bar{c} = c/n$. This type of scaling, according to the relative abundances in the population, was introduced in the original paper for the interaction to be dependent on the proportion of cell types in the environment, instead of their total count. Indeed, without the normalisation term, the interactions would be assumed to take place between all cells, even at long distances. The original paper does not include a formal definition of initial conditions. However, we can determine from the plot of the solutions that the system is initialised with 10 fibroblasts, 10 free cancer cells, and no fixed nor blocked cancer cells. A continuum description might

not be appropriate for such small cell numbers. If we consider n cells, and assume their properties to be independent and identically distributed, the average of the population is an acceptable approximation of the collective behaviour, provided that the population size n is large enough. According to the central limit theorem, the variation about the deterministic limit is of order $1/\sqrt{n}$. In order to obtain an indicative lower bound on n to justify the continuum description, we consider a small standard deviation, in the order of 0.1, corresponding to a population size of 100 cells. Despite the initial population size in the original paper being below this value, the results therein presented are not directly linked to experimental measurements and aim at a qualitative representation of the dynamics. In the following application we will consider a higher magnitude of the cell populations, representative of the experimental data available.

3.4.1 Results and Critique

In the paper by Flach et al., the previously described mathematical model is initially used to simulate the dynamics of tumour growth, after initiation, in a pre-treatment window of time. Subsequently, through the introduction of treatment, tumour regression is described. With a series of repeated bursts of therapy, the tumour is shown to regrow slowly, without flare. Nevertheless, fibroblasts are shown to be the key drivers in the tumour regrowth. A key assumption here is that therapy does not affect the stromal cells. These dynamics are illustrated in Figure 3.2, where intermittent treatment with targeted therapy is simulated.

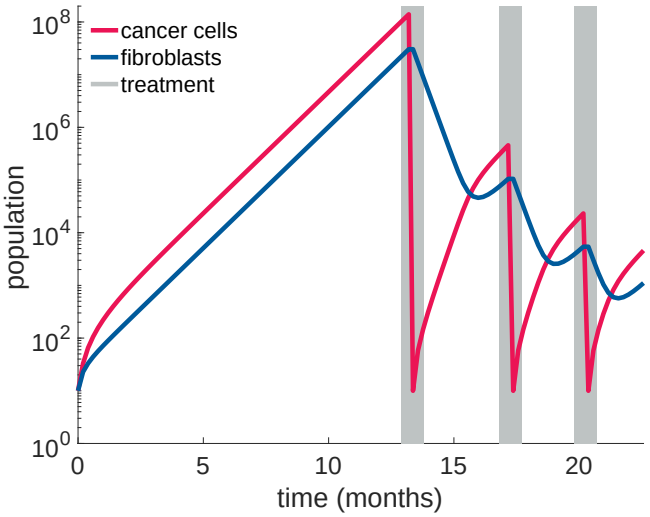


Figure 3.2: *Repeated treatment with targeted therapy in the Flach model (Flach et al., 2011). y axis in log scale. Parameter values:* $\vartheta = 1$, $\sigma = 1$, $\beta = 0.8$, $\varphi = 1$, $\delta = 0.1$. *Initial conditions:* $c(0) = f(0) = 10$, $s(0) = b(0) = 0$. *Initial conditions after treatment:* $c = 0$, $s = 10$, $b = 0$. *The results were obtained in Matlab with the numerical solver ode15s.*

The numerical implementation of the treatment consists of the solution of the system of ODEs in Eqs. (3.8), over consecutive time intervals, in which the drug is switched "on" or "off". At each burst of treatment the cancer cell population is reduced to 10 cells (independently of the magnitude of the cancer cell population present at the beginning of the treatment), whereas the fibroblast population is not affected by the drug. The overall cancer cell population is considerably reduced after consecutive bursts of treatment. Nevertheless the results are biased by the initial conditions imposed *a priori*, i.e. the constant number of cancer cells left behind by each drug administration. Clearly the feedback between the fibroblasts and the cancer cells allowing regrowth is hindered by the decreased initial cancer cell population. Consequently the regrowth of the fibroblast population will be delayed, affecting the growth dynamics in the following treatment-free window.

Finally, it is worthwhile to briefly discuss the approach to the modelling of interactions in Flach et al. (2011). In the original paper, recruitment and stabilisation are modelled by scaling the interaction rates with respect to the size of the interacting populations. The implicit assumption here is that the populations are well mixed, hence at each time the ratio between different cell types is spatially uniform. We would argue that the introduction of a spatial description of the system will circumvent this problem, while describing more realistically such interactions, which, by definition, are spatially characterised. In Chapters 6 and 7 we propose a spatial description of the local cell-cell interactions, and we discuss the advantages and drawbacks of introducing the well mixed approximation.

Having presented an overview of the biological background and the relevant mathematical models, in Chapter 4 we next present our application to the problem of tumour-stroma interactions and the emergence of drug resistance.

Chapter 4

Modelling Tumour-Stroma Dynamics in BRAF-wildtype Melanoma Growth and Treatment: Parameter Estimation

The aim of this thesis is to investigate the role of tumour and stromal interactions in mediating the treatment of metastatic melanoma (as a paradigm for molecularly targeted tumours). More specifically, we want to understand how these interactions facilitate drug resistance and how we can circumvent this resistance through smarter combination therapies.

Resistance can be described as the overall ability of the tumour to escape treatment, reducing response to the common therapeutic strategies and leading to further tumour progression. Intrinsic resistance due to a pre-existing mutant clone is one of the most common forms of resistance, however, our focus here is on microenvironment mediated resistance. To summarise the biological evidence described in Chapter 2, in the context of cancer therapy, we can identify two types of microenvironment modulated resistance. The first involves environment-driven phenotypical changes that confer an advantage to the cell and, through sequential genetic changes over time, lead to the emergence of a therapy-resistant phenotype. This is referred to as *acquired* resistance. The second kind of resistance is a *de novo* resistance, an environment-mediated type of therapeutic escape (Meads et al., 2009). It is referred to as *de novo* because it emerges from the transient action of the environment, inducing protection from apoptosis, through survival signals and structural support from host cells. *De novo* resistance is often transient, being induced by the protective action of reactive stroma, including:

a) cell adhesion mediated drug resistance (tumour cell integrins bind to ECM components or stroma receptors, inducing quiescence or evasion of apoptosis).

b) stroma-derived paracrine signalling, stimulating proliferation and survival in tumour cells.

The mechanisms driving tumour-stroma interactions that result in resistance are poorly understood. Starting from experimental observations, we aim to elucidate the key players and features that will allow us to describe the system with a simple, yet robust, mathematical model. The Flach model (Flach et al., 2011), described in Section 3.4, represents the result of an integrated mathematical and experimental framework and will be the starting point for our investigation. In addition to the previously presented experimental evidence of EMDR (Section 2.4), on which the Flach model is based, we will incorporate new experimental work.

We will present data from two distinct experimental models, with the scope of addressing the problem of drug resistance in two main types of melanoma. In this chapter we will introduce a model of BRAF-wildtype melanoma, treated with an AKT inhibitor in combination with chemotherapeutic agents. The second, presented in Chapter 5, is a model of BRAF-mutated melanoma, treated with a BRAF inhibitor in combination with a stromal-targeted agent.

This new work explores the effects of combined therapeutic strategies in regulating the emergence of drug resistance. Our ultimate goal here is to utilise the deeper understanding gained from our *in silico* modelling (aided by experimental observations) to develop better clinically relevant therapeutic strategies that exploit the interactions between tumour and stroma rather than ignore them.

4.1 Treating BRAF Wild-type Melanoma with AKT Inhibitor and Chemotherapy

Treatment options for melanomas characterised by aberrant MAPK activity, but lacking the BRAF mutation, are quite limited (see Section 2.1). The use of AKT inhibitors (AKTi) allows control of tumour burden. However, unlike BRAF inhibitors, AKTi induce a very limited amount of cell kill, and mostly work in a cytostatic manner. Therefore in the treatment of these tumours, AKT inhibition is often accompanied by a combination of chemotherapeutic agents, causing the bulk of cell death. In the following we will present an experimental model of BRAF-wildtype melanoma, formulate a mathematical model of the system, and introduce estimation techniques for model parametrisation. Finally we will replicate the dynamics of the system observed in clinical settings, and suggest an alternative course of treatment.

4.2 The Experimental Model for BRAF-wildtype Melanoma

Cell culture assays were performed by our collaborators in the Smalley laboratory at the Moffitt Cancer Center. The experimental *in vitro* data consist of several time series of melanoma cell counts for growth assays under different treatment and scheduling strategies. These data are summarised in Figure 4.1 and consist of monoculture[1] experiments where melanoma cells from two different cell lines (WM3918 and M257, both BRAF wild-type, RAS mutated melanoma cells) are treated with either:

- Chemotherapy (Paclitaxel and Carboplatin, cytotoxic agents), or
- Targeted therapy (MK-2206, an AKT inhibitor), or
- Combination therapy.

The assays cover a 16 day time span. The details of the therapy schedules are reported in Figure 4.1. Three replicas of each experimental setup were performed. Cell counts are reported at four time points (time = 4 days, 6 days, 8 days, 16 days). These experimental observations constituted the starting point in our process of understanding the effect of agents given in mono- and combination therapy upon melanoma cells. The outcome of combination therapy strategies varies between cell lines, making it hard to establish a ranking for the best treatment. However, we can observe that it is favourable to give a pulse of chemotherapy first for the AKT inhibitor to be more effective (compare T10 and T8 in Figure 4.1).

4.3 Modelling Tumour-Stroma Interactions and Emergence of Drug Resistance

In light of the new experimental data available, we developed a new dynamical system characterising the interactions occurring between the tumour and stromal cell populations under treatment.

As a first step, we propose to model the interactions observed in the context of these *in vitro* cell cultures. Here the dynamics are somewhat exaggerated in comparison to the more constrained growth of a melanoma spheroid, as observed in Figure 2.6 and modelled in Flach et al. (2011). Within the time frame of these experimental assays, we observe that the cell cultures exhibit unconstrained growth (see the control experiment T1 in

[1] *Monoculture* refers to an experimental setup where cells from a specific cell line alone are grown. *Coculture* experiments, instead, include cells from the cell line of interest, grown together with other cell types (typically stromal cells) to investigate mutual effects.

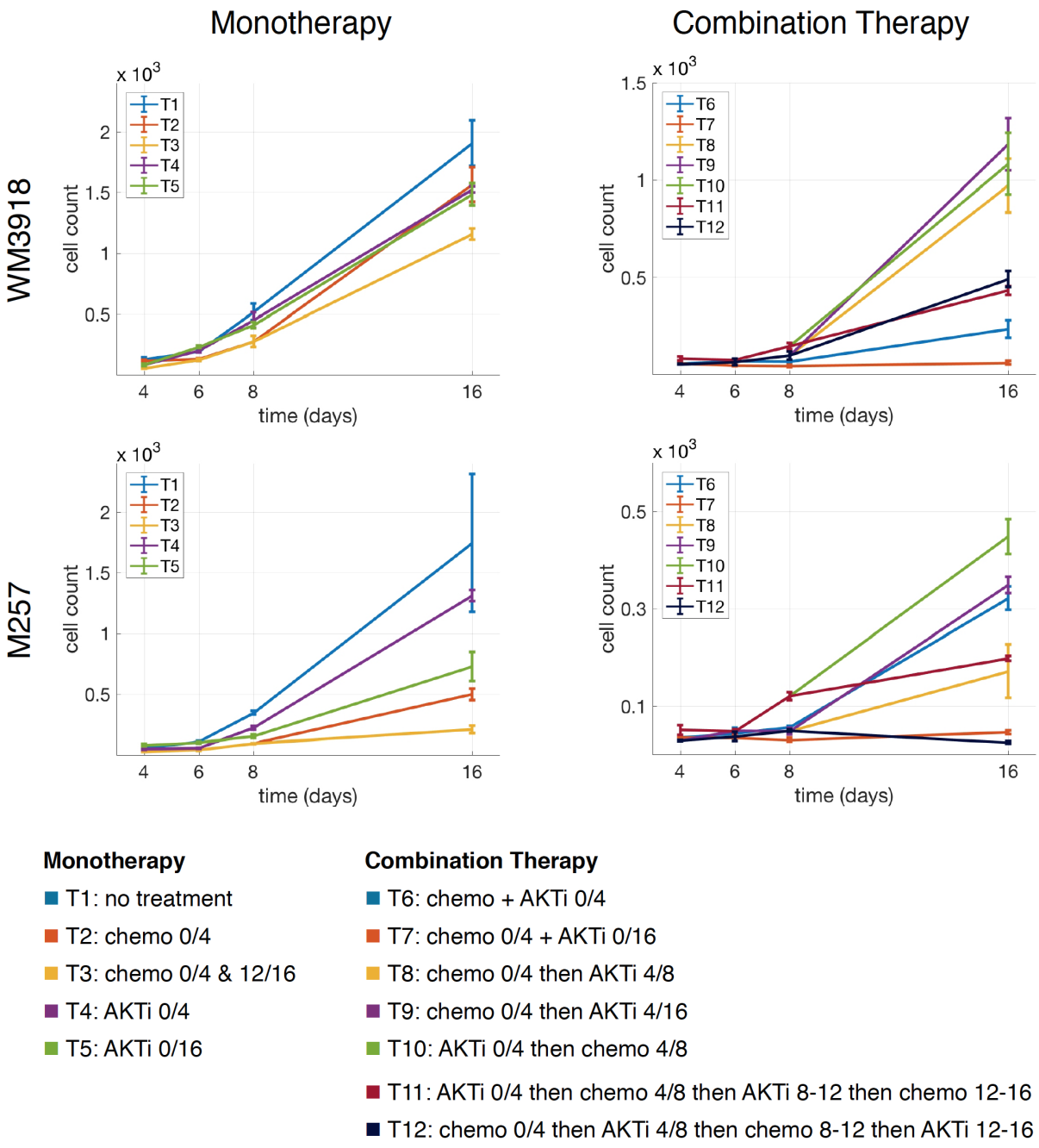


Figure 4.1: *In vitro monoculture experiments with BRAF-wildtype melanoma cell lines WM3918 and M257. The legend at the bottom explains the detailed scheduling (days at which cells are treated with chemotherapy, AKT inhibitor, or both). Mean cell counts with standard deviations are plotted for the three replicas of each experimental setup*[2]*. This figure allows for a comparison between monotherapy and combination therapy strategies. The latter are generally more effective, i.e. lead to a higher reduction in the number of viable cells. Data from Smalley laboratory, Moffitt Cancer Center.*

Figure 4.1). We therefore consider exponential growth to be a good approximation of the cell proliferation dynamics.

We aim to describe the observed tumour-stroma dynamics, and their modulation by treatment, with a system of ODEs. As illustrated in Figure 4.1, in the quantification of the *in vitro* experiments the cell numbers vary between 10^2 to 10^3. Cells grow on an area of approximately 1 cm^2. A continuum approximation of the cell population is appropriate for such cell densities (see considerations on the validity of the continuum approximation in Section 3.4).

Starting from the Flach model (Eqs. (3.8)), we will simplify the system of equations, by rearranging the tumour cell subpopulations into fewer compartments. We focus on reproducing the *in vitro* experimental setup, by considering two cancer cell compartments, characterised with respect to their response to the drug, and two stromal cell compartments, distinguished according to their role in the emergence of drug resistance. Additionally, we approach the implementation of drug treatment in a slightly more realistic way, where the drug has both a temporal and population-dependent effect on the death dynamics. Finally, as described below, a distinction is made between cytotoxic and cytostatic drugs in the model. This approach will allow us to utilise the new experimental data, in terms of combination therapy, in the model, and allow for a more realistic description of the mechanism of acquired drug resistance.

4.4 The ODE Model of AKTi and Chemotherapy

Our minimal model is defined by four cell compartments: sensitive cancer cells (S), resistant cancer cells (R), normal stroma (F), and reactive stroma (A). The dynamics are depicted in Figure 4.2. They include cooperation in the form of growth promotion provided by the reactive stroma to the cancer.

The model presented hereafter is built on the literature discussed in Sections 2.2 and 2.3, and the experimental results available for this study, presented in Section 2.4 and Figures 2.6 and 2.7. Specifically, the experimental evidence suggests the presence of a resistant subpopulation within the cancer cells, as a result of the protective action of a reactive stroma. We will incorporate two forms of resistance into the model, as follows:

- intrinsic pre-existing resistance, that will correspond to non-zero initial conditions for the resistant compartment.
- *de novo* or transient resistance induced by the reactive stroma, corresponding to the growth term ρ_R.

[2]Mean and standard deviation values for three measurements do not have much significance. However, in order to facilitate visual separation between experimental setups, error bars are used to summarise data relative to the three replicas of the same setup for a given time point.

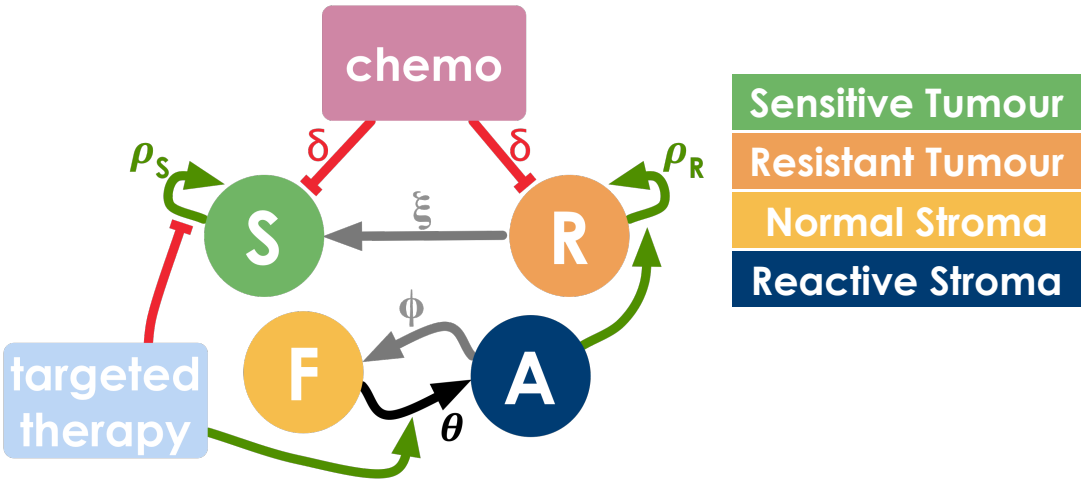


Figure 4.2: *Tumour-stroma dynamics as hypothesised in the model described in Eqs.* (4.1)*. Positive interactions are represented with green arrows, negative ones with red flat ends. Black arrows correspond to transitions. Grey arrows correspond to interactions happening once the targeted therapy is removed.*

Despite the fitness cost of resistance (i.e.reduced growth in the absence of drug compared to non-resistant populations), it has been previously shown that the resistant strain can grow exponentially (see Swieniak et al., 2009). Therefore we will assume exponential growth for both sensitive and resistant strains.

The rate δ mimics the fractional kill of cytotoxic drugs, almost exclusively acting on cells in the G_2/M phase of the cell cycle, where cell division occurs. Since the resistance, as it is defined in this work, is relative to the targeted therapy only, the two tumour cell subpopulations are indistinguishable to chemotherapy. Therefore chemotherapy is assumed to kill the two cancer cell populations indiscriminately. We assume that the stromal population is at equilibrium, i.e. birth and death balance out and the overall stromal population is constant. Therefore we only consider transitions of state between the normal and reactive forms, and disregard any cytotoxic effect of the chemotherapy on these cells, assuming that the stromal population is replenished after any drug-induced depletion. This is a reasonable assumption in the metastatic setting, where a small tumour cell population is seeded in a stroma-rich environment, characterised by a very slow turnover, hence, less susceptible to drugs targeting cell division.

The AKT inhibitor, which we refer to as a generic *targeted therapy*, acts differently on the two tumour cell types. Its effect on the sensitive pool is to inhibit their growth (i.e. cytostatic effect). Yet it acts indirectly on the resistant pool, inducing the transition of stromal cells from normal to reactive. The latter will promote the growth of these resistant tumour cells.

The transient action of the targeted therapy is modelled with renormalisation terms,

from resistant to sensitive tumour cells, and from reactive to normal stroma, once the therapy is removed (terms in ξ and ϕ of Figure 4.2).

The above scenario can be formalised in the following system of ODEs and initial conditions.

$$\begin{cases} \dfrac{dS}{dt} = \rho_S S(1-g(t)) - \delta S c(t) + \xi R h(t) \\ \dfrac{dR}{dt} = \rho_R A R - \delta R c(t) - \xi R h(t) \\ \dfrac{dF}{dt} = -\theta F g(t) + \phi A h(t) \\ \dfrac{dA}{dt} = +\theta F g(t) - \phi A h(t) \end{cases} \quad \text{with} \quad \begin{cases} S(0) = S_0 \\ R(0) = R_0 \\ F(0) = F_0 \\ A(0) = 0 \end{cases} \tag{4.1}$$

where S, R, F and A are sensitive tumour, resistant tumour, normal stroma and reactive stroma cell numbers, respectively. ρ_S and ρ_R are sensitive and resistant cancer cell growth rates, respectively. δ is the chemotherapy death rate. ξ is the rate of return of resistant cancer cells to sensitivity, once the targeted therapy is halted. θ is the activation rate of normal stromal cells, which under targeted therapy turn into reactive stromal cells. ϕ is the rate for the reverse event: inactivation of stromal cells, from reactive to normal, once the targeted therapy is halted. Parameters $\rho_S, \rho_R, \delta, \xi, \theta, \phi, S_0, R_0$, and F_0 are positive constants.

Functions g, h, and c allow a compact description of the dynamics (under any possible treatment regime) with a single system of ODEs. These binary functions switch "on" and "off" terms, depending on the treatment applied and are defined as follows:

$$g(t) = \begin{cases} 1 \text{ if } t_i^{TT} \leq t \leq t_f^{TT} \\ 0 \text{ else} \end{cases} \quad c(t) = \begin{cases} 1 \text{ if } t_i^{CH} \leq t \leq t_f^{CH} \\ 0 \text{ else} \end{cases} \quad h(t) = \begin{cases} 1 \text{ if } t \geq t_f^{TT} \\ 0 \text{ else.} \end{cases} \tag{4.2}$$

The AKT inhibitor (targeted therapy) is administered in the time interval $[t_i^{TT}, t_f^{TT}]$. The chemotherapy is administered in the time interval $[t_i^{CH}, t_f^{CH}]$. Therefore the step function $g(t)$ allows us to model the targeted therapy inhibition of sensitive tumour growth with the factor $(1-g)$ that nulls the growth term in the first of Eqs. (4.1) when the drug is being applied. Likewise, the step function $c(t)$ allows us to introduce death terms in the equations for both tumour cell types, when the chemotherapy is administered. Finally, in order to model the post-AKT inhibitor return to sensitivity of resistant tumour cells and the inactivation of reactive stroma, we make use of the step function $h(t)$. Time intervals for AKT inhibitor and chemotherapy can overlap or be composed of single pulses with holidays, allowing for any possible scheduling sequence or combination of therapies.

Analytical solutions obtained for relevant therapeutic setups are presented in Appendix B.

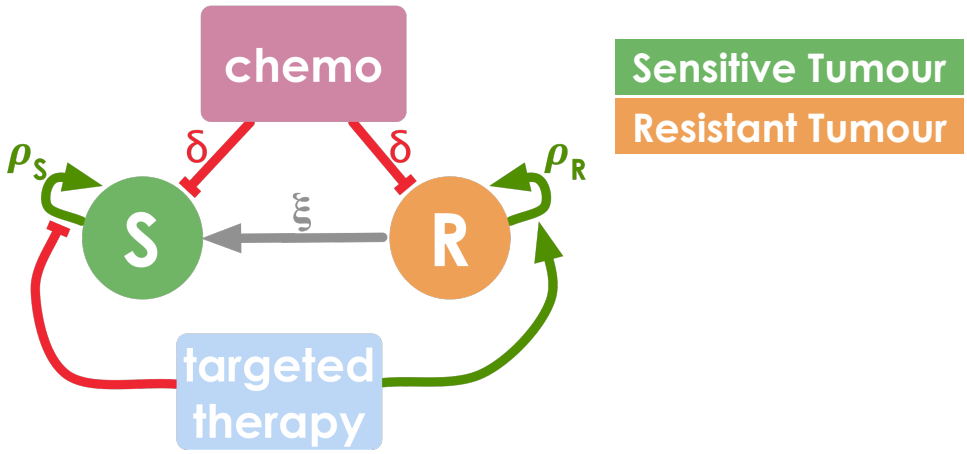


Figure 4.3: *Decoupled system as described in Eqs.* (4.3). *The intermediate role of reactive stroma is bypassed and targeted therapy is assumed to have a direct effect on proliferation of the resistant strain, R, while inhibiting growth in the sensitive strain, S.*

4.5 Parametrisation of the Decoupled System

With the data currently available (presented in Section 4.2), it is possible to estimate values for parameters related to the tumour cell dynamics in our model but not the stromal dynamics. In order to perform a direct comparison between the *in vitro* and the *in silico* results, we utilise a reduced version of our model which better describes the experimental setup of cancer cells growing in monoculture. We therefore decouple the system, removing both normal and reactive stroma, and assume that the targeted treatment directly stimulates the emergence of a resistant population (see Section 2.2 and Figure 2.5). This implicitly means that we are assuming that only intrinsic pre-existing resistance is active in the monoculture experiments.

The new system, as described in Eqs. (4.3) and illustrated in Figure 4.3, allows us to quantify the baseline growth of the tumour compartments, making use of the monoculture data. Additionally, since the death rate δ and the rate ξ of return to sensitivity are independent of the action of the stroma, they can be estimated with the same monoculture data. The model equations are:

$$\begin{cases} \dfrac{dS}{dt} = \rho_S S(1-g(t)) - \delta S c(t) + \xi R h(t) \\ \dfrac{dR}{dt} = \rho_R R g(t) - \delta R c(t) - \xi R h(t) \end{cases} \quad \text{with} \quad \begin{cases} S(0) = S_0 \\ R(0) = R_0 \end{cases} \tag{4.3}$$

with $c(t), g(t)$, and $h(t)$ as defined in Eqs. (4.2).

Given that we have temporal response data for two cell lines under five mono therapies and seven combination therapies, we have sufficient experimental data to fit the model parameters to the relevant *in vitro* outcomes, using a minimisation approach. In order

to facilitate direct comparison with experimental data, time t is measured in days. The quantity we want to minimise is the sum of square distances of the four data points (time = 4 days, 6 days, 8 days, 16 days) to the curve for the total population $(S + R)$ given by the solution of the ODE system. By selecting different experimental setups that correspond to an *in silico* simulation where only the parameter of interest appears in the Eqs. (4.3), we can systematically estimate each parameter.

Specifically we can utilise the T1 setup corresponding to the control case, with no treatment, to estimate the baseline tumour growth rate ρ_S.

Similarly we can utilise the T5 setup, where the AKT inhibitor is applied for the entire time span, to estimate the promotion rate, i.e. the growth rate of the resistant population ρ_R. Making use of the estimated values for these two parameters, we can consequently obtain an estimate for the death rate δ, using T2 (4 days of chemotherapy). Finally, T4 (4 days of AKT inhibitor treatment) allows estimation of the return parameter ξ.

No data point is available for the cell count at day 0. Hence, across all of these fits, two additional unknowns need to be estimated: S_0 and R_0, the initial sensitive and resistant tumour cell populations, respectively. Given the conceptual definition of the resistant population, though, it is not possible at this stage to experimentally distinguish between the two subpopulations. Therefore in each fit of the *in silico* curve to the *in vitro* data points, we also estimate values for S_0 and R_0. In spite of this additional uncertainty, having these two quantities as free parameters, and estimating them as part of the minimisation problem, it is possible to gain important information such as the initial ratio of resistant cells to sensitive cells in a given cell line.

Among the methods available in the literature for parameter estimation, we chose three techniques that we deemed appropriate for the data available. Initially the fit was performed using the Matlab routine *fmincon*, to obtain rough estimates of the parameter values, useful for tuning the search with the other techniques. Additionally, we adopted a Bayesian inference approach to calculate probability distributions of the parameters of interest, given the experimental data. Specifically, we used Approximate Bayesian Computation and Markov Chain Monte Carlo methods. The former allowed us to build a discretised posterior distributions, while the latter simulates a Markov Chain whose stationary distribution is the desired parameter distribution.

4.5.1 Parameter Estimation with Matlab *fmincon*

The following results were obtained with a function from the Matlab library, and no implementation was necessary. Hence, details on the *fmincon* minimisation routine and the fitting technique are reported in Appendix A. The results of the fit, performed per each cell line, are illustrated in Figure 4.4 and summarised in Table 4.1. It is worth

	ρ_S (from **T1**)	ρ_R (from **T5**)	δ (from **T2**)	ξ (from **T4**)
WM3918	0.2156 ($S_0 = 49, R_0 = 37$)	0.2530 ($S_0 = 67, R_0 = 19$)	0.2607 ($S_0 = 117, R_0 = 117$)	0.3123 ($S_0 = 28, R_0 = 55$)
M257	0.2625 ($S_0 = 23, R_0 = 19$)	0.2594 ($S_0 = 34, R_0 = 8$)	0.3486 ($S_0 = 15, R_0 = 27$)	0.1134 ($S_0 = 15, R_0 = 27$)

Table 4.1: *Parameter value estimates resulting from the fit of the model* (4.3) *to the in vitro data available (see Section 4.2 and Figure 4.1). See Appendix A for details on the fit. Unit of measurement for parameters* $\rho_S, \rho_R, \delta, \xi$*:* $[day^{-1}]$.

recalling that the variation of estimates for the initial conditions across experiments may be due to the varied experimental initial conditions, as well as the uncertainty caused by the lack of data at time 0. However, the initial conditions of single experiments are of little interest, as the aim of this parameterisation is to quantify the rate of processes hypothesised in our model.

In order to test how good our parameter estimates are, we simulated the *in silico* counterpart of the monotherapy strategies, illustrated in Figure 4.5. The treatment schedules applied correspond to assays T1 to T5, as described in the table in Figure 4.1. For these simulations we make use of the parameter values previously estimated for the two cell lines (see Table 4.1).

The results of the simulation are quantitatively and qualitatively consistent with the *in vitro* counterpart. Results are intuitive when we compare different scheduling of treatment with the same drug. Two pulses of chemotherapy (T3) are more effective than one pulse only (T2) in controlling the tumour burden. Similarly, a continuous application of AKTi (T5) more effectively slows down disease progression, as opposed to an initial pulse (T4). The latter strategy (initial pulse of AKTi alone) can be classified as the most ineffective of the treatment strategies, since its result is almost comparable to the control (T1). Finally, we can observe that the effectiveness of a continuous application of the AKTi is comparable to that of single pulses of chemotherapy, while having lower toxicity.

As previously mentioned, each cell line is unique as far as initial composition of sensitive and resistant populations, growth rates and responsiveness to the drugs. The above result is not meant to give a ranking of treatment options valid across cell lines and experimental setups (i.e. initial conditions). Instead, the aim is to reproduce the range of experimental assays for the given cell line (M257), in order to compare the ranking of treatment options, based on the ability to control growth, between *in vitro* and *in silico* results. A different ranking is obtained when we consider the *in vitro* results for another cell line (compare monotherapy results for WM3918 and M257 in Figure 4.1).

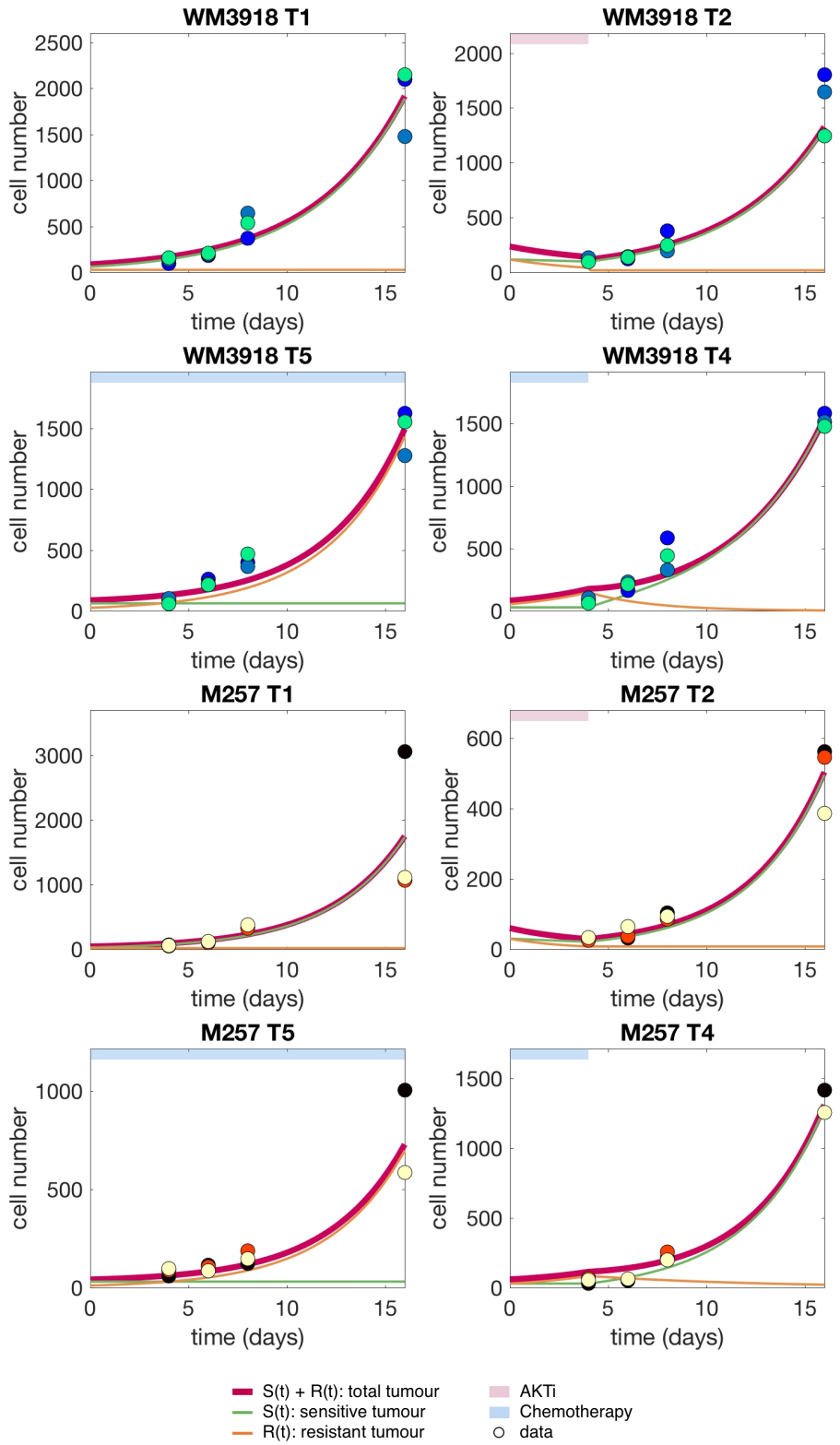


Figure 4.4: *fmincon fits of model* (4.3) *corresponding to estimates reported in Table 4.1. Treatment schedules, defined in Figure 4.1, are indicated with light blue or pink bars at the top of the plot. Different dot colours in each experimental setup represent single replicates.*

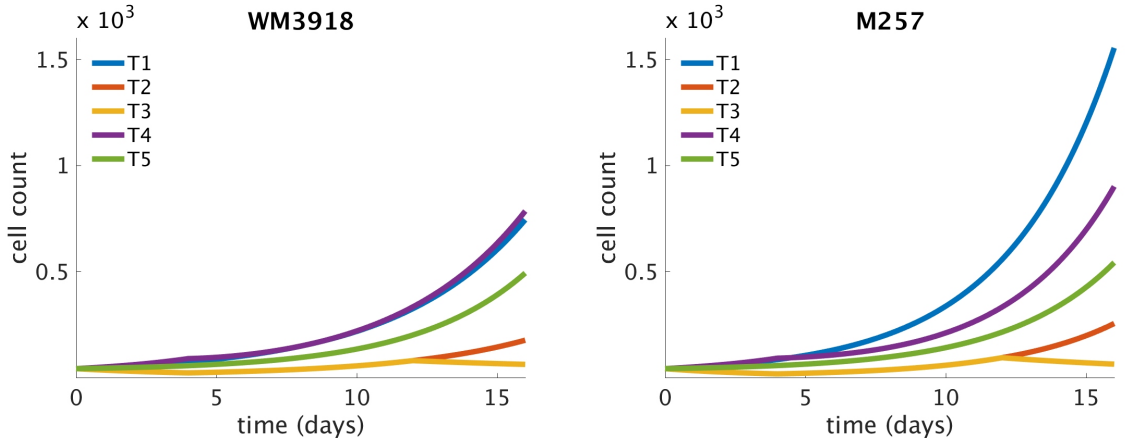


Figure 4.5: *fmincon fits of model* (4.3) *corresponding to estimates reported in Table 4.1. Treatment schedules defined in Figure 4.1.*

These preliminary results give an initial insight into the experimental data. However, the prepackaged Matlab function *fmincon* is designed as a generic routine for minimisation and does not allow full control of the implementation options. Furthermore, the outcome slightly changes at every run, hinting at the possibility that the parameter space search, depending on the initial guess and random generator routine, might end up in local minima. Therefore in the following we will implement alternative algorithms. These will be based on a Bayesian inference approach, and produce informative parameter distributions, using the currrent preliminary results as initial guess to inform the priors.

4.5.2 Parameter Estimation with Approximate Bayesian Computation

In the context of model parametrisation and experimental data, characterised by uncertainty and variation across replicates, probability distributions are often preferable to single value estimates of the parameters. Approximate Bayesian Computation (ABC) is a technique based on a Bayesian inference approach, that computes an approximation of the posterior distribution of parameters, given the observed experimental data [107]. Specifically, the *rejection algorithm* repeatedly draws proposed parameter values and accepts or rejects them according to a chosen metric. Over a sufficiently large number of iterations, the collection of accepted values will represent an approximation of the desired distribution. Let $\mathbf{y} \in \mathbb{R}^N_{>0}$ be a dataset of N temporal observations and $\mathcal{M} = \mathcal{M}(\zeta)$ the summary statistic for the model that we chose to explain the observed data, where ζ is the vector of model parameters, taking values in $\Omega \in \mathbb{R}^q$. In our application we chose as $\mathcal{M}$ the array of tumour size values $S(t) + R(t)$ at the times of experimental readings. We want to estimate values of parameters ζ that best explain the data $\mathbf{y}$, with the model (4.3). The ABC rejection algorithm allows us to build a discrete approximation

Algorithm 1 Basic ABC Rejection

function MAIN($\bar{\pi}$) ▷ Where $\bar{\pi}$ is the target acceptance ratio
  $\epsilon_{old} \leftarrow 1.$
  $\epsilon_{new} \leftarrow 1.$
  $\epsilon_{min} \leftarrow 0.$
  ABC(ϵ_{new})
  while $P/J \neq \bar{\pi}$ **do**
    if $P/J = 0$ and $\epsilon_{new} > \epsilon_{min}$ **then**
      $\epsilon_{min} \leftarrow \epsilon_{new}.$
    end if
    if $P/J > \bar{\pi}$ **then**
      $\epsilon_{old} \leftarrow \epsilon_{new}.$
      $\epsilon_{new} \leftarrow \epsilon_{min} + \frac{\epsilon_{old} - \epsilon_{min}}{2}.$
    else
      $\epsilon_{new} \leftarrow \epsilon_{new} + \frac{\epsilon_{old} - \epsilon_{new}}{2}.$
    end if
    ABC(ϵ_{new})
  end while
end function

function ABC(ϵ)
  $P \leftarrow 0.$
  for $j \leftarrow 1 : J$ **do**
    draw $\zeta' \sim \mathcal{U}(\bar{\Omega})$
    if $\|\mathbf{y} - \mathcal{M}(\zeta')\| \leq \epsilon$ **then**
      accept ζ'
      $P++$
    end if
  end for
end function

of the posterior distribution of ζ. Specifically, the algorithm iteratively draws a proposed q-tuple of values for ζ from a uniform prior on some region $\bar{\Omega}$. If the model, simulated with the proposed parameter set, falls close to the data within tolerance ϵ, the q-tuple is accepted, otherwise rejected. The collection of all accepted q-tuples constitutes an approximation of the posterior distribution. We chose the Eucledian distance as our distance metric. The smaller the tolerance ϵ, the more reliable is the approximated posterior distribution. However, too small an ϵ will result in zero acceptance ratio π (defined as number of accepted q-tuples over J). The value of ϵ giving satisfactory results has to be adjusted for every set of data and model. In order to obtain consistent results across estimates, we fix the desired acceptance ratio to $\bar{\pi} = 0.0002$, and iteratively run the ABC rejection algorithm with increased or decreased ϵ, until the targeted acceptance ratio is

	ρ_S (from **T1**)	ρ_R (from **T5**)	δ (from **T2**)	ξ (from **T4**)
model	$S(t) = S_0 e^{\rho_S t}$ $R(t) = R_0$	$S(t) = S_0$ $R(t) = R_0 e^{\rho_R t}$	$S(t) = S_0 e^{\rho_S t - 4\delta}$ $R(t) = R_0 e^{-4\delta}$	$S(t) = \frac{e^{-\xi t - 4\rho_S}}{\xi + \rho_S} \{\xi [S_0 e^{t(\xi+\rho_S)} + + R_0 e^{4\rho_R} (e^{t(\xi+\rho_S)} - e^{4(\xi+\rho_S)})] + + \rho_S S_0 e^{t(\xi+\rho_S)}\}$ $R(t) = R_0 e^{4\rho_R} e^{-\xi(t-4)}$
WM3918	0.19 [0.18, 0.22] ($S_0 = 87.12$, $R_0 = 1.15$)	0.18 [0.17, 0.20] ($S_0 = 0.30$, $R_0 = 79.6$)	0.15 [3e-4, 0.17] ($S_0 = 128.82$, $R_0 = 0.03$)	0.99 [0.87, 1] ($S_0 = 102.82$, $R_0 = 28.02$)
M257	0.23 [0.22, 0.25] ($S_0 = 42.66$, $R_0 = 0.32$)	0.22 [0.18, 0.29] ($S_0 = 29.41$,) $R_0 = 21.24$)	0.22 [5e-4, 0.26] ($S_0 = 28.71$, $R_0 = 11.66$)	0.99 [0.82,1] ($S_0 = 67.92$, $R_0 = 6.41$)

Table 4.2: *Parameter value estimates resulting from the fit using the ABC rejection algorithm, model* (4.3) *and in vitro data for BRAF wildtype melanoma cell lines WM3918 and M257 (Section 4.2 and Figure 4.1). Unit of measurement for parameters* $\rho_S, \rho_R, \delta, \xi$*:* $[day^{-1}]$*; for* S_0 *and* R_0 : $[cells]$. $J = 10^7, \bar{\pi} = 2e - 4$. *Square brackets indicate the range of accepted values.*

reached (see Algorithm 1). In the following notation, a prime apex indicates a proposed parameter value drawn from some distribution.

Using the same sequential approach presented in 4.5.1, we apply the ABC estimation algorithm to each experimental setup (T1, T5, T2 and T4) to obtain estimates of triplets of parameters. The model is analytically tractable, so in computing the summary statistic $\mathcal{M}$ we make use of the analytical solutions for functions $S(t)$ and $R(t)$. Similarly to the previous technique, for each experimental setup we want to obtain the best fit to all of the three replicates. To this end the Euclidean distance (line 24 in Algorithm 1) is calculated on the array of concatenated data of length $3N$:

$$\|\mathbf{y} - \mathcal{M}(\zeta')\| = \sqrt{\sum_{r=1}^{3} \sum_{i=1}^{N} \left(y_i^r - R_0' - S_0' e^{\rho_S' t_i}\right)^2} \tag{4.4}$$

The resulting posterior distributions are shown in Figure 4.6. The numerical ranges and single estimates (i.e. the value minimising the Eucledian norm (4.4)) are reported in Table 4.2. The corresponding fits to each experimental setup are plotted in Figure 4.7.

For both cell lines the marginal posterior distributions reveal a decrease in fitness when grown under treatment with the AKTi. The error bars in Figure 4.6 indicate the deficit in growth rate that can be interpreted as the fitness cost to resistance. It is worth noting that the parameter values chosen as best fit do not necessarily correspond to the peak of the marginal distribution. Instead, they are the values minimising the distance to the data, and for sufficiently large J, correspond to the maximum of the

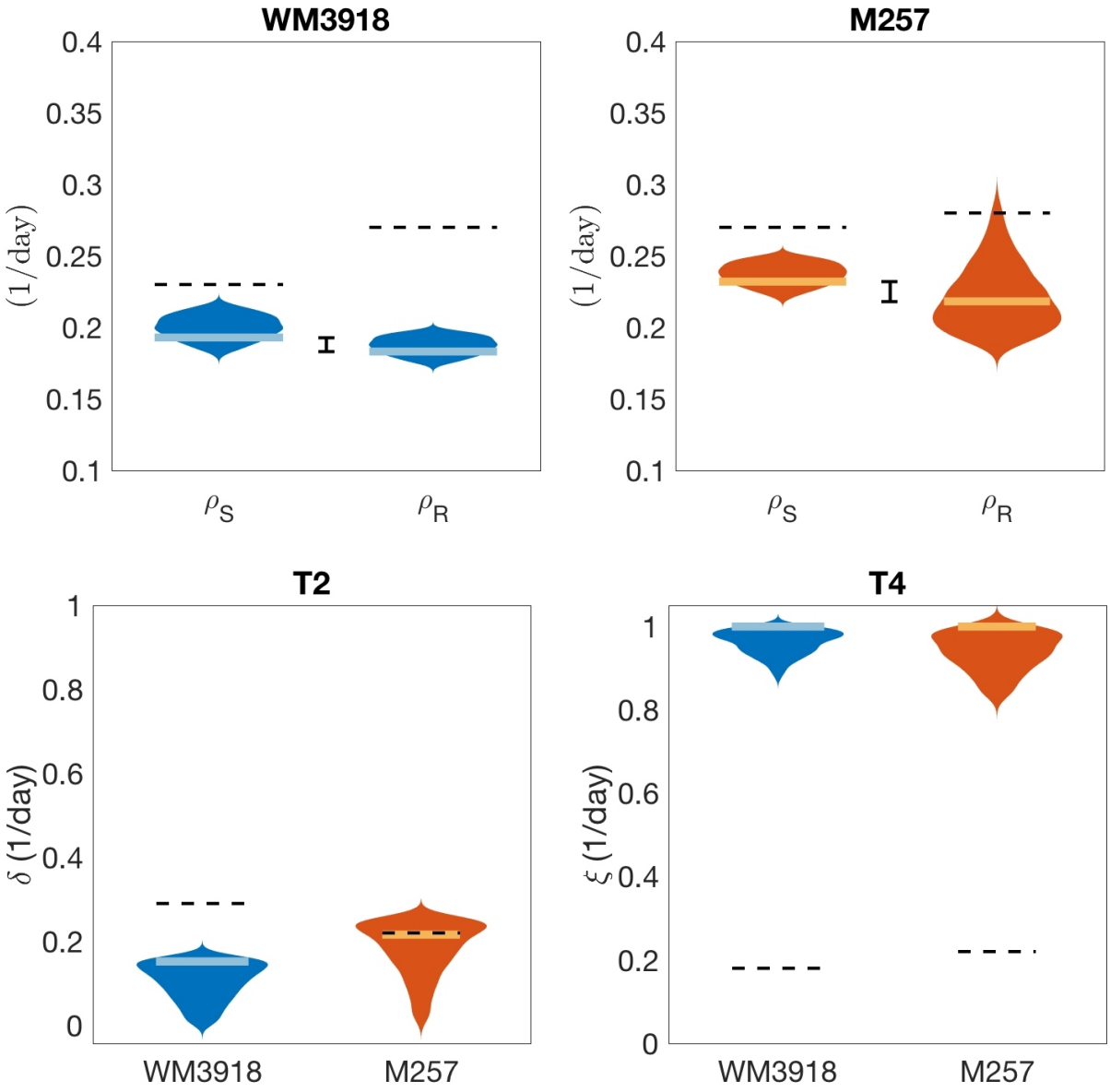


Figure 4.6: *Parameter estimates obtained with the ABC rejection algorithm, model* (4.3) *for WM3918 and M257 cell lines, experiments T1, T5, T2 and T4. Horizontal solid lines in lighter colour indicate the parameter value giving the best fit. Dashed horizontal lines indicate the corresponding fmincon estimates.*

probability distribution for the q-tuple. The disagreement in the parameter estimates from the ABC algorithm and the Matlab routine *fmincon* (dashed black lines in Figure 4.6) requires further investigation into the data and the estimate method. In the first place estimates of δ and ξ are dependent on the values ρ_S and ρ_R, obtained from the previous estimates. Additionally, the data available from the experimental model have a non-uniform sampling step, missing both the initial growth (day 0 through day 4) and a significant window of time (day 8 through day 16). The lack of information on

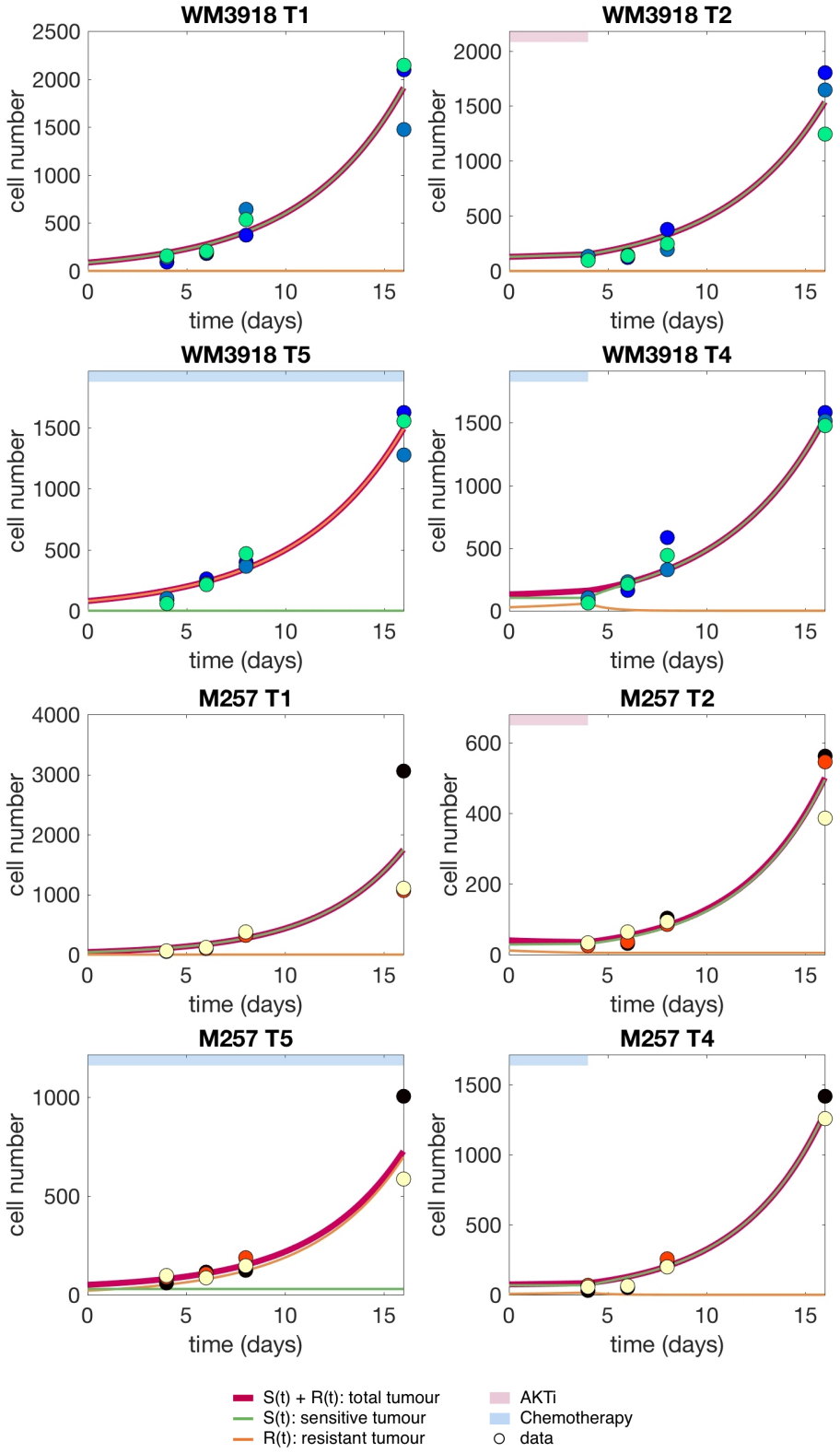


Figure 4.7: *ABC fits of model* (4.3) *corresponding to estimates reported in Table 4.2. Different dot colours in each experimental setup represent single replicates. Treatment schedules, defined in Figure 4.1, are indicated with light blue or pink bars at the top of the plot.*

the initial growth is likely the cause of the large variation in the estimate of the initial populations (R_0 and S_0). Furthermore, given the nature of the experimental system, the initial conditions vary across the twelve experimental setups. Therefore estimates for these two parameters are of little interest, and we want to focus on the rates ρ_S, ρ_R, δ and ξ, describing the dynamics of the system. We ask whether the quality of estimates vary with the sampling size N. If this was the case, we could use our model and estimation method to suggest improvement in the experimental protocol. For example we could identify the minimum sampling size and sampling step to obtain accurate estimates of the growth rate, necessary to quantify the dynamics experimentally observed. To this end, we apply our ABC algorithm to simulated data, obtained for an untreated virtual cell line with known parameter values (R_0^*, S_0^*, ρ_S^*), sampling at n_j equally spaced time points in the time interval $[0, 16]$ days. In order to obtain simulated data similar to the experimental data, we introduce Gaussian noise with standard deviation σ, and produce three replicates:

$$\begin{aligned} &\mathbf{y^r} = \{y_i^r\}, \quad r = 1, 2, 3; \quad i = 1, \ldots, n_j; \\ &\text{where} \quad y_i^r = R_0^* + S_0^* \exp(\rho_S * t_i) + \mathcal{N}(0, \sigma), \quad t_i = \frac{(i-1)16}{n_j - 1}. \end{aligned} \tag{4.5}$$

In order to monitor the accuracy of the estimates as we vary the sampling size and the noise, we repeatedly apply the ABC algorithm to simulated data varying n_j and σ. For all simulations we use $J = 10^6$, and $\bar{\pi} = 0.0002$. We vary n_j between 4 and 17, the latter corresponding to one reading per day. The resulting posterior distributions are shown in Figure 4.8. For $\sigma = 0$ (first row) we expect our algorithm to accurately estimate the values (R_0^*, S_0^*, ρ_S^*). Indeed, for all three parameters, the single estimates fall close to the real values. We expect the accuracy to increase for larger number of iterations J. No additional accuracy is observed for increased n_j, as a sampling size of three is sufficient to accurately fit the model with three unknown parameters. It is worth noting that running the ABC estimate on simulated data with no noise gives us the opportunity to test the validity of the algorithm. This result gives us confidence in the implementation of the algorithm and the validity of its estimates on real data.

For increased σ the ABC estimates shift from the real parameter values, both over- and underestimating, without a clear relationship to the sampling size. For large noise ($\sigma = 10$), despite the inaccurate single estimate, the real values fall in the range spanned by the posterior distributions. This gives us further confidence in the validity of the ABC algorithm. Overall we can conclude that increasing n_j does not give improvement in estimation accuracy, therefore no increase in sampling size can be recommended.

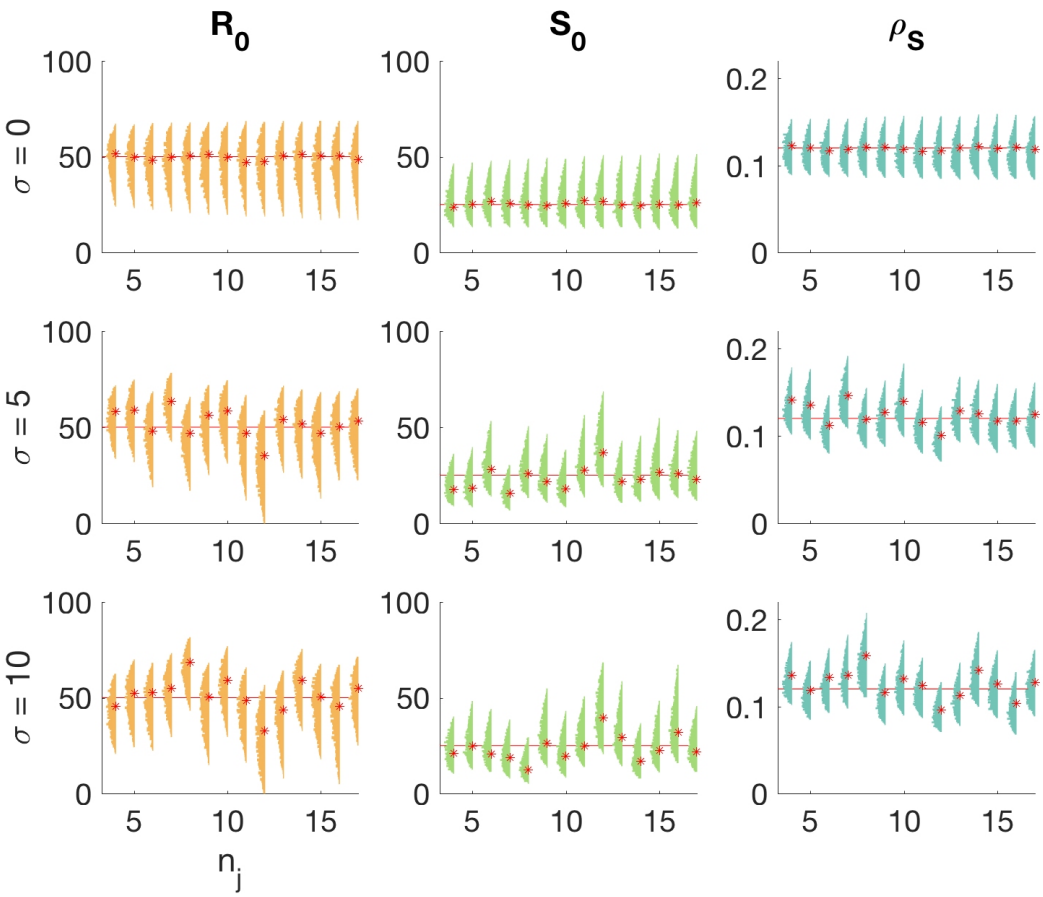


Figure 4.8: *ABC fits of model* (4.3) *to simulated data with Gaussian error of varied standard deviation* σ *and varied sampling size* n_j*. Each column shows the marginal posterior distribution of a parameter. Histograms, rotated and stacked horizontally in each subplot, represent the posterior distributions obtained by varying the sampling size* n_j *from 4 to 17 in the time interval [0, 16] days. Horizontal red lines indicate the known parameter values (*$R_0^* = 50, S_0^* = 25, \rho_S^* = 0.12$*). Red stars indicate the ABC single estimate (best fit) for the combination of* σ *and* n_j*.*

The ABC method presented here, despite its intuitive nature, does not have a solid theoretical justification. In the following we will introduce assumptions on the observed data allowing us to redefine the estimation problem in the form of a Markov Chain.

4.5.3 Parameter Estimation with Markov Chain Monte Carlo

With a similar Bayesian inference approach, we can use a Markov Chain Monte Carlo (MCMC) method to estimate the model parameters [93]. Specifically, we will implement a basic Metropolis-Hastings (MH) algorithm to estimate the parameters corresponding to the experimental setup T1. This method requires that key assumptions are made on the distribution of the observed data, and the prior of the parameters. We hypothesise

that the observed data can be explained with the model (4.3) and Gaussian error:

$$y_i \sim \mathcal{N}\left(R_0 + S_0 \exp\left(\rho_S t_i\right), \sigma^2\right), \tag{4.6}$$

where σ is the standard deviation of the error, that will be estimated as an additional parameter, together with the ODE model parameters. We define the array of parameters to be estimated as $\zeta = \{R_0, S_0, \rho_S, \sigma\}$. For these parameters we also assume a multivariate uniform prior.

Given the current state $\zeta_{\mathbf{m}}$, the MH algorithm samples the next proposed state ζ' from a proposal distribution $q\left(Z|\zeta_{\mathbf{m}}\right)$ and compares relative likelihoods as follows:

$$\alpha = \min\left(\frac{p(\zeta'|data)}{p(\zeta_{\mathbf{m}}|data)}\frac{q(\zeta_{\mathbf{m}}|\zeta')}{q(\zeta'|\zeta_{\mathbf{m}})}, 1\right) = \min\left(\frac{p(\zeta'|data)}{p(\zeta_{\mathbf{m}}|data)}, 1\right). \tag{4.7}$$

Typically a multivariate normal distribution is used as the proposal distribution, which, being symmetric, allows the last simplification in Eq. (4.7).

From Bayes theorem we know that the posterior is proportional to the product of the likelihood and the prior:

$$p(\zeta|data) \propto l(data|\zeta)p(\zeta). \tag{4.8}$$

We identify a region $\bar{\Omega}$ in the 4-dimensional space where to set our uniform prior:

$$p(\zeta) = \begin{cases} C & \text{in } \bar{\Omega} \\ 0 & \text{otherwise.} \end{cases} \tag{4.9}$$

This region can be defined by finite intervals where we believe the range of parameter values lie. In this application we use the estimates from the methods previously presented.

The algorithm rejects proposed parameters ζ' that fall outside $\bar{\Omega}$. Therefore we can use Eq. (4.8) and the uniform prior to further simplify Eq. (4.7) to:

$$\alpha = \min\left\{\frac{l(data|\zeta')}{l(data|\zeta_{\mathbf{t}})}, 1\right\}. \tag{4.10}$$

Given the assumptions on the data, we can write the probability distribution function for a single observation y_i at time t_i as:

$$f(y_i|R_0, S_0, \rho_S, \sigma, t_i) = \frac{1}{\sqrt{2\pi\sigma^2}} \exp\left(\frac{-\left(y_i - R_0 - S_0 e^{\rho_S t_i}\right)^2}{2\sigma^2}\right). \tag{4.11}$$

Assuming that the observations y_i are independent, we can write the likelihood as:

$$l = \prod_{i=1}^{N} f(y_i) = (2\pi)^{-N/2}\,\sigma^{-N} \exp\left(-\frac{1}{2\sigma^2}\sum_{i=1}^{N}\left(y_i - R_0 - S_0 e^{\rho_S t_i}\right)^2\right). \tag{4.12}$$

Since this likelihood is the product of terms smaller than 1, it is convenient to use the logarithm:

$$L = log(l) = -\frac{N}{2}\log(2\pi) - N\log(\sigma) - \frac{1}{2\sigma^2}\sum_{i=1}^{N}\left(y_i - R_0 - S_0 e^{\rho_S t_i}\right)^2. \tag{4.13}$$

Taking the logarithm of Eq. (4.10) we obtain:

$$\log(\alpha) = \min\left\{L(data|\zeta') - L(data|\zeta_{\mathbf{t}}), 0\right\}. \tag{4.14}$$

The first term of Eq. (4.13) is constant for any ζ, therefore in evaluating Eq. (4.14) we can ignore it. Having defined the offset likelihood as

$$\tilde{L}(\zeta) = -N\log(\sigma) - \frac{1}{2\sigma^2}\sum_{i=1}^{N}\left(y_i - R_0 - S_0 e^{\rho_S t_i}\right)^2, \tag{4.15}$$

the MCMC algorithm reads as follows:

Algorithm 2 Basic Metropolis-Hastings MCMC

1: **function** MAIN(ζ_0) ▷ Where ζ_0 is the initial guess for parameters
2: $\quad\zeta_{\mathbf{m}} \leftarrow \zeta_{\mathbf{0}}$.
3: $\quad$**for** $t \leftarrow 1 : J$ **do**
4: $\quad\quad$draw $\zeta' \sim q(Z|\zeta_{\mathbf{m}})$.
5: $\quad\quad$**if** $p(\zeta') = 0$ **then**
6: $\quad\quad\quad$skip to line 13.
7: $\quad\quad$**end if**
8: $\quad\quad log(\alpha) \leftarrow \min\left\{\tilde{L}(\zeta_{\mathbf{m}}) - \tilde{L}(\zeta'), 0\right\}$.
9: $\quad\quad$draw $u \sim \mathcal{U}(0,1)$.
10: $\quad\quad$**if** $u < \alpha$ **then**
11: $\quad\quad\quad\zeta_{\mathbf{t+1}} \leftarrow \zeta'$.
12: $\quad\quad$**else**
13: $\quad\quad\quad\zeta_{\mathbf{t+1}} \leftarrow \zeta_{\mathbf{m}}$.
14: $\quad\quad$**end if**
15: $\quad$**end for**
16: **end function**

In this algorithm J is the number of iterations. Intuitively, α represents the probability of accepting the proposed sample, depending on its relative likelihood. If the proposed value is more probable than the current one, then it is always accepted. However, if the proposed value is less probable than the current one, it can still be accepted with a probability inversely proportional to the drop in likelihood (line 8). Existence and uniqueness of the stationary distribution can be proved using the standard properties of

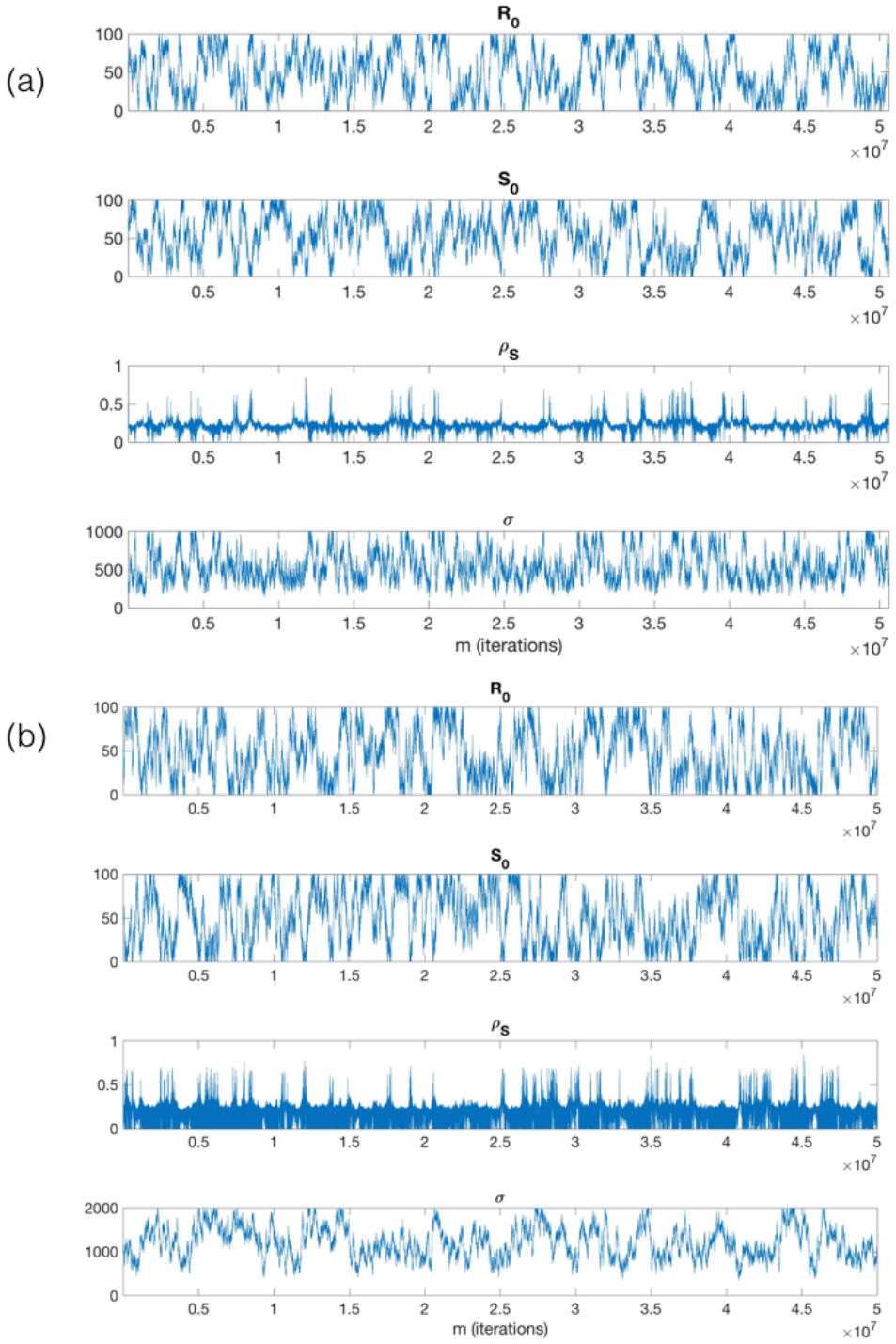


Figure 4.9: *MCMC estimate for WM3918 (a) and M257 (b) cell line, experiment T1.*

the Markov process [93]. However, the derivation of these proofs is out of the scope of this work.

Figure 4.9 shows a realisation of the algorithm for both cell lines. Growth rate ρ_S converges around the *fmincon* and ABC value estimates. Similarly to the previous methods, this algorithm cannot capture accurately the distribution for the initial conditions R_0

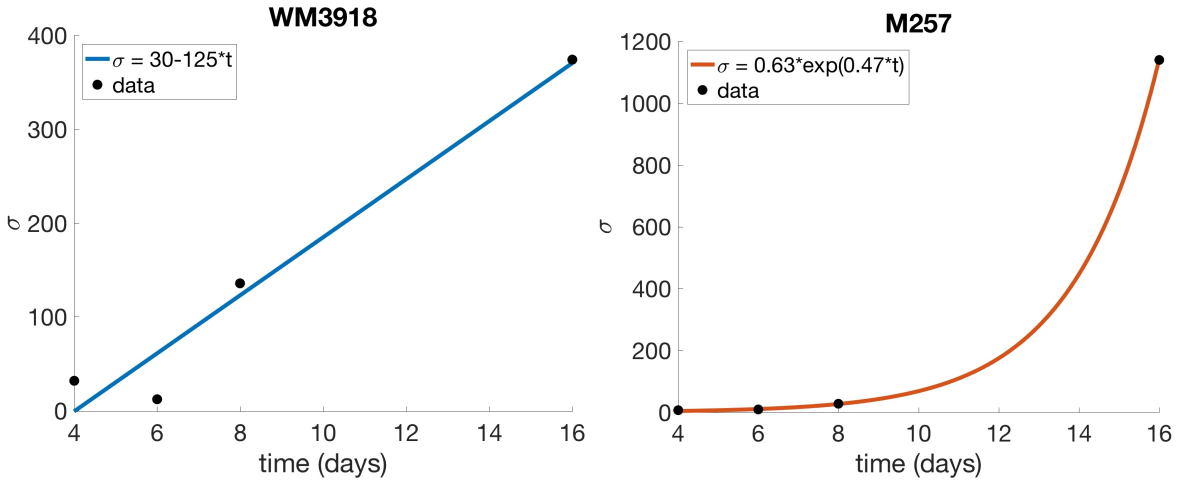


Figure 4.10: *Standard deviation in data for WM3918 and M257 cell lines, experiment T1 (black dots). Curves represent the best fits describing the standard deviation for each cell line as a function of time: linear and exponential, respectively.*

and S_0. As previously concluded, this uncertainty is of no practical concern as our main goal is to calibrate the general growth dynamics with growth rates, as single experimental realisations are less informative. The convergence of the ρ_S estimate for the WM3918 cell line is more evident than in its M257 counterpart. The most plausible explanation for this is the much more elevated standard deviation in the data (plotted in Figure 4.10), which is reflected in the ranges of σ estimates (Figure 4.9). In order to improve the estimates, we considered models of the noise alternative to $\mathcal{N}(0, \sigma)$. We reformulated the MH algorithm, hypothesising linear $\mathcal{N}(0, C + Dt)$, parabolic $\mathcal{N}(0, at^2 + bt + c)$, exponential $\mathcal{N}(0, ae^{bt})$ variation. No convergence was achieved for any of these standard deviation models, despite their accurate representation of the data variation (Figure 4.10). Figures of the evolution of the Markov Chains obtained from these attempts are not reported here, as they are very noisy and uninformative.

4.6 Coupled Model System Behaviour

Having obtained estimates for parameters relevant to the tumour compartments, we consider the full coupled model as presented in Section 4.4. The dynamical system defined in Eqs. (4.1) can be used to investigate a range of observed clinical behaviours, without parameterisation. Analysis of the growth dynamics of the system in the absence of treatment is of little interest in the study of drug resistance and is therefore relegated to Appendix B.

4.7 Simulating the Standard of Care

In this section we present three examples of different treatment strategies, showing that even this simple model can reproduce some clinically observed dynamics, including the standard of care for malignant melanoma.

Chemotherapy acts indistinctly on all proliferating cells, including those forming the normal tissue surrounding the tumour. Despite normal tissue not being included in the modelled system, it is important to account for toxicity. Therefore in this model we allow chemotherapy to be administered in limited dose. Additionally, holidays between consecutive doses are necessary to allow recovery of damaged normal cells as well as the recovery of treatment sensitive populations. Furthermore different chemotherapeutic agents have different efficacies, and different tolerated dosage. This model can account for the effects of different concentrations or efficacy of drug, implicitly, in the parameter δ.

In the following simulations, values for those parameters that could be estimated with the currently available experimental data (Section 4.5) are used. Other parameter values were obtained with an educated guess or chosen within the order of magnitude of physically relevant values. For example, the value for the resistant growth rate, ρ_R, corresponds to the estimate obtained in Section 4.5 for the decoupled model (hence independent of the reactive stroma abundance), adjusted for number of initial stromal cells. In order to simulate a realistic and clinically relevant setup, we will consider densities of a considerably higher order of magnitude compared to the *in vitro* experimental ones. For the results shown in the following figures we use the parameter values calibrated to the M257 cell line (Table 4.2) and initial conditions:

$$\rho_S = 0.23 \text{ day}^{-1};\ \delta = 0.22 \text{ day}^{-1};\ \rho_R = 4.4 \times 10^{-5} \text{ day cells}^{-1};$$

$$\xi = 0.99 \text{ day}^{-1};\ \phi = 0.1 \text{ day}^{-1};\ \theta = 0.03 \text{ day}^{-1};$$

$$S_0 = 10^4 \text{ cells};\ R_0 = 50 \text{ cells};\ F_0 = 10^4 \text{ cells};\ A_0 = 0 \text{ cells}. \tag{4.16}$$

Values are kept unchanged throughout all three simulations, only treatment strategies are altered. The results were obtained in Matlab with the numerical solver *ode15s*, whose results were tested against analytical solutions for a few basic treatment scenarios (Appendix B).

The dynamics shown in Figure 4.11 represent a realisation of the current standard of care, consisting of a pulse of chemotherapy, accompanied by a continuous treatment with the targeted drug. The former kills a fraction of the tumour cells, corresponding to the proliferating pool and leading to an evident decrease in the tumour burden (red). The latter inhibits the growth of the sensitive pool of the tumour cells (green). The

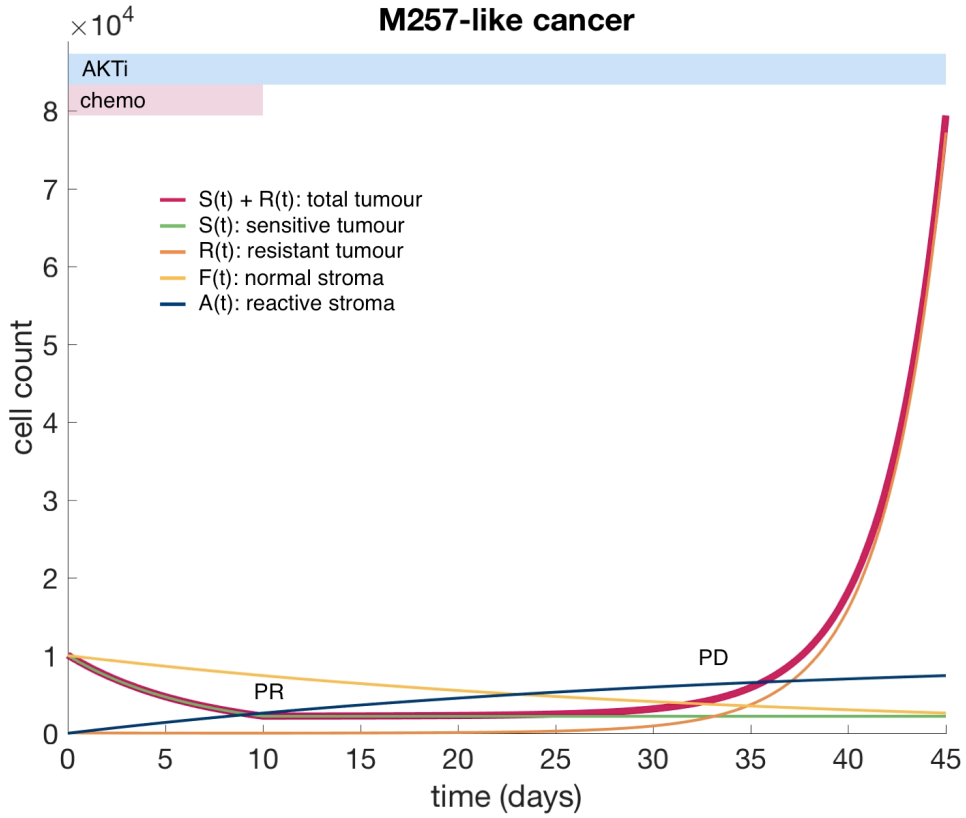


Figure 4.11: *Tumour-stroma dynamics, as described in Eqs.* (4.1)*, when standard of care treatment is applied. This includes continuous treatment with the AKTi and a dose of chemotherapy given over the course of 5 days. The light blue and pink bands represent the time windows in which treatments are applied. We can observe that the pulse of chemotherapy leads to tumour burden decrease (red). Targeted therapy, applied throughout the simulation, allows control of growth in the sensitive portion of the tumour (green), resulting in a partial response (PR). Its side effect, however, is to stimulate recruitment of reactive stroma (blue) from normal stroma (yellow). The reactive stroma stimulates the proliferation of the resistant tumour compartment (orange). Despite its evolutionary disadvantage (smaller growth rate and initial count, compared to the sensitive tumour), over time the resistant tumour grows driving disease progression (PD). Indeed, after day 33, resistant cells make up the bulk of the tumour population, which grows above the initial value.*

dynamics obtained with this simulation can be compared with the schematic in Figure 2.3, representing a typical response curve for the same treatment sequence, as is observed in the clinic. Initially, the joint action of the drugs allows a stabilisation of the tumour burden (compare with PR point in Figure 2.3), even after the chemotherapy is removed. Nevertheless, the AKTi stimulates the switch of the normal stromal cells (yellow) to reactive cells (blue). The reactive stroma stimulates the proliferation of those tumour cells not affected by the drug, leading eventually to an abrupt increase in tumour burden (compare with PD point in Figure 2.3), mainly composed of resistant cells.

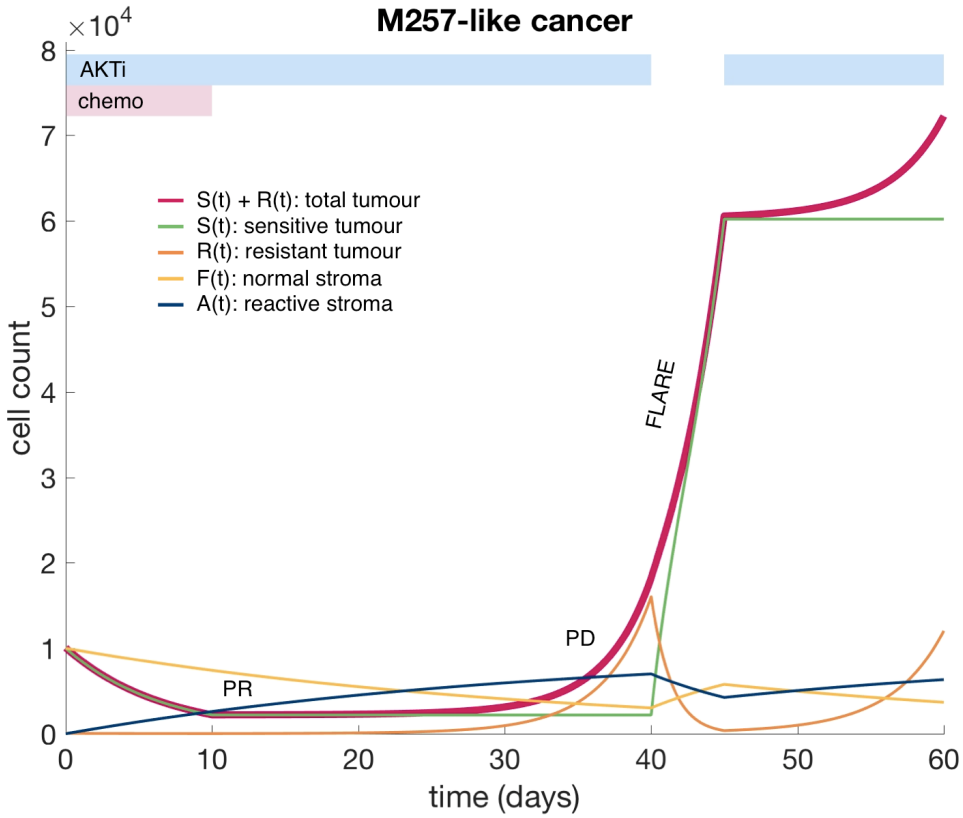


Figure 4.12: *Tumour-stroma dynamics, as described in Eqs.* (4.1)*, showing the clinically observed flare response (Lee et al., 2013). Compare also PD (progressive disease) and PR (partial response) stages with Figure 2.3. Standard of care treatment (see Figure 4.11 for details) is simulated. Around day 40, when disease progression is observed, the targeted therapy is halted. The removal of the inhibitor leads to a sharp increase in the total tumour burden, mainly composed of sensitive cells (green). At day 45 the targeted therapy is reintroduced, resulting in a slower increase in the tumour burden, as the growth of the sensitive portion of the tumour is inhibited again.*

4.8 Simulating the Flare Response

When progression is observed in patients treated with a targeted drug, the next most sensible strategy seems to be withdrawal of the patient from such treatment. This constitutes the current therapeutic paradigm, as described in Chapter 2, and illustrated in Figure 2.3. Our mathematical model is able to capture a similar response, which can be related to the clinically observed flare response. Figure 4.12 shows the *in silico* counterpart of this event. The initial response to the AKTi, with adjuvant initial pulse of chemotherapy, seems to reduce the disease to a managed condition. Around day 40, however, when treatment failure and disease progression are becoming evident, the patient is removed from the therapy (compare with PD point in Figure 2.3). The transient protective effect of the stroma disappears: the reactive stroma soon becomes inactive

(it reverts to normal stroma), cancelling the proliferation enhancement to the tumour. Nevertheless, due to the transient nature of the resistance to the targeted drug, the sensitive tumour compartment is replenished and the inhibiting action of the cytostatic drug cancelled. Therefore the bulk of the tumour is soon composed of sensitive cells, now free to proliferate. Finally, the simulation shows the importance of the inhibiting action of the AKTi. The reintroduction of the targeted drug at day 45 results in a slower growth of the total tumour burden. Nevertheless, the gap in the treatment and the delay of the second application leads to the emergence of a large proportion of resistant cells, whose proliferation is further enhanced by the reintroduction of the AKTi.

4.9 Simulating a Disease Management Strategy

To summarise, the prolonged action of targeted therapy leads to the emergence of resistance in the cancer population. Removing the patient from the therapy when progression is observed is an even worse strategy: a flare response often follows. Currently no optimal treatment sequence of approved therapies for metastatic melanoma is available [53]. Far from suggesting that our model represents a clinical predictive tool, we would like to explore the potential of this model to design an intelligent treatment schedule that optimises sensitive cancer kill, and yet keeps the resistant population at a minimal level. Figure 4.13 illustrates a possible strategy to achieve this, involving a trade-off between the application of toxic chemotherapy and the management of the aggressive resistant clones that arise during the continuous application of the targeted drug. Under the working hypothesis that these two drugs are the only options available to a clinician[3], we can recognise that multiple pulses of chemotherapy are necessary to keep the resistant population from emerging. Figure 4.13 stresses the importance of continuous application of the cytostatic drug, which allows inhibition of further increase in tumour burden, while the patient is benefiting from a holiday between pulses of chemotherapy. This holds as long as the bulk of the tumour is composed of sensitive cells and the chemotherapy pulses are scheduled sufficiently close in time to allow for fractional kill of the resistant strain that has been emerging following the application of the AKTi. We can observe that at the start of the last pulse of chemotherapy (day 40), the resistant strain now makes up the bulk of the tumour. Therefore, this last cytotoxic treatment is not as effective as the previous ones. It is worthwhile remarking that the AKTi is administered continuously throughout the simulation. This cytostatic drug enhances the recruitment of reactive

[3]A three inhibitor strategy is currently under investigation (Jang et al., 2014). Its use involves constant monitoring of the tumour and adaptive therapy. This topic is outside the scope of this work, given that the *in vitro* data available make use of specific cell lines, where single alterations in a specific pathway are investigated.

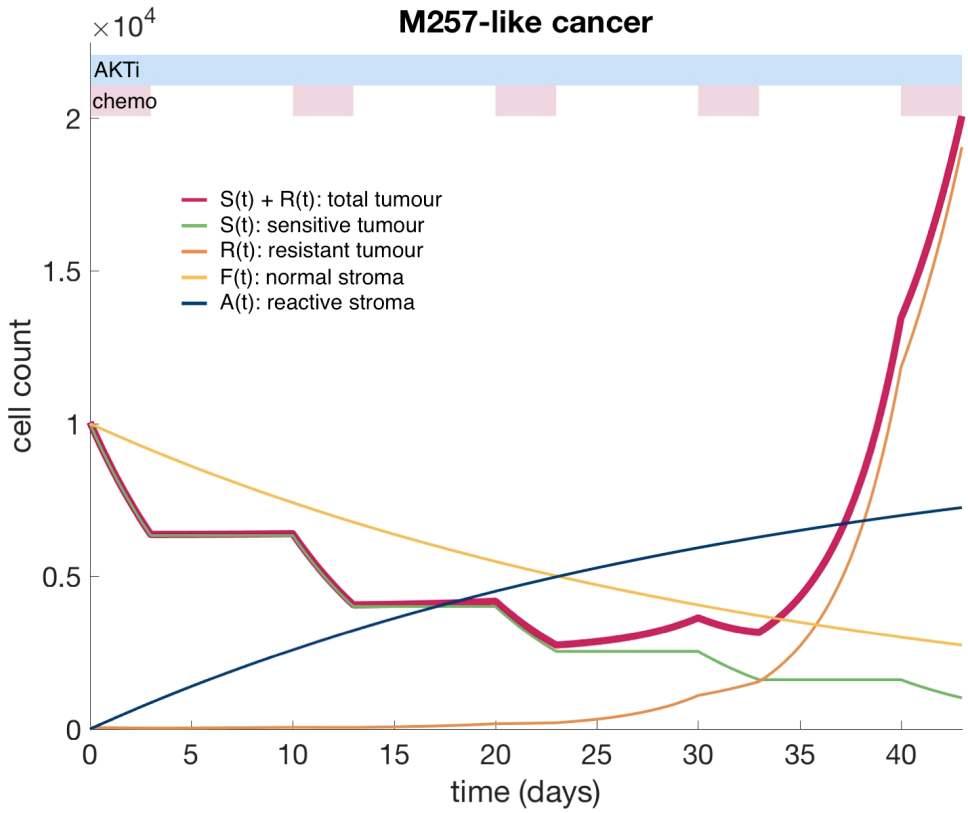


Figure 4.13: *Tumour-stroma dynamics, as described in Eqs.* (4.1)*, in an example of "control therapy", given by continuous targeted therapy with adjuvant pulses of chemotherapy with 7 day holidays. The targeted therapy inhibits the growth of the sensitive tumour (green) while promoting the emergence of reactive stroma (blue) which stimulates growth of the resistant tumour (orange). The pulses of chemotherapy act on the tumour reducing both populations, most importantly, controlling the growth of the resistant strain, responsible for disease progression in the previous simulations.*

stroma, leading to growth promotion of the sensitive tumour, counteracting the effects of the chemotherapy. Comparing the different responses to consecutive pulses of chemotherapy, we can conclude that its effect in a treatment regime depends on the abundance of resistant versus sensitive cells in the tumour.

The solution presented in Figure 4.13 is just one example of a possible optimal schedule that controls the emergence of the resistant strain during holidays from chemotherapy. Nevertheless a further investigation, including a formal definition of a minimisation problem with constraints related to the drug toxicity, is needed. A constrained minimisation can be performed with the Matlab routine *fmincon*, optimising, for example, the spacing between chemotherapy pulses, while minimising the total tumour burden.

An equally effective strategy is to exploit the transient nature of the EMDR-associated mechanisms to design an effective intermittent targeted therapy. Both of these avenues will be explored in the next chapter.

4.10 Conclusion

We have developed a mathematical model for tumour-stroma interactions, with the aim of describing the effects of combination therapy (cytotoxic and cytostatic agents) under different treatment regimes. The model takes the form of a system of coupled ODEs that allows exploration of any given treatment schedule. The four compartments include tumour cells, classified as sensitive or resistant to the targeted drug, and stromal cells. The latter can accomplish a switch from normal to reactive, following treatment with the targeted drug. The reactive pool of stromal cells enhances proliferation in the resistant tumour cells. The chemotherapy is assumed to kill both tumour cell populations indiscriminately.

Using the available experimental data and a reduced version of the model, we parameterised the dynamics relative to the cancer cell population. We first approached the parameter estimation with a standard Matlab routine, *fmincon*. This is useful to obtain rough parameter estimates, but does not allow too much freedom in tweaking the parameter search method to make sure the algorithm does not fall into local minima. Therefore we formulated the problem of parameter estimation using Bayesian inference, and developed two algorithms that gave us complementary information about the data. The ABC rejection algorithm allows us to build an approximated posterior distribution for the parameters. The MCMC Metropolis-Hastings algorithm is a theoretically more rigorous method, however it requires that assumptions are made about the distribution of the observed data. The intuitive nature of the ABC method, and the lack of assumptions required, makes it the preferable method for obtaining an approximated posterior distribution of the model parameter values. In the next chapter of this thesis we will use the ABC rejection algorithm for parameter estimation.

The parametrisation allowed us to reproduce the *in silico* counterpart of the treatment strategies for monotherapy, that were consistent with the experimental *in vitro* results. For each one of the estimation runs we obtained different estimated initial conditions (in terms of sensitive and resistant cell populations). It is worthwhile remarking that the current focus of this work is the dynamical interaction between tumour and stromal cells in the context of a variety of treatment strategies. Ultimately the goal is to gain insight into the interactions between cells in an *in vitro* or *in vivo* context, facilitating the transition to a more clinically relevant description. The variety of initial condition estimates across the cell lines and treatments will be of value in future work, as they will allow us to simulate *in silico* heterogeneity, both within an individual metastasis (intra-tumour heterogeneity) and across different metastases (inter-tumour heterogeneity) in terms of different degrees of intrinsic resistance. Similarly, the variation in estimated

rates across cell lines indicates the quantitative variability of the dynamics, even within a genetically defined cancer type (e.g. BRAF wildtype melanoma). This reveals how cautious one has to be when interpreting the outcome of experimental or computational models that have been calibrated on a specific cell line. Moving from *in vitro* culture to *in vivo* mouse models, and even more so from mice to human models, the level of complexity of the system increases remarkably. A key aspect of this complexity is the heterogeneous composition of the cancer, which includes multiple clones, with many more emerging in the course of progression and treatment. Our compartmental model is not suited for accounting for such dynamical heterogeneity and in Chapters 6 and 7 we will address this important issue within a different modelling framework.

It is worth noting that the dynamical system was parametrised on the BRAF-wildtype melanoma experimental model, consisting of melanoma cells grown in the absence of stroma. While this experimental setup allowed us to calibrate the growth dynamics of the cancer cells, it did not allow characterisation of the EMDR. Despite the limitations of the available data, we used the partially parametrised model to investigate a few treatment scenarios of interest. Initially we simulated the current *standard of care*, consisting of an initial pulse of chemotherapy, supported by continuous targeted therapy. Secondly, we simulated the effect of targeted drug removal, and observed the *flare response*, consistent with clinical results. Finally, we illustrated a possible scenario for a *control therapy*.

In the next chapter we will present a different experimental model of melanoma, and we will focus on the problem of bridging scales between *in vitro* and *in vivo* models to identify the role of the stroma in the resistance dynamics. Teasing apart the relative contribution of the environment to drug resistance is a necessary step toward designing intermittent targeted therapy schedules that effectively control the emergence of EMDR.

Chapter 5

Dual Targeting of Tumour and Stroma in BRAF-mutated Melanoma: Bridging Scales

A common paradigm for the treatment of advanced stage BRAF-mutated melanoma includes targeted therapy in the form of a BRAF inhibitor (BRAFi), such as vemurafenib, recently approved for patients carrying the V600E mutation (Bollag et al., 2010). Kinase inhibitors such as vemurafenib specifically block a molecular pathway on which the cancer cells are strongly dependent, resulting in reduced toxicity for the whole body and increased specificity for the tumour. While this treatment can keep the cancer in check for many months, recurrence will eventually occur. Having identified the environment as a main factor in therapy failure, alternative blockades of stromal-derived processes are being investigated. Here we model the FAK inhibitor (FAKi) that preliminary results have proved effective in pre-clinical settings (Hirata et al., 2015).

We present a version of the ODE model presented in Chapter 4, adapted with the scope of bridging the growth dynamics of cancer from *in vitro* and *in vivo* experimental models. Specifically, by using exponential growth dynamics from cells growing *in vitro* we can calibrate baseline unconstrained growth dynamics. Then using the same cancer cell line *in vivo* (mouse allograft) we can capture the saturation dynamics. Using these two experimental model systems, under treatment, we can then quantify the relative contribution of the environment to tumour growth.

The modelling framework we propose allows a fuller exploration of the role of stroma in the promotion of drug resistance, which is critical for the design of optimal treatment strategies. Indeed this model can be used to explore treatment schedules that exploit tumour-stromal interactions to limit and/or delay the emergence of EMDR.

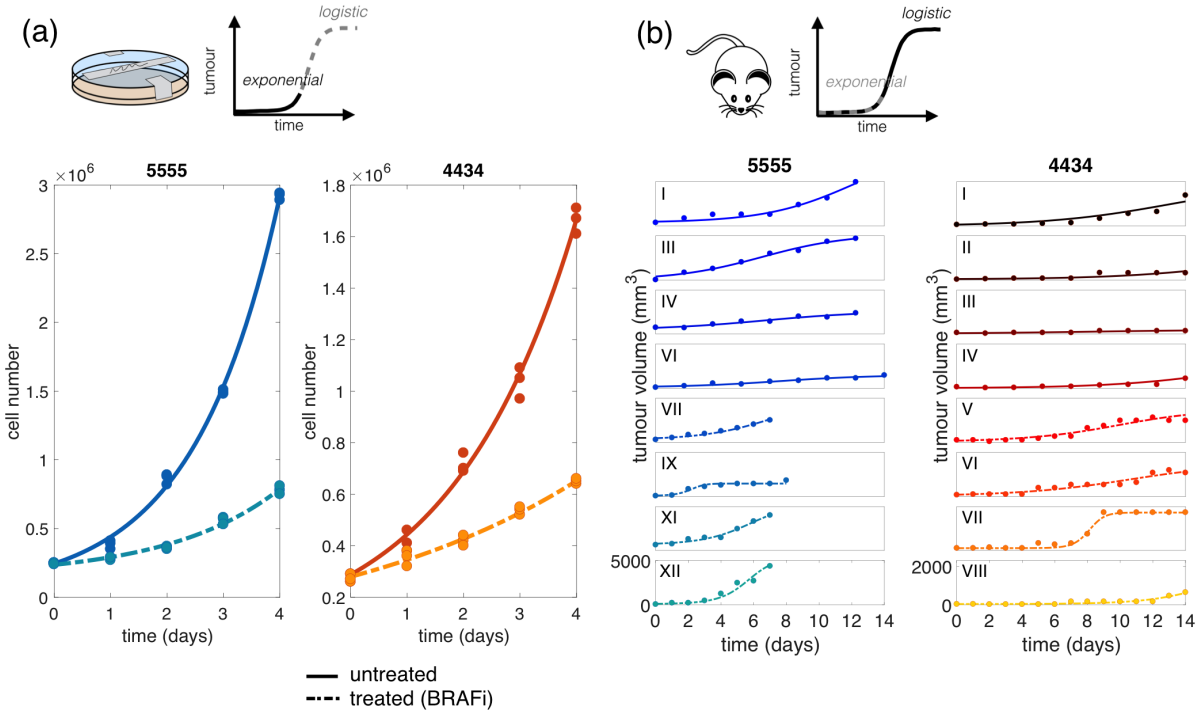


Figure 5.1: *Unpicking the relative contributions of intrinsic resistance and extrinsic environment conferred tolerance (EMDR). (a) In vitro data and fit. For each condition the model (Eqs.* (5.3)*) is fitted to three replicates. (b) In vivo data and fit of representative mice. For each condition the model (Eqs.* (5.4)*) is fitted individually to each replicate (mouse). Solid and dashed lines correspond to untreated and BRAFi treated tumour, respectively. All fits were obtained with the ABC rejection method (Section 4.5.2). Note different y axis scale for the two cell lines.*

5.1 The Experimental Model for BRAF-mutated Melanoma

We make use of published data from Hirata et al. (2015), investigating the effects of BRAF inhibition *in vitro* and *in vivo*, making use of two BRAF mutated melanoma cell lines: 5555 and 4434. Figure 5.1 shows the experimental data for BRAF mutated melanoma cell lines 5555 and 4434. These cells were both cultured *in vitro* (Figure 5.1(a)) and injected *in vivo* (Figure 5.1(b)). Growth was observed over time, both in the absence of drug and under treatment with PLX4720, a BRAF inhibitor. Additionally, 5555 tumours were treated *in vivo* with a combination of the BRAF inhibitor and PF562271, a FAK inhibitor (Figure 5.2). In the following we will build a model for BRAF-mutated melanoma and adapt it to represent each one of these experimental conditions.

5.2 The ODE Model of BRAFi and FAKi

We propose a model of EMDR in BRAF-mutated melanoma. Figure 5.3 shows a schematic of the interactions between key players in our system: cancer cells classified as either sen-

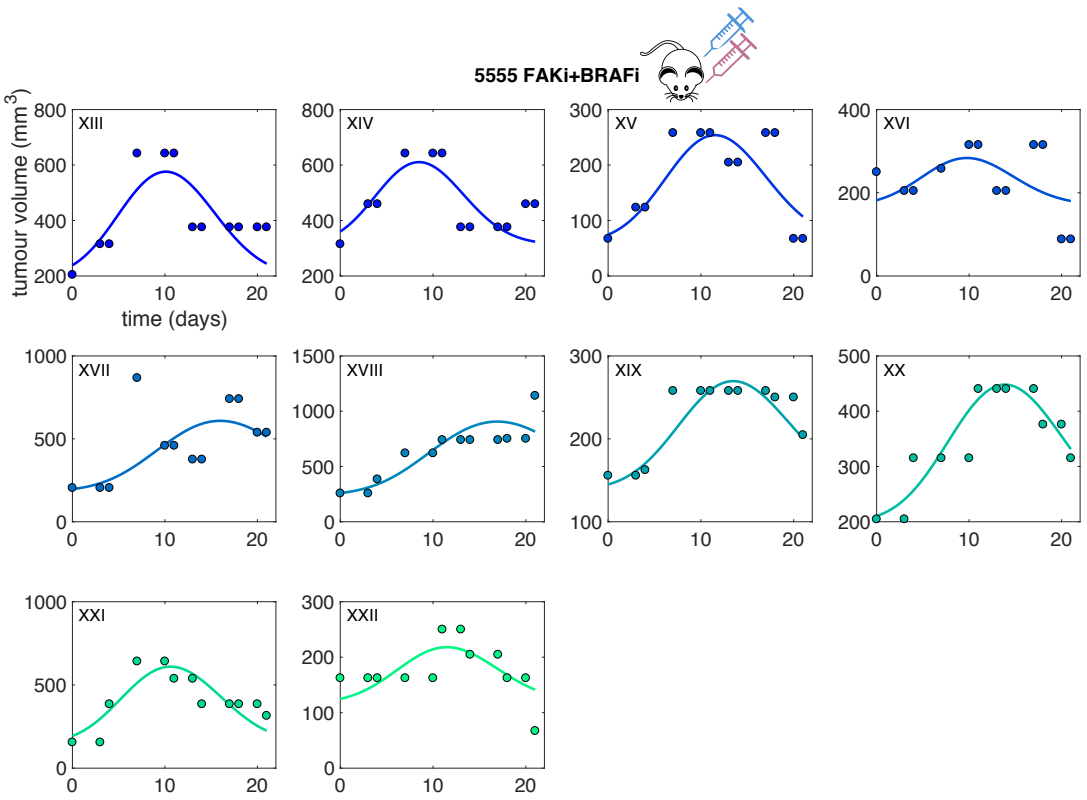


Figure 5.2: *In vivo data and fit for 5555 mice XIII through XXII, treated with PLX4720 (BRAFi) and PF562271 (FAKi). Fit obtained with the ABC rejection method (Section 4.5.2). Note different y axis scales.*

sitive or resistant to the targeted drug (S and R, respectively), and stroma cells in normal or reactive form (F and A, respectively). The R compartment includes intrinsically resistant cancer cells as well as cells that are transiently drug-tolerant through the action of EMDR. It is worth noting that this "catch all" compartment does not correspond to a single biological phenotype or genotype, however, it allows us to analyse growth regimes with or without targeted treatment, and most importantly to quantify the relative contribution of the environment to tumour growth dynamics under treatment. The interactions between the cell compartments, modulated by the two drugs (BRAFi and FAKi), can be

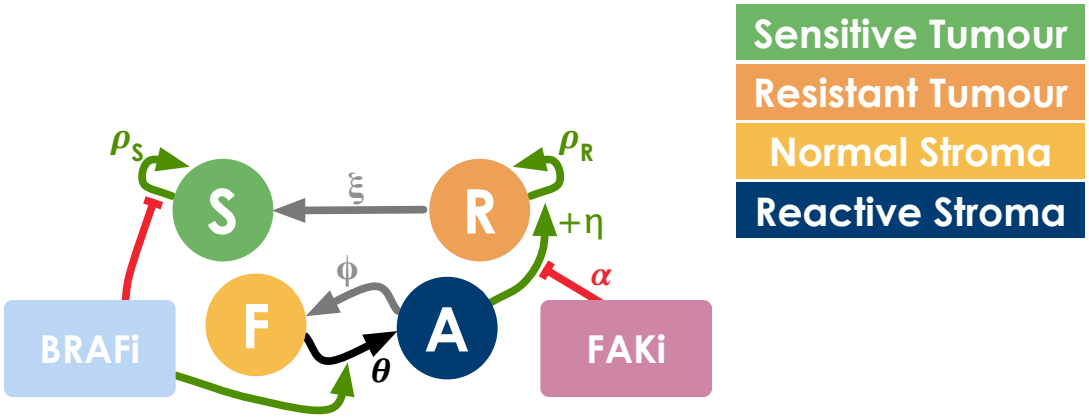


Figure 5.3: *Interactions hypothesised in the compartmental model: positive interactions are represented with green arrows, negative ones with red flat ends. The BRAFi (targeted to the tumour) inhibits growth in the drug-sensitive portion of the tumour (S) and induces activation of normal stroma (F). In turn, reactive stroma (A) promotes growth in the drug-tolerant portion of the tumour (R). The stroma-targeted inhibitor FAKi dampens the effect of stromal-induced growth promotion. Upon removal of BRAFi the tumour requires sensitivity to the drug and the stroma renormalises (grey arrows).*

formalised into a set of ODEs:

$$\begin{cases} \dfrac{dS}{dt} = \overbrace{\rho_S S(1-g(t))\left(1-\dfrac{S+R}{K}\right)}^{\text{growth}} + \overbrace{\xi R h(t)}^{\text{return to sensitivity}} \\ \dfrac{dR}{dt} = \overbrace{(\rho_R R g(t)}^{\text{growth}} + \overbrace{\eta A R}^{\text{stromal promotion}} - \overbrace{\alpha A R f(t))}^{\text{FAKi}}\left(1-\dfrac{S+R}{K}\right) - \overbrace{\xi R h(t)}^{\text{return to sensitivity}} \\ \dfrac{dF}{dt} = - \overbrace{\theta F g(t)}^{\text{stromal activation}} + \overbrace{\phi A h(t)}^{\text{stromal renormalisation}} \\ \dfrac{dA}{dt} = \overbrace{\theta F g(t)}^{\text{stromal activation}} - \overbrace{\phi A h(t)}^{\text{stromal renormalisation}} \end{cases} \tag{5.1}$$

with initial conditions: $S(0) = S_0$, $R(0) = R_0$, $F(0) = F_0$, $A(0) = A_0$. g, h and f are binary functions of time allowing to switch on and off terms in the equations, depending on the treatment scheduling. Given a protocol calling for targeted therapy for the time interval $[t^i_{TT}, t^f_{TT}]$, and the FAKi for the time interval $[t^i_{FF}, t^f_{FF}]$, the binary functions are defined as follows:

$$f(t) = \begin{cases} 1 & \text{if } t^i_{FF} \le t \le t^f_{FF} \\ 0 & \text{else} \end{cases} \quad g(t) = \begin{cases} 1 & \text{if } t^i_{TT} \le t \le t^f_{TT} \\ 0 & \text{else} \end{cases} \quad h(t) = \begin{cases} 1 & \text{if } t \ge t^f_{TT} \\ 0 & \text{else.} \end{cases} \tag{5.2}$$

The tumour is classified into two subpopulations, with respect to their sensitivity to the targeted inhibitor. S and R are, respectively, drug sensitive and drug tolerant populations. The first grows in the absence of treatment with growth rate ρ_S the second grows under targeted treatment at rate ρ_R. They both share a carrying capacity K, representing the maximum packing capacity of the tissue where the tumour is growing. The stroma is divided in normal cells F (i.e. fibroblasts) and reactive cells A (i.e. cancer associated fibroblasts). The latter compartment represents fibroblasts in a transformed, secretory phenotype that promotes survival and tumour growth under drug treatment. Targeted therapy (BRAFi) induces the stroma to switch to its reactive form. In turn reactive stroma (A) will promote tumour growth by an additional growth rate η. Upon removal of the targeted inhibitor, stromal renormalisation occurs at rate ϕ and cancer cells are re-sensitised at rate ξ. The stromal-targeted inhibitor (FAKi) is assumed to reduce the stromal promotion by rate α. The key advantage of this model is that it can be adapted to the description of experimental models and to the application of the treatment regime of choice.

5.3 Model Parametrisation with Experimental Data

We can adapt model (5.1) to represent each one of the experimental conditions. Starting from the *in vitro* experimental setup, corresponding to a simplified system of equations with fewer unknown parameters, we will obtain parameter estimates by data fitting and consequently use these values for the data fitting of the *in vivo* experimental setup. Doing so we significantly reduce the number of unknown parameters for each fit, as well as the risk of overfitting. A summary of the analysis and estimation method used to parameterise the model is given in Table 5.1.

The *in vitro* setup (with a time scale on the order of a few days, Figure 5.1(a)) can be represented by an exponential growth regime, and lacks the stromal component. This corresponds to reducing Eqs. (5.1) for small time t and $F_0 = 0$, obtaining:

$$\begin{cases} \dfrac{dS}{dt} = \rho_S S(1 - g(t)) \\ \dfrac{dR}{dt} = \rho_R R g(t) \end{cases} \quad \text{with} \quad \begin{cases} S(0) = S_0 \\ R(0) = R_0 \end{cases} \tag{5.3}$$

where the only unknown parameters are: R_0, S_0, ρ_S for the untreated case ($g = 0$), and R_0, S_0, ρ_R for the treated case ($g = 1$). Parameter estimation for these triplets is carried out by the ABC method which builds a discrete approximation of the posterior distribution. This method is extensively described in the previous chapter (Section 4.5.2).

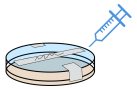
Experimental Model	Mathematical Model	Analytical Solution	Parameters
Untreated Cell Line 	$\begin{cases} \frac{dS}{dt} = \rho_S S \\ \frac{dR}{dt} = 0 \end{cases}$	$S(t) = S_0 \exp(\rho_S t)$ $R(t) = R_0$	S_0, R_0, ρ_S
BRAFi Treated Cell Line 	$\begin{cases} \frac{dS}{dt} = 0 \\ \frac{dR}{dt} = \rho_R R \end{cases}$	$S(t) = S_0$ $R(t) = R_0 \exp(\rho_R t)$	S_0, R_0, ρ_R
Untreated Mice (5555 I-VI 4434 I-IV) 	$\begin{cases} \frac{dS}{dt} = \rho_S S\left(1 - \frac{S+R}{K}\right) \\ \frac{dR}{dt} = 0 \\ \frac{dF}{dt} = 0 \\ \frac{dA}{dt} = 0 \end{cases}$	$S(t) = \frac{K - R_0}{1 + \left(\frac{K-R_0}{S_0} - 1\right)\exp\left[\left(\frac{R_0}{K} - 1\right)\rho_S t\right]}$ $R(t) = R_0$ $F(t) = F_0$ $A(t) = 0$	S_0, R_0, K
BRAFi Treated Mice (5555 VII-XII 4434 V-IX) 	$\begin{cases} \frac{dS}{dt} = 0 \\ \frac{dR}{dt} = (\rho_R + \eta A) R\left(1 - \frac{S+R}{K}\right) \\ \frac{dF}{dt} = -\theta F \\ \frac{dA}{dt} = \theta F \end{cases}$	$S(t) = S_0$ $R(t) = \frac{K - S_0}{1 + \left(\frac{K-S_0}{R_0} - 1\right)\exp\left[\left(\frac{S_0}{K} - 1\right)\left((\rho_R + \tilde{\eta})t - \frac{\tilde{\eta}}{\theta}(1 - e^{-\theta t})\right)\right]}$ $F(t) = F_0 \exp(-\theta t)$ $A(t) = F_0(1 - \exp(-\theta t))$	$S_0, R_0, \tilde{\eta}$ $(\tilde{\eta} = \eta F_0)$
BRAFi + FAKi Treated Mice (5555 XIII-XXII) 	$\begin{cases} \frac{dS}{dt} = 0 \\ \frac{dR}{dt} = (\rho_R + (\eta - \alpha)A) R\left(1 - \frac{S+R}{K}\right) \\ \frac{dF}{dt} = -\theta F \\ \frac{dA}{dt} = \theta F \end{cases}$	$S(t) = S_0$ $R(t) = \frac{K - S_0}{1 + \left(\frac{K-S_0}{R_0} - 1\right)\exp\left[\left(\frac{S_0}{K} - 1\right)\left((\rho_R + \tilde{\eta} - \tilde{\alpha})t - \frac{\tilde{\eta} - \tilde{\alpha}}{\theta}(1 - e^{-\theta t})\right)\right]}$ $F(t) = F_0 \exp(-\theta t)$ $A(t) = F_0(1 - \exp(-\theta t))$	$S_0, R_0, \tilde{\alpha}$ $(\tilde{\alpha} = \alpha F_0)$

Table 5.1: *Data are fitted to $S(t) + R(t)$. Initial conditions for the cell line model are: $S(0) = S_0, R(0) = R_0$, for the mouse model: $S(0) = S_0, R(0) = R_0, F(0) = F_0, A(0) = 0$. Note that S_0 and R_0 represent different quantities depending on the model (cell count for cell line model, and tumour volume for mouse model).*

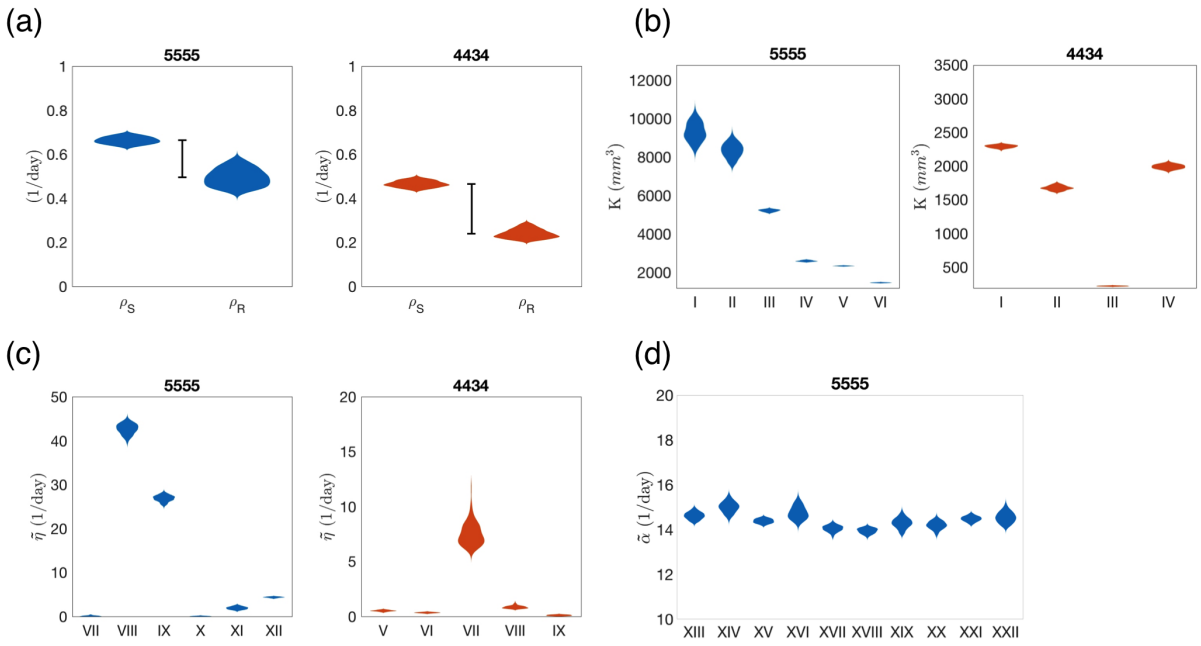


Figure 5.4: *Approximated posterior distribution of estimated parameters. (a) Estimates for cancer growth rates: ρ_S (untreated cancer), ρ_R (treated cancer). The black bar highlights the fitness cost of intrinsic resistance. (b) Estimates for K reveal heterogeneity of carrying capacity across mice. ρ_S from previous estimate. (c) Estimates for $\tilde{\eta}$ reveal heterogeneity of stromal-derived protection found in vivo. $\theta = 0.03$ 1/day. ρ_R from previous estimates. (d) Estimates for $\tilde{\alpha}$ for ten 5555 mice treated with BRAFi and FAKi combination. $\theta = 0.03$ 1/day. $\rho_R = 0.49539$ 1/day. $\tilde{\eta} = 12.67$ 1/day (average of previous estimates, Table 5.2).*

Data are fitted to the analytical solution of Eqs. (5.3). Figure 5.4(a) shows the marginal distributions for the growth rates of each cell line. Comparing the estimates for control and treated conditions, we see a reduction in growth rate for the treated cancer. The deficit in growth rate reveals the fitness cost of drug tolerance, consistent with the concept of a tradeoff (Das Thakur et al., 2013), already observed in the BRAF-wildtype melanoma experimental model (Figure 4.6).

We assume that the growth dynamics of the cancer cells treated *in vitro* can be solely attributed to pre-existing drug tolerant subpopulations. On the other hand, in order to quantify the role of the environment on the dynamics of resistance, we turn to the mouse allografts. When the same cell lines are injected in mice, growth is significantly constrained and experiments cover a longer time scale (Figure 5.1(b)). The observed

Parameter	Cell Line	Estimate		Range of Accepted Values
ρ_S (1/day)	5555	0.66325		[0.6264, 0.7002]
	4434	0.4652		[0.4336, 0.5011]
ρ_R (1/day)	5555	0.49543		[0.4170, 0.5922]
	4434	0.23942		[0.2008, 0.2942]
K (mm^3)	5555	I	9318.8984	[8344.3248, 10435.095]
		II	8352.5141	[7587.9093, 9264.7683]
		III	5222.2471	[5086.7338, 5336.5553]
		IV	2600.883	[2540.8448, 2672.0427]
		V	2345.1481	[2316.3892, 2371.1414]
		VI	1475.6726	[1449.7419, 1504.5806]
		average	4818.62	
	4434	I	2290.201	[2232.7464, 2334.0511]
		II	1673.7862	[1612.0517, 1749.9593]
		III	215.6403	[206.5229, 225.9717]
		IV	1989.7505	[1919.6823, 2067.3783]
		average	1543.6147	
$\tilde{\eta}$ (1/day)	5555	VII	0.12569	[0.000906, 0.41951]
		VIII	42.6592	[39.73, 45.02]
		IX	26.876	[24.9689, 28.4394]
		X	0.07974	[0.001035, 0.22109]
		XI	1.9371	[1.2953, 2.63]
		XII	4.3748	[4.0746, 4.6022]
	4434	V	0.52429	[0.36648, 0.6682]
		VI	0.34886	[0.25731, 0.44138]
		VII	7.54	[6.1132, 11.9923]
		VIII	0.8568	[0.65997, 1.3352]
		IX	0.10473	[0.003147, 0.20759]
$\tilde{\alpha}$ (1/day)	5555	XIII	14.6163	[14.2953, 14.9547]
		XIV	15.0018	[14.441, 15.5339]
		XV	14.3818	[14.182, 14.5668]
		XVI	14.7552	[14.2099, 15.4362]
		XVII	14.0455	[13.6516, 14.3181]
		XVIII	13.9436	[13.6503, 14.1428]
		XIX	14.2911	[13.7735, 14.859]
		XX	14.1929	[13.6946, 14.5971]
		XXI	14.4799	[14.2231, 14.729]
		XXII	14.5452	[14.082, 15.1437]
		average	14.42533	

Table 5.2: *Estimated parameter values for BRAF-mutated melanoma cell lines 5555 and 4434.*

dynamics are more accurately captured with a logistic growth regime, as described by:

$$\begin{cases} \dfrac{dS}{dt} = \rho_S \left(1 - \dfrac{S+R}{K}\right) S(1-g(t)) \\ \dfrac{dR}{dt} = (\rho_R g(t) + \eta A) \left(1 - \dfrac{S+R}{K}\right) R \\ \dfrac{dF}{dt} = -\theta F g(t) \\ \dfrac{dA}{dt} = \theta F g(t) \end{cases} \quad \text{with} \quad \begin{cases} S(0) = S_0 \\ R(0) = R_0 \\ F(0) = F_0 \\ A(0) = 0 \end{cases} \tag{5.4}$$

By assuming that cells from the same line grow at the same exponential rate in an unconstrained environment, we are able to use the growth rates estimated from the *in vitro* data (i.e. and ρ_S and ρ_R).

Fitting the model to the data from the untreated mice we can obtain estimates for parameters R_0, S_0, K. Note that in the absence of treatment ($g = 0$), the equations for the tumour and stromal populations are decoupled, therefore the estimate of the tissue carrying capacity is independent of the quantification of interacting stromal cells. However, K is intrinsically dependent on the nutrient constraint as well as the packing capacity of the tissue. Indeed, variations of this quantity are captured in the range of estimated values (see Figure 5.4(b) and Table 5.2). Posterior distributions are wider in mice with higher values of carrying capacity (e.g. mice I, II cell line 5555). For low K, logistic curves reach carrying capacity within the time window of the *in vivo* experiments. Curves with higher K, however, have later inflection point and their characteristic shape is not captured in the same time window, resulting in more uncertain estimates. It is worth noting that for some mice, the data do not capture the saturating dynamics, as the experiment had to be interrupted due to animal welfare (for details on the original experiments see Hirata et al., 2015).

For the treated mice setup ($g = 1$), the equations are coupled. We can solve the last of Eqs. (5.4) analytically, to write A as a function of F_0 and θ. Defining $\tilde{\eta} = \eta F_0$ we reduce the parameter number in the analytical solution of Eqs. (5.4) (see Table 5.1). At this stage quantification of the rate of stromal activation is difficult, therefore the estimates for the parameters $R_0, S_0, \tilde{\eta}$ will be carried out with a guessed value of θ. The estimation routine has been run for a range of θ values, finding high sensitivity of the estimates to this experimentally undefined parameter (Figure 5.5). Figure 5.4(c) shows the estimated values for $\tilde{\eta}$ for each mouse. This reveals considerable variation in the stromal support across mice, hinting at an underlying heterogeneity in stromal habitats and activation.

Since estimates of K and $\tilde{\eta}$ are dependent on the previously estimated growth rates (ρ_S and ρ_R, respectively), the ABC estimation was run for values of growth rates within

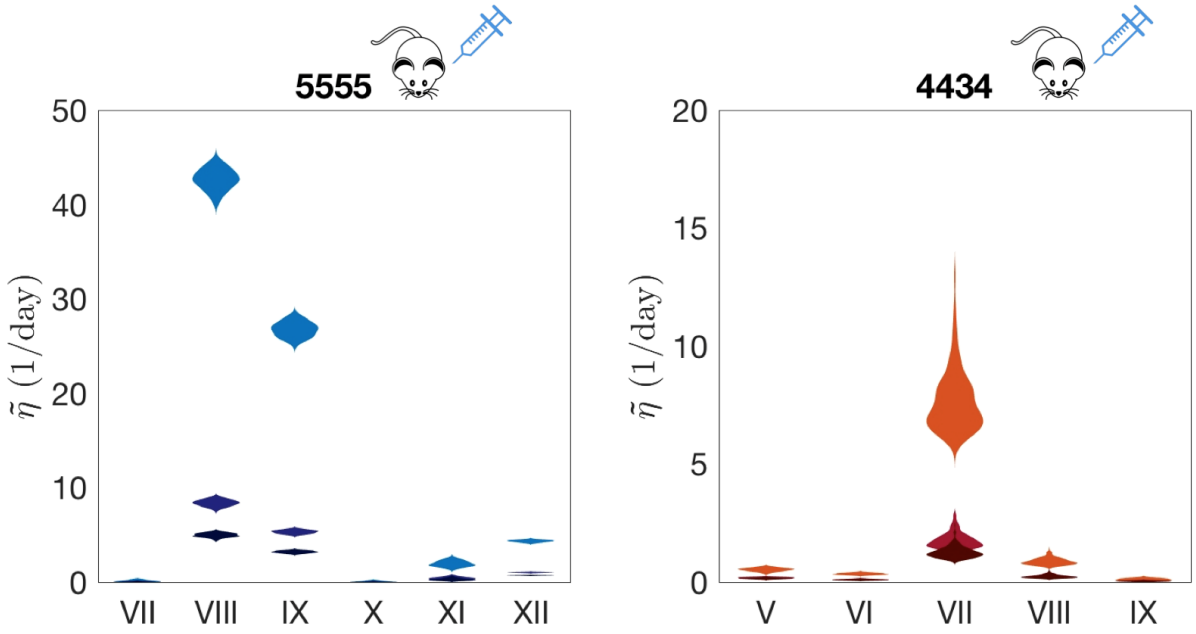


Figure 5.5: *Posterior distribution for $\tilde{\eta}$ as θ is varied, and average ρ_R value from previous estimate (Table 5.2). The lighter colour violin plots correspond to the value used in the estimates reported in Figure 5.4(c) ($\theta = 0.03$ 1/day). The intermediate and darker coloured violin plots are obtained with $\theta = 0.165$ 1/day and $\theta = 0.3$ 1/day, respectively.*

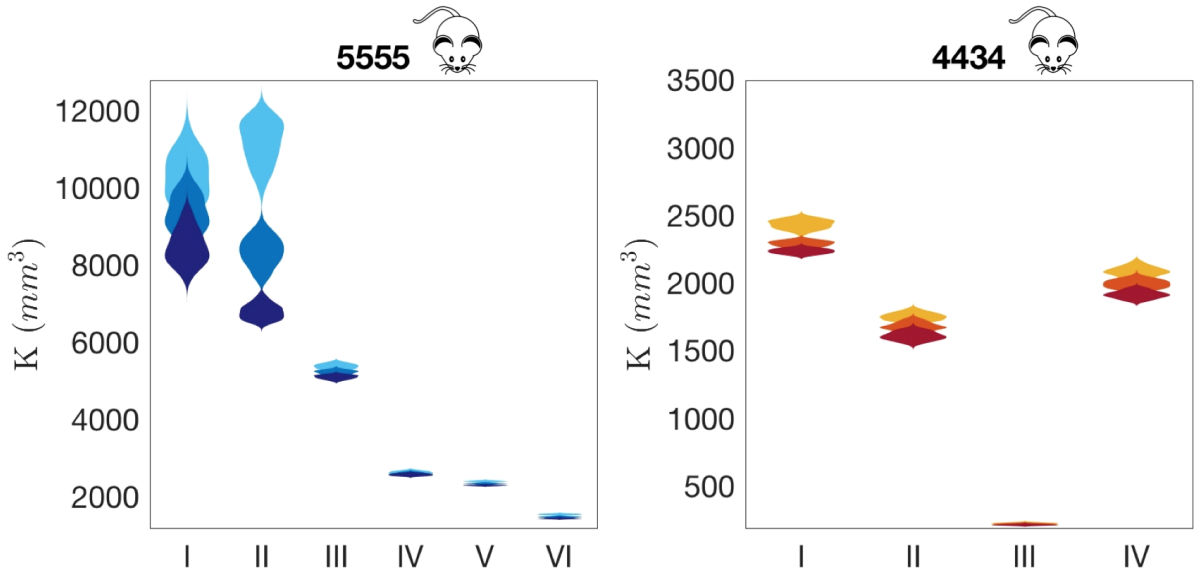


Figure 5.6: *Posterior distribution for K as ρ_S is varied within the range of estimates obtained with fit to in vitro data of corresponding cell line. The lighter (darker) coloured violin plots are obtained with ρ_S value corresponding to the lower (upper) bound of the range reported in Table 2. The intermediate colour violin plots correspond to the average ρ_S value, as are those reported in Table 5.2.*

the range captured by the fit to the *in vitro* data (see Figure 5.4(a)). The resulting posterior distribution varying in relation to the growth rates are shown in Figures 5.6

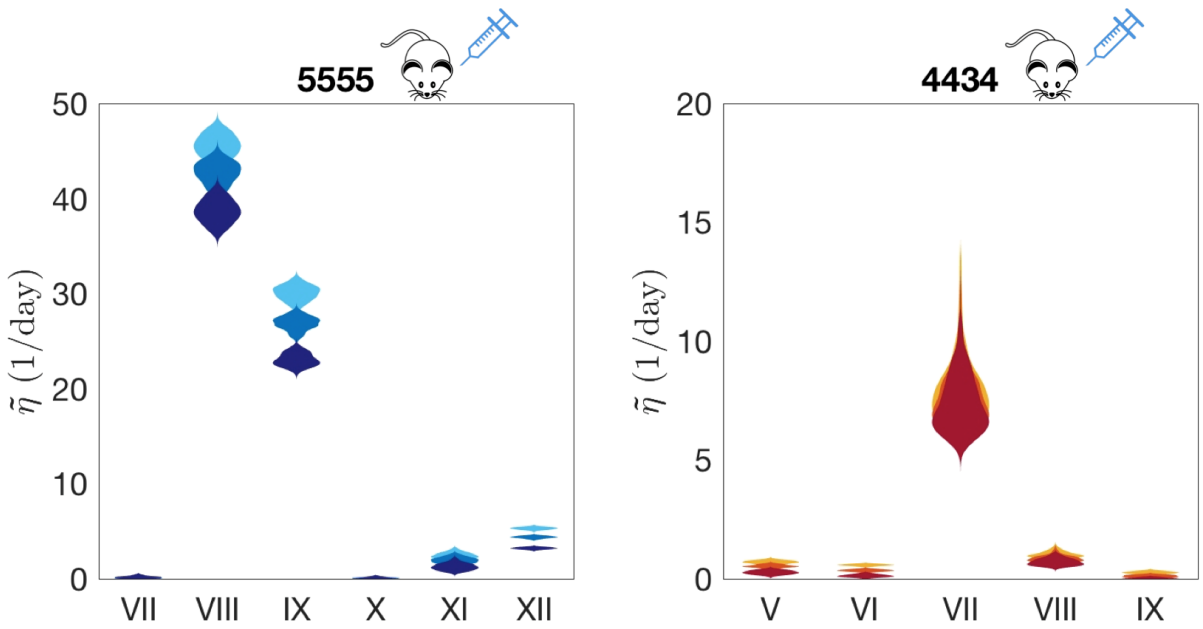


Figure 5.7: *Posterior distribution for $\tilde{\eta}$ as ρ_R is varied within range of estimates obtained with fit to in vitro data of the corresponding cell line. The lighter (darker) coloured violin plots are obtained with ρ_R value corresponding to the lower (upper) bound of the range reported in Table 5.2. The intermediate colour violin plots correspond to the average ρ_R value, as are those reported in Figure 5.4(d).*

and 5.7, respectively.

The variation of response to BRAF inhibition across replicates could be the result of underlying heterogeneity both in tissue carrying capacity and in stromal support. Our estimation protocol for the stromal promotion parameter $\tilde{\eta}$ makes use of an average carrying capacity K previously estimated. However, the variation across replicates could as well be explained by the heterogeneity in carrying capacity. Therefore we further investigated the BRAFi treated mice data, to infer the posterior distribution of $\tilde{\eta}$ as K is varied and *vice versa*. Figure 5.8 shows the resulting posterior distributions in the $(K, \tilde{\eta})$ space for a sample mouse. For every estimation we evaluate the goodness of the fit in terms of distance of the fit to the data (see line 19 of ABC algorithm, Section 4.5.2). The posterior distribution of K is highly sensitive to the variation of $\tilde{\eta}$ (see yellow violin plots), and *vice versa*. However, the best overall fits of $\tilde{\eta}$ and K are located in the same region of the space. This means that for a given mouse we can unequivocally identify a combination of values for the carrying capacity and stromal support that explains the data.

Finally, we can quantify the inhibiting action of the stromal-targeted drug in the form of $\tilde{\alpha} = \alpha F_0$, fitting data from mice treated with both BRAFi (PLX4720) and FAKi

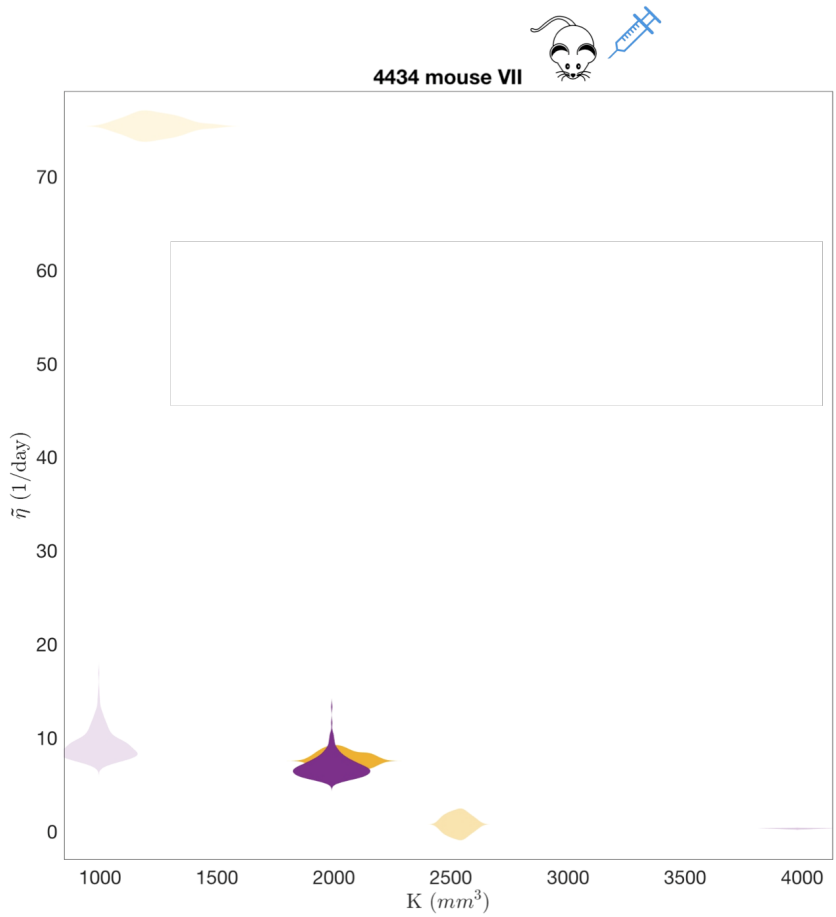


Figure 5.8: *Posterior distribution for $\tilde{\eta}$ as K is varied (purple) and K as $\tilde{\eta}$ is varied (yellow). Mouse VII, cell line 4434, treated with BRAFi. The intensity of the colour of each violin plot is proportional to the goodness of the fit. $\theta = 0.03$ 1/day. ρ_R from previous estimates (Table 5.2).*

(PF562271) to the following version of the model:

$$\begin{cases} \dfrac{dS}{dt} = 0 \\ \dfrac{dR}{dt} = (\rho_R + (\eta - \alpha)\, A)\left(1 - \dfrac{S+R}{K}\right) R \\ \dfrac{dF}{dt} = -\theta F \\ \dfrac{dA}{dt} = \theta F \end{cases} \quad \text{with} \quad \begin{cases} S(0) = S_0 \\ R(0) = R_0 \\ F(0) = F_0 \\ A(0) = 0 \end{cases} \tag{5.5}$$

Despite the variability of responses across replicates (see data and fits in Figure 5.2), the resulting estimates for $\tilde{\alpha}$ show little variation (Figures 5.4(d) and Table 5.2). This implies that the variability in treatment response can be attributed to the heterogeneous stromal composition of the tissue (highlighted in Figure 5.4(c)), as opposed to the efficacy of the stromal inhibition.

5.4 Treatment Strategies for BRAF-wildtype Melanomas

Calibrating our model across *in vitro* and *in vivo* data allows us to gain insight into the dynamics of the system that a qualitative analysis of these experiments cannot capture. Figure 5.4(a) shows the marginal posterior distribution for growth rates ρ_S and ρ_R, with a reduction of the latter quantifying the fitness cost of drug tolerance.

Comparing *in vitro* and *in vivo* dynamics allows us to assess the relative contribution of the environment to drug resistance. This analysis reveals significant heterogeneity across replicates (mice), both in terms of tissue carrying capacity, and stromal protection (Figures 5.4 (b) and 5.4(c)). This heterogeneity translates to a high variability of response to treatments that target both the tumour and the stroma, despite the more homogeneous inhibition of the latter (Figures 5.2 and 5.4(d)).

Analysis of the ODE model with the combination treatment of BRAFi and FAKi (Eqs. (5.5)) gives insight into the dynamics of the system as a function of stromal promotion and tumour growth rate. Specifically, we can discriminate two distinct cases:

1. If $(\alpha < \eta)$ or $\left(\alpha > \eta \text{ and } \dfrac{\rho_R}{F_0\,(\alpha - \eta)} > 1\right)$ then $\dfrac{d(S+R)}{dt} \geq 0 \quad \forall\, t \geq 0$,

2. If $\left(\alpha > \eta \text{ and } 0 < \dfrac{\rho_R}{F_0\,(\alpha - \eta)} < 1\right)$ then $\dfrac{d(S+R)}{dt} \geq 0 \quad \forall\, 0 \leq t \leq t^*$,
   where $t^* = -\dfrac{1}{\theta} \log\left(1 - \dfrac{\rho_R}{F_0\,(\alpha - \eta)}\right)$.

In the first case, either the stromal promotion is too strong to be compensated by the FAKi, or the stromal promotion is weak, but the tumour growth rate is elevated. Then the overall tumour burden is monotonically increasing. In the second case, when stromal promotion is weak and the tumour growth rate is reduced, the therapy is effective provided that it is administered for a sufficiently large period of time.

As an example, consider the cohort of 5555 BRAFi-treated mice (VII through XII) and using the parameterised model (5.1), with α taken as the average of the previous estimates (Table 5.2) we can sub-classify the mice. According to our estimates, mice VII, X, XI, XII fall in case 2, meaning that with a combination of BRAFi and FAKi it is possible to achieve control as long as we treat past time t^*. On the other hand, mice VIII and IX fall in case 1, hence the tumour is always growing under treatment. Figures 5.9 and 5.10 show a simulated treatment combination of BRAFi + FAKi calibrated on two representative mice, case 1 and case 2, respectively. For a tumour-stroma system falling in case 1, recurrence is inevitable, but may be delayed with alternative scheduling strategies. Given that the phenotypic changes underlying EMDR are transient and reversible upon drug removal, we hypothesise that the introduction of drug holidays could

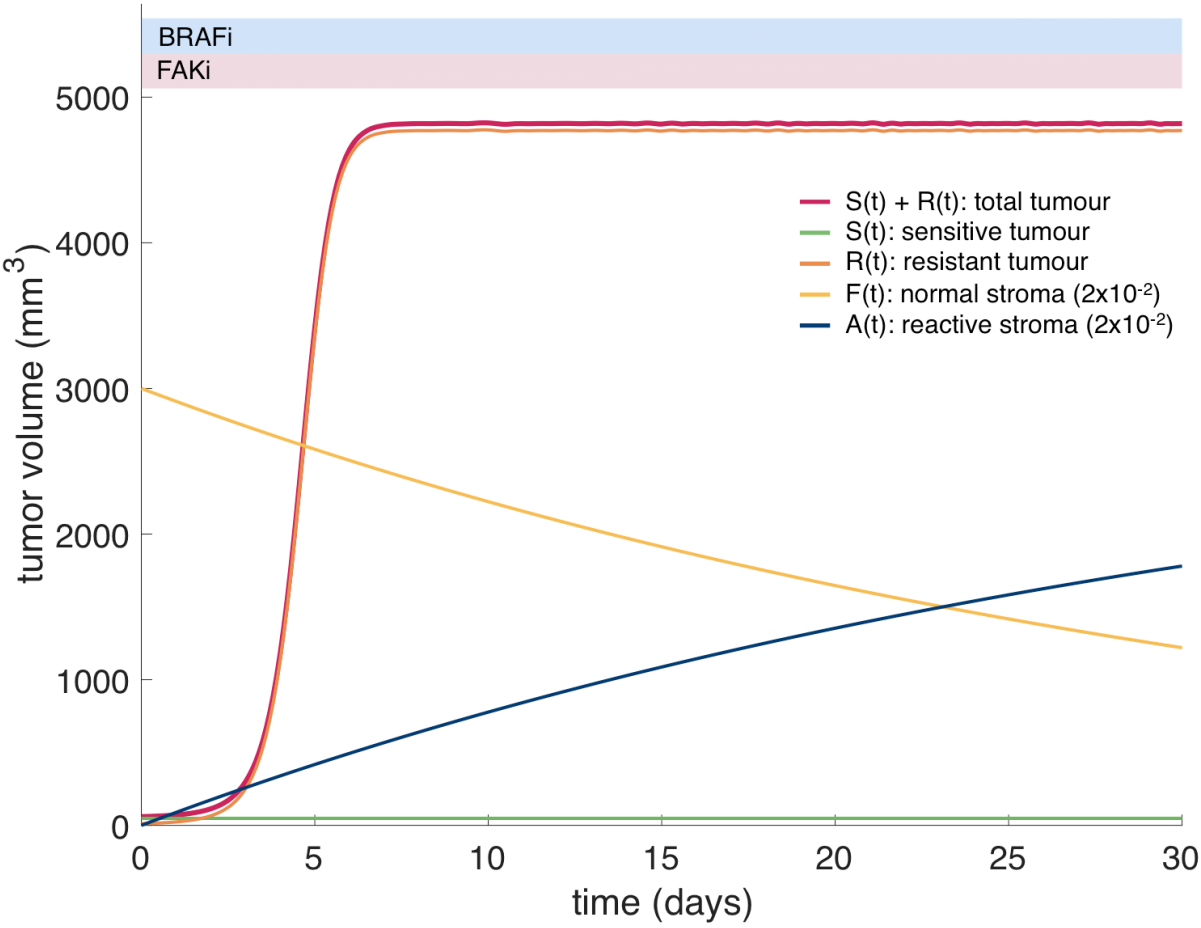


Figure 5.9: *Example of case 1. The model is parameterised on mouse IX of cell line 5555.* $\rho_S = 0.66325$ *1/day,* $\rho_R = 0.49543$ *1/day,* $K = 4818.62$ mm^3, $\tilde{\eta} = 26.876$ *1/day,* $\tilde{\alpha} = 14.4$ *1/day,* $\theta = 0.03$ *1/day,* $S_0 = 48$ mm^3, $R_0 = 12$ mm^3, $F_0 = 60$ mm^3, $A_0 = 0$ mm^3. *The tumour burden (red) is monotonically increasing under treatment combination of BRAFi and FAKi.*

significantly improve treatment response and recurrence times. Intermittent application of vemurafenib has proved to be successful in melanoma xenograft models (Das Thakur et al., 2013) and ongoing clinical trials are testing intermittent versus continuous dosing of a combination of BRAF and MEK inhibitors (NCT02196181). However, we believe that a mechanistic and quantitative approach to treatment scheduling can improve the success of the otherwise empirical approach that these studies offer. We therefore systematically explored the space of holiday versus treatment days of an intermittent schedule treatment with BRAFi, combined with continuous FAKi. Specifically, the targeted inhibitor is administered during the time windows $\left[t_i^{TT,k}, t_f^{TT,k}\right]$ for $k \in \mathbb{N}^0$ with $t_f^{TT,k} - t_i^{TT,k} = T_T$, $t_i^{TT,k+1} - t_f^{TT,k} = H$, $\forall k \geq 0$. A useful measure of tumour burden control over a window

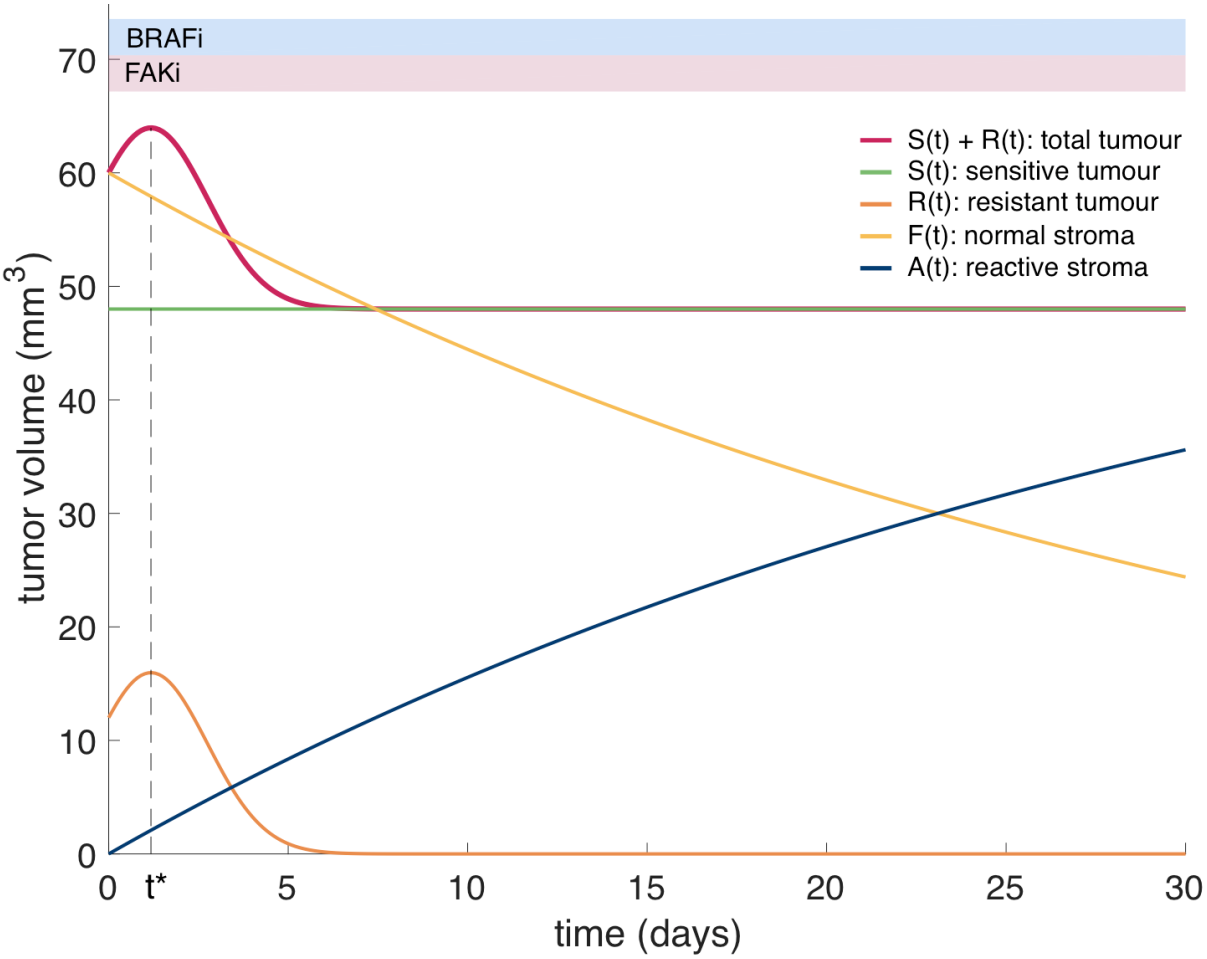


Figure 5.10: *Example of case 2. The model is parameterised on mouse VII of cell line 5555.* $\rho_S = 0.66325$ *1/day,* $\rho_R = 0.49543$ *1/day,* $K = 4818.62$ mm^3, $\tilde{\eta} = 0.1257$ *1/day,* $\tilde{\alpha} = 14.4$ *1/day,* $\theta = 0.03$ *1/day,* $S_0 = 48$ mm^3, $R_0 = 12$ mm^3, $F_0 = 60$ mm^3, $A_0 = 0$ mm^3. *Under treatment combination of BRAFi and FAKi, the tumour burden (red) is monotonically increasing after time* $t^* = 1.1771$ *day.*

of time $[t_A, t_B]$ is the inverse of the area under the curve, defined as follows:

$$\Pi = \frac{1}{\int_{t_A}^{t_B} \left(S(t) + R(t)\right) dt}. \tag{5.6}$$

Figure 5.11 shows the treatment outcome in the holiday vs treatment (H, T_T) space, where the outcome of each treatment strategy over the time frame of $[0, 70]$ days is quantified with Π, defined in Eq. (5.6). This reveals that the region corresponding to tumour burden minimisation (Π maximisation) is concentrated around the line $H = 2T_T$. Intuitively this means that the length of holiday needed to renormalise the system is proportional to the pulse of treatment. Additionally, it indicates that longer treatment holidays are more effective at controlling tumour burden, while the total number of treatment days is reduced.

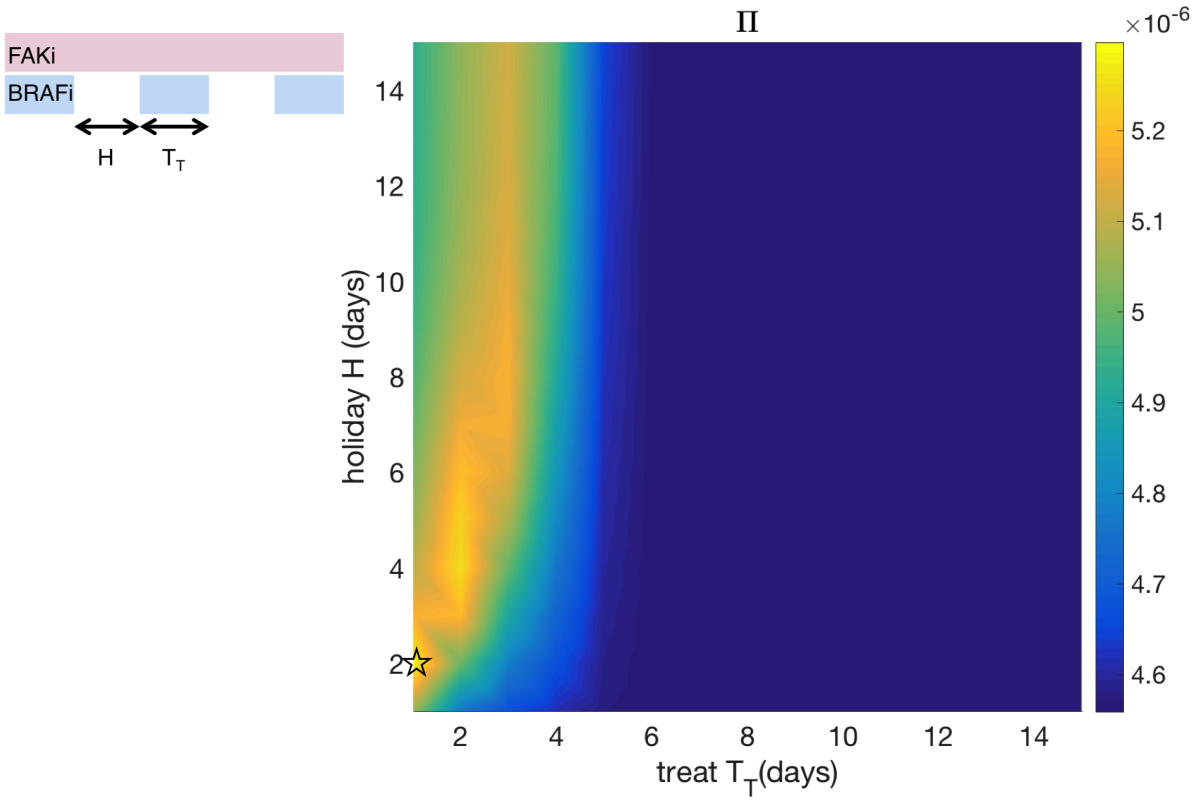


Figure 5.11: *Exploration of treatment/holiday space for intermittent BRAFi combined with continuous FAKi to maximise control of tumour burden. Model parameterised on mouse IX of cell line 5555.* $\rho_S = 0.66325$ *1/day,* $\rho_R = 0.49543$ *1/day,* $K = 4818.62$ mm^3, $\tilde{\eta} = 26.876$ *1/day.* $\tilde{\alpha} = 14.4$ *1/day,* $\theta = 0.03$ *1/day,* $\xi = 0.01$ *1/day,* $\phi = 1$ *1/day,* $S_0 = 48$ mm^3, $R_0 = 12$ mm^3, $F_0 = 60$ mm^3, $A_0 = 0$ mm^3. *The star indicates the treatment schedule simulated in Figure 5.12.*

Figure 5.12 shows the temporal dynamics for one of the best combination treatment schedules predicted by our model. FAKi is continuously administered, and helps control the tumour burden when EMDR sets in, whereas BRAFi is given periodically for 1 day, then off for 2 days. This treatment induces only minimal stromal activation and delays progression by approximately ten days when compared to the untreated tumour. When compared to the continuous treatment, this intermittent treatment delays progression by approximately twenty days, while using a third of the amount of BRAFi. Although this study does not explicitly account for drug toxicity, total dose reduction is a desirable outcome, especially in the case of combination therapy, where resulting toxicity might be a significant issue.

Given the successful outcome of this strategy, and the limited toxicity of the kinase inhibitors at clinically relevant dosing, we ask how the combination of chemotherapy and inhibitor compares to the dual tumour/stroma inhibition in BRAF-mutated melanomas.

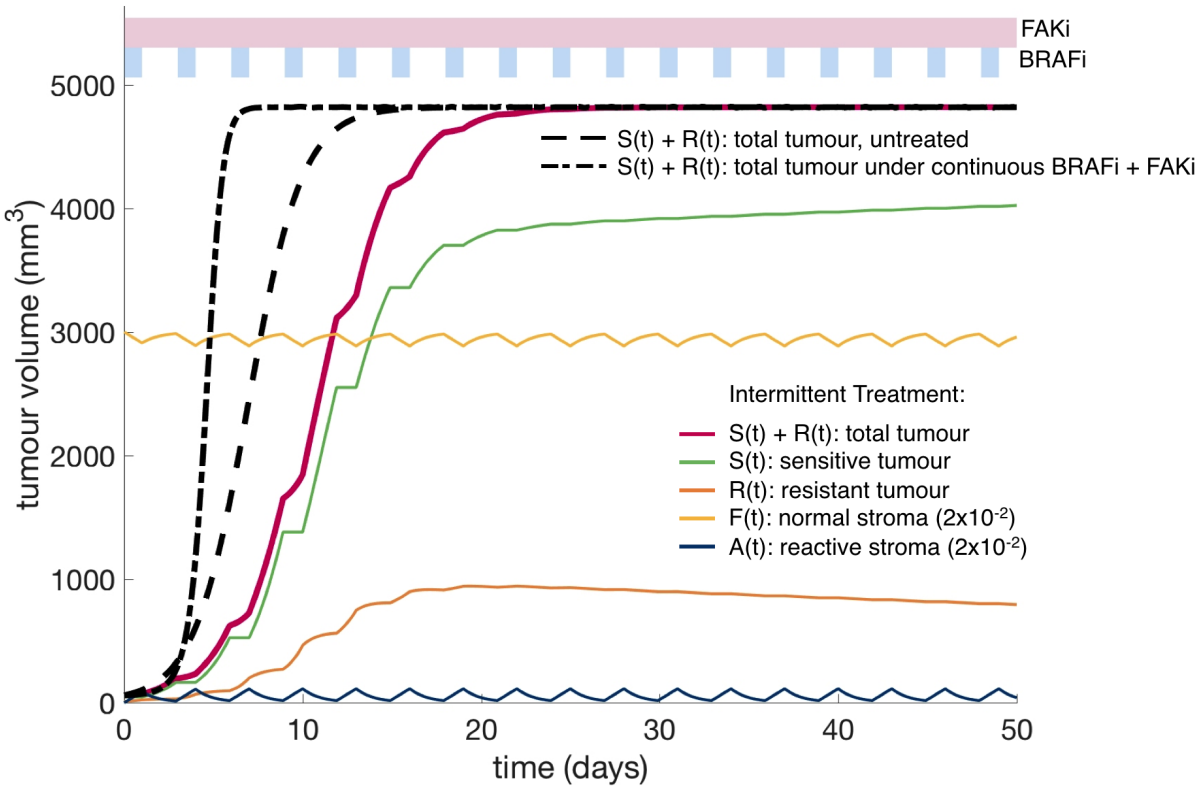


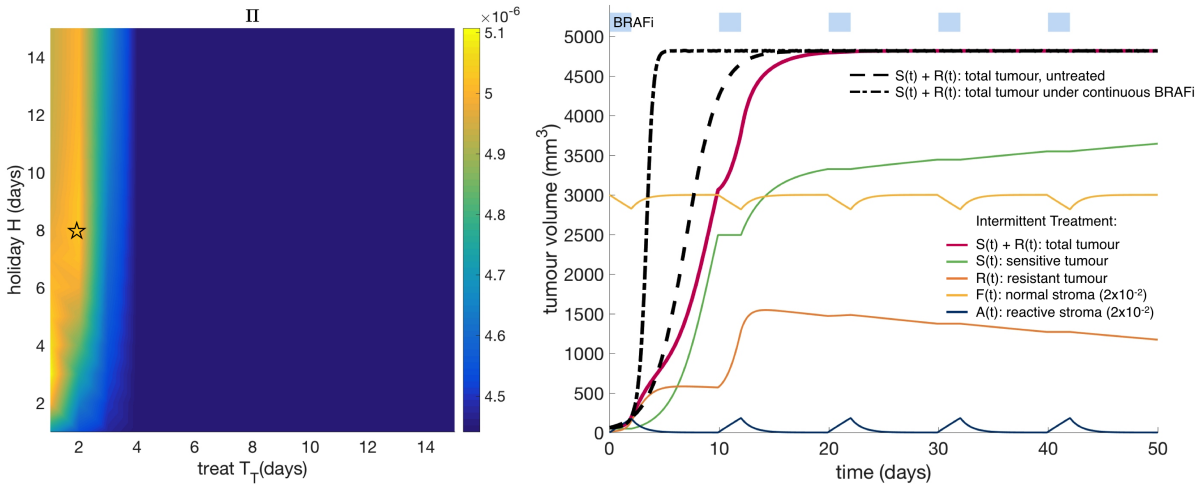
Figure 5.12: *Example of combination therapy schedule (BRAFi+FAKi) to exploit tumour-stroma interactions. The model is parameterised as reported in Figure 5.11. Blue and pink bands above the graph indicate the BRAFi and FAKi administration windows. The BRAFi is intermittently administered for 1 day with 2 days holidays. The FAKi is continuously administered. This treatment schedule delays the disease progression by approximately ten days (compare red and dashed black lines) while using a third of the BRAFi dose.*

To this end, we consider the following version of the model:

$$\begin{cases} \dfrac{dS}{dt} = (\rho_S S(1-g(t)) - \delta S c(t))\left(1 - \dfrac{S+R}{K}\right) + \xi R h(t) \\ \dfrac{dR}{dt} = (\rho_R R g(t) - \delta R c(t) + \eta A R g(t) - \alpha A R f(t))\left(1 - \dfrac{S+R}{K}\right) - \xi R h(t) \\ \dfrac{dF}{dt} = -\theta F g(t) + \phi A h(t) \\ \dfrac{dA}{dt} = \theta F g(t) - \phi A h(t) \end{cases} \tag{5.7}$$

$$\text{with} \quad \begin{cases} S(0) = S_0 \\ R(0) = R_0 \\ F(0) = F_0 \\ A(0) = 0 \end{cases}$$

where g, c, and h are the binary functions defined in Eqs. (4.2).



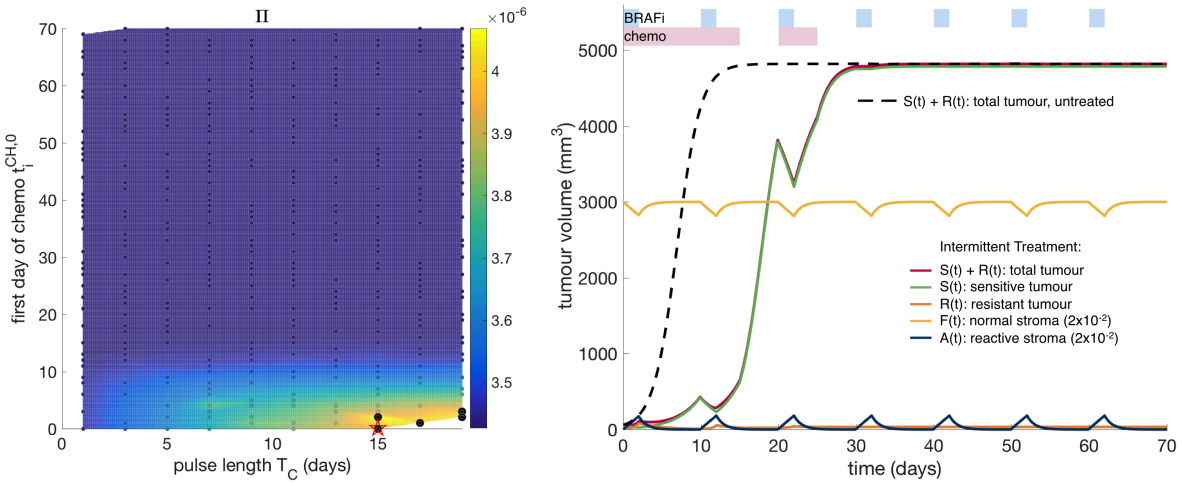
(a) (b)

Figure 5.13: *(a) Exploration of treatment/holiday space for intermittent BRAFi used as single agent to maximise control of tumour burden. Model parameterised on mouse IX of cell line 5555.* $\rho_S = 0.66325$ *1/day,* $\rho_R = 0.49543$ *1/day,* $K = 4818.62$ mm^3, $\tilde{\eta} = 26.876$ *1/day.* $\theta = 0.03$ *1/day,* $\xi = 0.01$ *1/day,* $\phi = 1$ *1/day,* $S_0 = 48$ mm^3, $R_0 = 12$ mm^3, $F_0 = 60$ mm^3, $A_0 = 0$ mm^3. *(b) Tumour burden with the best intermittent BRAFi schedule (corresponding to the star in the* (H, T_T) *space). Blue bands above the graph indicate the BRAFi administration windows. The BRAFi is intermittently administered for 2 day with 8 days holidays.*

We aim at exploring the space of possible treatment schedules for the combination of intermittent BRAFi and chemotherapy. In this model the application of chemotherapy corresponds to a reduction of the growth rates of both cancer cell populations. Therefore we first aim at finding the best intermittent schedule for the BRAFi administered as single agent. Using this optimal BRAFi intermittent schedule we then vary the chemotherapy schedule to find effective combination schedules. In doing so, we have to account for toxicity of the chemotherapeutic agent. Because our model does not explicitly account for drug dose, we simply impose the limitations of toxicity in the form of maximum tolerated treatment days M.

For the exploration of the BRAFi holiday-treatment space, we consider pulsed drug application in time windows $\left[t_i^{TT,k}, t_f^{TT,k}\right]$, as previously defined, and explore the (H, T_T) space. Figure 5.13(a) shows the treatment outcome in the holiday vs treatment (H, T_T) space, where the outcome of each treatment strategy over the time frame of $[0, 70]$ days is quantified with Π, defined in Eq. (5.6). The maximum Π corresponds to a schedule calling for 2 days BRAFi administration, followed by 8 days of holiday. The breakdown of the temporal dynamics for this schedule is shown in Figure 5.13(b).

Finally, we utilise the best BRAFi treatment schedule and vary chemotherapy application times to find effective combination schedule. For simplicity and practicality, we restrict our analysis to the case of dose fractionation in pulses of equal length T_C, and



(a) (b)

Figure 5.14: *(a) Exploring fractionation of chemotherapy maximum tolerated dose in combination with best intermittent BRAFi schedule (Figure 5.13). The plot shows the interpolated surface. Each circle corresponds to a randomly generated chemotherapy schedule. Black circles indicate top five best outcomes.* $\rho_S = 0.66325$ *1/day,* $\rho_R = 0.49543$ *1/day,* $\delta = 0.3046$ *1/day,* $K = 4818.62\ mm^3$, $\tilde{\eta} = 26.876$ *1/day.* $\theta = 0.03$ *1/day,* $\xi = 0.01$ *1/day,* $\phi = 1$ *1/day,* $S_0 = 48\ mm^3$, $R_0 = 12\ mm^3$, $F_0 = 60\ mm^3$, $A_0 = 0\ mm^3$. *(b) Tumour burden with the best intermittent BRAFi schedule and chemotherapy fractionation corresponding to the star in the* $(T_C, t_i^{CH,0})$ *space. Blue and pink bands above the graph indicate the BRAFi and chemo administration windows respectively. The BRAFi is intermittently administered for 2 days with 8 days holidays. The chemotherapy is administered for 15 days at day 0 and the remaining available dose at day 20.*

randomly choose the times of application $t_i^{CH,k}$ for $0 \leq k \leq M/T_C$. We generate J random chemotherapy schedules and quantify the outcome of combination treatment with Π over the time window $[0, 70]$ days. Since chemotherapy is not BRAF mutation-specific, we can use the value for δ estimated for the BRAF-wildtype dataset in Chapter 4. In Figure 5.14(a) we plot Π with respect to T_C, two informative quantities allowing us to extract general guidelines for an effective chemotherapy fractionation within a combination therapy plan. Specifically, we can identify an area of best outcome for medium-long pulses, with an early first chemotherapy application. This treatment induces only minimal stromal activation but delays progression by approximately 20 days. This prediction is consistent with the experimental observation that early application of chemotherapy is more effective (Section 4.2).

Comparing with Figure 5.12 we can conclude that for a tumour calibrated on this specific mouse, use of chemotherapy does not offer a better tumour burden control, and does not justify the additional toxicity that the patient would have to sustain.

5.5 Discussion and Conclusion

Molecularly targeted therapies for cancers with known driver mutations are extremely effective for six to eight months (McArthur et al., 2014) and are accompanied by lower toxicity when compared to cytotoxic chemotherapeutic agents (Chapman et al., 2011). However, with continuous and prolonged treatment, emergence of drug resistance seems to be inevitable. Upon removal of the targeted drug, due to relapse, a typical disease flare is observed (Chaft et al., 2011), suggesting that the treatment has somehow selected for a more aggressive clonal population in the tumour. However, subsequent treatments with the same inhibitor often leads to an additional response (Lee et al., 2013 and Mackiewicz-Wysocka et al., 2014), suggesting that selection of resistant clones alone cannot explain this disease etiology. The environment is now considered an important source of non-intrinsic drug resistance mechanisms (Mueller and Fusenig, 2004), collectively referred to as Environment Mediated Drug Resistance (EMDR). Since the changes accompanying EMDR are considered transient and therefore reversible, the possibility of regulating EMDR dynamics with smarter treatment scheduling is promising. However, a necessary first step towards the design of such treatment strategies is a more quantitative understanding of the interactions and dynamics occurring between the tumour and the stroma.

In vitro model systems can accurately quantify temporal tumour growth and treatment response in controlled environments, whereas *in vivo* models more readily capture the native environment that is directly relevant to patients. However, both of these are models of human disease and only capture specific aspects of reality over very specific spatial and temporal scales. The ODE model we develop here bridges between these experimental scales, in order to integrate relevant information from each of them.

Starting from analysis of BRAF mutated melanoma cell lines, we quantified the baseline dynamics of cancer cells in a uniform nutrient rich environment. By comparing the fitness of cells untreated or treated with a BRAF inhibitor, we were able to quantify the fitness cost of growth under drug application. Our model facilitates this analysis by classifying the cancer into two separate populations, growing with or without drug (R and S). Then using Approximate Bayesian Computation we calculate plausible regions of parameter values. This information can be particularly useful when assessing the error in fitting.

Subsequent analysis of data from mice xenografts implanted with the same cell lines, allowed us to identify the relative contribution of the environment to drug resistance. This analysis revealed heterogeneity in both the local tissue carrying capacity and in the stromal promotion of tumour growth. This heterogeneity offers one explanation of the

observed spectrum of responses, hence representing a necessary characteristic to account for when designing treatment. In the context of metastatic disease, with tumours seeded across a variety of tissues, heterogeneity in tissue composition could be an important discriminating factor in the success of a systemic treatment.

Within the current experimental and modelling framework, assessing the strength of stromal protection is non-trivial. This quantity is dependent on the abundance of the interacting stroma (we could only estimate the overall promotion rate $\tilde{\eta} = \eta F_0$) as well as the speed of drug-induced stromal activation θ. We found high sensitivity of parameter estimates to θ. At the same time, with the available data, we can explain the variability of responses across mice by variation of carrying capacity and/or stromal promotion (Figure 5.8). Further investigation of the heterogeneity that this study revealed, would require additional experimental quantification of these stromal-related processes.

Analysis of our ODE model revealed that the degree of stromal protection η, and cancer fitness ρ_R under drug treatment, are key in discriminating between responses of the tumour-stroma system to the combined action of inhibitors targeting tumour and stromal processes (BRAFi and FAKi, respectively). We found that for slower growing tumours it is possible to keep growth in check provided treatment with the BRAFi is applied for a sufficient period of time. Conversely, for fast growing tumours or elevated stromal protection, the tumour burden inevitably grows over time, despite the administration of the inhibitors. For these tumours, however, exploiting the transient nature of the EMDR-associated mechanisms makes it possible to delay the progression. Specifically, scheduling treatment holidays for the mouse- (patient-) specific calibrated model allows renormalization of the system that translates to better control of the disease burden. We used our parameterised ODE model to explore the space of intermittent treatment strategies, with the hope of improving response in cancers falling into the treatment refractory category. Neglecting toxicity of targeted drugs, we searched the space of holiday versus treatment length for intermittent BRAFi application, combined with continuous FAKi. We found that most effective tumour control is achieved with short BRAFi treatment pulses and longer holidays, requiring significantly less inhibitor, when compared to the continuous treatment.

It is worth noting that in optimising treatment schedule for these inhibitors, we are only modulating the dynamics by reducing the emergence of EMDR. This allows us to delay recurrence by approximately twenty days. We then asked whether by combining an optimal intermittent BRAFi treatment with a cytotoxic treatment, such as chemotherapy, which provides additional reduction of the tumour burden, could further delay recurrence. However, in order to consider additional treatments for combination therapies it is necessary to account for toxicity of the single agents, as well as toxicity resulting from

their combination. The latter would impose an additional constraint in the optimisation problem. We imposed a maximum tolerated dose in order to account for chemotoxicity. However, we allowed any length of continuous targeted drug administration, assuming that toxicity of inhibitors, at the dose used in experiments, is minimal. The model, calibrated on a specific mouse, did not show sufficient benefit in terms of disease progression delay, to justify using toxic chemotherapy compared to FAKi.

The heterogeneity our study revealed from the *in vivo* experiments indicates the importance of accounting for mouse- (human-) specific parameters to accurately capture response dynamics. This heterogeneity is often ignored in pre-clinical models, as they aim at establishing general relationships of causality between biological mechanisms. However, as our study suggests, heterogeneity can be key in explaining the variation observed across replicates of an experimental model. Furthermore, models that exploit the transient nature of EMDR must rely on individually calibrated dynamics in order to propose effective and improved treatment strategies.

This study can be expanded to consider more comprehensive and flexible scheduling options. Within the practical constraints of frequency in monitoring the patient's tumour burden and tissue characteristics, our model can be used to inform the design of adaptive therapy (see, for example, Enriquez-Navas et al., 2016). Adaptive therapy is a novel paradigm that takes into account the impact of treatment on the evolution of the tumour and its microenvironment. By replacing a fixed treatment regime with an adaptive one, it is possible to steer the cancer into a more controlled state indefinitely (Gatenby et al., 2009, Orlando et al., 2012). For example the disease can be treated sequentially with two drugs, where the first drives tumour evolution to make it susceptible to the second drug. This strategy is called the *evolutionary double bind* (Basanta et al., 2012). An ongoing clinical trial, taking place at the Moffitt Cancer Center (NCT02415621), is testing the adaptive therapy approach in patients with metastatic prostate cancer treated with intermittent Abiraterone. For an extensive review on evolutionarily-driven mathematical and computational approaches to adaptive therapy, see Basanta and Anderson, 2013 and 2016.

In the next chapter we will extend the minimal description of the biological system. Specifically, we will address the spatial characterisation of the local interactions and the system heterogeneity by including spatial components in the model.

Chapter 6

The Hybrid Discrete Continuum Model

In the previous chapters we presented an ODE description of the emergence of drug resistance in the context of tumour-stromal interactions. This approach described the dynamics at the cell population level, and was ideal for modelling experimental data from *in vitro* and *in vivo* models. This population dynamics approach includes the implicit assumption of a well mixed system and does not account for local interactions and heterogeneity.

Local interactions between cancer and stromal cells are key drivers in the dynamics of resistance, as strikingly captured in spheroid co-culture experiments (Figure 2.6). In the experiment presented in Figure 6.1, the ERK activity (a kinase downstream of the MAPK pathway, indicative of cell viability, see Figure 2.4), is monitored with single cell resolution over the course of the treatment with a BRAF inhibitor. Initially the inhibitor effectively decreases ERK signalling. However, within 12 hours a rebound of the ERK activity can be observed in those cancer cells at the interface with the stroma.

Metastatic melanoma is characterised by a high degree of heterogeneity and distinct morphological and invasive behaviours depending on the site of the metastasis. Inter-tumour heterogeneity proved to be key in explaining variation in response to therapy across experimental replicates when treating melanoma cell lines with a BRAF inhibitor (see Section 5.3). Intra-tumour spatial heterogeneity can be observed in fluorescence images of *in vitro* spheroid assays showing the effects of treatment on cell viability. An example for the M368 cell line is illustrated in Figure 6.2, along with quantification of cell death for the indicated treatment: chemotherapy (mix of carboplatin and paclitaxel), an AKT inhibitor (MK2206), and their combination. We can observe that the system appears to be composed of an inner core of cells which are sensitive to the treatment, but harder to reach with the drug, due to their position, and an external shell of cells that proliferate due to the availability of resources such as space and nutrient. In the clinical

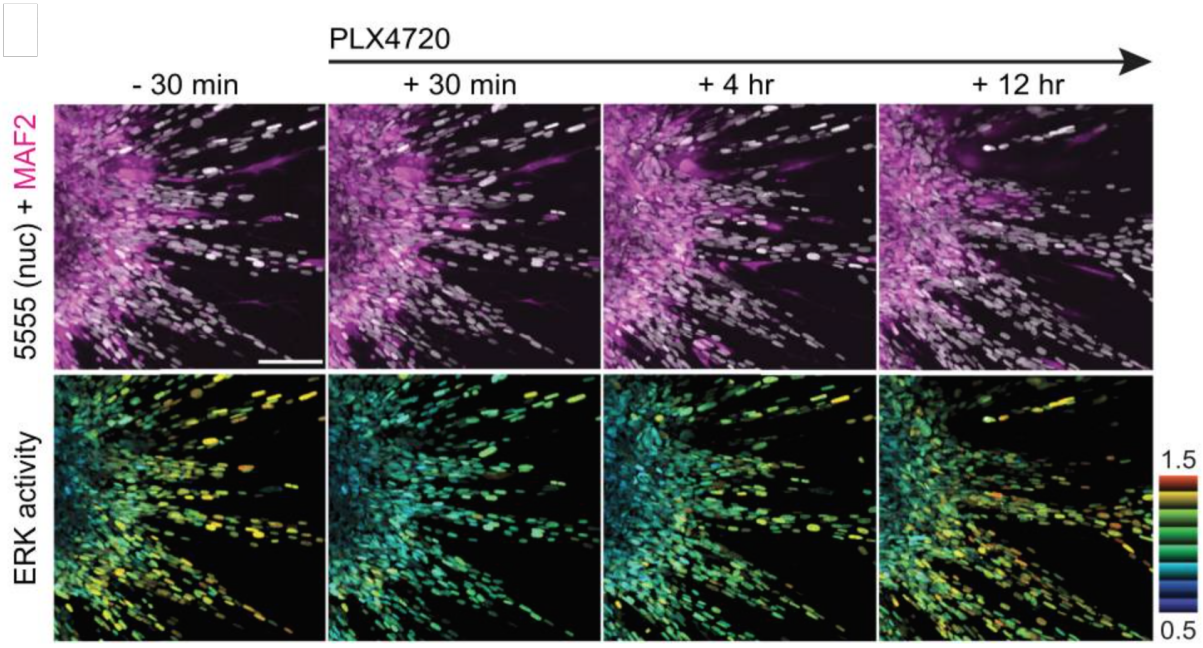


Figure 6.1: *5555 (BRAF-mutated melanoma) cell line and Melanoma Associated Firbroblast (MAF) spheroids co-cultured in collagen gel, treated with 1 μM BRAFi PLX4720 at time 0. Upper panel: 5555 nuclei in gray, MAFs in magenta. Lower panel: ERK activity read with single cell resolution via a FRET sensor (see intensity colour map on the right). Figure from Hirata et al., 2015, reproduced under CC BY-NC-ND 4.0.*

scenario of an advanced stage melanoma patient, whose entire body is infiltrated with metastases such as the case illustrated in Figure 2.1, we also see how spatial variation, in terms of organ location and growth characteristics of the visible disease, underlies the heterogeneity of the cancer throughout the body.

When examining these experimental models, the necessity to account for spatial variation and local interactions becomes evident. Despite the ODE framework allowing us to account for constrained growth (e.g. logistic growth, see Chapter 5), it cannot account for spatially-related features of the system. We propose to build a minimal spatial model that will isolate the effects of the targeted therapy administered as a single agent. This new modelling approach will consider spatial heterogeneity introduced by elements such as the vasculature, a drug gradient, and local interactions between stromal and cancer cells. In order to explore the dynamics at the single cell scale, we will adopt a Hybrid Discrete Continuum modelling approach, that will be referred to as HDC. The key feature of this modelling framework is that it allows for both discrete and continuous variables to be captured spatially and temporally. This approach is therefore ideally suited for modelling tumour-microenvironment interactions, easily integrating discrete cell dynamics (e.g. proliferation, migration, interaction with other cells), and continuum microenvironmental fields (extracellular matrix, nutrients, diffusible drugs, etc.).

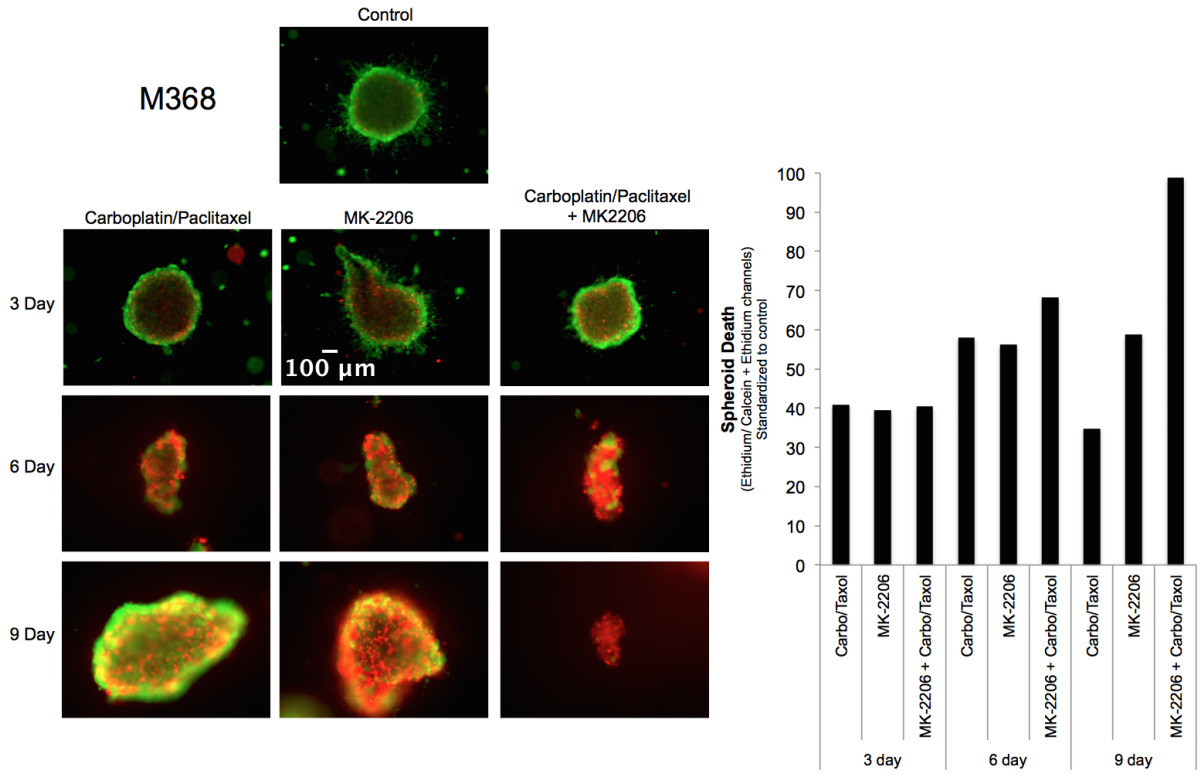


Figure 6.2: *Spheroid assays with the M368 cell line (BRAF wild-type, RAS mutated melanoma cells). The preformed spheroid is treated either with a chemotherapeutic mix of carboplatin and paclitaxel, or MK220 (an AKT inhibitor), or their combination. Fluorescence images allow identification of viable cells (green) and dying cells (red). The quantification of cell death (histogram on the right) shows fold increase of death caused by the drugs compared to the control. Image courtesy of the Smalley laboratory, Moffitt Cancer Center, Tampa.*

This technique was first used by Anderson et al. (1997) to model nematode movement through heterogeneous microenvironments, but is better known for its application to tumour induced angiogenesis (Anderson and Chaplain, 1998). Sun et al. (2005) extended the angiogenesis work by considering the coupled interactions between endothelial cells, growth factors and fibronectin, in their deterministic model of growth factor-induced angiogenesis. Patel et al. (2001) used it to investigate the role of pre-existing vascularity and lactic acid (a byproduct of tumour cell metabolism) in early tumour growth, and found the optimal range of microvessel densities and acid production for effective growth and invasion. Alarcón et al. (2003) focused on the role of blood flow in shaping the heterogeneous environment in which the tumour grows. They introduced a detailed description of the vascular dynamics, including rheology and red blood cell circulation, and investigated the behaviour of normal and cancer cells interacting with the vasculature. An extension of this work included vascular remodelling, driven largely by endothelial tip cells that respond chemotactically to a VEGF field (Owen et al., 2009). Perfahl et al. (2011) extended this multiscale model of vascular tumour growth to 3D, and directly

incorporated experimental images of vasculature.

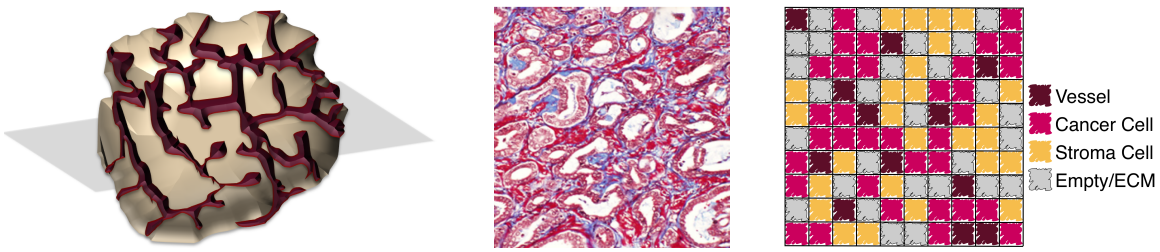
McDougall et al. (2006) considered the effects of blood flow during angiogenesis, and investigated the effects of chemotherapy treatment on the vasculature. Similarly Macklin et al. (2009) proposed a model that couples cancer growth and invasion with tumour-induced angiogenesis. Their model includes a detailed description of the flow and mechanical/hydrostatic pressure. They show that ECM degradation can have a significant effect on both tumour growth and vascular development, and that nutrient penetration is impeded by internal tumour pressure.

This hybrid modelling approach has been used beyond applications to angiogenesis. In fact, Anderson further used it to model tumour evolution and invasion through different ECM microenvironments (Anderson, 2005 and Anderson et al., 2006). Gerlee et al. (2008) extended this to explicitly investigate the clonal evolution of the glycolytic phenotype in cancer under different environmental conditions i.e. tissue oxygenation and matrix density. Piotrowska et al. (2009) built on these results, investigating the emergence of necrosis in tumour spheroid cores. They suggest the need for additional processes to explain the onset of necrosis before nutrients drop below viable levels. Smallbone et al. (2006) considered somatic evolution in early tumour growth in the context of tumour metabolism. Specifically, the successful growth dominated by glycolitic cancer cells leads to excess acidification that causes cell death and further invasion and eventually promotes the emergence of an acid-resistant tumour phenotype. More recently, Robertson-Tessi et al. (2015) modelled metabolic heterogeneity to understand the evolutionary dynamics driving treatment response and leading to resistance. Wang et al. (2008) developed a model of non-small-cell lung cancer growth, where the cells' intrinsic EGFR-ERK signal transduction pathway is dynamically modulated by the microenvironment. Basanta et al. (2009) presented a model of tumour-stroma interactions in prostate cancer that investigated the promoting/inhibiting effects of the growth factor TGF-β.

All of the above models share a common feature: they use the HDC approach to study the complex interplay between discrete cellular components and continuum microenvironmental fields. Here we will apply the HDC paradigm to study the interactions between discrete tumour and stromal cells through continuous microenvironmental factors that either promote or inhibit growth, in order to investigate the mechanisms of EMDR.

6.1 The Modelling Setup and the HDC Coupling

For simplicity, and in order to focus on the spatial heterogeneity without overcomplicating the model, we consider a 2D slice through a vascularised normal epithelial tissue. The blood vessels are assumed to be approximately perpendicular to the slice of tissue



(a) (b) (c)

Figure 6.3: *Capturing spatial heterogeneity. From a 3D vascularised tissue (a) a 2D tissue slice approximately perpendicular to the blood vessels is obtained (b) which can be digitised and simplified on to a square lattice where each site is occupied by either a tumour or stromal cell, or a blood vessel or is empty (i.e. occupied only by ECM). (b) from Figure 7.1.*

considered (Figure 6.3(a)) and therefore appear as a point distribution of blood vessels that can be modelled as nutrient and drug point sources within the 2D domain (Figure 6.3(b)).

The discrete portion of the HDC model consists of a 2D lattice-based cellular automaton. We consider a regular square grid that tessellates our entire tissue domain, where each lattice point can be occupied by at most one cell or blood vessel (Figure 6.3(c)). It is important to recognise that the cross-section of a vessel is bigger than the area occupied by a single cancer cell. However, in our model vessels and cells both occupy a single lattice site. This is a simplistic representation of the real geometry of the system, however it allows us to easily introduce spatial gradients to investigate heterogeneity.

In the design of this model we have tried, whenever possible, to translate model variables and processes from the previous ODE model (5.1) to the HDC framework in order to obtain an extension of the former that explicitly incorporates spatial interactions. Therefore we will consider three cell types: cancer cell (S), normal stromal cell (F), reactive stromal cell (A). The drug-tolerant or drug-sensitive phenotype will be defined for every individual cancer cell, and allowed to vary over time, depending on the context, as explained in the following.

The continuum part of the HDC consists of phenomenological PDEs, describing the non-cellular components (i.e. growth factors and drug concentration) and their relevant dynamics such as diffusion, production and degradation. Since the experimental observations available do not include a description of the processes of matrix remodelling in the context of drug resistance, as a first approximation we do not explicitly model the ECM. However, a future natural extension of the model could include the ECM density among the continuum variables of the model.

The key to coupling continuum and discrete elements is ensuring that the lattice, where the cells are positioned, matches the grid for the numerical solution of the PDEs

that we will use to define the continuum variables. At each time step the spatio-temporal evolution of the continuum model is updated according to the distribution of the discrete cells on the lattice. The new continuum distribution informs the individual cell-based rules, driving proliferation, death and phenotypic changes on the lattice. The new configuration of cells on the lattice will in turn modulate the continuum variables and so on.

6.2 The Proliferation Signal

The effects of kinase inhibitors used to target a range of different cancers, with a given mutation (e.g. Erlotinib for EGFR-mutated non-small-cell lung cancer, Vemurafenib for BRAF-mutated melanoma and Lapatinib for amplified-HER2 breast cancer), vary significantly, from effective cell kill to growth inhibition or no effect at all (Sharma et al. 2010, Menzies et al. 2014). The reason for this spectrum of response is not completely clear, although it can be attributed to the compensatory mechanisms that some cancer cells put in place (see Section 2.1). Some examples are: expression of competitor molecules binding to the drug, alternative pathways that circumvent the inhibition of the oncoprotein being targeted, or upregulation of compensatory pro-proliferative or anti-apoptotic signalling. Some of these mechanisms can be put in place with the help of reactive stroma, recruited by the tumour itself, and eventually facilitating EMDR (Hirata et al., 2015).

Given the multifaceted and complex nature of these mechanisms, we will model the effect of collective pro-growth and pro-death signals on cancer, with a simple first principles approach, in terms of an integrated signal.

Normal cells integrate pro-proliferative and pro-apoptotic signals from their environment that allow for progression through the cell cycle and controlled proliferation (Figure 6.4(a)). Normal tissue is composed of a collection of such cells, characterised by tightly regulated proliferation, resulting in a homeostatic balance. However, in "oncogene addicted" cancer cells (Section 2.1) this balance is shifted such that the cell is constantly in proliferative mode (Figure 6.4(b)). Targeted drugs act to counter this imbalance and reinstate the equilibrium (Figure 6.4(c)). Therefore, for simplicity, we shall aggregate targeted resistance mechanisms as forces that promote proliferation and suppress apoptotic signalling (Figure 6.4(d)). It is important to note that the modulation of this equilibrium not only depends on a combination of autocrine and paracrine mechanisms, but also upon the cell's capacity to be receptive to such signalling. Namely, the same environmental stimulus can be read and translated differently by two cells with different surface receptors or mutations.

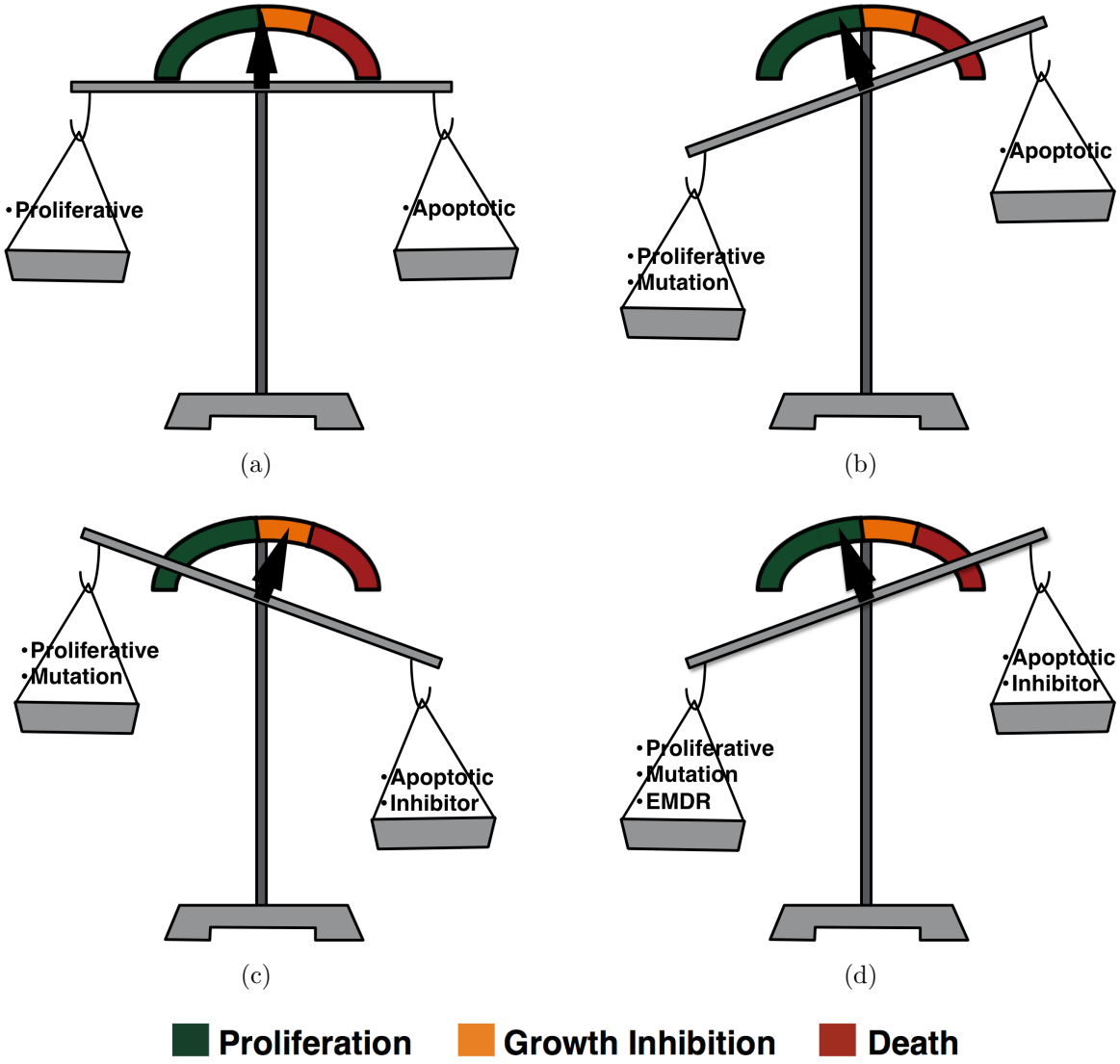


Figure 6.4: *The proliferation signal. (a) In normal homeostatic tissue proliferation is controlled by a tight balance between proliferative and apoptotic signalling. (b) Mutations in cancer provide continuous proliferative cues, disrupting the equilibrium. (c) The targeted drug counterbalances to control or inhibit proliferation. (d) Resistance mechanisms such as EMDR counteract the action of targeted drugs.*

To capture this behaviour we introduce the *proliferation signal* function, $g = g(\mathbf{x}, t)$, where $\mathbf{x}$ is the position vector in the domain Ω that will be defined in the following. This function models the net effect of pro-proliferative minus pro-apoptotic signalling. This variable is modulated by signals from the environment and the cancer cells themselves, and defines a cell's viability (Figure 6.5). Namely a cell can either be:

- kept in a proliferative state, given sufficient proliferation signal, i.e. $g \geq h_p$;
- driven to cell-death, given insufficient proliferation signal, i.e. $g < h_d$;



Figure 6.5: *The cell viability is determined by the reading of the proliferation signal concentration in the environment, according to two cell-specific thresholds h_p and h_d. This model recapitulates the variability of response in a cell population to the non-cell autonomous modulation of the signalling cues.*

- forced in to a growth-arrested state for intermediate level of proliferation signal, i.e. $h_d \leq g < h_p$.

The two thresholds, h_p and h_d, are two model parameters that allow a simple yet effective representation of cell responsiveness to environmental modulation of pro-growth and pro-death signals. We can then easily capture normal and mutated cell states by changing these parameters. For example we can model a mutated cell, unresponsive to the normal regulatory signalling, by setting its thresholds to zero, so that regardless of the external stimulus, this cell will always be in proliferative mode. However, in this chapter we will focus on cells which respond equally to the same environmental stimulus, i.e. we keep h_p and h_d fixed for all cancer cells.

6.3 The Continuum Model of Environmental Signals

Many targeted drugs are also known as inhibitors, because they are aimed at blocking tyrosine kinases involved in a specific downstream proliferative or survival pathway. Here, we define the inhibitor drug concentration as $d = d(\mathbf{x}, t)$ and assume it diffuses into the tissue from all vessel sites, and, most importantly, modulates the local proliferation signal. Specifically, the inhibitor will represent one of the anti-proliferative forces shifting the cell toward a growth-inhibited and eventually apoptotic state.

The phenomenological description of the proliferation signal and inhibitor can be formalised in the following system of coupled PDEs,

$$\begin{cases} \dfrac{\partial d}{\partial t} = D_d \nabla^2 d - \mu v(\mathbf{x}, t) d, \\ \dfrac{\partial g}{\partial t} = D_g \nabla^2 g + \beta s(\mathbf{x}, t) + \gamma a(\mathbf{x}, t) - \delta d, \end{cases} \tag{6.1}$$

where D_d, D_g are the diffusion coefficients and $\mu, \beta, \gamma, \delta$ are positive constants. $v(\mathbf{x}, t)$, $s(\mathbf{x}, t)$, and $a(\mathbf{x}, t)$ are the binary functions determining, respectively, the presence of a

blood vessel, tumour cell or reactive stromal cell at position $\mathbf{x}$ and time t. D_d and D_g are the inhibitor and proliferation signal diffusion coefficients, respectively. Growth factors and other signalling molecules that make up the proliferation signal can be transported through the tissue, but generally they are stored between the ECM fibres and utilised as needed by the cells (Flaumenhaft and Rifkin, 1991). Therefore in our model we allow some diffusion of the proliferation signal and targeted inhibitor, yet keep the diffusion coefficients two orders of magnitude below the typical diffusion coefficients of nutrient and chemotherapeutic drugs (Robertson-Tessi et al., 2015). μ is the rate at which the drug is washed out at a vessel site. Drug delivery is implemented as a boundary condition at point sources (corresponding to the vessel sites) during the time of treatment i.e. $d(\mathbf{x}, t) = d_0 v(\mathbf{x}, t)$, for $t \in [t_i^{TT}, t_f^{TT}]$. β and γ are rates of autocrine and stromal-derived paracrine proliferation signal production, respectively. δ is the rate at which the inhibitor reduces the proliferation signal. All parameter values, and sources, are reported in Table 6.1. The initial conditions are varied, so will be described for each application below. We impose no flux boundary conditions:

$$\frac{\partial d}{\partial \mathbf{n}} = 0, \quad \frac{\partial g}{\partial \mathbf{n}} = 0 \quad \text{on } \partial\Omega, \ \forall t, \tag{6.2}$$

where $\mathbf{n}$ is the unit outward-pointing vector normal to the domain boundary $\partial\Omega$, and $\Omega = [0, L] \times [0, L]$ represents a 2D slice of tissue.

Note that both variables are positive and normalised to their maximum concentration:

$$\tilde{d} = d_0 d, \quad \tilde{g} = g_0 g, \tag{6.3}$$

where $\tilde{d}$ and $\tilde{g}$ are the corresponding dimensional quantities. d_0 is the concentration at delivery point, assumed constant (consistent with clinical trial delivery, Mok et al., 2009), and g_0 is the maximum concentration of proliferation signal in the system (we assume the build up of growth factors to be limited). Therefore both nondimensional variables will take values in the $[0, 1]$ range. In principle g can accumulate unbounded or go negative. In the implementation of the numerical solver (explained in details in the following section), we will introduce upper and lower bounds, so that g is restricted to the unit interval.

The interactions between cancer cells and the environmental factors are shown in Figure 6.6.

6.4 The Numerical Solution of the System of PDEs

We will implement a *central difference* approximation for both the first and the second order spatial derivatives, and a *forward Euler explicit* scheme for the discretisation of

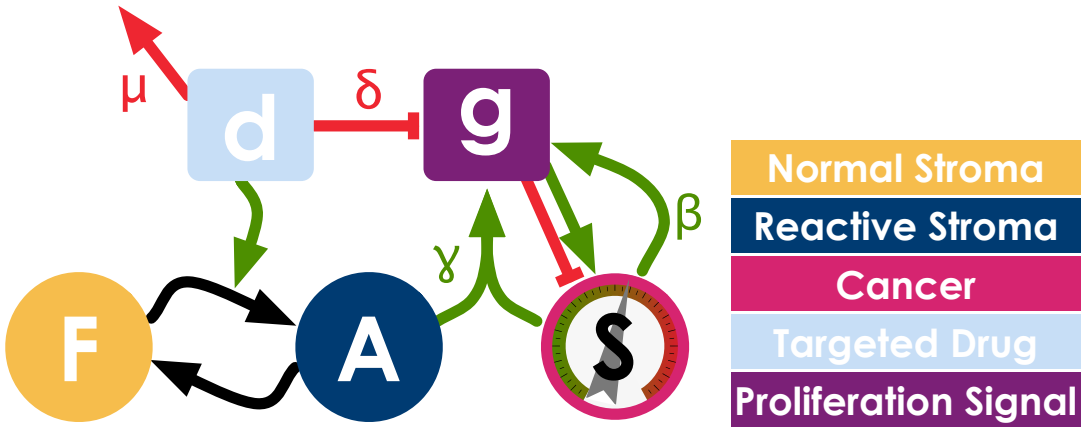


Figure 6.6: *Interactions hypothesised in the HDC model: positive interactions are represented by green arrows, negative ones by red flat ends. Black arrows represent phenotypic transitions. The dial represents the viability of cancer cells S, modulated by the proliferation signal g. Cancer cells have a baseline production of g. The targeted drug d depletes g and stimulates the transition of stroma from normal (F) to reactive (A). The latter produce additional signal g when in proximity to a cancer cell. The net local intensity of g determines the cell's viability (represented by the double promotion/inhibition link of g to S).*

the time derivative. Space and time steps are Δx and Δt, respectively, and a minimal condition to ensure numerical stability (Crank, 1979) is:

$$D\frac{\Delta t}{(\Delta x)^2} < \frac{1}{4}, \tag{6.4}$$

where D is the maximum diffusion coefficient in Eqs. (6.1). This numerical approximation results in the following set of equations:

$$\begin{cases} d_{i,j}^{q+1} = d_{i,j}^{q} + \Delta t \left[D_d \dfrac{d_{i,j-1}^{q} + d_{i-1,j}^{q} - 4d_{i,j}^{q} + d_{i+1,j}^{q} + d_{i,j+1}^{q}}{(\Delta x)^2} - \mu v_{i,j}^{q} d_{i,j}^{q} \right], \\ g_{i,j}^{q+1} = g_{i,j}^{q} + \Delta t \left[D_g \dfrac{g_{i,j-1}^{q} + g_{i-1,j}^{q} - 4g_{i,j}^{q} + g_{i+1,j}^{q} + g_{i,j+1}^{q}}{(\Delta x)^2} + \beta s_{i,j}^{q} + \gamma a_{i,j}^{q} - \delta d_{i,j}^{q} \right]. \end{cases} \tag{6.5}$$

Subscripts i, j indicate the position on the mesh (see Figure 6.7) where the numerical solution is being evaluated. Superscript q refers to the time step at which the numerical solution is being computed. Specifically:

$$d_{i,j}^{q} \approx d(\mathbf{x}_{i,j}, t^q), \quad g_{i,j}^{q} \approx g(\mathbf{x}_{i,j}, t^q), \tag{6.6}$$

where $\mathbf{x}_{i,j} = (x_i, y_j)$, $x_i = i\Delta x$, $y_j = j\Delta x$, and $t^q = q\Delta t$, with $i = 0, \ldots, M$ $j = 0, \ldots, M$ $q = 0, \ldots, N$. N is the total number of iterations in a simulation. In order to bound g to the unit interval, we impose $g_{i,j}^{q}$ to be one (zero) if its value is above one (below zero), respectively. The numerical scheme described in Eqs. (6.5) is valid

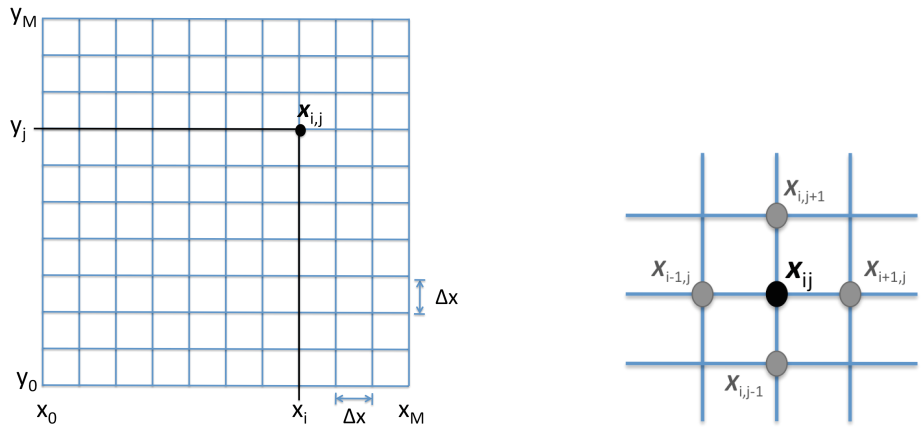


Figure 6.7: *Space discretisation. The numerical solution of Eqs.* (6.1) *will be computed at grid points* x_{ij}*. The same discretisation will be used as the lattice in the individual cell-based setup.*

for internal nodes only, as for boundary lattice points (i.e. i or j equal to 0 or M), some neighbouring positions are undefined. Therefore, we apply the boundary conditions defined in Eqs. (6.2), to obtain an approximation of the functions at such non-defined lattice points. For example, in order to compute the approximation of $d^q_{i+1,j}$ for $i = M$ and $0 \leq j \leq M$, we discretise the first of Eqs. (6.2) to obtain:

$$\frac{d^q_{i+1,j} - d^q_{i-1,j}}{2\Delta x} = 0, \tag{6.7}$$

which gives $d^q_{M+1,j} = d^q_{M-1,j}$, on the boundary.

The binary functions represent the presence/absence of a cell type in the corresponding position of the lattice. Specifically,

- $v_{ij} = 1$, if a vessel is located at lattice position (i, j). 0 otherwise.
- $s_{ij} = 1$, if a sensitive tumour cell is located at lattice position (i, j). 0 otherwise.
- $a_{ij} = s_{ij} \sum_{l,m} \alpha_{l,m}$, with (l, m) one of the eight neighbouring position of (i, j), and $\alpha_{l,m} = 1$ if a reactive stroma cell is located at lattice position (l, m). 0 otherwise.

Hence, $a(\mathbf{x}, t)$ models the contact of a tumour cell with one or more reactive stroma cells, whose presence will locally increase the proliferation signal, giving transient protection to the sensitive tumour cell. It is worth noting that in this model, any cancer cell, depending on its threshold values (h_p, h_d) and the environmental conditions, can be transiently resistant and escape drug-induced death.

6.5 The Cell-based Rules

The discrete portion of the HDC model consists of individual cell-based rules that define how cells interact with one another and their environment. This approach captures the

dynamic feedback between spatially and temporally evolving environmental conditions and cell behaviours (including response to and modulation of environmental conditions). Thus the dynamics at the entire tissue scale emerge from the collection of individual interactions between tumour and stromal cells and their environment.

The flowcharts in Figure 6.8 describe the decision process for each cell type, including rules that determine division, viability, death and the conversion between cell types. At each time step each cell goes through the decision process as defined by its flow chart. Every cell has an internal clock that determines the timing of division, defined by the cell's inter-mitotic time I_S. Progression of a cancer cell (S) through the cell cycle can be interrupted by unfavourable conditions such as a drop in the proliferation signal concentration below the viability threshold h_p, or even worse, below the death threshold h_d. It is worth noting that this signal, taken together with the internal clock, acts like a model of the cell cycle. More accurate and sophisticated models of progression through the cell cycle phases in relation to intrinsic and extrinsic factors are available in the literature (see, for example, Powathil et al., 2015).

One of the several ways in which cancer cells express their fitness advantage, *in vitro* and *in vivo*, is through a higher carrying capacity (Hanahan and Weinberg, 2011). We capture this advantage in the form of stronger contact inhibition for stromal cells (F and A) compared to tumour cells. More specifically, stromal cell division is allowed only when the number of occupied neighbouring sites is below n_{CI}. Furthermore, in order to recapitulate homeostatic tissue growth, we introduce turnover in the stromal population. Specifically, each stromal cell is assigned a probability p_T of death. In the absence of cancer, the model will recapitulate a dynamic equilibrium of a homeostatic stromal tissue maintaining a constant tissue density, regulated by the carrying capacity and contact inhibition constraint.

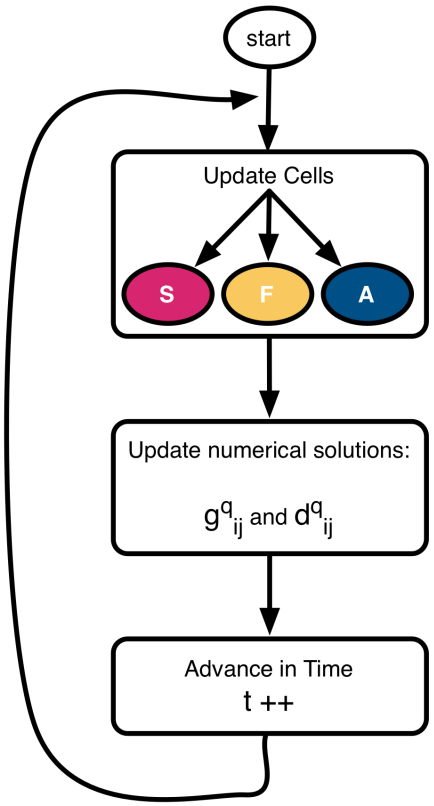
Finally, in order to model the key regulator of EMDR, the reactive stroma, we introduce rules that define a phenotypic switch from a normal stromal cell (F) to a reactive stromal cell (A). This happens under the recruiting action of the surrounding tumour and when treatment is applied. As described in Sections 2.3 and 2.4, cancer cells under drug treatment recruit stromal cells in their proximity. The resulting reactive stroma express a secretory phenotype (e.g. fibronectin deposition, see Figure 2.7), and enhanced paracrine signalling, involving mainly survival and growth promoting factors. Therefore, in our model a normal stromal cell will become reactive with probability p_{FA} when both the following constraints are satisfied:

i) it is in direct contact with at least one cancer cell,

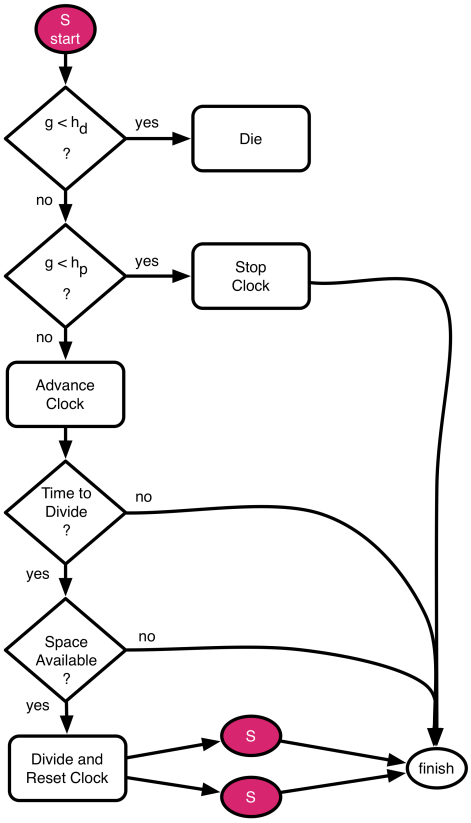
ii) the local concentration of drug is above a threshold h_r.

Parameter	Description	Value	Reference
Δx	lattice spacing	10 μm	average cell diameter [70]
Δt	time step	0.6 hours	determined by Eq. (6.4)
D_d	drug diffusion	1×10^{-5} cm^2/day	[88], [77]
D_g	proliferation signal diffusion	1×10^{-7} cm^2/day	model specific
μ	drug removal rate at vessel site	10 day$^-$1	model specific
β	autocrine proliferation signal production (by cancer cells)	0.65 day$^-$1	model specific
γ	paracrine proliferation signal production (by cancer cells near reactive stroma)	1.54 day$^-$1	model specific
δ	proliferation signal degradation by drug	0.79 day$^-$1	model specific
h_d	proliferation signal threshold for death	0.1	model specific
h_p	proliferation signal threshold for proliferation	0.8	model specific
I_S	cancer cell inter mitotic time	1 day	typical cell cycle length [23]
n_{CI}	min number of stomal neighbours triggering contact inhibition	6	model specific
p_T	stroma turnover probability (per day)	$0.001/\Delta t$	model specific
σ_{min}	minimum vessel spacing	0.008 cm	[94]
σ_{mean}	*in vivo* average vessel spacing	0.016 cm	[94]
h_r	drug threshold for reactivity	0.9	model specific
p_{FA}	probability of stromal activation and normalisation (per day)	$0.01/\Delta t$	model specific

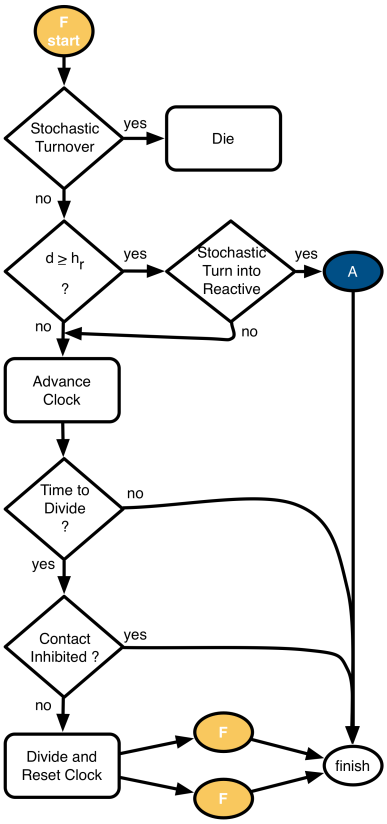
Table 6.1: *Parameter values for the HDC model.*



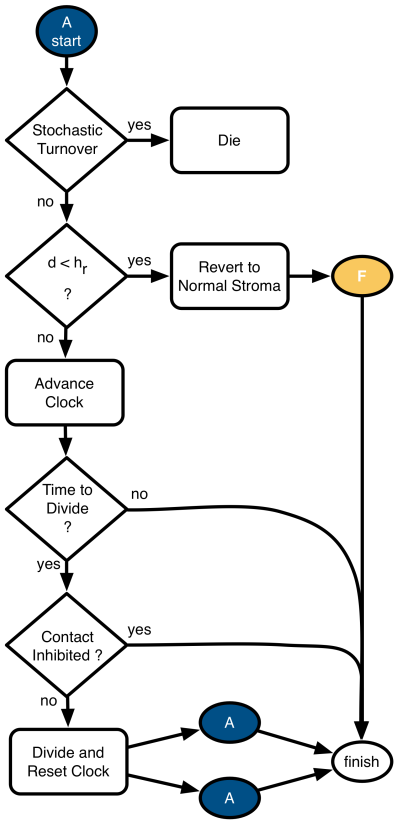
(a) HDC algorithm



(b) S = sensitive cancer cell



(c) F = normal stroma cell (e.g. fibroblast)



(d) A = reactive stroma cell (e.g. cancer associated fibroblasts)

Figure 6.8: *The HDC algorithm and the individual cell-based life cycle flowcharts for each cell type.*

We specifically introduce the element of stochasticity (via probability p_{FA}) in order to mimic the heterogeneity observed in stromal reactivity. These hypothesised conditions of stromal activation are based on circumstantial evidence only. Since an agreement on the mechanisms is lacking, in the following we will also relax these hypotheses and explore alternative mechanisms (Section 7.5).

6.6 The Vessel Distribution

At this initial stage neither angiogenesis nor vascular degradation are considered. Therefore the generated distribution of vessels will be static throughout the simulations in this chapter. We utilise a circle-packing algorithm (Robertson-Tessi et al., 2015) to initialise the field of lattice-point blood vessels in the domain Ω. Starting from an *in vivo* measured average vessel spacing σ_{mean}, we first determine N_V, the average number of vessels to be positioned:

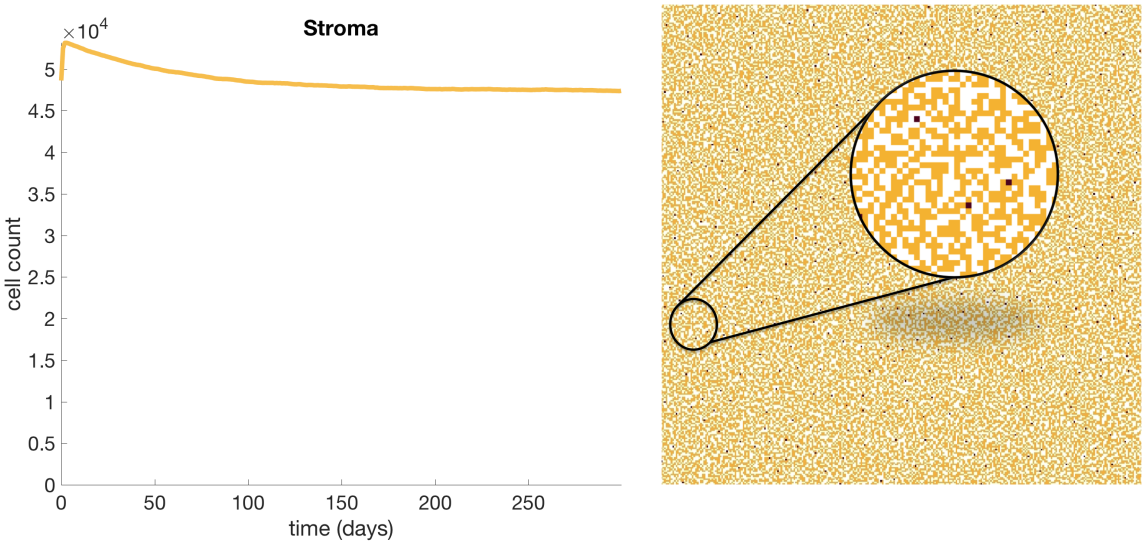
$$N_V = \frac{|\Omega|}{(\sigma_{mean})^2},$$

where $|\Omega|$ is a measure of the size of the domain, in this application $|\Omega| = 0.09$ cm^2. We choose a random position in the domain and place a new vessel in that position if there are no vessels within a radius of σ_{min}. This operation is iterated until N_V vessels are positioned in the domain. The vessel distribution obtained with this method determines the binary function $v_{i,j}$ necessary to update the drug numerical solution with Eq. (6.5). Additionally this distribution will determine the boundary condition for the drug density function, namely if drug is being administered at time t^q, then we set $d^q_{i,j} = v_{i,j}$.

6.7 Homeostasis of Normal Tissue

The first building block in the study of EMDR is the analysis of the healthy tissue. Not only does it constitute the constraining landscape in which the tumour will grow, but most importantly it represents a major component of the tumour environment that can be recruited as a cooperative player. Therefore, we initially analyse the behaviour of normal tissue homeostasis, represented in our model by normal stroma cells, before it is perturbed by cancer cells. We will simulate a (0.3 cm $\times$ 0.3 cm) domain i.e. $L = 0.3$ cm, corresponding to a 300×300 lattice i.e. M=300. The time frame of each simulation varies depending on the specific application, in order to capture the dynamics of interest, but all simulations have a time step of $\Delta t = 0.6$ hours.

Starting from an empty domain, with a vessel distribution already in place (as defined above), we first place normal stroma cells at random positions. We then let the HDC model run until homeostasis is reached i.e. stromal cell count converges (Figure 6.9(a)).



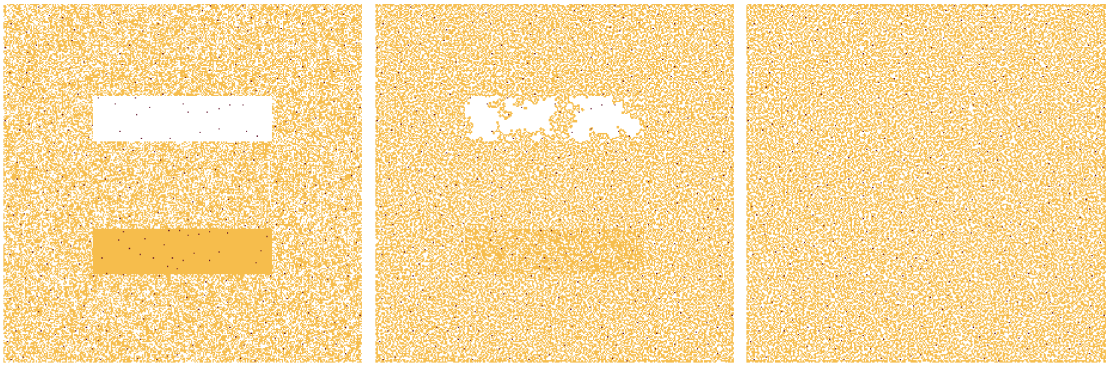
(a) Convergence of cell density.

(b) $t = 300$ days

Figure 6.9: *Setting up normal tissue. After seeding the blood vessel distribution (coloured in* ***dark red****), we introduce normal stromal cells (coloured in* ***yellow****) in random positions. We then let the system reach confluence, i.e. constant cell density (a). The final configuration will be used in all of the following simulations as the initial stroma distribution (b).*

In absence of cancer and treatment, no reactive stroma will appear and the system will converge when the turnover (caused by random death) and proliferation (controlled by contact inhibition) reach a balance.

Despite the simplistic rules governing the normal stroma population, our model is able to recreate a dynamic equilibrium characteristic of homeostatic tissues. More importantly this cancer-free configuration is robust to perturbations that alter the homeostatic density. To put this to the test we consider a domain with two perturbed regions: one fully packed with stroma cells and one completely empty. As shown in Figure 6.10, given enough time, the overcrowded region returns to normal density levels, while the empty region is repopulated. Since our model does not account for cell migration, the timescale for healing in this experiment is orders of magnitude larger than true wound healing events. Mechanisms of cell-directed migration and active repair are key to wound healing, as captured in many mathematical models (Dale et al. 1994, Cai et al. 2007, to name but a few) but are beyond the scope of this work. Additionally, in the presence of cancer the true wound healing timescale would be dominated by tumour growth. It is important to note that the configuration in Figure 6.9(b) is utilised in every subsequent application and only modified in terms of how cancer cells are seeded depending on the scope of the specific application.



(a) $t = 0$ days (b) $t = 100$ days (c) $t = 500$ days

Figure 6.10: *Tissue homeostasis. Two regions with abnormal cell density are introduced in the homeostatic configuration. Homeostasis is reestablished when the simulation is run for a sufficient length of time.*

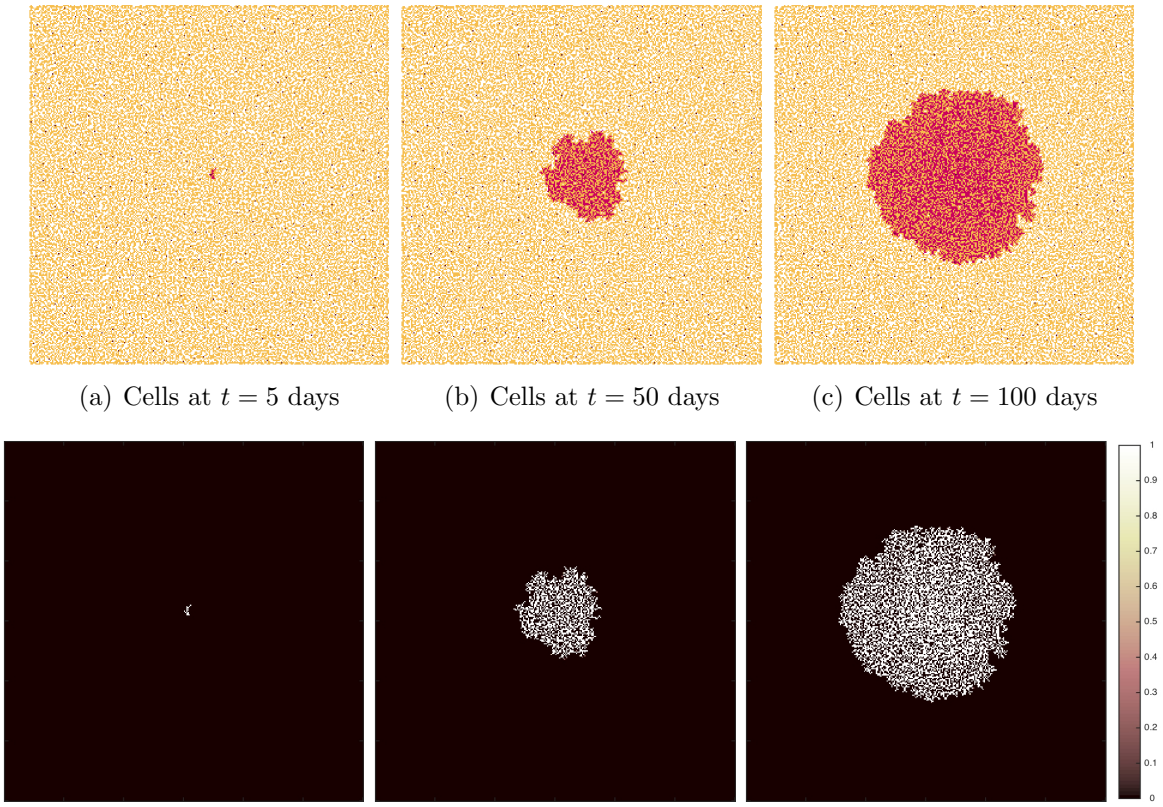
6.8 Tumour Metastasis

In the context of metastatic cancer, we define *metastatic tumour growth* as the state where a tumour cell seeded from a vessel is, in the absence of therapy, able to disrupt the normal tissue, self-sustain a proliferative state, grow and invade. In our model this translates to a cancer whose proliferation signal production is sufficient to maintain concentrations above the proliferative threshold h_p. We logically assume that cancer cells require proliferation signal concentrations in excess of normal tissue homeostasis. For the sake of clarity, the initial condition $g = 0$ corresponds to the homeostatic proliferation signal concentration in the absence of tumour. Therefore any proliferation signal concentration that is observed in the following simulations is either tumour- or reactive stoma-driven.

To specifically investigate how a metastatic event affects normal tissue homeostasis, we introduce a single cancer cell in a neighbouring position of a blood vessel (an extremely simplistic mimicry of extravasation). The cancer cell produces proliferation signal at rate β, initiating a build-up of factors that create an expanding region of growth-promoting signal concentrations ($g > h_p$). The tumour growth is self-sustained because of the growth-promoting environment it creates for its daughter cells (Figure 6.11(a-c)). This is a simplistic yet effective description of the autocrine-paracrine proliferative signalling in a tumour. The sharp gradients appearing in the proliferation signal distribution (Figure 6.11(d-f)) are caused by the low diffusivity of the proliferation signal, mostly composed of growth factors that are anchored and stored in the ECM.

In the plot of the cell count over time (Figure 6.12) we observe an approximately exponential growth of the tumour, while the homeostatic density of the stroma is gradually being eroded by the stronger competition from the tumour. The higher fitness of

the tumour is given by the lack of contact inhibition, which allows cancer cells to take advantage of the stromal turnover and gradually infiltrate the tissue at higher density.



(a) Cells at $t = 5$ days (b) Cells at $t = 50$ days (c) Cells at $t = 100$ days

(d) Proliferation signal at $t = 5$ days (e) Proliferation signal at $t = 50$ days (f) Proliferation signal at $t = 100$ days (g)

Figure 6.11: *Time evolution of metastatic tumour growth. A cancer cell is introduced next to a blood vessel, to simulate a metastatic event. The tumour is introduced in the homeostatic normal tissue previously described. (a-c) Evolution of the cell distribution in the lattice. Lattice colour code:* ***blood vessels****,* ***stroma cells****,* ***cancer cells****. (d-f) Evolution of proliferation signal concentration. (g) Colour map for (d-f).*

6.9 Conclusion

In this chapter we introduced the hybrid discrete-continuum (HDC) modelling framework that allowed us to model key spatial features and interactions relevant to metastatic disease. Specifically, we were able to capture the tumour-stroma dynamics in more detail, including local cell-cell interactions, the effects of spatial gradients of drug, and the local modulation of the proliferation signal. This HDC approach describes individual cell-based behaviour in response to local cues, specifically the vasculature-delivered drug and the proliferation signal, determining the cancer cell's viability. In turn, the cellular components of the system modulate the local environment. This feedback loop between the tumour and its microenvironment results in a complex dynamic that allows us to

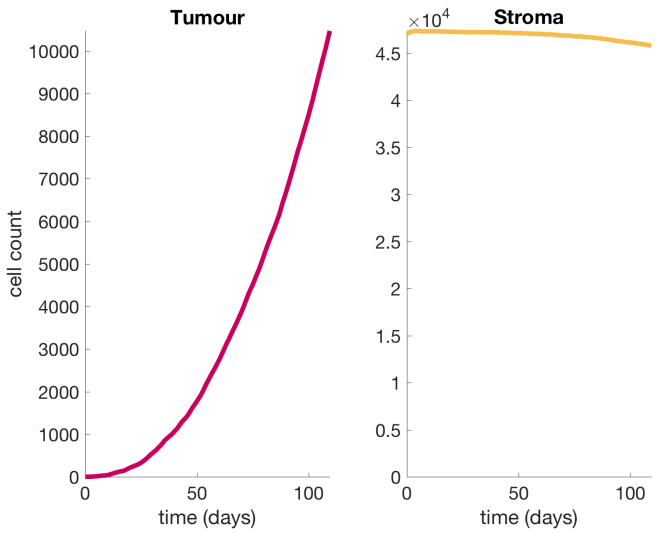


Figure 6.12: *Tumour homeostasis. Evolution of cancer and stroma cell counts over time.*

model EMDR at a much finer level of detail, when compared to the ODE model presented in the previous chapters. Having defined the HDC model, in the next chapter we will present applications of it to the design of treatment strategies that address inter- and intra-tumour heterogeneity, and we will explore mechanisms of stromal activation and renormalisation.

Chapter 7

Exploration of Treatment Strategies and Mechanisms of EMDR

Tumour microenvironment heterogeneity, specifically stromal composition, is a key factor that must be taken into account in order to fully understand EMDR. For example, in prostate cancer, the amount of stromal reactivity was found to be a predictor of recurrence and survival in patients receiving radical prostatectomy (Yanagisawa et al. 2007). Examples of tissues with different stromal composition and reactivity are shown in Figure 7.1. We previously found that variability in treatment response across mice can be attributed to different levels of stromal promotion (see Chapter 5). Compelling experimental evidence shows that a large degree of variation in stromal composition correlates with treatment outcome (Ayala et al., 2003). Melanoma metastasises to several organs, including bone, liver, brain and lung (Tas, 2012). Each organ is characterised by a different tissue composition, for example the population of fibroblasts susceptible to treatment-induced changes can be more or less abundant, potentially altering the extent of stromal protection and EMDR.

In this chapter we will present applications of the HDC model introduced in Chapter 6 to address the problem of designing treatment strategies that account for environmental heterogeneity and mechanisms of stromal activation and renormalisation. In order to capture this variability, we extend the HDC model to include a third stromal population that represents all the non-reactive stromal cells that make up the tissue. This population is identified with P (see Figure 7.2), it does not interact with (or turn into) other cell types, but competes for the same shared resources (space), and is unaffected by the drug. In the following simulations we will initialise the system with the same configuration previously used, and assign phenotype F to a fraction π of stromal cells, and phenotype P to the remaining stromal cells. It is worth noting that no A cells are initially present, and upon drug applications only F cells, under given conditions, can turn into A. Varying π allows us to recapitulate the spectrum of stromal composition that can be observed

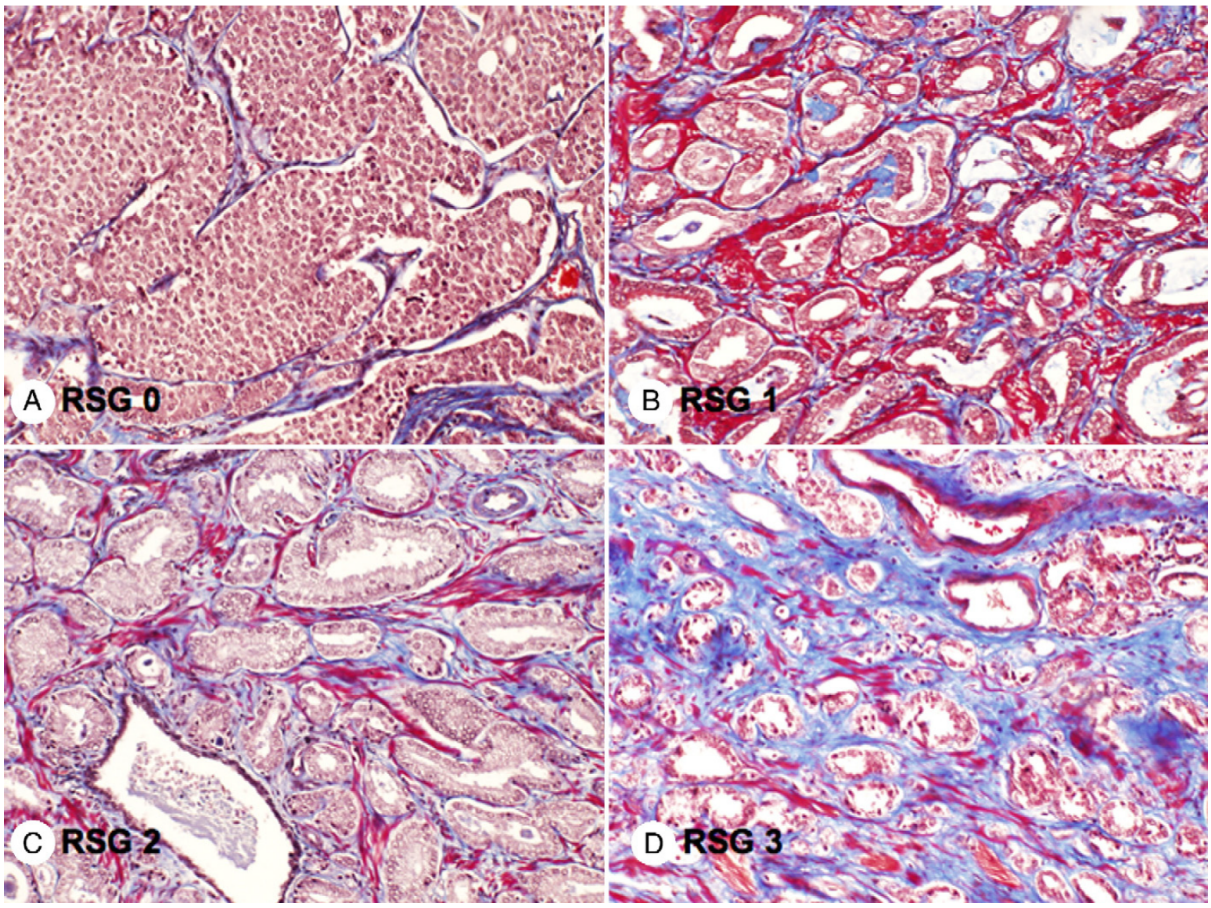


Figure 7.1: *Reactive stroma grade (RSG) staining in different tissues of prostate cancer. Normal stroma (mostly epithelial) stained in red, reactive stroma in blue. RSG 0 corresponds to lower stroma reactivity, RSG 4 to high stroma reactivity. Figure reproduced with permission from Yanagisawa et al., 2007.*

across metastatic sites: with $\pi = 0$ corresponding to a completely unreactive stroma, and $\pi = 1$ corresponding to a fully reactive stroma. The latter case corresponds to the previous version of the model, where all stroma cells have the potential to undergo some transformation. In Section 7.6 we will address the problem of treatment scheduling for a distribution of metastases characterised by different stromal composition (π).

Stromal activation and stromal renormalisation are the two main timescales governing the dynamics of response to treatment. These phenomena, given their biological complexity, are also among the most difficult to quantify experimentally. For example, it is possible to show that CAFs, in the presence of treatment, shift to a secretory phenotype, and increase the production of growth factors and ECM components such as fibronectin, and remodelling of the matrix (Hirata et al., 2015). Additionally, it has been observed that this phenotypic switch is transient and reversible upon removal of the drug. However, the complex remodelling of the tumour microenvironment resulting from the action of reactive stroma includes some long-term changes that, on the timescale

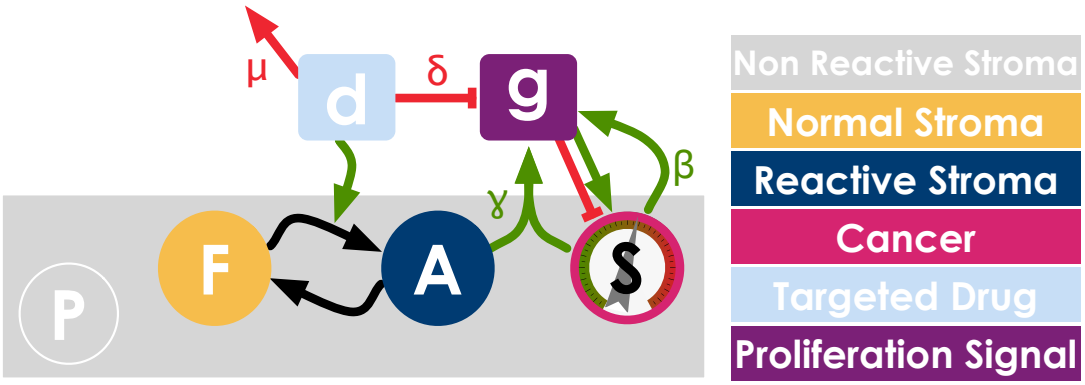


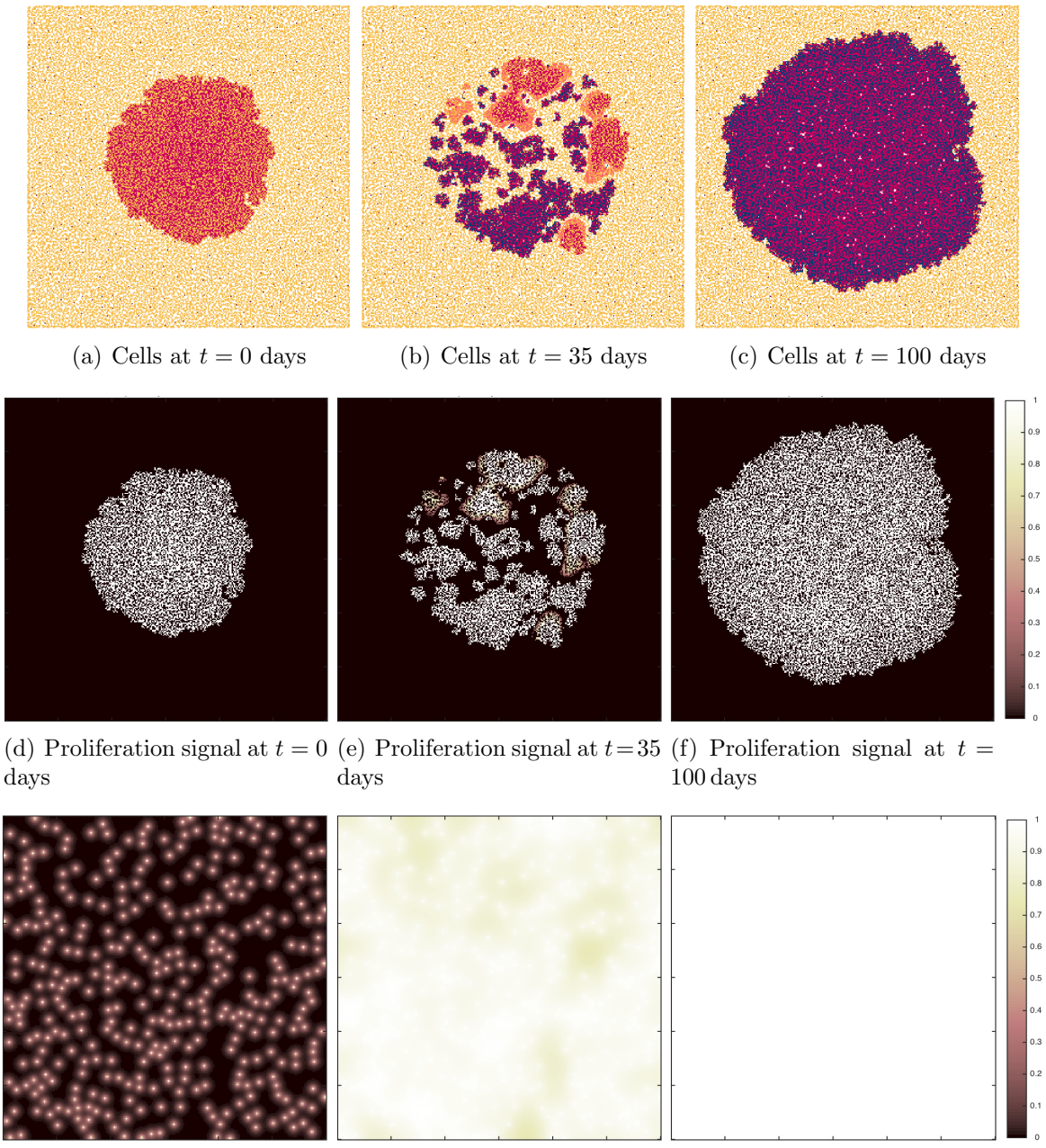
Figure 7.2: *An extension of the HDC model to include a non-reactive stromal population P. Interactions are the same as in the previous model (see Figure 6.6).*

we consider, are irreversible. Some examples are the rearrangement of the ECM fibers and the vascular network. Furthermore, the secretome produced by the reactive stroma is often cancer- and context-dependent (see Chapter 2). Locally deposited fibrobectin, for example, changes the composition of the ECM, modifying adhesion-related properties of the resident cancer cells. Certain growth factors (such as HGF) can be transported throughout the tissue, benefiting cancer cells on a larger range, while others are anchored and stored in the ECM, locally (Flaumenhaft et al., 1991). Despite the complexity and the unknowns of the system, we aim at a general description that allows a first principles investigation of the problem of EMDR. Specifically, in Section 7.5 we will use the HDC modelling framework as an hypothesis-testing tool to explore possible mechanisms of drug-dependent stromal phenotypic transitions that can explain experimentally observed phenomena, and drive experiments to further investigate the problem.

Before presenting these applications we are going to start with the simple case of treatment with a targeted inhibitor applied to a tumour characterised by maximum stromal reactivity: $\pi = 1$. This simple case will allow us to introduce the problem of treatment scheduling and treatment optimisation.

7.1 Treatment with Targeted Therapy

Having studied the dynamics of normal and cancerous tissues in a metastatic site, we have an appropriate system setup to explore the effects of a targeted therapy on the tumour. Specifically, we simulate the application of a generic targeted inhibitor that acts on the tumour by shifting the balance of the proliferative signalling towards a growth-controlled state (see Figure 6.4(c)). In order to show the impact of therapy we initially let the tumour grow for 110 days untreated, when it reaches approximately the size of 10^4 cells. This



(a) Cells at $t = 0$ days (b) Cells at $t = 35$ days (c) Cells at $t = 100$ days

(d) Proliferation signal at $t = 0$ days (e) Proliferation signal at $t = 35$ days (f) Proliferation signal at $t = 100$ days

(g) Inhibitor at $t = 1$ days (h) Inhibitor at $t = 35$ days (i) Inhibitor at $t = 100$ days

Figure 7.3: *Time evolution of tumour response to continuous treatment with targeted inhibitor. The tumour to be treated is grown for 110 days from the metastatic event, as described in Section 6.8. The treatment is introduced at time* 0*. The targeted therapy diffuses out of the vessels in the metastatic tissue. Stroma, recruited by the tumour under treatment, becomes reactive and upregulates proliferation signal, rescuing cells from death or growth inhibition. (a-c) Evolution of the cell distribution in the lattice. Lattice colour code:* ***blood vessels****,* ***normal stroma cells****,* ***reactive stroma cells****,* ***cancer cells****,* ***growth-inhibited cancer cells****. (d-f) Evolution of proliferation signal concentration. (g-i) Evolution of inhibitor concentration. At day* 100 *the inhibitor reaches maximum concentration everywhere in the domain* ($d = 1$)*.*

initial configuration and the corresponding proliferation signal distribution are shown in Figures 7.3(a), and 7.3(d), respectively. Assuming that this tumour is now our initial condition, we apply treatment at time $t = 0$. The inhibitor diffuses from the blood vessels (see Figure 7.3(g)), and gradually reaches all the cells in the tissue. The primary effect of the therapy is downregulation of the expression of proliferation signal, triggering growth-inhibition (if $g < h_p$) or death (if $g < h_d$), depending on the local concentration a given tumour cell senses. In the top portion of the treated mass we can clearly distinguish a wave of growth inhibition (**salmon** coloured cells in Figure 7.3(b)), and the corresponding gradient of proliferation signal concentrations (see Figure 7.3(e)). The secondary effect is the stimulus by cancer cells to recruit stromal cells, inducing their activation. Hence we observe the emergence of reactive stroma intermixed with the surviving tumour cells, and upregulation of proliferation signal that will subsequently protect the tumour cells from the treatment. Therefore, depending on the local concentration of proliferation signal produced by the reactive stroma, a cancer cell can be rescued from death and pushed into a growth-inhibited state ($h_d \leq g < h_p$), or even into a proliferative state ($g > h_p$). The dynamics presented here represent an instance of EMDR, a mechanism of resistance that determines relapse over a prolonged application of the inhibitor. The resulting configuration (Figure 7.3(c)) is a growing tumour mass, infiltrated with reactive stroma, reminescent of the *in vitro* observation presented in Figure 2.6.

In Figure 7.4 the temporal evolution of cell counts is shown. The number of cells in growth-inhibited state as a function of time is plotted in **salmon**. It is worth noting that this state corresponds to a transient and context-dependent state of cancer cells and does not represent a cell type. We observe that the overall tumour burden (the magenta thick line) initially keeps growing, despite the application of inhibitor from day 0, and only after 20 days are the effects of the inhibitor evident. This reflects the spatial heterogeneity in the tumour environment, specifically the vessel distribution, that causes the drug to reach the tumour in a delayed and non-homogeneous fashion. The initial delay in response and subsequent relapse characterising the time evolution of the tumour burden, are important features that the spatially-defined model can capture. Indeed the distance from the nearest vessel and the access to stroma-rich areas are crucial in the modulation of the treatment response.

After a prolonged application of targeted therapy, the stromal activation becomes significant and drives tumour relapse, not only rescuing cancer cells from death, but also inducing proliferation in the tumour. In conclusion, it is clear that a prolonged application of inhibitor is ultimately futile as it leads inevitably to treatment resistance, largely driven by stromal activation. A smarter therapy should maximise the kill effect

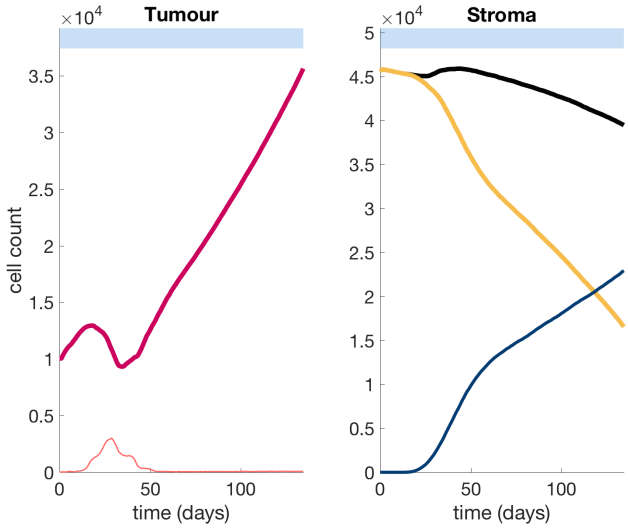


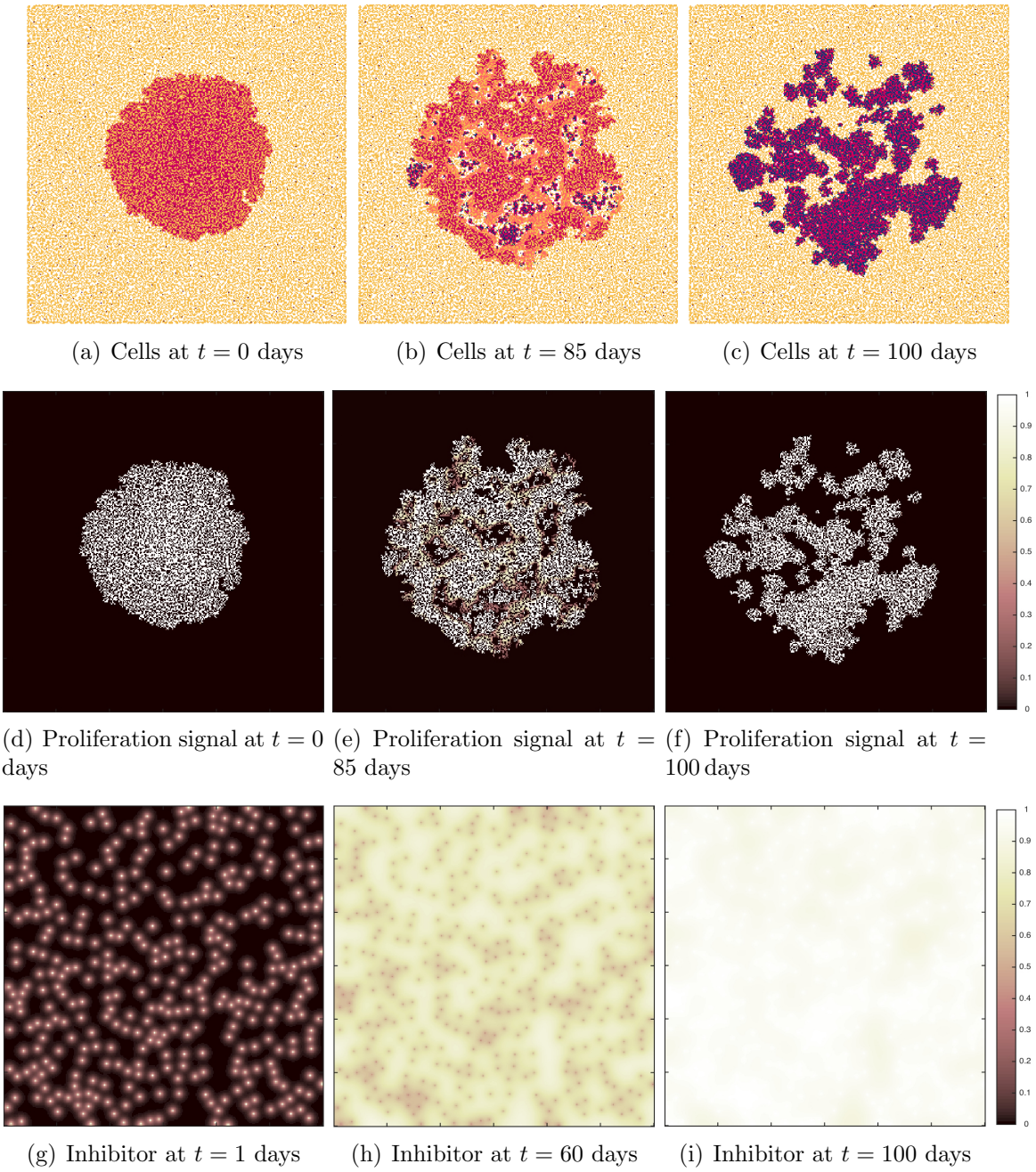
Figure 7.4: *Continuous treatment with targeted inhibitor. Evolution of cancer and stroma cell counts over time. The light blue bar shows the window of time when the inhibitor is being applied. The initial response of the tumour to the inhibitor is followed by relapse, corresponding with the activation of the stroma. Legend:* ***total tumour****,* ***growth-inhibited tumour****,* ***normal stroma****,* ***reactive stroma****,* ***total stroma****.*

of the inhibitor, yet minimise the deleterious activation of the stroma. One possible way to do this is through treatment holidays.

7.2 Drug Holiday Limits Stromal Activation

Despite the uncontrolled growth resulting from the absence of the targeted inhibitor, pauses in the treatment become necessary to avoid substantial activation of the recruited stroma, which is responsible for progression and, ultimately, relapse. The effects of EMDR are mostly transient, therefore in the absence of drug treatment, stromal reactivity and environmental resistance can be reversed.

In order to ensure results are directly comparable, we start from the same initial conditions as the previous simulation (Figures 7.5(a) and 7.5(d)), applying the inhibitor at day 0. However, instead of the continuous treatment administration, we remove the inhibitor at day 50 and reintroduce it at day 70. This 20 day treatment holiday should allow the drug to be gradually washed out of the system (via the vasculature) and facilitate renormalisation of the stroma. Without the protective action of the reactive stroma, tumour sensitivity to therapy should be restored. Indeed, when at day 70 the drug is reapplied, we obtain a secondary response, as seen by the drop in tumour burden in Figure 7.6. During the drug holiday the reactive stroma renormalises, essentially removing the effects of the EMDR when the second pulse of treatment is applied. However, continued treatment results in stromal activation and once again we see tumour progression (after



(a) Cells at $t = 0$ days (b) Cells at $t = 85$ days (c) Cells at $t = 100$ days

(d) Proliferation signal at $t = 0$ days (e) Proliferation signal at $t = 85$ days (f) Proliferation signal at $t = 100$ days

(g) Inhibitor at $t = 1$ days (h) Inhibitor at $t = 60$ days (i) Inhibitor at $t = 100$ days

Figure 7.5: *Time evolution of tumour response to treatment with targeted inhibitor with a holiday between days* 50 *and* 70*. The initial condition and setup are identical to the previous simulation. When the targeted therapy is paused the recruited stroma transitions back to normal while the tumour starts growing again. (a-c) Evolution of the cell distribution in the lattice. Lattice colour code as in Figure 7.3. (d-f) Evolution of proliferation signal concentration. (g-i) Evolution of inhibitor concentration.*

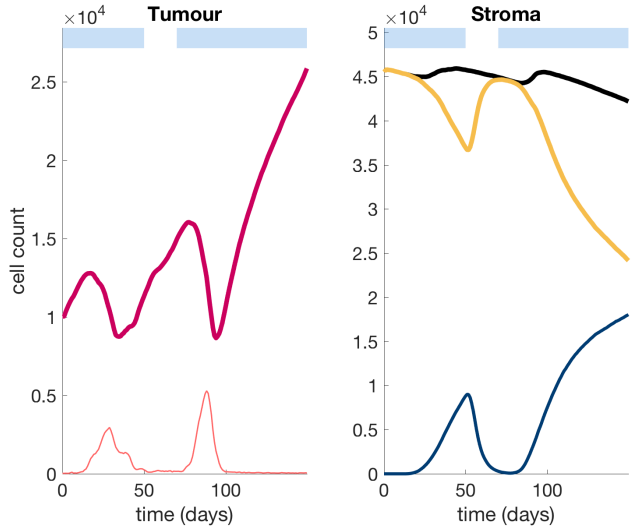


Figure 7.6: *Treatment with targeted inhibitor with a holiday between days* 50 *and* 70*. Evolution of cancer and stroma cell count over time. The light blue bars show the windows of time when the inhibitor is being applied. The holiday allows renormalisation of the stroma, facilitating response to the second drug application. Legend:* ***total tumour****,* ***growth-inhibited tumour****,* ***normal stroma****,* ***reactive stroma****,* ***total stroma****.*

day 100) and, eventually, relapse. Nevertheless, the overall progression is considerably delayed (compare Figures 7.6 and 7.4), and characterised by a more fracturated tumour mass (Figure 7.5(c)), that may be easier to target with additional pulses of drug, as opposed to the compact tumour mass obtained with continuous treatment (Figure 7.3(c)). Indeed, a dense mass of cancer cells gives rise to a significant build-up of proliferation signal that will be harder for the drug to deplete. A more sparse distribution of cancer cells will instead create lower concentrations of proliferation signal, and therefore be easier to degrade with therapy.

In Figures 7.5(g-h) we can observe the vessels acting as drug sources when the therapy is being delivered (Figure 7.5(g)), and sinks when no therapy is applied, causing residual drug to be washed away through the vasculature (Figure 7.5(h)). Despite the beneficial treatment holiday, EMDR-driven progression seems inevitable, unless the therapy is paused once again. In the following section we will explore a range of intermittent treatment schedules, aimed at tumour growth control.

7.3 Pulsed Drug Treatment to Control Growth

The cancer research community is slowly coming to terms with the concept of *disease management*, instead of cure or eradication, as a more realistic and longer term treatment strategy. With the rapid development of new targeted therapies and numerous attempts to combine treatment strategies, it has become clear that the complexity of cancer, and its

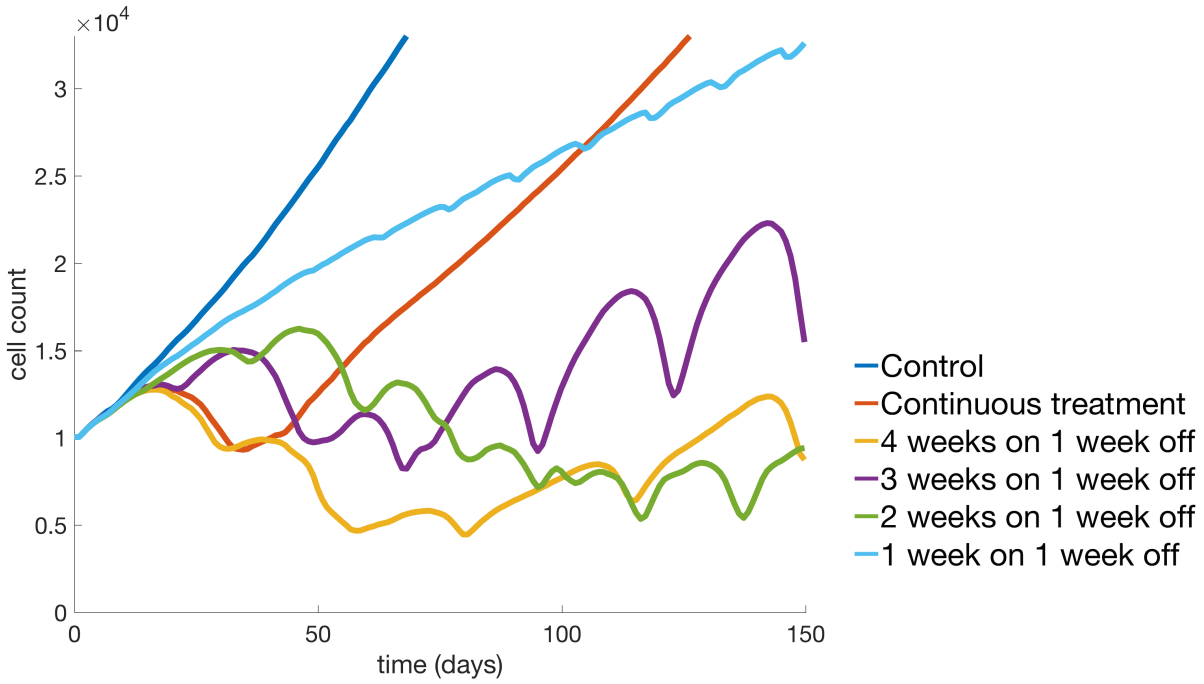
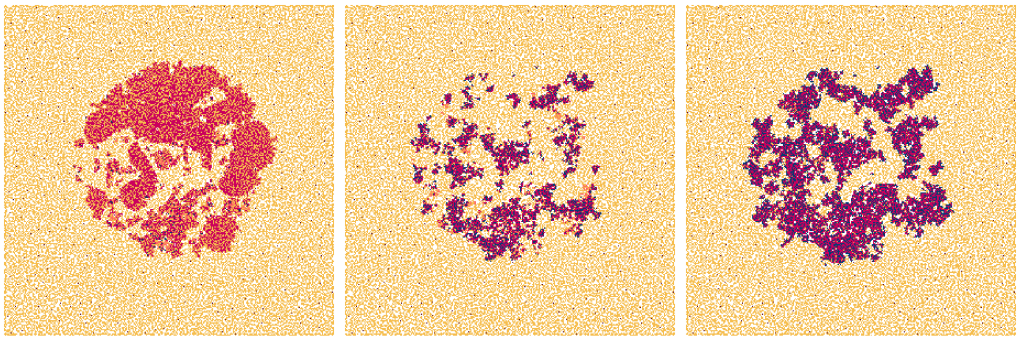


Figure 7.7: *Pulsed treatments with varied lengths. Evolution of tumour burden (cancer cell count) over time. The short term response to a treatment strategy is not necessarily predictive of the long term response.*

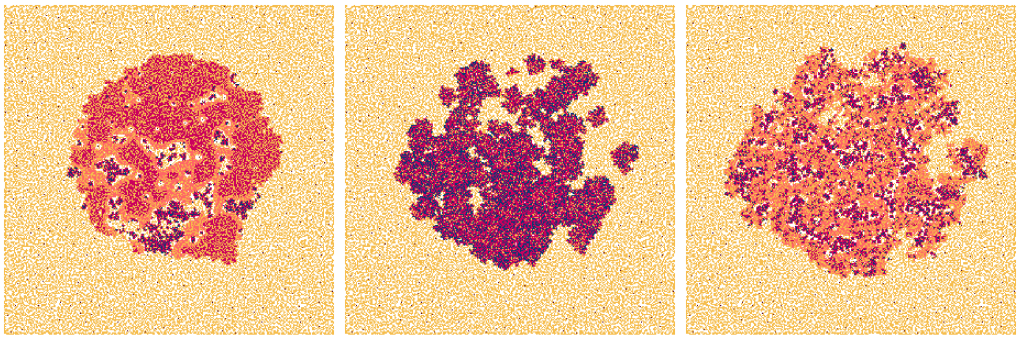
ability to adapt and evolve, makes it a difficult moving target in the quest to cure cancer. In the context of EMDR, the source of this complexity is in the cross-talk between the tumour and its environment. A possible management strategy consists of treatment windows maximising tumour kill, alternated with drug holidays that allow renormalisation of the environment.

As a first attempt to explore this strategy we utilise the previously developed setup to simulate a variety of treatment schedules consisting of pulses of therapy of varied length. In Figure 7.7 we show the evolution of the tumour burden resulting for intermittent treatment of $4, 3, 2$, or 1 week length and fixed 1 week holidays, starting from the same initial conditions. All of these strategies are consistently better than the untreated case (control). Too short a treatment window (1 week) leads to insufficient tumour kill within the time scale of stromal activation. Early on (up to day 50) longer treatment windows seem to be as effective as, or slightly worse than, the continuous treatment. However, when considering the long term evolution of the system, those strategies that initially seem to be disadvantageous (3 and 2 weeks), appear to have a better control of tumour growth, compared to the continuous treatment. The most successful long term strategies are those that minimise overall stromal activation, even though they compromise on the extent of tumour kill.

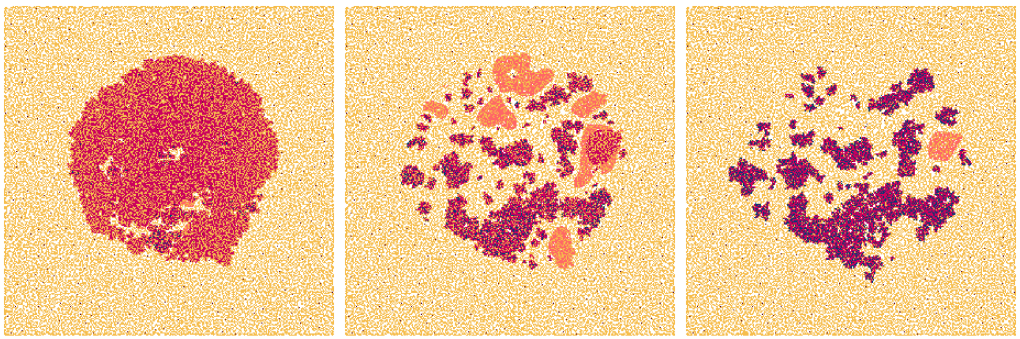
We can follow the temporal evolution of each treatment strategy in Figure 7.8 where snapshots at 40, 80 and 120 days are shown. Comparing the progression of the same



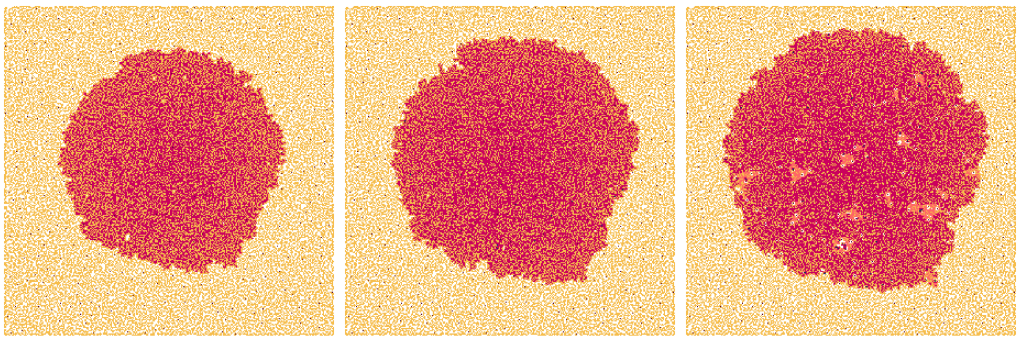
(a) Cells at $t = 40$ days (b) Cells at $t = 80$ days (c) Cells at $t = 120$ days



(d) Cells at $t = 40$ days (e) Cells at $t = 80$ days (f) Cells at $t = 120$ days



(g) Cells at $t = 40$ days (h) Cells at $t = 80$ days (i) Cells at $t = 120$ days



(j) Cells at $t = 40$ days (k) Cells at $t = 80$ days (l) Cells at $t = 120$ days

Figure 7.8: *Time evolution of tumour response to pulsed treatment with varied lengths. Targeted inhibitor is administered with holidays of 1 week and varied pulse length: (a-c) 4 weeks, (d-f) 3 weeks, (g-i) 2 weeks, (j-l) 1 week. The initial condition and setup is the same in each instance and identical to the previous simulations.*

initial tumour mass treated with pulses of different lengths, three main observations can be made. First, the longer the treatment, the sooner and stronger the reactive stroma appears. For example, 4 week-long pulses (Figure 7.8(a-c)) induce stromal activation by day 80, while 1 week long pulses (Figure 7.8(j-l)) do not induce activation until day 120. Secondly, the length of each pulse of treatment, with respect to the drug perfusion time scale, determines the cytostatic versus cytotoxic effect of the drug. Specifically, in our simulated drug regime, the 3 week-long pulses (Figure 7.8(d-f)) induce a wave of growth-inhibition (**salmon** coloured cells) that can only be reversed by the appearance of reactive stroma or a drug holiday. Indeed, 1 week pulses are short enough that drug is easily washed out of the system between pulses (allowing the proliferation signal to increase above h_p); 4 week pulses are long enough to induce consistent stromal activation that rescues cells from the growth-inhibition zone. In both cases the effect is a sharp modulation of the proliferation signal that drives cells to the extremes: cell death or proliferation. We can also observe that, according to the temporal dynamics shown in Figure 7.7, at approximately day 60 the 4 week pulse of treatment seems to be much better than 2 week pulses. However, on a longer timeframe (at day 120) the tumour treated with 4 week long pulses comes back more aggressively, because of a buildup of reactive stroma, combined with the elimination of spatial competition following drug kill. Observing the evolution of the tumour treated with 2 week pulses, we see consistent activation of the stroma, and the fractured distribution of residual tumour (Figure 7.8(i)), which predicts a similar but delayed response.

In conclusion, the timescales of stromal activation and tumour growth are key in determining the overall success or failure of a therapeutic strategy. These timescales are determined by a large number of tissue and tumour-specific parameters: vessel spacing, diffusivity of chemicals in the tissue, stromal reactivity and spatial distribution, to name a few. Furthermore, the overall temporal dynamics reported in Figure 7.7 are the result of the integration over complex spatial dynamics driven by local interactions (Figure 7.8).

7.4 A Multi-model Approach to Treatment Optimisation

The trade-off between maximising tumour kill and minimising stromal activation poses an optimisation problem that cannot be easily approached in the individual cell-based framework. The broad problem of designing anti-cancer therapies to control resistance has produced a vast literature that has been collected in a comprehensive review by Swierniak and colleagues (Swierniak et al., 2009). The majority of the techniques available for

HDC rule	ODE interaction
β : autocrine proliferation signal production	$\hat{\rho}$: growth rate
γ : paracrine proliferation signal production	$\hat{\gamma}$: stromal-induced growth rate
δ : proliferation signal degradation by inhibitor	$\hat{\delta}$: rate of death caused by inhibitor
p_{FA} : probability of stromal activation	$\hat{\theta}$: stromal activation rate
p_{FA} : probability of stromal normalisation	$\hat{\phi}$: stromal normalisation rate

Table 7.1: *Interaction parameters translated from individual cell-based rules to population dynamics rates.*

treatment optimisation are confined to non-spatial (and mostly linear) models. For example, optimal control approaches can be applied to compartmental models to determine optimal treatment schedules (Ledzewicz et al., 2013). For obvious reasons, in the context of individual-based models, treatment optimisation represents a more challenging problem. The development of a comprehensive mathematical framework that allows treatment optimisation in individual-based models is outside the scope of this work. Heuristic optimisation, to find suboptimal solutions where full exploration of the solution space is infeasible, is currently the preferred approach. To this end Oremland and Laubenbacher developed a toolkit to standardise model description and compute suboptimal solutions (Oremland and Laubenbacher, 2014). However, the reduction of our HDC model interactions through their protocol for model specification (Hinkelmann et al., 2010) is not straightforward and would represent a challenging, although interesting, application that we leave to future investigations.

We propose a dynamical systems approximation of the HDC model that reduces the complexity of the individual cell dynamics to a system of ordinary differential equations (ODEs) describing each cell type as a compartment. This ODE model approximation is more amenable to analysis and optimisation techniques. In Chapters 4 and 5 we already considered an ODE model of similar processes, although this explicitly included a resistant compartment (see Eqs. (4.1) and (5.1)). We will simplify this system by only considering three cell populations, corresponding to the cell types defined in the individual-based model: cancer cells (s), normal stroma (f) and reactive stroma (a). The stochastic interactions between cell types in the HDC model are translated into interactions between cell populations, occurring at predefined rates. The implicit assumption being that the system is well-mixed, i.e. each cell within the population interacts equally with cells of the other populations, hence neglecting spatial configurations (e.g. segregation, clustering) that might limit the effective interactions between any two cells within the domain. Table

7.1 explains the correspondence between the interactions in the HDC model and the ODE approximation. Parameters of the ODE model are both real and positive and marked with a hat (ˆ) annotation. Interactions between the different cell populations are depicted in Figure 7.9, and can be formalised in the following system of dimensional ODEs:

$$\begin{cases} \dfrac{ds}{dt} = \hat{\rho}s - \hat{\delta}s\alpha(t) + \hat{\gamma}as, \\ \dfrac{da}{dt} = \hat{\theta}f\alpha(t) - \hat{\phi}a(1-\alpha(t)), \\ \dfrac{df}{dt} = -\hat{\theta}f\alpha(t) + \hat{\phi}a(1-\alpha(t)), \end{cases} \quad \text{with} \quad \alpha(t) = \begin{cases} 1 \text{ when drug ON,} \\ 0 \text{ when drug OFF,} \end{cases} \tag{7.1}$$

with initial conditions:

$$s(0) = s_0, \quad a(0) = 0, \quad f(0) = f_0. \tag{7.2}$$

We define new non-dimensional parameters (marked with an asterisk *) and variables as:

$$\delta^* = \frac{\hat{\delta}}{\hat{\rho}},\ \gamma^* = \frac{\hat{\gamma}f_0}{\hat{\rho}},\ \theta^* = \frac{\hat{\theta}}{\hat{\rho}},\ \phi^* = \frac{\hat{\phi}}{\hat{\rho}},\ S_0 = \frac{s_0}{f_0}, \tag{7.3}$$

$$S = \frac{s}{f_0},\ A = \frac{a}{f_0},\ F = \frac{f}{f_0},\ \tau = t\hat{\rho}, \tag{7.4}$$

and observe that:

$$\frac{d}{dt}(a+f) = 0, \text{ i.e. } a(t) + f(t) = a(0) + f(0) = const\ \forall t, \tag{7.5}$$

hence:

$$f(t) = f_0 - a(t) \quad \forall t. \tag{7.6}$$

Therefore, we can reduce the system to a set of two non-dimensional ODEs describing the evolution in time of the cancer cell (S) and reactive stroma (A) populations, and a simple algebraic equation for the normal stroma (F). To simplify the notation we drop the asterisk sign from the non-dimensional parameters. The resulting system of equations is:

$$\begin{cases} \dfrac{dS}{d\tau} = S\left(1 - \alpha(t)\delta + \gamma A\right), \\ \dfrac{dA}{d\tau} = \alpha(t)\left(A(\phi - \theta) + \theta\right) - \phi A, \end{cases} \quad \text{and} \quad F = 1 - A \quad \forall \tau, \tag{7.7}$$

with initial conditions:

$$S(0) = S_0, \quad A(0) = 0, \quad F(0) = 1. \tag{7.8}$$

Since we are interested in understanding the impact of pulsed drug administration, we introduce a generic formulation that can account for a range of different treatment

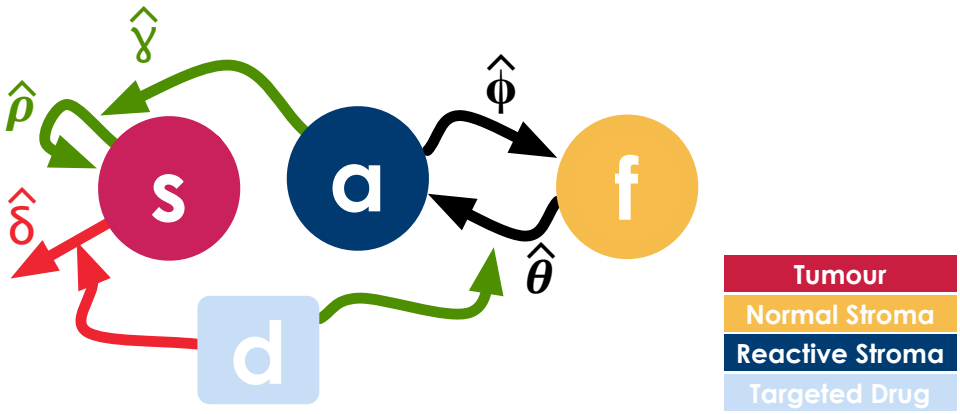


Figure 7.9: *ODE approximation of the HDC model (Eqs. (7.1)). Spatial interactions are reduced to a well-mixed compartmental model approximation. Green arrows indicate positive interactions, red arrows indicate negative interactions, black arrows indicate phenotypic transitions.*

schedules. The i^{th} pulse of drug will begin at time τ_T^i, with initial cancer and reactive stromal populations S_T^i, and A_T^i, respectively. Similarly, the i^{th} holiday will begin at time τ_H^i, with initial cancer and reactive stromal populations S_H^i and A_H^i, respectively, corresponding to the populations at the end of the i^{th} pulse of drug. We can then rewrite our system of ODEs for both of these cases as follows:

$$\begin{cases} \dfrac{dS}{d\tau} = S\left(1-\delta+\gamma A\right), \quad S(\tau_T^i) = S_T^i, \\ \dfrac{dA}{d\tau} = \theta(1-A), \quad A(\tau_T^i) = A_T^i, \end{cases} \quad \text{when drug is on,} \quad \tau \in [\tau_T^i, \tau_H^i). \tag{7.9}$$

$$\begin{cases} \dfrac{dS}{d\tau} = S\left(1+\gamma A\right), \quad S(\tau_H^i) = S_H^i, \\ \dfrac{dA}{d\tau} = -\phi A, \quad A(\tau_H^i) = A_H^i, \end{cases} \quad \text{when drug is off,} \quad \tau \in [\tau_H^i, \tau_T^{i+1}), \tag{7.10}$$

with $S_T^0 = S_0$ and $A_T^0 = 0$.

This new modelling framework is suitable for deriving analytical solutions that will allow the formulation of an analytical "control therapy".

7.4.1 Cancer and Reactive Stroma Monotonicity Regimes under Drug Administration

We now analyse separately the system under drug administration and drug holiday. Starting from the first case, we solve the equation for the reactive stroma in (7.9), and obtain the simple exponential solution:

$$A(\tau) = 1 + \left(A_T^i - 1\right)\exp\left(\theta(\tau_T^i - \tau)\right) \quad \forall\, \tau \in [\tau_T^i, \tau_H^i]. \tag{7.11}$$

The non-dimensional variables A and F are non-negative and always sum to 1, therefore it is always true that $A_T^i \leq 1$. Hence $A(\tau)$, describing the stromal activation, is monotonically increasing in the time interval of interest. Substituting this into the first equation of (7.9), we solve for the cancer cell population:

$$S(\tau) = S_T^i \exp\left[(\tau - \tau_T^i)(1 - \delta + \gamma) + \gamma \frac{A_T^i - 1}{\theta}\left(1 - \exp\left(\theta(\tau_T^i - \tau)\right)\right)\right] \ \forall\, \tau \in [\tau_T^i, \tau_H^i]. \tag{7.12}$$

In order to study the behaviour of the system as a function of the parameter values, we rewrite the derivative for the cancer cell population making use of the analytical form of $S(\tau)$:

$$\frac{dS}{d\tau} = S_T^i \left[C + B^i \theta \exp(\theta(\tau_T^i - \tau))\right] \exp\left[C(\tau - \tau_T^i) + B^i\left(1 - \exp\left(\theta(\tau_T^i - \tau)\right)\right)\right], \tag{7.13}$$

where,

$$B^i = \gamma \frac{A_T^i - 1}{\theta},\ C = 1 - \delta + \gamma. \tag{7.14}$$

We study the sign of the derivative, in order to define the monotonicity of the solution, and we find the following stationary point:

$$\tau_*^i = \tau_T^i - \frac{1}{\theta} \ln\left[\frac{1 - \delta + \gamma}{\gamma(1 - A_T^i)}\right]. \tag{7.15}$$

The sign of the logarithm argument will determine the existence and type of stationary point, so we let

$$E^i = \frac{1 - \delta + \gamma}{\gamma(1 - A_T^i)}. \tag{7.16}$$

Since $A_T^i < 1$, and $\gamma > 0$, it follows that E^i is positive if and only if $1 - \delta + \gamma > 0$. Setting

$$A_L = \frac{\delta - 1}{\gamma}, \tag{7.17}$$

we observe that

$$1 - \delta + \gamma > 0 \iff A_L < 1. \tag{7.18}$$

Inequality (7.18) must be satisfied if the stationary point τ_*^i exists. Furthermore, from Eq. (7.13), we get

$$\frac{dS}{d\tau} \geq 0 \iff \exp(\theta(\tau_T^i - \tau)) \leq E^i \iff \tau \geq \tau_*^i. \tag{7.19}$$

Therefore the stationary point τ_*^i, when it falls in the interval of interest $[\tau_T^i, \tau_H^i]$, is a minimum.

Finally, we determine the condition for which τ_*^i falls in the time domain of interest, i.e. the time interval where Eqs. (7.9) are defined. From Eq. (7.15):

$$\begin{gathered} \tau_*^i > \tau_T^i \iff E^i < 1 \\ \iff 1-\delta+\gamma < \gamma(1-A_T^i) \iff \frac{1-\delta}{\gamma} + 1 < 1 - A_T^i \iff \\ A_T^i < A_L. \end{gathered} \tag{7.20}$$

Summarising the previous results, we identified three regimes depending on the values of A_L (i.e. rate of death caused by inhibitor δ, and additional growth rate from stromal promotion, γ) and A_T^i.

- If $A_L < 1 \quad (\ i.e.\ \delta < 1+\gamma\ )$
  the value of A_T^i discriminates between the two cases:
  - if $A_T^i < A_L$
    then $S(\tau)$ has a minimum at τ_*^i that we rewrite as:
    $$\tau_m^i = \tau_T^i - \frac{1}{\theta}\ln\left(\frac{1-\delta+\gamma}{\gamma(1-A_T^i)}\right), \tag{7.21}$$
    and corresponding minimum value:
    $$S_m^i = S_T^i\left[\frac{\gamma(1-A_T^i)}{1-\delta+\gamma}\right]^{\frac{1-\delta+\gamma}{\theta}} \exp\left(\frac{1-\delta+\gamma A_T^i}{\theta}\right); \tag{7.22}$$
  - if $A_T^i \geq A_L$
    then $S(\tau)$ is monotonically increasing in the interval of interest $[\tau_T^i, \tau_H^i]$. This is the case where treatment will only worsen the disease progression, because of excessive initial stromal activation. Therefore, we want to avoid this scenario by keeping the level of stromal activation during any application of the drug under the critical limit A_L.

- If $A_L \geq 1 \quad (\ i.e.\ \delta \geq 1+\gamma\ )$
  then $S(\tau)$ is monotonically decreasing, because
  $$\frac{dS}{dt} \leq 0 \iff \exp(\theta(\tau_T^i - \tau)) \geq E^i, \tag{7.23}$$
  which is always true since $E^i < 0$.

The latter case corresponds to a scenario where the drug's dimensional killing rate $\hat{\delta}$ is consistently greater than the tumour growth rate given by the combination of intrinsic tumour growth, $\hat{\rho}$, and stromal promotion, $\hat{\gamma}$. In this case, there is no minimum after which the treatment (causing excessive stromal activation) becomes detrimental and continued treatment results in a monotonically decreasing tumour burden. In the rest of this chapter we do not consider this case because it does not require treatment optimisation.

7.4.2 Cancer and Reactive Stroma Monotonicity Regimes under Drug Holiday

We now solve Eqs. (7.10) to study the system's behaviour in the absence of drug. The equation for the reactive stroma is once again solved with an exponential solution:

$$A(\tau) = A_H^i \exp\left(\phi(\tau_H^i - \tau)\right) \quad \forall\, \tau \in [\tau_H^i, \tau_T^{i+1}]. \tag{7.24}$$

This function, describing the renormalization of the stroma, is monotonically decreasing in the time interval of interest. Substituting this into the first of Eqs. (7.10), we can solve for the cancer cell population:

$$S(\tau) = S_H^i \exp\left(\tau - \tau_H^i + A_H^i \frac{\gamma}{\phi}\left(1 - \exp\left(\phi(\tau_H^i - \tau)\right)\right)\right) \quad \forall\, \tau \in [\tau_H^i, \tau_T^{i+1}]. \tag{7.25}$$

Similar to the previous case, we rewrite the derivative for the cancer cell population using the analytical form of $S(\tau)$, in order to study the behaviour of the system:

$$\frac{dS}{d\tau} = S_H^i \left[1 + \gamma A_H^i \exp(\phi(\tau_H^i - \tau))\right] \exp\left[\tau - \tau_H^i + A_H^i \frac{\gamma}{\phi}\left(1 - \exp\left(\phi(\tau_H^i - \tau)\right)\right)\right]. \tag{7.26}$$

Hence $\dfrac{dS}{d\tau} > 0 \;\forall\; \tau \in [\tau_H^i, \tau_T^{i+1}]$ i.e. S(t) is monotonically increasing in the interval of interest $[\tau_H^i, \tau_T^{i+1}]$.

During treatment holidays $S(\tau)$ and $A(\tau)$ are monotonically increasing and decreasing, respectively. Therefore it is necessary to limit the holiday period to avoid relapse, i.e. we want to maximise the renormalisation of reactive stroma, while keeping $S(\tau) \leq S_T^i$.

In order to find the time at which relapse occurs, we evaluate S_H^i and A_H^i from Eqs. (7.12) and (7.11), respectively, and substitute in Eq. (7.25) to obtain a new expression for $S(\tau)$ during the treatment holiday:

$$S(\tau) = S_H^i \exp\left[\tau + M^i + L^i\left(1 - \exp\left(\phi(\tau_H^i - \tau)\right)\right)\right], \tag{7.27}$$

having defined the new auxiliary constants

$$L^i = \frac{\gamma}{\phi}\left(1 + \left(A_T^i - 1\right)\exp\left(\theta(\tau_T^i - \tau_H^i)\right)\right), \tag{7.28}$$

and

$$M^i = (C-1)\tau_H^i - C\tau_T^i + B^i\left(1 - \exp\left(\theta(\tau_T^i - \tau_H^i)\right)\right). \tag{7.29}$$

We define τ_R^i as the upper limit on the drug holiday time before relapse, i.e.

$$S(\tau) \leq S_T^i \quad \text{for } \tau \in [\tau_H^i, \tau_R^i]. \tag{7.30}$$

Making use of the *Lambert $\mathcal{W}$ function*, defined as the inverse function of $f(\mathcal{W}) = \mathcal{W}e^{\mathcal{W}}$, it is possible to solve inequality (7.30) defining τ_R^i as:

$$\tau_R^i = -M^i - L^i + \frac{1}{\phi}\mathcal{W}(\phi L^i \exp\left(\phi\left(M^i + L^i + \tau_H^i\right)\right)). \tag{7.31}$$

7.4.3 Treatment Schedule Guidelines for the Well Mixed System

To summarise the previous results, the analysis suggests that:

- If reactive stroma in the tissue is initially below the critical limit ($A_T^i < A_L$), the tumour will respond to the therapy until time τ_m^i. After this point, additional treatment will only worsen the disease because of the substantial stromal activation. It is worth noting that under drug treatment the stroma cell population will grow and reach the critical limit A_L exactly at time τ_m^i. Indeed substituting (7.21) in Eq. (7.11), we obtain:

$$\begin{aligned} A(\tau_m^i) &= 1 + \left(A_T^i - 1\right) \exp\left[\theta\left(\tau_T^i - \left(\tau_T^i - \frac{1}{\theta}\ln\left(\frac{1-\delta+\gamma}{\gamma(1-A_T^i)}\right)\right)\right)\right] = \\ &= 1 + \left(A_T^i - 1\right)\left(\frac{1-\delta+\gamma}{\gamma(1-A_T^i)}\right) = A_L. \end{aligned} \tag{7.32}$$

  Despite τ_m^i representing the maximum time for drug application, and therefore maximum tumour kill, the overall therapy might benefit from stopping treatment before τ_m^i to avoid driving stromal activation to the critical limit. In the following we will explore the strategies that limit the drug application to a percentage of the maximum tumour kill (or alternatively, to a percentage of the maximum stromal activation).

- During a drug holiday the tumour burden will monotonically increase and the reactive stroma population will monotonically decrease. Therefore the only constraint on the duration of the drug holiday is the time at which relapse occurs (Eq. (7.30)). The expression for the time to relapse in Eq. (7.31) is not analytically tractable and as such we are unable to obtain simple parameter-dependent conditions.

In conclusion, the limitation for the length of a pulse of drug is the stromal activation critical limit A_L (corresponding to maximum kill at τ_m^i) whilst the limitation for the length for a drug holiday is relapsing tumour burden S_0. However, a successful therapeutic strategy could benefit from interrupting the drug holiday long before the time of relapse, at the cost of leaving behind some residual reactive stroma. Similarly, interrupting treatment before maximum tumour kill is achieved would limit stromal activation, and could be beneficial to the following rounds of treatment. In this chapter we intend to examine the trade-off between stromal activation during treatment and tumour regrowth during holiday. Specifically, we will explore strategies that interrupt the drug holiday when the tumour reaches a percentage of the relapse size, and interrupt the drug administration when the stroma reaches a percentage of the critical limit. We define two treatment parameters:

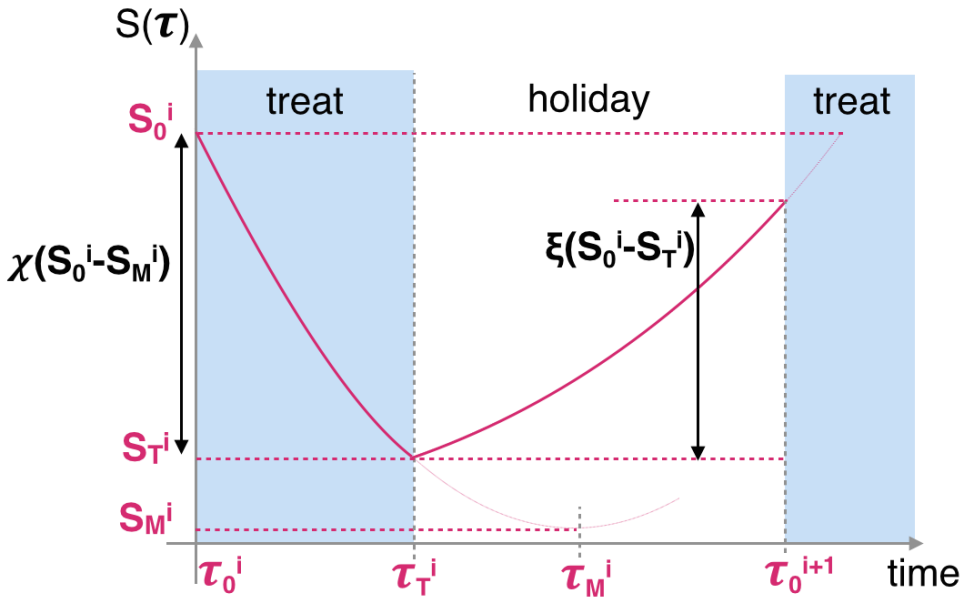


Figure 7.10: *Sketch of treatment outcome following a (χ, ξ) therapeutic strategy. Treatment can reduce tumour burden up to S_m^i (analytical minimum), however, to reduce stromal activation we interrupt the treatment at a fraction χ of the maximum kill. Similarly, in order to limit tumour regrowth, we reintroduce treatment at a fraction ξ of the relapse tumour burden S_0^i.*

χ : percent of maximum tumour burden reduction allowed during drug treatment, i.e.

$$S(\tau) \geq S_0^i - \chi\left(S_0^i - S_m^i\right) \quad \tau \in (\tau_T^i, \tau_H^i]. \tag{7.33}$$

ξ : percent of recurrence allowed during drug holiday, i.e.

$$S(\tau) \leq S_T^i + \xi\left(S_0^i - S_T^i\right) \quad \tau \in (\tau_H^i, \tau_T^{i+1}]. \tag{7.34}$$

Given fixed values for χ and ξ, we will solve the ODEs (7.9) for the time interval when condition (7.33) is met, determining the start of a drug holiday. We will then solve the ODEs (7.10) simulating drug holiday until condition (7.34) is not met anymore, determining the need for the next pulse of therapy. Figure 7.10 provides a visual explanation of the parameters χ and ξ and conditions for therapy decision. The simulation stops when the therapeutic strategy fails, i.e. when neither conditions (7.33) and (7.34) can be satisfied, because excessive stromal activation would require a treatment holiday whereas a large tumour burden requires further treatment. We explore all the possible combinations of these two parameters in the range $(0, 1]$ and measure Progression Free Survival (PFS) time as treatment outcome. PFS is a measure of the success of the treatment often used to assess the outcome of clinical trials. Specifically, it measures the time that the disease, with a given therapy, does not get worse. In Figure 7.11 we report the PFS for strategies allowing therapy pulses killing 10 to 100% of the maximum tumour kill (y axis) and holidays allowing 10 to 100% of relapse of the initial tumour burden (x axis).

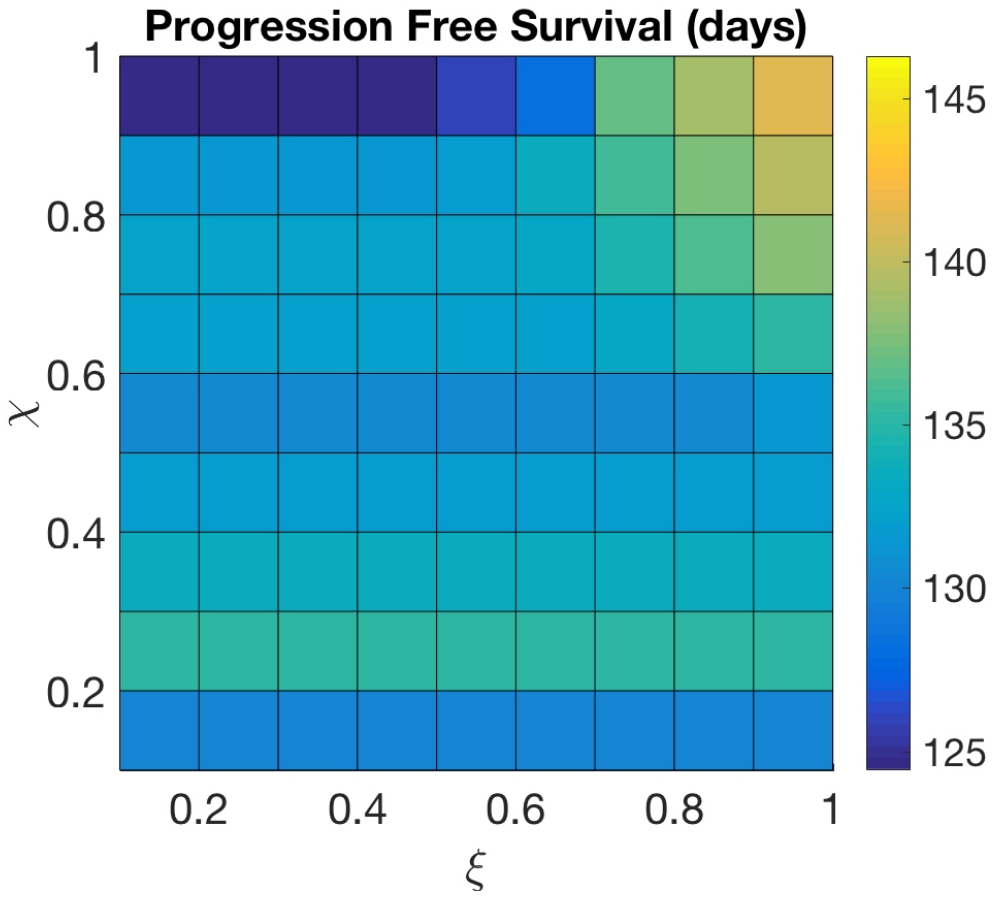


Figure 7.11: *Progression-free survival for strategies of pulsed therapy with varied length of drug treatment and holiday, simulated with ODE model* (7.1).

PFS is calculated from each simulation run as the time at which the tumour returns to its initial size. Results show that for low values of χ (shorter treatment) varying the length of holiday does not affect the PFS because of the poor stromal activation during the pulses of treatment. For higher values of χ, more considerable stromal activation requires longer holiday windows (larger ξ) to increase PFS. Finally, with a fixed low value of ξ, and increasingly larger values of χ, we observe that increasing the length of treatment pulses is initially advantageous. However, beyond 50% of maximum tumour kill, the excessive activation of the stroma and the short holiday strategy penalise the PFS outcome. Overall, the best strategy in terms of PFS is to interrupt treatment when the critical stromal activation limit A_L is reached, and to restart treatment when recurrence occurs.

The algorithm presented here does not have any physical constraints on the minimum time for a switch of strategy. Indeed, in some simulations it switches between treatment and holiday as often as the time step chosen for the numerical discretisation of the ODEs. Such therapeutic strategies cannot be achieved in reality and should therefore not be considered. Furthermore, while the condition for the length of a pulse of treatment is

dictated by the analysis, the condition of the holiday length is loosely related to the worst case scenario, where relapse is allowed in order to favour stromal normalisation.

Despite these shortcomings, the current framework gives analytical guidelines for approaching the problem of treatment scheduling. In the following we will translate these guidelines to the HDC model in a spatially-defined system.

7.5 Mechanisms of Stromal Activation and Renormalisation

We utilise the HDC model (Figure 7.2) to explore possible modalities of drug-dependent stromal activation and renormalisation, in an attempt to address the current gaps in the knowledge of the biological processes. Specifically, we hypothesise the following mechanisms of:

Stromal Activation. A key spatial consideration is the tumour's ability to co-opt the surrounding stroma to create a growth-promoting niche. However, it is unclear if this cross-talk is:

1) limited to the tumour-stroma interface, as in the previous version of the model (see Section 6.5);

2) acts on a larger range, i.e. only condition (*ii*) (Section 6.5) is imposed on phenotypic transitions F to A.

Stromal Deactivation. Two hypotheses could explain the renormalization of this system:

I) when drug concentration falls under the activation threshold h_r, the reactive stroma reverts to a normal phenotype (A to F).

II) the stroma acts in a wound healing, immune response, fashion intervening to rescue the cancer under drug treatment, and dying after fulfilling this role, i.e. A cells undergo stochastic death with probability p_A.

The mechanisms of stroma activation 1 and 2 represent the extreme behaviours that we intend to investigate here. Indeed, in any tumour the complexity of the mechanisms involved in stromal activation cannot be accurately described by any one of these mechanisms alone. For example, a tumour might exhibit an intermediate behaviour, with a range of cross-talk reaching stroma cells within a finite distance, beyond the first line of neighbours.

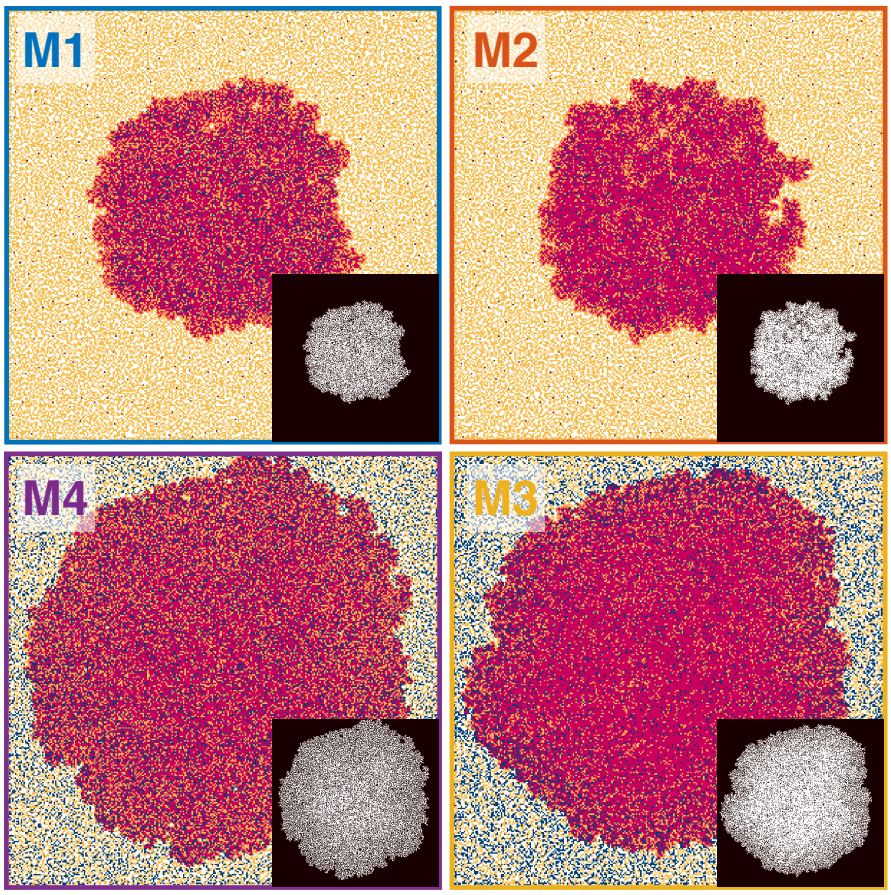


Figure 7.12: *Snapshot of simulations for the HDC model Figure 7.2 with* $\pi = 1$, $p_A = 10\,p_T$, *at day 130. Combinations of mechanisms of stromal activation and normalisation are hypothesised: M1 (1,I), M2 (1,II), M3 (2,II), and M4 (2,I). Lattice colour code:* ***blood vessels***, ***normal stroma cells***, ***reactive stroma cells***, ***non reactive stroma cells***, ***cancer cells***, ***growth-inhibited cancer cells***. *Insets shows proliferation signal, colour map as in previous simulations.*

By combining the hypothesised mechanisms of stromal activation and deactivation we obtain four variations of the model. Sample simulations for each one of the four models (M1 through M4) are run for a metastatic tissue with $\pi = 1$. Treatment is applied at day 0 to a tumour mass previously grown to approximately 10^4 cells (see detailed description in Section 6.8). At day 100 the drug application is interrupted to observe the post-treatment regrowth. Snapshots of the simulations at day 130 are shown in Figure 7.12. The black insets show the distribution of the proliferation signal modulated by tumour and environment. Figure 7.13 shows the temporal dynamics of the four simulations. The most striking difference in the post-treatment regrowth dynamics is in the size of the tumour mass. Mechanism 2 of stromal activation (M3 and M4), consists of long range tumour-stromal cross-talk. Upon drug treatment, reactive stroma appears throughout the domain. As the tumour grows post-treatment, it expands in regions where the stroma

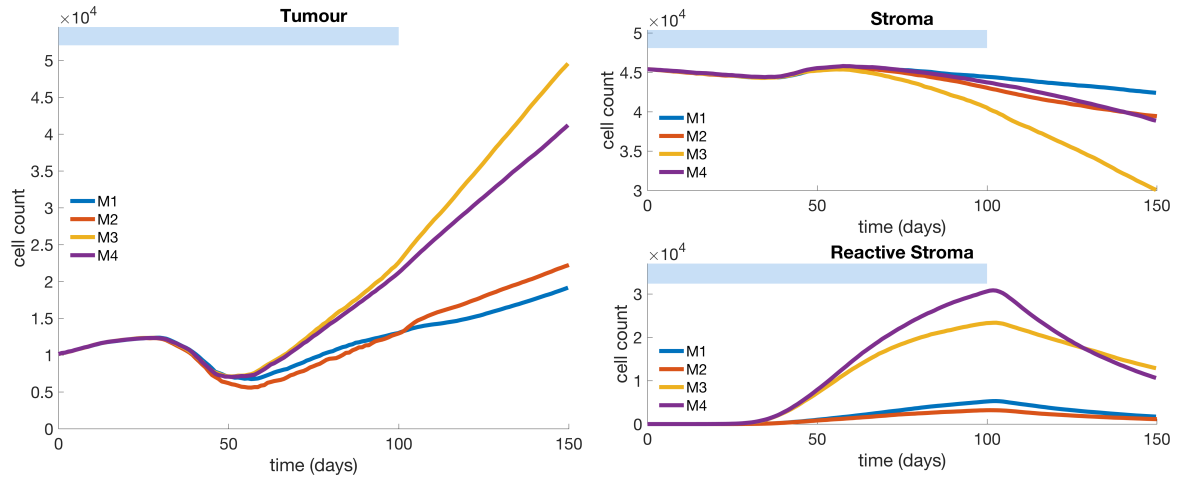


Figure 7.13: *Temporal dynamics for models M1 through M4, presented in 7.12. Plots show evolution of cancer (S), stroma (P+F+A), and reactive stroma (A) cell counts over time. The light blue bar shows the window of time when the inhibitor is being applied.*

is already reactive. The result is a faster growth, when compared to mechanism 1 of stromal activation (M1 and M2), where emergence of reactive stroma is only stimulated upon direct contact of stroma and cancer cells. Additionally, we can observe that in both M1 and M2 the tumour mass appears to be encapsulated in a yellow rim of normal stroma. This is a consequence of the mechanism of stromal activation that requires direct recruitment of stroma by the cancer cells. Therefore, as the cancer grows, additional stromal cells are recruited at the interface in the outward region of expansion.

In these post-treatment snapshots, however, the stroma is undergoing the renormalisation process, and the mass is infiltrated both with normal and reactive stroma cells. The quantitative difference in stromal activation can be observed in the temporal evolution of the A population (Figure 7.13, bottom right). Finally, comparing mechanisms of stromal renormalisation, we can observe that mechanism I (i.e. reversible phenotypic switch) generates spatially mixed distributions of cancer and stromal populations, as opposed to clusters of same cell-type populations obtained with mechanism II (i.e. immune-like stromal response). The spatial segregation, particularly evident in M2, Figure 7.12, is determined by the death of reactive stromal cells, which frees up space within the mass, into which the cancer cells can proliferate. The difference in spatial distribution of the stroma cells infiltrated into the tumour mass (clustered versus homogeneous) is a key qualitative feature that can be tested against experimental observations.

Figure 7.14 shows the same four combinations of stromal activation and renormalisation mechanisms for a tissue with lower stroma reactivity ($\pi = 0.5$), at day 130, after treatment is interrupted. The simulations are initialised with the same distribution of cells previously used, however 50% of stromal cells are randomly assigned phenotype P.

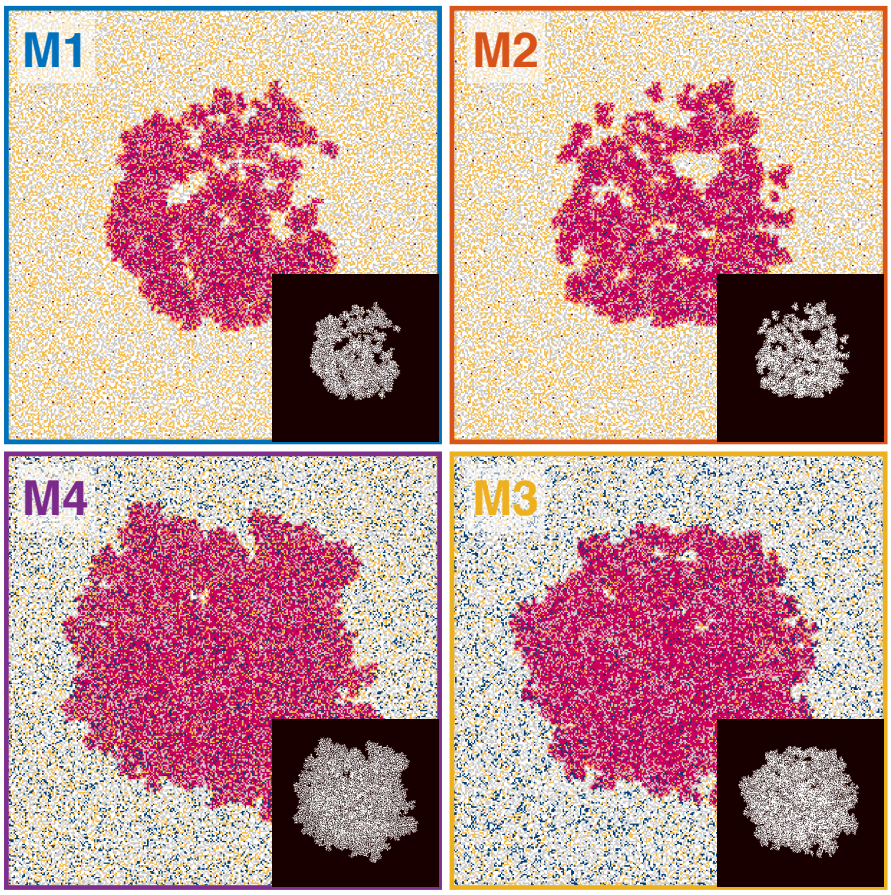


Figure 7.14: *Snapshot of simulations for the HDC model in Figure 7.2, with* $\pi = 0.5$*, at day 130. Combinations of mechanisms of stromal activation and normalisation are hypothesised: M1 (1,I), M2 (1,II), M3 (2,II), and M4 (2,I). Treatment schedule, lattice and proliferative signal colour map as in previous simulations.*

Since the source of stromal protection (F) is more sparse, clustering effects are more evident when compared to tissues with $\pi = 1$. The only striking difference across the four simulations is the speed of expansion of the tumour mass post-treatment. The biggest mass is obtained with M4, as long-range stromal activation (mechanism 2) and reversion of A into F (mechanism I) maintain the highest pool of stroma cells (compared to other mechanisms, see Figure 7.15 bottom right), that, in turn, promote additional growth. While the cancers in the snapshots shown for M1 and M2 appear more fragmented than the others, observing the full course of the simulation, we can predict that the fragmented masses will grow to a compact mass similar to the ones in M3 and M4. Therefore, in the case of a moderately reactive tissue ($\pi = 0.5$), the four mechanisms considered give the same qualitative growth dynamics.

Ultimately, the qualitative outcome of the hypothesised mechanisms is remarkably different in the case of a highly reactive tissue ($\pi = 1$) but similar in the case of a less reactive one ($\pi = 0.5$). The main qualitative difference observable in the spatial configu-

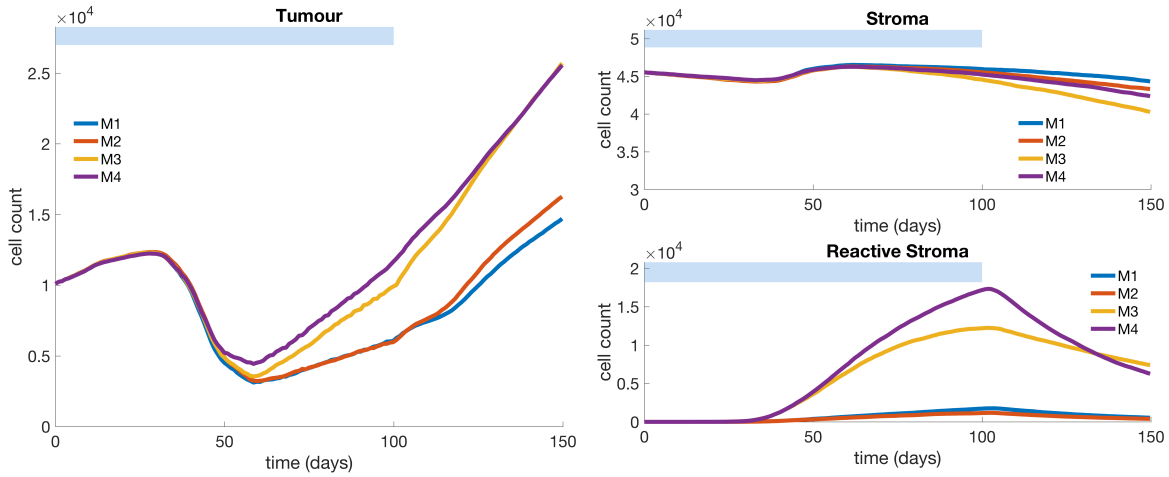


Figure 7.15: *Temporal dynamics for models M1 through M4, presented in 7.14. Plots show evolution of cancer (S), stroma (P+F+A), and reactive stroma (A) cell counts over time.*

ration concerns the clustering of same-type cells as opposed to an homogeneously mixed distribution of cancer and stromal cells. The analytical treatment guidelines obtained with the multi-model approach (Section 7.4) have to be carefully reconsidered in the light of the current results. Since the analysis is based on the assumption of a well mixed system, the results will not be valid in the case of significant phenotypic clustering (e.g. M2 in a highly reactive tissue). The problem of validity of mean-field approximation of individual-based models with respect to clustering and spatial configurations has been addressed extensively by Markham (2014).

In the following, we will adopt model M2, including short-range stromal activation (mechanism 1) and immune-like stromal response (mechanism II). This model, in agreement with the experimental collaborators, appears to be the most realistic up to a qualitative comparison of the outcome.

7.6 Systemic Treatment of Multiple Metastases. Addressing Inter-site Heterogeneity

Finally, we consider an important aspect of heterogeneity, in the context of metastatic disease, where each metastatic site may be characterised by a different stromal composition. Often times, localised treatement is not an option (see, for example, patient in Figure 2.1) and a systemic treatment is necessary. Inter-site heterogeneity must be taken into account when designing such treatment, as the same dosing and schedule might benefit one site while worsening another.

Here we specifically focus on the dynamics of EMDR, and make use of the HDC setup presented in Figure 7.2, and model M2 to determine the effect of a single therapeutic

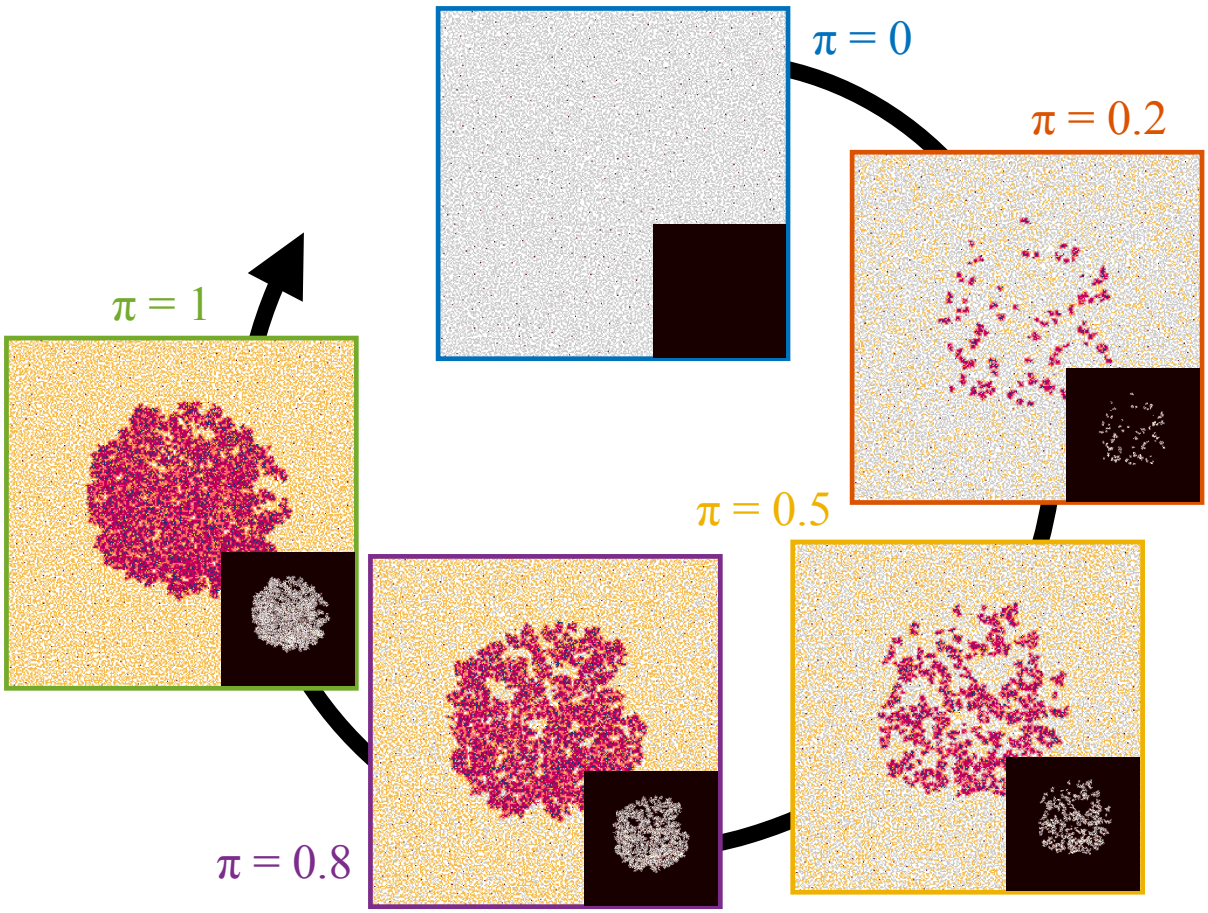


Figure 7.16: *Snapshot of simulations for the HDC model in Figure 7.2, model M2 and varied π at day 110. Treatment schedule, lattice and proliferative signal colour map as in previous simulations.*

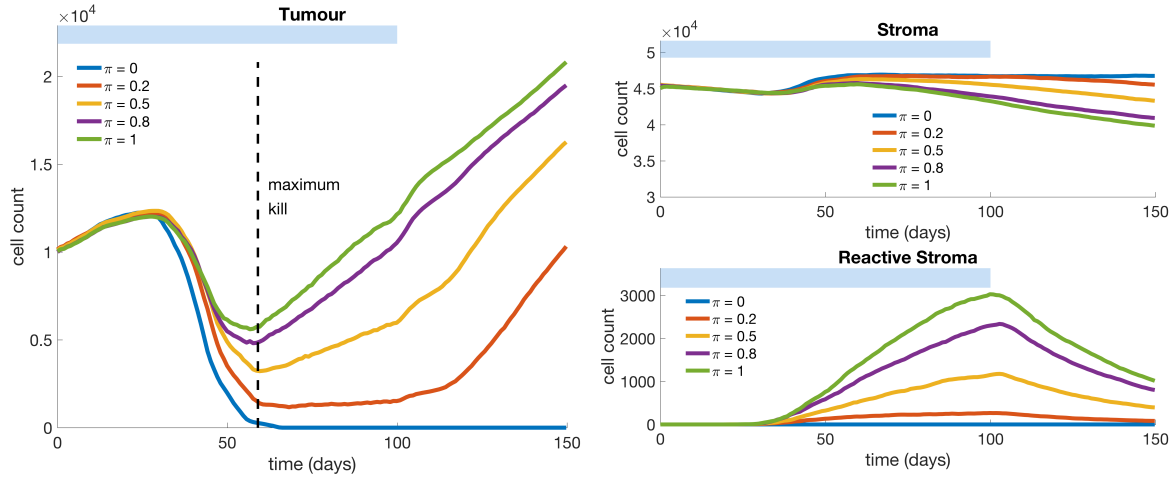


Figure 7.17: *Temporal dynamics for models M2, presented in 7.16. Plots show evolution of cancer (S), stroma (P+F+A), and reactive stroma (A) cell counts over time.*

strategy on a set of tissues, characterised by a different stromal composition π. In Figure 7.16 we can compare the response of the various sites, characterised by different fibroblast

prevalence, to the same 100 days treatment. For simplicity we consider metastases of similar size (approximately 10^4 cells). The treatment leads to full eradication in the tissue with no stromal reactivity ($\pi = 0$), and is less successful for increasing levels of π. For sites with lower fibroblast prevalence (e.g. $\pi = 0.2$), the resulting cancer population is spatially fragmented, which may make it easier to target with additional treatment (e.g. chemotherapy). However, such fragmented masses may not be visible on clinical imaging and therefore give the false appearance of being eradicated. In sites with higher fibroblast prevalence (e.g. $\pi = 1$) the cancer population is barely depleted and the tumour grows back as a compact mass. This configuration leads to a higher build up of proliferative signal (compare insets for $\pi = 0.2$ and $\pi = 1$), a bad prognostic of treatment outcome. Figure 7.17 shows the temporal evolution of the cancer and stroma populations. We notice that the maximum kill before onset of EMDR appears at approximately the same time for all tissues. This may be an important prediction if we want to design a systemic treatment for a patient with disseminated disease modulated by a heterogeneous stromal composition across organ sites. We can apply the principles of an *adaptive therapy* (Enriquez-Navas et al., 2016) to adaptively adjust treatment schedule, based on the current evolution of the cancer. Specifically, we monitor the course of the tumour burden, indicative of the onset of EMDR, and interrupt the treatment when the tumour starts growing back (past the minimum value of tumour burden). Since the maximum tumour kill is achieved at approximately the same time across tissues, we repeatedly apply this adaptive strategy to design a treatment schedule tailored to a set of metastatic tissues. Figure 7.19 shows the outcome for a sample run of the adaptive algorithm. As previously predicted, the tumour burden in the tissue with low stromal composition ($\pi = 0.2$) can be kept in check for longer times, while the other tumours grow back aggressively (compare curves at day 150). Figure 7.18 shows the spatial distribution of the tumours at day 200, during the third pulse of treatment. The intermittent treatment schedule determines a much different tumour composition, when compared to continuous treatment (e.g. compare $\pi = 1$ in Figures 7.16 and 7.18). The local modulation of the proliferative signal by autocrine signalling, stromal reactivity, and drug diffusion, determines pockets of growth-inhibited cancer cells. This configuration is beneficial for the overall success of the treatment, and preferable to a sharp modulation of the proliferative signalling causing more cell death, hence free space, as well as additional stromal reactivity. This simulation is an example of a control treatment schedule. However, this schedule is far from optimal. A rigorous protocol to design an optimal treatment strategy would require a more sophisticated algorithm to pick up minima among stochastic fluctuations of the populations, to determine the exact times t_H^i when the treatment should be interrupted.

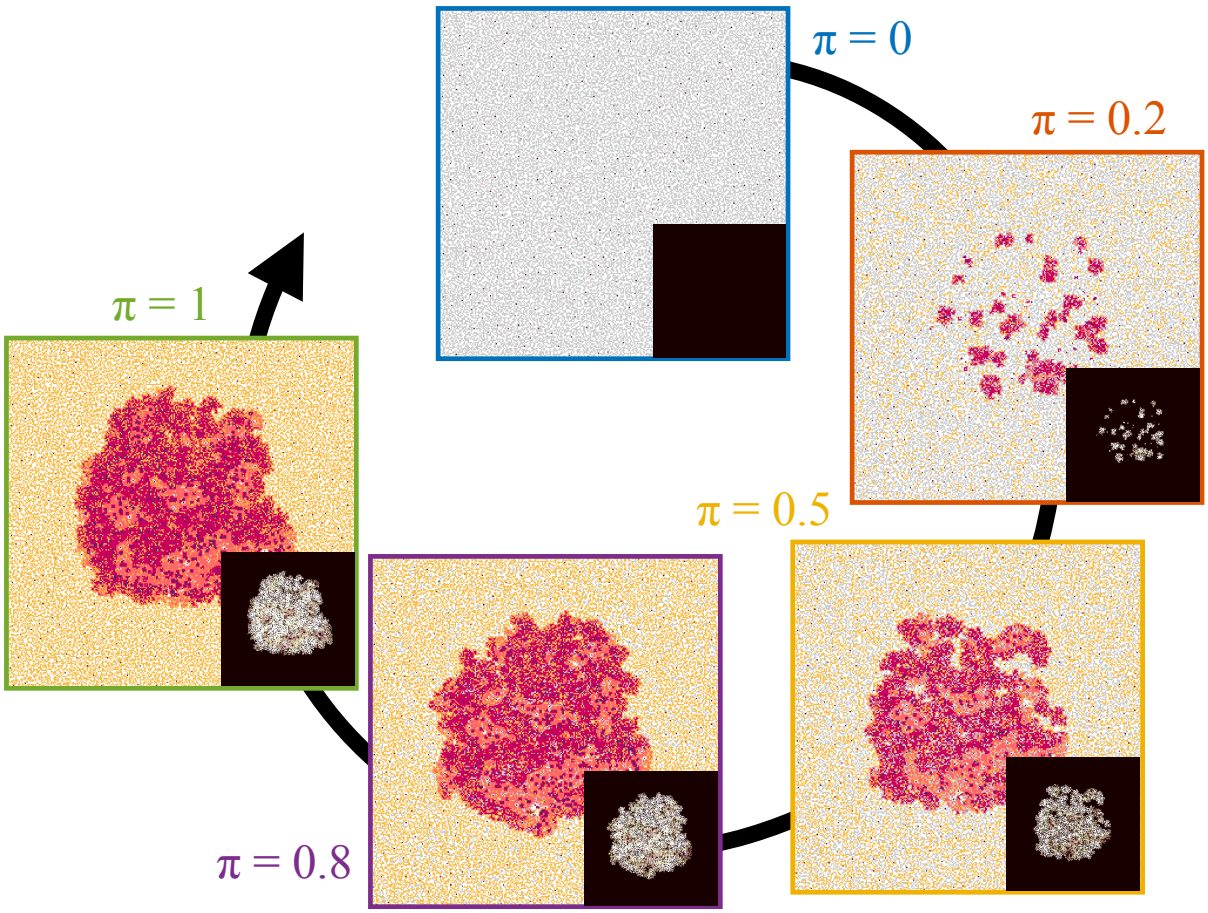


Figure 7.18: *Snapshot of simulations for the HDC model in Figure 7.2, model M2 and varied π at day 200. Intermittent treatment schedule. Lattice and proliferative signal colour map as in previous simulations.*

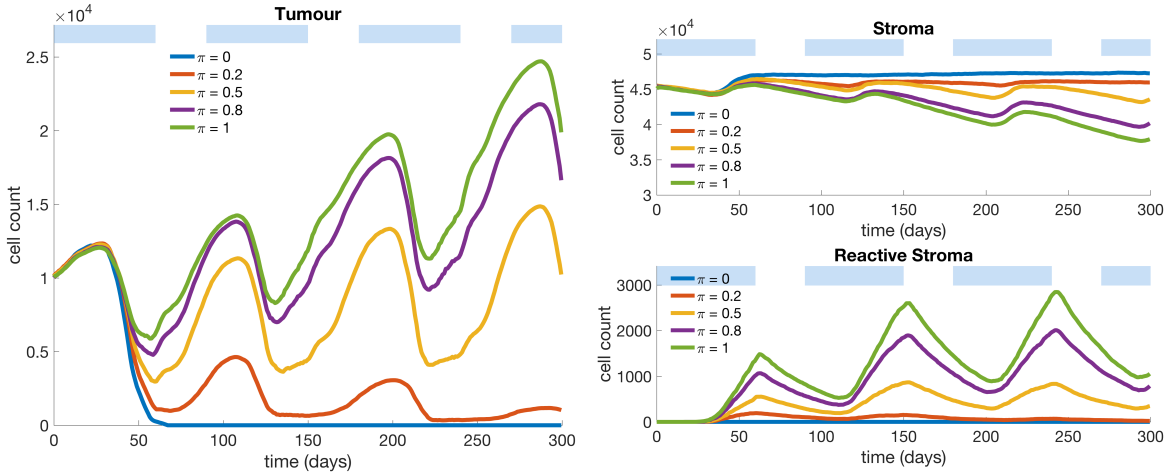


Figure 7.19: *Temporal dynamics for the model M2, presented in 7.18. Intermittent treatment schedule. Plots show evolution of cancer (S), stroma (P+F+A), and reactive stroma (A) cell counts over time.*

Finally, a necessary step toward the integration of the analytical results previously obtained, and a clinically relevant application of this framework, is model calibration through experimental observation. Comparing the temporal evolution of tumour and reactive stroma (Figure 7.19), we can identify the stochastic counterpart of A_L, the critical limit of stromal activation identified in the analysis (see Eq.(7.32)), corresponding to the point of minimum tumour burden under continuous treatment. However, integrating this analytical result to guide the design of treatment schedules via stochastic simulations, requires experimental quantification of the rates of stromal activation and renormalisation θ and ϕ. Currently these quantities are difficult, if not impossible, to obtain *in vivo* or in patients.

7.7 Combination of Targeted Inhibitors

Most of molecularly targeted cancers are characterised by heterogeneity in terms of driving mutations. Often a single tumour has multiple different mutations, for example EGFR and KRAS mutations can appear simultaneously in non-small-cell lung cancer. In this case each subpopulation within the cancer has to be targeted with the appropriate inhibitor (Stella et al., 2012). In other instances, a new mutation arises in an alternative pathway to circumvent the mutation initially being targeted by the therapy. For example, BRAF mutated melanoma can respond to BRAF inhibition with upregulation of downstream kinases that contribute to the proliferative signalling. In this case the preferred strategy is to target simultaneously key hubs in the network regulating the proliferative activity (Smalley, 2010).

In general all of these mutations, regardless of their nature or the sequentiality with which they appear, cause uncontrolled proliferation and tumourigenesis and the current clinical practice calls for the combination or sequence of several targeted inhibitors. A logical extension of our modelling framework would be to consider combinations of targeted therapies. When designing the most effective treatment strategy, the choice of drug sequence will further add to the problem of schedule optimisation we previously tackled. Therefore, in the following we will consider the case of combination therapy only at an introductory level, with the sole scope of presenting a simple extension of our framework to the multi-drug scenario. Many examples of mathematical modelling of combination therapy can be found in the literature. The most relevant to our application is the work by Bozic and colleagues studying the evolutionary dynamics of molecularly targeted solid tumours as a multitype branching process (Bozic et al., 2013).

We consider the case of non-small-cell lung cancer, simultaneously targeted with EGFR and MEK inhibitors. Within the HDC framework these two inhibitors are mod-

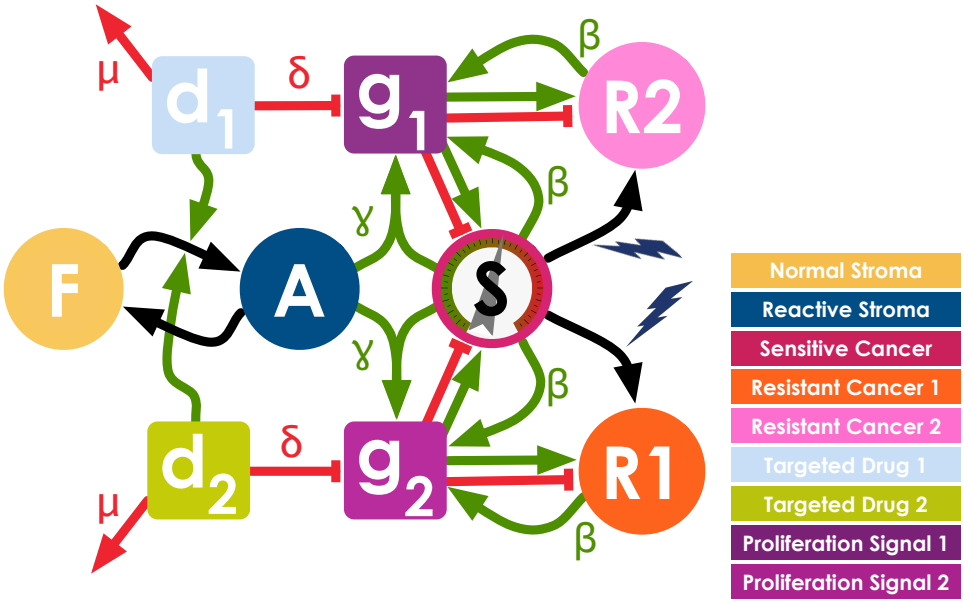


Figure 7.20: *An extension of the HDC model to the combination of two targeted inhibitors (d_1 and d_2). Green arrows indicate promotion, red arrows indicate negative interactions, black arrows indicate phenotypic transitions. The dial represents the viability of cancer cells, modulated by the proliferation signals g_1 and g_2. Two resistant cell types can arise following stochastic mutational events (lightning bolt). The complexity of the model and its dynamics is considerably increased.*

elled as continuous variables, functions of both space and time: $d_1 = d_1(\mathbf{x}, t)$ and $d_2 = d_2(\mathbf{x}, t)$. Similarly, the corresponding proliferation signalling molecules upon which these two drugs act are $g_1 = g_1(\mathbf{x}, t)$ and $g_2 = g_2(\mathbf{x}, t)$. We distill the heterogeneity of this cancer into three cell types:

S: sensitive cancer cell, requiring sufficient concentration of both g_1 and g_2 to maintain a proliferative state;

R1: cancer cell resistant to d_1, i.e. not susceptible to variations in the concentration of g_1. Only g_2 will determine its viability;

R2: cancer cell resistant to d_2, i.e. not susceptible to variations in the concentration of g_2. Only g_1 will determine its viability.

We do not consider double resistance because, in principle, the presence of a fully resistant phenotype would require the introduction of a third drug targeting such mutation. Additionally, in the case of NSCLC, concurrent EGFR/RAS mutations are extremely rare, since it is evolutionary and energetically unfavourable to develop more than one mutation that allows uncontrolled proliferation (Benesova et al. 2010). The interaction networks represented in Figure 7.20 are a symmetric extension of the single inhibitor

case. Each inhibitor concurrently degrades the corresponding proliferation signal and stimulates the activation of the stroma. The reactive stroma increases the local production of proliferation signal to rescue the cancer cells from cell death or growth inhibition. The viability of each cancer cell is determined according to its sensitivity phenotype. The setup described for the case of single inhibitor (parameter values, initial conditions, individual-based rules) is utilised in this extension of the model. The mutant cell types $R1$ and $R2$ are introduced as a stochastic event with probabilities p_1 and p_2, respectively, during any mitotic event of an S cell. Figure 7.21 shows sample simulations for treatment with the two inhibitors either as single agents (second and third row), or in combination (fourth row). In order to highlight the effect of EMDR, we run the same set of simulations where no F to A transition is allowed hence silencing EMDR. The snapshots showing the temporal evolution of the tumour mass can be compared with the untreated case (first row). Comparing the case where EMDR is simulated with the case where the stromal activation is silenced, we observe that the cooperative action of the stroma is necessary to drive the disease progression after the initial response to therapy. The last simulation shows that, unless EMDR is somehow targeted and kept in check, double targeting of the two tumour proliferative pathways results in strong selection for a resistant population. Having the therapy eradicate the targetable portion of the tumour, the leftover population is given a growth advantage in terms of space availability and will eventually colonise the entire tissue.

7.8 Conclusions

A key feature of the HDC approach is its ability to couple discrete and continuous variables, by integrating tumour, stromal and vascular cell types with proliferation signal and drug concentration. In Chapter 6 we were able to initially define a disease-free tissue that was both homeostatic and robust (Section 6.7). Disruption of this homeostatic tissue was then used to simulate a metastatic event, i.e. seeding a single tumour cell extravasating into the homeostatic tissue (Section 6.8). Having calibrated the model with these simple applications, we then made use of the framework to simulate treatment with a targeted inhibitor. In this chapter we considered a range of treatment strategies in order to gain an initial understanding of the role of the reactive stroma in facilitating therapeutic escape, i.e. the role of EMDR.

Despite this model being an accurate representation of the mechanisms and dynamics occurring at the single-cell-scale, it is severely limiting when trying to design an optimal, parameter-dependent (hence patient-specific) therapeutic strategy, due to its computationally intensive nature. Therefore we developed a simplified ODE model approximating

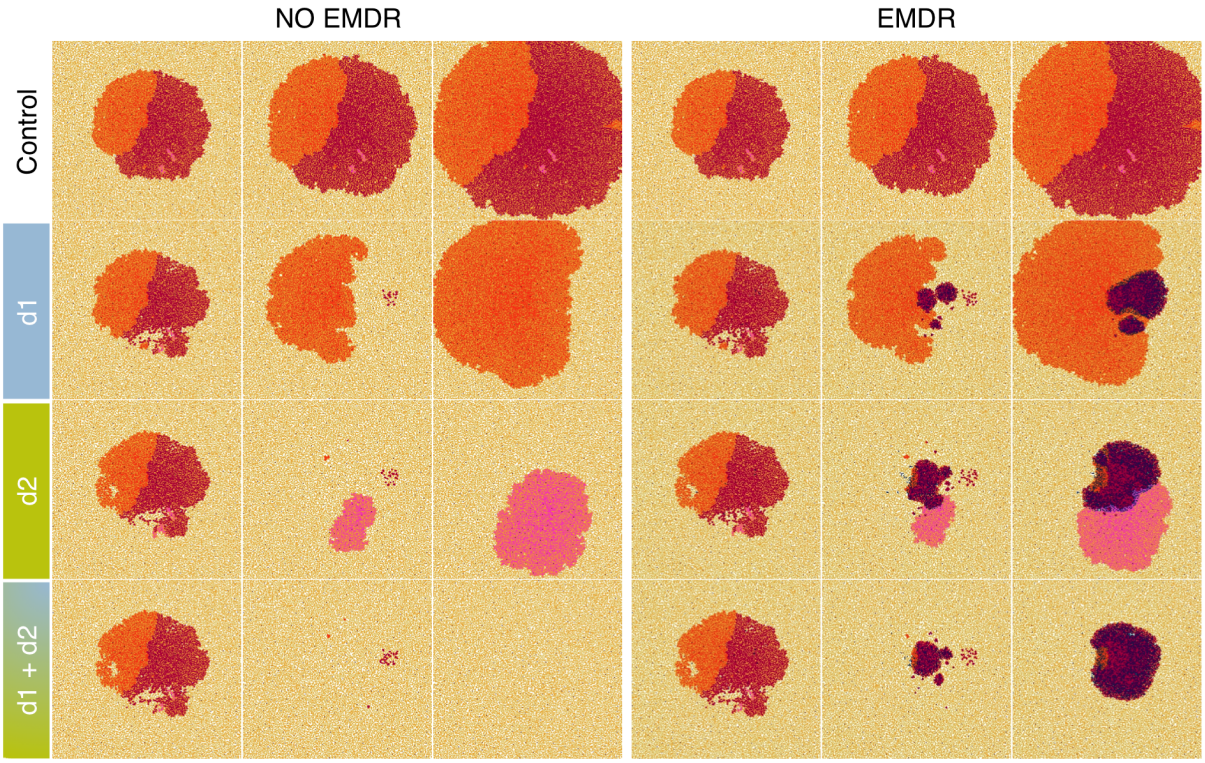


Figure 7.21: *Time evolution of tumour response to continuous treatment with targeted inhibitors as monotherapies (d1 and d2 rows) or combination therapies (d1 + d2 row), compared to the untreated case (control row). The tumour to be treated is grown for 110 days from a metastatic event, with stochastic mutations that transform* ***cancer cells*** *to* ***type 1 resistant cancer cells*** *or* ***type 2 resistant cancer cells****. In this simulation an R1 mutation appeared early enough to be able to expand, while and R2 mutation appeared in a spatially constricted region, forming a pocket within the tumour mass. The simplistic mutational theory (NO EMDR column) predicts complete response, provided that all existing mutations are targeted. If we introduce the mechanisms of stromal cooperation (EMDR column) we can show the initial response followed by progression driven by stromal activation.*

the HDC model (Section 7.4). This ODE model, being analytically tractable, can more readily be used to extract optimal therapeutic schedules and subsequently more easily inform the HDC model.

We addressed the problem of inter-tumour heterogeneity, specifically designing a systemic treatment for a patient with a distribution of metastases characterised by different stromal composition (Section 7.6). In the stochastic simulations of the HDC model, the tumour burden follows the same monotonicity regime predicted by the analysis of the ODE approximation. Additionally, the minimum value of tumour burden across metastatic sites is reached at approximately the same time. We exploited this result to build an adaptive treatment schedule that interrupts drug administration when EMDR sets in and the tumour burden starts growing. In a clinically realistic setting monitoring the trend of a patient's tumour size would allow us to adjust the prediction to simulate

the next window of treatment and adjust the treatment schedule. As previously observed, control of disease burden, rather than complete eradication, is becoming a more feasible option when designing treatment strategies.

The HDC model was used in several other applications, to simulate combination of multiple targeted inhibitors (Section 7.7), and as an hypothesis-testing framework, to discriminate between possible mechanisms of stromal activation and deactivation (Section 7.5). Throughout these applications, and consistent with the ODE models presented in Chapters 4 and 5, the biggest challenge is quantification of timescales of stromal activation and renormalisation that, to the best of our knowledge, cannot be easily obtained experimentally or clinically.

Overall our simulations suggest that the simplistic vision of cancer as a genetic disease, which can be eliminated by targeting all the mutants present, cannot explain the progression and relapse of the disease in the majority of patients. However, if we integrate the role of the environment as a modulator of the dynamics of response to treatment, we can capture mechanisms of transient resistance that we can harness to design better therapies that more realistically control the cancer rather than try to cure it. For instance, integrating treatments that target stromal processes (such as the FAK inhibitor presented in Chapter 5) will result in a faster stromal renormalisation and better control of EMDR.

Chapter 8

Conclusion

In this project we aimed to investigate the dynamics driving the emergence of drug resistance in the context of the interactions between the tumour and its environment (EMDR). We focussed our study on oncogene addicted tumours, such as non-small-cell lung cancer and malignant melanoma at the aggressive metastatic stage, which are molecularly targetable with specific inhibitors. This is a multiscale problem, for which several approaches are available on both the experimental and mathematical modelling fronts. Our integrative approach involves developing theoretical models that allow hypothesis testing and generation via direct comparison with *in vitro* and *in vivo* experimental observations. Understanding how drug resistance emerges will allow us to develop smarter treatment strategies that incorporate tumour-stromal interactions, rather than ignore them.

In Chapter 2 we introduced the relevant biological background, highlighting the current knowledge and open questions in the study of EMDR and molecularly targeted tumours. We presented the state of the art in the treatment of metastatic melanoma and non-small-cell lung cancer, and the problem of treatment failure and disease recurrence. In Chapter 3 we reviewed the relevant mathematical literature, summarising representative mathematical and computational models for the different aspects of the disease, including growth, response to treatment, resistance, and interactions with the tumour microenvironment.

In the subsequent chapters we presented a suite of models that address different aspects of the overarching problem: tumour-stroma interactions and drug resistance in the context of targeted therapy. For each specific application the mathematical model most suitable to represent the biological reality was chosen based on the experimental data available, and the validity of its assumptions.

In Chapter 4 we proposed a deterministic approach to the dynamics of BRAF-wildtype melanoma cell lines treated *in vitro*. Using the law of mass action, we built a system of nonlinear ODEs describing the population dynamics of melanoma cells under the application of different therapeutic strategies. The therapies tested include a cytotoxic drug,

which kills proliferating cells, and a cytostatic drug, which inhibits cell cycle progression, without killing the cells. This spatially averaged formulation allowed straightforward comparison with the experimental data available. We explored a suite of parameter estimation techniques, including approximate Bayesian computation, Markov Chain Monte Carlo, and a standard Matlab routine, allowing us to calibrate the ODE model with experimental data and to reproduce the dynamics observed in the clinic, such as the flare response.

In Chapter 5 we adapted the ODE model to describe EMDR in BRAF-mutated melanoma when treated with inhibitors targeting processes both in the tumour and in the stroma. The resulting system of ODEs described the evolution of four populations (sensitive and resistant tumour, normal and reactive stroma) under any given treatment. The experimental data available included observations of growth and treatment response dynamics of two cell lines, both *in vitro* and *in vivo*. Our model was able to capture the different time scales and growth regimes characteristic of the two experimental models. In fact, this new modelling framework was able to bridge between the experimental scales, in order to integrate relevant information from each of them, and identify the relative contribution of the environment to drug resistance. We applied approximate Bayesian computation to calibrate tumour- and stroma-specific parameters for each experimental replicate. This analysis revealed heterogeneity in both the local tissue carrying capacity and in the stromal promotion of tumour growth. This highlighted the importance of mouse-specific model parameterisation, in order to accurately capture treatment response dynamics. In turn, this inter-mouse heterogeneity emphasises the need to consider individual patients in the same way - there is no single parameter set that fits all tumours. Finally, our model allowed us to explore intermittent treatment strategies that exploit the transient nature of EMDR. Combining drugs that target both tumour and stromal processes, we were able to make treatment recommendations that limit the emergence of EMDR and delay the recurrence of the disease.

These spatially-averaged models are well-suited for capturing the whole population dynamics and quantifying the effects of treatment or stromal interactions on the growth dynamics of the tumour under homogeneous conditions. However, most tumours are characterised by a large degree of spatial heterogeneity, where local gradients (e.g. nutrients and drugs) and local interactions are key in determining the dynamics at the macroscale. We therefore turned our attention to more spatially explicit models.

In Chapter 6 we focused on the interactions occurring at the single cell scale and between cell types, using the hybrid discrete-continuum (HDC) approach. The HDC approach is ideal for introducing spatial features and for describing the local interactions, which are crucial in the feedback between the tumour and its environment, that

characterises EMDR. Specifically, a stochastic individual-based model for the single cell dynamics is coupled to a set of PDEs that describe, phenomenologically, the spatial and temporal evolution of proliferative signalling and drug concentrations. This spatial stochastic model recapitulated a range of dynamics, including normal tissue homeostasis and metastatic growth.

In Chapter 7 we presented applications of the HDC model to key biological and clinical open questions. We used the model as an hypothesis testing tool to explore a range of possible mechanisms of stromal activation and renormalisation that can explain the experimental observations. Additionally, we investigated the effect of systemic treatment on a distribution of metastases characterised by different stromal composition. We simulated a variety of treatment strategies, where the targeted inhibitor is administered in pulses, to allow stromal renormalisation during drug holidays. Despite this model representing a more realistic description of the tumour-stroma dynamics, its complexity limited our ability to design an optimal treatment strategy. Therefore, we introduced a mean-field approximation of the stochastic model, obtaining a deterministic ODE, which, while simplified, was able to capture the trade-off between tumour kill and stromal activation during treatment, and, more importantly, is analytically tractable. From the analysis of the resulting model we obtained analytical guidelines for an effective treatment schedule, including maximum length of drug application and drug holiday. The outcome of this schedule optimisation depends on model parameterisation. Therefore, translating this to a clinically relevant scenario requires patient-specific measurements. We found that treatment outcome is dependent on the time scales of stromal activation and tumour growth, which dictate the length of drug pulses or drug holidays, and eventually determine the failure or success of the strategy.

In summary, different modelling frameworks were adopted, depending upon the specific question being asked. Figure 8.1 summarises the workflow that brings together the pieces of the integrative modelling presented in this thesis. The deterministic ODE models provide a description of the dynamics at the population level (Figure 8.1(a)). Not only did they allow quantification of tumour growth dynamics and stromal heterogeneity, but they could also bridge experimental scales, unpicking the relative contributions of intrinsic versus environmental resistance (Figure 8.1(b)). The deterministic interactions hypothesised in the ODE model informed a spatially-resolved individual cell-based description of the system (Figure 8.1(c)). Despite the lack of relevant experimental data, stochastic simulations allowed us to gain insight into the complexity of tumour-stroma interactions in the context of EMDR. This model can be used to describe metastatic disease, characterised by heterogeneity of tissue composition across distinct metastatic

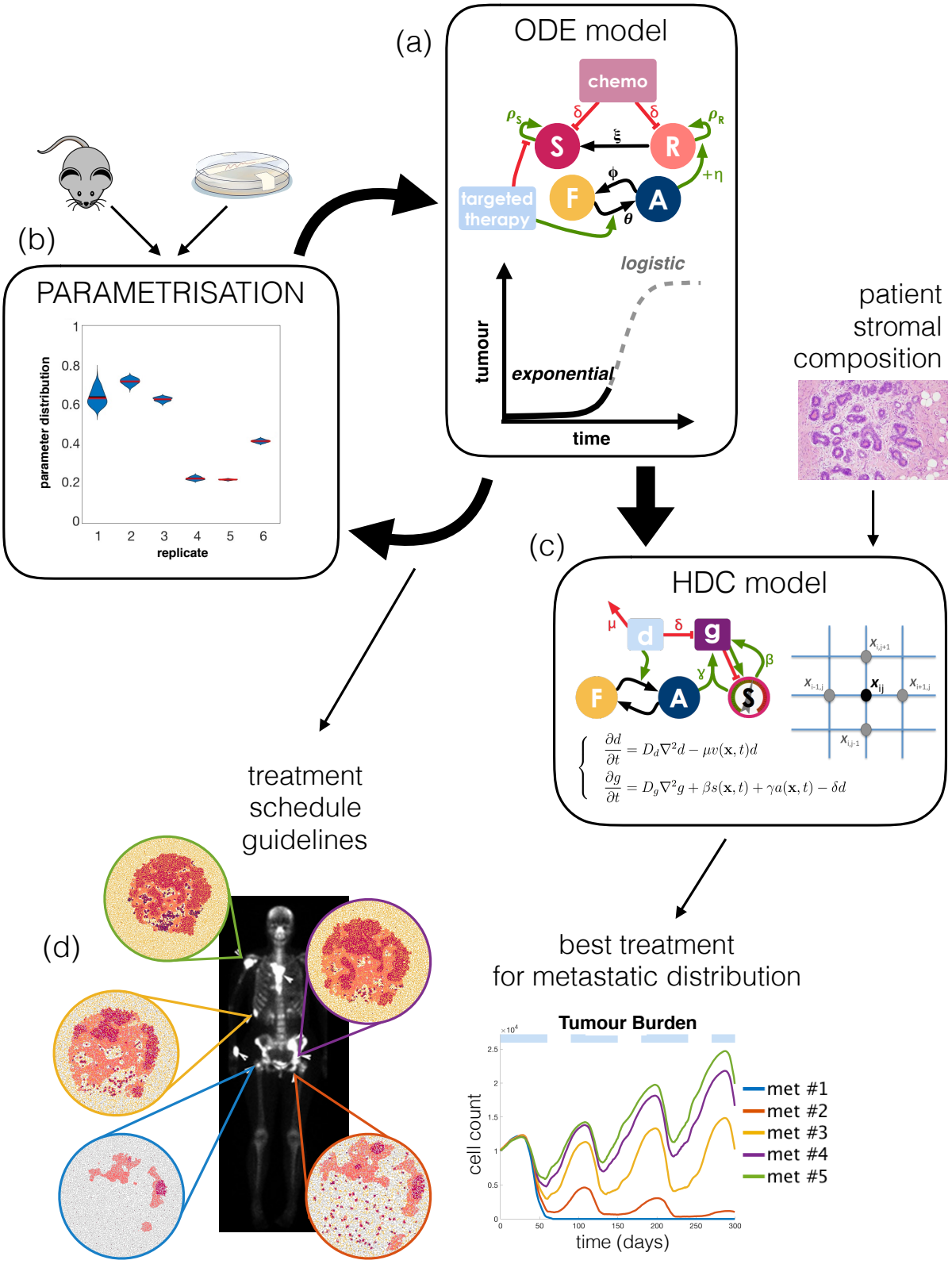


Figure 8.1: *Conceptual map of modelling framework. See text for details.*

sites. Finally, stochastic simulations can be used to design an adaptive systemic treatment aiming at the minimisation of tumour burden and overall control of growth across metastatic sites (Figure 8.1(d)). All in all, this framework allows us to quantify and exploit tumour-stromal interactions systemically, in order to design more effective and longer lasting therapeutic strategies.

This work has been focused on integrating experimental data and mathematical models to better understand two crucial aspects of drug resistance in cancer: the contribution of the stroma in the emergence of environment-mediated drug resistance (EMDR), and the role of intra- and inter-tumour heterogeneity as a predictor of treatment outcome and prognosis. Models that exploit the transient nature of EMDR must rely on patient-calibrated dynamics in order to propose effective and improved treatment strategies.

This work highlights the important role of modelling in cancer research and, more broadly, quantitative biology. It shows how mathematical and computational approaches can be used to make testable predictions and answer pressing questions in biology. Specifically, the modelling frameworks presented in this application bridge the divide between experimental models carried out in a simple homogeneous environment and the complex heterogeneity of the human system. Finally, given its intuitive visual representation, the individual-based model facilitates natural communication between mathematicians and experimentalists and can be used to guide and facilitate novel experimental studies.

8.1 Future Directions

Each step in the development of the proposed pipeline for the design of an optimal treatment strategy can be the object of refinement, as discussed in the relevant chapters. As combination therapy is currently the preferred strategy in clinics, our model should be extended to include multiple drugs targeting different processes in the heterogeneous cancer. As shown in Section 7.7, the extension of the model to account for additional drugs and mutational pathways is straightforward. An equally immediate extension of this work can be achieved once experimental quantification of stromal activation and deactivation time scales is available. These quantities can be used to calibrate the analytical scheduling times found in Section 7.4. Consequently, the ABC parameter fitting technique developed in Section 4.5.2 can be applied to the HDC model to find the parameter values that match the temporal population dynamics ($S(t)$ in the ODE approximation, and cell count in the HDC model).

Furthermore, as highlighted in Chapter 5, a more exhaustive, although computationally expensive, exploration of treatment strategies is necessary. The HDC modelling framework introduced in this thesis leaves many questions unanswered. Some examples

are: model identifiability, parameter sensitivity, optimisation. These are less straightforward steps in the future development of this work. These problems have been addressed for much simplified models (e.g. linear, spatially averaged). However, in the context of stochastic and spatially defined models, they remain a mostly unexplored avenue of research, and we have to resort to model simplification, sacrificing the complexity that characterises the individual-based model. While we have investigated these issues in the context of cancer biology, they are relevant to the whole area of modelling in mathematical biology, especially as we are now beginning to obtain spatiotemporally resolved data.

Over the course of my thesis it has become clear to me that mathematical modelling is not only important in describing cancer, but required in its treatment. The more we learn about this complex evolving spatially and temporally dynamic system, the more the need to integrate this understanding increases. This is especially true in the emerging field of EMDR research, where treatment responses are implicitly difficult to separate in terms of tumour- versus environment-centric mechanisms. Slowly, but surely, experimental approaches are emerging that allow for more detailed characterisation of the microenvironment in and around the tumour. However, much of this work is *in vivo* and there are limited clinical equivalents. Thus, a pressing avenue of future research is how we can connect *in vitro* and *in vivo* results with clinical ones - how do tumour growth kinetics, vascular, immune, and stromal features change when we move from mouse to human?

Within this thesis we explored three modelling paradigms - ODEs, PDEs and individual-based - each representing a different level of granularity. While the latter is the most faithful to the biology, it is the least tractable to study with the tools that we presently have. Therefore an open question in the general area of modelling is how to derive ODE and PDE descriptions from discrete-based models and under which conditions are they valid. This question is of central importance to the advancement of the field.

Appendix A

Minimisation Problem and the Matlab Routine *fmincon*

Let

- ς be the parameter to be estimated, taking values in $\Sigma \subset \mathbb{R}$.
- $\tilde{\mathbf{p}} = \tilde{\mathbf{p}}(\varsigma)$ be the vector of the fitted curve values at the 4 time points (time = 4 days, 6 days, 8 days, 16 days), with the estimated parameter value ς.
- $\mathbf{p}_i$ be the vector of cell count for the i^{th} replica of the given experiment ($T1, T2 \ldots,$ $T12$), with $1 \leq i \leq 3$.

The quantity we wish to minimise is the sum of the square distances of the fitted curve with each replica of the same experiment, i.e.:

$$\min_{\varsigma \in \Sigma} \left(\sum_{i=1}^{3} \|\tilde{\mathbf{p}} - \mathbf{p}_i\|_2^2 \right), \tag{A.1}$$

The *fmincon* routine is part of the Matlab Optimization Toolbox. It can be used to find the minimum of nonlinear multivariable functions subject to constraints. Its inputs are:

- the function itself (such as the quantity in eq (A.1)),
- an initial guess of the variables ($\{\varsigma, S_0, R_0\}$ in the present application),
- constraint parameters, such as upper or lower bounds for parameters, and linear equalities or inequalities that the minimising variables have to respect,
- tolerance parameters on variables, function value and contraint violation.

fmincon uses a Sequential Quadratic Programming algorithm (SQP), which splits the job into subproblems at each iteration. This algorithm approximates Newton's method, a hill-climbing optimisation technique that considers gradient and curvature to efficiently search

the variable space. In the SQP algorithm, the Lagrangian and Hessian are updated with the iterative BFGS algorithm (Broyden-Fletcher-Goldfarb-Shanno, see Broyden, 1970). The BFGS technique computes an approximated estimate of the Hessian matrix using the gradients, i.e. the elements of the Lagrangian itself.

Appendix B

Analysis of the ODE system (4.1)

In order to obtain more analytically tractable expressions, with a reduced number of parameters, and normalised variables, we write the following non-dimensional version of the ODE equations:

$$\begin{cases} \dfrac{ds}{d\tau} = s(1-g) - \delta^* sc + \xi^* \beta r h \\ \dfrac{dr}{d\tau} = \rho a r - \delta^* r c - \xi^* r h \\ \dfrac{df}{d\tau} = -\theta^* g f + \phi^* a h \\ \dfrac{da}{d\tau} = \theta^* g f - \phi^* a h \end{cases} \quad \text{and} \quad \begin{cases} s(\tau = 0) = 1 \\ r(\tau = 0) = 1 \\ f(\tau = 0) = 1 \\ a(\tau = 0) = 0 \end{cases} \tag{B.1}$$

Eqs. (B.1) were obtained from Eqs. (4.1) by defining new nondimensional variables as follows:

$$S = S_0\, s,\ R = R_0\, r,\ F = F_0\, f,\ A = F_0\, a,\ t = \frac{1}{\rho_S}\, \tau,$$

and nondimensional parameters:

$$\beta = \frac{R_0}{S_0},\ \rho = \frac{\rho_R F_0}{\rho_S},\ \delta^* = \frac{\delta}{\rho_S},\ \xi^* = \frac{\xi}{\rho_S},\ \theta^* = \frac{\theta}{\rho_S},\ \phi^* = \frac{\phi}{\rho_S}.$$

The asterisk notation for the new parameters will now be dropped for notational simplicity.

We shall consider all the possible treatment scenarios, in order to formally analyse the system of ODEs and test our numerical solutions against the corresponding analytical solution. In the following sample runs dimensional parameter values are the same as those used in Section 4.7. Corresponding nondimensional values were obtained:

$$\beta = 0.005;\ \rho = 1.91;\ \delta = 0.96;\ \xi = 4.30;\ \theta = 0.13;\ \phi = 0.43.$$

B.1 No Treatment

$$\begin{cases} \dfrac{ds}{d\tau} = s \\ \dfrac{dr}{d\tau} = \rho a r \\ \dfrac{df}{d\tau} = 0 \\ \dfrac{da}{d\tau} = 0 \end{cases} \quad \text{and} \quad \begin{cases} s(\tau = 0) = 1 \\ r(\tau = 0) = 1 \\ f(\tau = 0) = 1 \\ a(\tau = 0) = 0 \end{cases} \tag{B.2}$$

The analytical solution of this system of equations (illustrated in Figure B.1) is trivial:

$$s(\tau) = \exp(\tau), \quad r(\tau) = 1 \; \forall \tau, \quad f(\tau) = 1 \; \forall \tau, \quad a(\tau) = 0 \; \forall \tau.$$

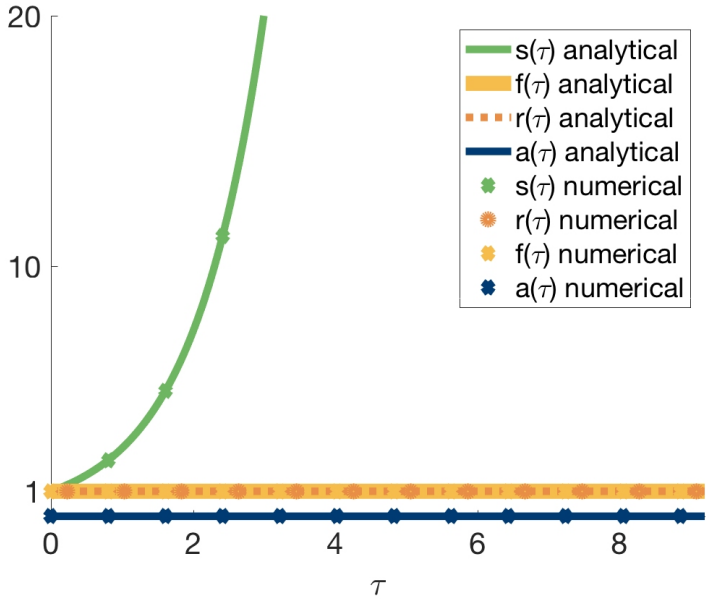


Figure B.1: *Analytical and numerical solution for the model in Eqs.* (B.2)*: absence of treatment.*

B.2 Chemotherapy

$$\begin{cases} \dfrac{ds}{d\tau} = s - \delta s \\ \dfrac{dr}{d\tau} = \rho a r - \delta r \\ \dfrac{df}{d\tau} = 0 \\ \dfrac{da}{d\tau} = 0 \end{cases} \quad \text{and} \quad \begin{cases} s(\tau = 0) = 1 \\ r(\tau = 0) = 1 \\ f(\tau = 0) = 1 \\ a(\tau = 0) = 0 \end{cases} \tag{B.3}$$

The analytical solution of this system of equations is:

$$s(\tau) = \exp((1-\delta)\tau), \quad r(\tau) = \exp(-\delta\tau), \quad f(\tau) = 1 \; \forall\tau, \quad a(\tau) = 0 \; \forall\tau,$$

illustrated in Figure B.2. The value of δ will determine the trend of the solution for s: exponentially increasing if $\delta < 1$, exponentially decreasing if $\delta > 1$. The latter case corresponds, in dimensional form, to a death rate larger than the growth rate.

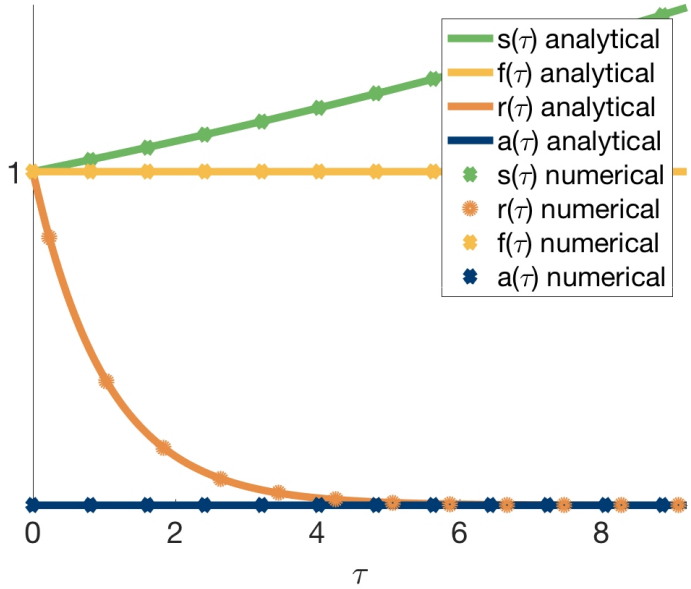


Figure B.2: *Analytical and numerical solution for the model in Eqs.* (B.3)*: treatment with chemotherapy.*

B.3 Targeted Therapy

$$\begin{cases} \dfrac{ds}{d\tau} = 0 \\ \dfrac{dr}{d\tau} = \rho a r \\ \dfrac{df}{d\tau} = -\theta f \\ \dfrac{da}{d\tau} = \theta f \end{cases} \quad \text{and} \quad \begin{cases} s(\tau=0) = 1 \\ r(\tau=0) = 1 \\ f(\tau=0) = 1 \\ a(\tau=0) = 0 \end{cases} \tag{B.4}$$

We first note that $s(\tau) = 1 \; \forall\tau$, $f(\tau) = \exp(-\theta\tau)$ and $\dfrac{d(f+a)}{d\tau} = 0$, hence $a(\tau) = 1 - \exp(-\theta\tau)$, and we can rewrite the differential equation for r as:

$$\frac{dr}{d\tau} = \rho(1 - \exp(-\theta\tau))r,$$

and obtain the following solution:

$$r(\tau) = \exp\left(\rho\left(\tau + \frac{\exp(-\theta\tau) - 1}{\theta}\right)\right),$$

illustrated in Figure B.3.

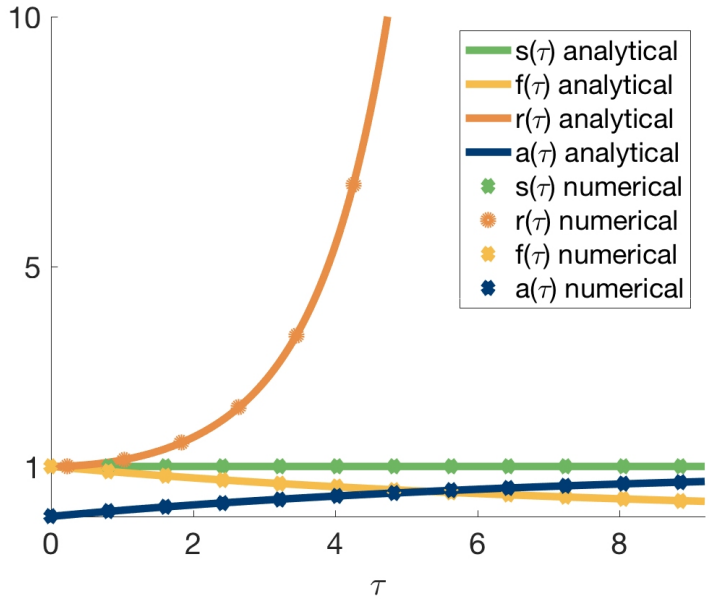


Figure B.3: *Analytical and numerical solution for the model in Eqs.* (B.4)*: treatment with targeted therapy.*

B.4 Chemotherapy and Targeted Therapy Combination

$$\begin{cases} \dfrac{ds}{d\tau} = -\delta s \\ \dfrac{dr}{d\tau} = \rho a r - \delta r \\ \dfrac{df}{d\tau} = -\theta f \\ \dfrac{da}{d\tau} = \theta f \end{cases} \quad \text{and} \quad \begin{cases} s(\tau = 0) = 1 \\ r(\tau = 0) = 1 \\ f(\tau = 0) = 1 \\ a(\tau = 0) = 0. \end{cases} \tag{B.5}$$

Similarly to the previous case we obtain:

$$s(\tau) = \exp(-\delta\tau), \quad f(\tau) = \exp(-\theta\tau), \quad a(\tau) = 1 - \exp(-\theta\tau),$$

$$r(\tau) = \exp\left((\rho - \delta)\,\tau + \frac{\rho}{\theta}\left(\exp(-\theta\tau) - 1\right)\right).$$

This solution is illustrated in Figure B.4.

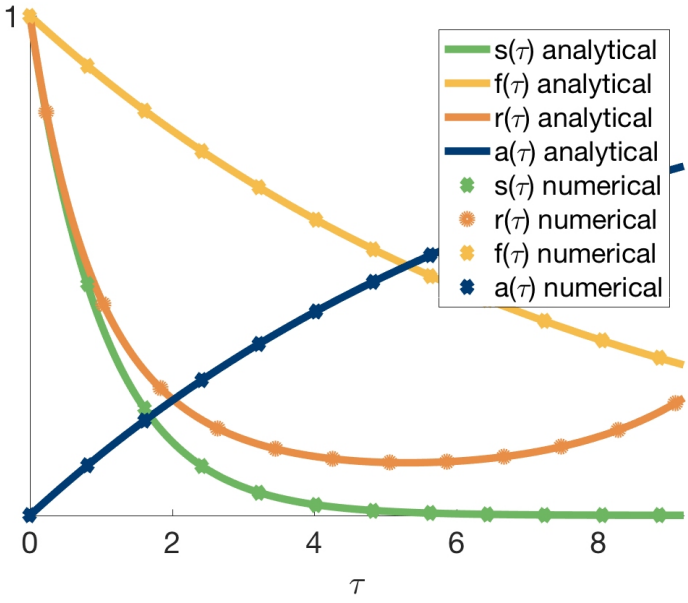


Figure B.4: *Analytical and numerical solution for the model in Eqs.* (B.5)*: treatment with targeted therapy and chemotherapy in combination.*

B.5 After Targeted Therapy is Removed

$$\begin{cases} \dfrac{ds}{d\tau} = s + \xi\beta r \\ \dfrac{dr}{d\tau} = \rho a r - \xi r \\ \dfrac{df}{d\tau} = -\phi a \\ \dfrac{da}{d\tau} = \phi a \end{cases} \quad \text{and} \quad \begin{cases} s(\tau = 0) = s_0 \\ r(\tau = 0) = r_0 \\ f(\tau = 0) = f_0 \\ a(\tau = 0) = a_0 \end{cases} \tag{B.6}$$

where s_0, r_0, f_0, a_0 are the normalised initial conditions, corresponding to the cell counts at the end of treatment with targeted therapy.

We first note that $\dfrac{d(f+a)}{d\tau} = 0$, hence $f(\tau) = f_0 + a_0 - a(\tau)\ \forall\tau$. Solving for a we obtain:

$$a(\tau) = a_0 \exp(-\phi\tau), \quad f(\tau) = f_0 + a_0\left(1 - \exp(-\phi\tau)\right).$$

Hence the equation for r becomes

$$\frac{dr}{d\tau} = \rho a_0 \exp(-\phi\tau) r - \xi r,$$

whose solution is:

$$r(\tau) = r_0 \exp\left(\frac{\rho a_0}{\phi}\left(1 - \exp(-\phi\tau)\right) - \xi\tau\right).$$

Finally the equation for s becomes

$$\frac{ds}{d\tau} = s + \xi\beta r_0 \exp\left(\frac{\rho a_0}{\phi}\left(1 - \exp(-\phi\tau)\right) - \xi\tau\right). \tag{B.7}$$

We define

$$m(\tau) = \xi\beta r_0 \exp\left(\frac{\rho a_0}{\phi}\left(1 - \exp(-\phi\tau)\right) - \xi\tau\right)$$

and seek the solution of eqn B.7 in the form $s(\tau) = u(\tau)v(\tau)$, where v is any function that satisfies $\frac{dv}{d\tau} = v$ (i.e. $v = \exp(\tau)$), and u a function that satisfies the separable equation: $v(\tau)\frac{du}{d\tau} = m(\tau)$. We can write the solution to the last equation as:

$$u(\tau) = \int \frac{m(\tau)}{v(\tau)} d\tau + C = \xi\beta r_0 \exp\left(\frac{\rho a_0}{\phi}\right) \int \exp\left(-(1+\xi)t - \frac{\rho a_0}{\phi}\exp\left(-\phi t\right)\right) d\tau + C.$$

To my knowledge this integral cannot be expressed analytically.
The solution is illustrated in Figure B.5.

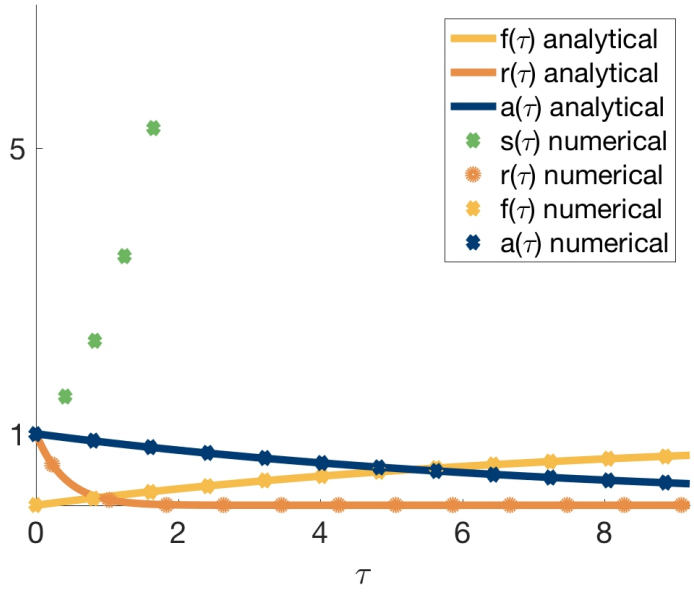


Figure B.5: *Analytical and numerical solution for the model in Eqs.* (B.6)*: removal of targeted therapy.*

References

[1] T. Alarcón, H. M. Byrne, and P. K. Maini. A cellular automaton model for tumour growth in inhomogeneous environment. J Theor Biol, 225(2):257–274, 2003.

[2] P. M. Altrock, L. L. Liu, and F. Michor. The mathematics of cancer: integrating quantitative models. Nat Rev Cancer, 15(12):730–745, 2015.

[3] A. R. A. Anderson. A hybrid mathematical model of solid tumour invasion: the importance of cell adhesion. Math Med Biol, 22(2):163–186, 2005.

[4] A. R. A. Anderson and M. A. J. Chaplain. Continuous and discrete mathematical models of tumor-induced angiogenesis. Bull of Math Biol, 60:857–900, 1998.

[5] A. R. A. Anderson, M. A. J. Chaplain, E. L. Newman, R. J. C. Steele, and A. M. Thompson. Mathematical modelling of tumour invasion and metastasis. J Theor Med, 2(2):129–154, 2000.

[6] A. R. A. Anderson and V. Quaranta. Integrative mathematical oncology. Nat Rev Cancer, 8(3):227–234, 2008.

[7] A. R. A. Anderson, K. A. Rejniak, P. Gerlee, and V. Quaranta. Microenvironment driven invasion: a multiscale multimodel investigation. J Math Biol, 58(4-5):579–624, 2009.

[8] A. R. A. Anderson, B. D. Sleeman, I. M. Young, and B. S. Griffiths. Nematode movement along a chemical gradient in a structurally heterogeneous environment. 2. theory. Fundam Appl Nematol, 20(2):165–172, 1997.

[9] A. R. A. Anderson, A. M. Weaver, P. T. Cummings, and V. Quaranta. Tumor morphology and phenotypic evolution driven by selective pressure from the microenvironment. Cell, 275(5):905–915, 2006.

[10] A. Baldi, E. Dragonetti, B. T, A. M. Groeger, V. Esposito, G. Baldi, and D. Santini. Detection of circulating malignant cells by RT-PCR in long-term clinically disease-free I stage melanoma patients. Anticancer Res, 20(5C):3923–3928, 2000.

[11] D. Basanta and A. Anderson. Homeostasis back and forth: An eco-evolutionary perspective of cancer. bioRxiv, 2016.

[12] D. Basanta and A. R. A. Anderson. Exploiting ecological principles to better understand cancer progression and treatment. Interface Focus, 3(4):20130020, 2013.

[13] D. Basanta, R. A. Gatenby, and A. R. Anderson. Exploiting evolution to treat drug resistance: combination therapy and the double bind. Mol Pharm, 9(4):914–921, 2012.

[14] D. Basanta, D. W. Strand, R. B. Lukner, O. E. Franco, D. E. Cliffel, G. E. Ayala, S. W. Hayward, and A. R. Anderson. The role of transforming growth factor-mediated tumor-stroma interactions in prostate cancer progression: an integrative approach. Cancer Res, 69(17):7111–7120, 2009.

[15] L. Benesova, M. Minarik, D. Jancarikova, B. Belsanova, and M. Pesek. Multiplicity of EGFR and KRAS Mutations in non-small cell lung cancer (NSCLC) patients treated with tyrosine kinase inhibitors. Anticancer Res, 30(5):1667–1672, 2010.

[16] L. V. Bertalanffy. Problems of organic growth. Nature, 163(4135):156–158, 1949.

[17] G. Bollag, P. Hirth, J. Tsai, J. Zhang, P. N. Ibrahim, H. Cho, W. Spevak, C. Zhang, Y. Zhang, G. Habets, E. A. Burton, B. Wong, G. Tsang, B. L. West, B. Powell, R. Shellooe, A. Marimuthu, H. Nguyen, K. Y. Zhang, D. R. Artis, J. Schlessinger, F. Su, B. Higgins, R. Iyer, K. D'Andrea, A. Koehler, M. Stumm, P. S. Lin, R. J. Lee, J. Grippo, I. Puzanov, K. B. Kim, A. Ribas, G. A. McArthur, J. A. Sosman, P. B. Chapman, K. T. Flaherty, X. Xu, K. L. Nathanson, and K. Nolop. Clinical efficacy of a RAF inhibitor needs broad target blockade in BRAF-mutant melanoma. Nature, 467(7315):596–599, 2010.

[18] H. Bolouri. Network dynamics in tumor microenvironment. Semin Cancer Biol, 30:52–9, 2015.

[19] I. Bozic, J. G. Reiter, B. Allen, T. Antal, K. Chatterjee, P. Shah, Y. S. Moon, A. Yaqubie, N. Kelly, D. T. Le, E. J. Lipson, P. B. Chapman, L. A. Diaz Jr, B. Vogelstein, and M. A. Nowak. Evolutionary dynamics of cancer in response to targeted combination therapy. Elife, 2:e00747, 2013.

[20] C. G. Broyden. The convergence of a class of double-rank minimization algorithms. J Appl Math, 6(1):76–90, 1970.

[21] H. M. Byrne. Dissecting cancer through mathematics: from the cell to the animal model. Nat Rev Cancer, 10(3):221–230, 2010.

[22] A. Q. Cai, K. A. Landman, and B. D. Hughes. Multi-scale modeling of a wound-healing cell migration assay. J Theor Biol, 245(3):576–594, 2007.

[23] P. Calabresi, P. S. Schein, and S. A. Rosenberg. Medical oncology: basic principles and clinical management of cancer. MacMillan Pub. Co., New York, NY, 1985.

[24] M. Castells, B. Thibault, J.-P. Delord, and B. Coudere. Implication of tumor microenvironment in chemoresistance: tumor-associated stromal cells protect tumor cells from cell death. Int J Mol Sci, 13(8):9545–9571, 2012.

[25] J. E. Chaft, G. R. Oxnard, and C. S. Sima. Disease flare after tyrosine kinase inhibitor discontinuation in patients with EGFR–mutant lung cancer and acquired resistance to erlotinib or gefitinib: Implications for clinical trial design patients with EGFR–mutant lung cancer and acquired resistance. Clin Cancer Res, 17(19):6298–6303, 2011.

[26] P. B. Chapman, A. Hauschild, C. Robert, J. B. Haanen, P. Ascierto, J. Larkin, R. Dummer, C. Garbe, A. Testori, M. Maio, D. Hogg, P. Lorigan, C. Lebbe, T. Jouary, D. Schadendorf, A. Ribas, S. J. O'Day, J. A. Sosman, J. M. Kirkwood, A. M. Eggermont, K. Dreno, B Nolop, J. Li, B. Nelson, J. Hou, R. J. Lee, F. K. T, and G. A. McArthur. Improved survival with vemurafenib in melanoma with BRAF V600E mutation. N Engl J Med, 26:2507–2516, 2011.

[27] A. J. Coldman and J. H. Goldie. A model for the resistance of tumor cells to cancer chemotherapeutic agents. Math Biosci, 65(2):291–307, 1983.

[28] J. Crank. The Mathematics of Diffusion. Oxford science publications. Clarendon Press, 1979.

[29] P. D. Dale, J. A. Sherratt, and P. K. Maini. The speed of corneal epithelial wound healing. Appl Math Lett, 7(2):11–14, 1994.

[30] M. Das Thakur, F. Salangsang, A. S. Landman, W. R. Sellers, N. K. Pryer, M. P. Levesque, R. Dummer, M. McMahon, and D. D. Stuart. Modelling vemurafenib resistance in melanoma reveals a strategy to forestall drug resistance. Nature, 494(7436):251–255, 2013.

[31] L. G. de Pillis, A. E. Radunskaya, and C. L. Wiseman. A validated mathematical model of cell-mediated immune response to tumor growth. Cancer Res, 65(17):7950–7958, 2005.

[32] L. A. Dethlefsen, J. M. Prewitt, and M. M. L. Analysis of tumor growth curves. J Natl Cancer Inst, 40(2):389–405, 1968.

[33] D. Drasdo and S. Hohme. Individual-based approaches to birth and death in avascular tumors. Math Comput Model, 37(11):1163–1175, 2003.

[34] S. Eikenberry, C. Thalhauser, and Y. Kuang. Tumor-immune interaction, surgical treatment, and cancer recurrence in a mathematical model of melanoma. PLoS Comp Biol, 5(4):1–18, 2009.

[35] P. M. Enriquez-Navas, Y. Kam, T. Da, S. Hassan, A. S. Silva, P. Foroutan, E. Ruiz, G. Martinez, S. Minton, R. J. Gillies, and R. A. Gatenby. Exploiting evolutionary principles to prolong tumor control in preclinical models of breast cancer. Sci Transl Med, 8(327):327ra24, 2016.

[36] R. A. Fisher. The wave of advance of advantageous genes. Ann Eugenics, 7:355–369, 1937.

[37] E. H. Flach, V. W. Rebecca, M. Herlyn, K. S. M. Smalley, and A. R. A. Anderson. Fibroblasts contribute to melanoma tumor growth and drug resistance. Mol Pharm, 8(6):2039–2049, 2011.

[38] R. Flaumenhaft and D. B. Rifkin. Extracellular matrix regulation of growth factor and protease activity. Curr Opin Cell Biol, 3(5):817–823, 1991.

[39] R. A. Gatenby and E. T. Gawlinski. A reaction-diffusion model of cancer invasion. Cancer Res, 15(56):5745–5753, 1996.

[40] R. A. Gatenby, A. S. Silva, R. J. Gillies, and B. R. Frieden. Adaptive therapy. Cancer Res, 69(11):4894–4903, 2009.

[41] P. Gerlee. The model muddle: in search of tumour growth laws. Cancer Res, 15(73):2407–2411, 2013.

[42] P. Gerlee and A. R. A. Anderson. A hybrid cellular automaton model of clonal evolution in cancer: the emergence of the glycolytic phenotype. J Theor Biol, 250(4):705–722, 2008.

[43] P. Hahnfeldt, J. Folkman, and L. Hlatky. Minimizing long term tumor burden: The logic for metronomic chemotherapeutic dosing and its antiangiogenic basis. J Theor Biol, 220(4):545–554, 2002.

[44] D. Hanahan and R. A. Weinberg. Hallmarks of cancer: the next generation. Cell, 144(5):646–674, 2011.

[45] T. N. Hartmann, J. A. Burger, A. Glodek, N. Fujii, and M. Burger. CXCR4 chemokine receptor and integrin signaling co-operate in mediating adhesion and chemoresistance in small cell lung cancer (SCLC) cells. Oncogene, 24(27):4462–4471, 2005.

[46] L. A. Hazlehurst, R. F. Argilagos, and W. S. Dalton. β1 integrin mediated adhesion increases BIM protein degradation and contributes to drug resistance in leukaemia cells. Br J Haematol, 136(2):269–275, 2007.

[47] F. Hinkelmann, D. Murrugarra, A. S. Jarrah, and R. Laubenbacher. A mathematical framework for agent based models of complex biological networks. Bull Math Biol, 73(7):1583–1602, 2010.

[48] P. Hinow, P. Gerlee, L. J. McCawley, V. Quaranta, M. Ciobanu, S. Wang, J. M. Graham, B. P. Ayati, J. Claridge, K. R. Swnason, M. Loveless, and A. R. A. Anderson. A spatial model of tumor-host interaction: Application of chemotherapy. Math Biosci Eng, 6(3):521–546, 2009.

[49] E. Hirata, M. R. Girotti, A. Viros, S. Hooper, B. Spencer-Dene, M. Matsuda, J. Larkin, R. Marais, and E. Sahai. Intravital imaging reveals how BRAF inhibition generates drug-tolerant microenvironments with high integrin β1/FAK signaling. Cancer Cell, 27:574–588, 2015.

[50] M. Holzel, A. Bovier, and T. Tuting. Plasticity of tumour and immune cells: a source of heterogeneity and a cause for therapy resistance? Nat Rev Cancer, 13(5):365–376, 2013.

[51] O. G. Isaeva and V. A. Osipov. Different strategies for cancer treatment: mathematical modeling. Comput Math Methods Med, 10(4):253–272, 2009.

[52] K. Iwata, K. Kawasaki, and N. Shigesada. A dynamical model for the growth and size distribution of multiple metastatic tumors. J Theor Biol, 203(2):177–186, 2000.

[53] S. Jang and M. B. Atkins. Treatment of BRAF-mutant melanoma: the role of vemurafenib and other therapies. Clin Pharmacol Ther, 95(1):24–31, 2014.

[54] A. B. Keeton, E. A. Salter, and G. A. Piazza. The RAS–effector interaction as a drug target. Cancer Res, 77(2):221–226, 2017.

[55] E. Kim, V. W. Rebecca, I. V. Fedorenko, J. L. Messina, R. Mathew, S. S. Maria-Engler, D. Basanta, K. S. M. Smalley, and A. R. A. Anderson. Senescent fibroblasts in melanoma initiation and progression: an integrated theoretical, experimental, and clinical approach. Cancer Res, 73(23):6874–6885, 2013.

[56] A. N. Kolmogorov, I. G. Petrowskii, and N. Piscounov. Etude de l'equation de la diffusion avec croissance de la quantite de matiere et son application a un probleme biologique. Moscow Univ Math Bull, 1:1–25, 1937.

[57] O. Lavi, M. M. Gottesman, and D. Levy. The dynamics of drug resistance: a mathematical perspective. Drug Resist Update, 15(1-2):90–97, 2012.

[58] U. Ledzewicz, H. Schattler, M. R. Gahrooi, and S. M. Dehkordi. On the MTD paradigm and optimal control for multi-drug cancer chemotherapy. Math Biosci Eng, 10(3):803–819, 2013.

[59] J. C. Lee, S. H. Jang, K. Y. Lee, and Y.-C. Kim. Treatment of non-small cell lung carcinoma after failure of epidermal growth factor receptor tyrosine kinase inhibitor. Cancer Res Treat, 45(2):79–85, 2013.

[60] M. Mackiewicz-Wysocka, L. Krokowicz, J. Kocur, and J. Mackiewicz. Resistance to vemurafenib can be reversible after treatment interruption. Medicine (Baltimore), 27(e157), 2014.

[61] P. Macklin, S. McDougall, A. R. Anderson, M. A. Chaplain, V. Cristini, and J. Lowengrub. Multiscale modelling and nonlinear simulation of vascular tumour growth. J Math Biol, 58(4-5):765–798, 2009.

[62] D. C. Markham. Spatial correlation models for cell populations. PhD thesis, University of Oxford, 2014.

[63] N. K. Martin, E. A. Gaffney, R. A. Gatenby, and P. K. Maini. Tumour-stromal interactions in acid-mediated invasion: a mathematical model. J Theor Biol, 267(3):461–470, 2010.

[64] G. A. McArthur, P. B. Chapman, C. Robert, J. Larkin, J. B. Haanen, R. Dummer, A. Ribas, D. Hogg, O. Hamid, P. A. Ascierto, C. Garbe, A. Testori, M. Maio, P. Lorigan, C. Lebbe, J. T, D. Schadendorf, S. J. O'Day, J. M. Kirkwood, A. M. Eggermont, B. Dreno, J. A. Sosman, K. T. Flaherty, M. Yin, I. Caro, S. Cheng,

K. Trunzer, and A. Hauschild. Safety and efficacy of vemurafenib in BRAFV600E and BRAFV600K mutation-positive melanoma (BRIM-3): extended follow-up of a phase 3, randomised, open-label study. Lancet Oncol, 15(3):323–332, 2014.

[65] J. B. McCarthy, M. L. Basara, S. L. Palm, D. F. Sas, and L. T. Furcht. The role of cell adhesion proteins - laminin and fibronectin - in the movement of malignant and metastatic cells. Cancer Metastasis Rev, 4(2):125–152, 1985.

[66] J. A. McCubrey, L. S. Steelman, W. H. Chappell, S. L. Abrams, E. W. Wong, F. Chang, B. Lehmann, D. M. Terrian, M. Milella, A. Tafuri, F. Stivala, M. Libra, J. Basecke, C. Evangelisti, A. M. Martelli, and R. A. Franklin. Roles of the RAF/MEK/ERK pathway in cell growth, malignant transformation and drug resistance. Biochem Biophys Acta, 1773(8):1263–1284, 2007.

[67] S. R. McDougall, A. R. Anderson, and M. A. Chaplain. Mathematical modelling of dynamic adaptive tumour-induced angiogenesis: clinical implications and therapeutic targeting strategies. J Theor Biol, 241(3):564–589, 2006.

[68] D. W. McMillin, J. M. Negri, and C. S. Mitsiades. The role of tumour–stromal interactions in modifying drug response: challenges and opportunities. Nat Rev Drug Discovery, 12:217–228, 2013.

[69] M. B. Meads, R. A. Gatenby, and W. S. Dalton. Environment-mediated drug resistance: a major contributor to minimal residual disease. Nat Rev Cancer, 9(9):665–674, 2009.

[70] M. M. Melicow. The three steps to cancer: a new concept of carcinogenesis. J Theor Biol, 94(2):471–511, 1982.

[71] A. M. Menzies, L. E. Haydu, M. S. Carlino, M. W. F. Azer, P. J. A. Carr, R. F. Kefford, and G. V. Long. Inter- and intra-patient heterogeneity of response and progression to targeted therapy in metastatic melanoma. PLoS one, 9(1):1–9, 2014.

[72] T. S. Mok, Y.-L. Wu, S. Thongprasert, C.-H. Yang, D.-T. Chu, N. Saijo, P. Sunpaweravong, B. Han, B. Margono, Y. Ichinose, Y. Nishiwaki, Y. Ohe, J.-J. Yang, B. Chewaskulyong, H. Jiang, E. L. Duffield, C. L. Watkins, A. A. Armour, and M. Fukuoka. Gefitinib or carboplatin–paclitaxel in pulmonary adenocarcinoma. N Engl J Med, 316(10):947–957, 2009.

[73] H. C. Monro and E. A. Gaffney. Modelling chemotherapy resistance in palliation and failed cure. J Theor Biol, 257(2):292–302, 2009.

[74] M. M. Mueller and N. E. Fusenig. Friends or foes - bipolar effects of the tumour stroma in cancer. Nat Rev Cancer, 4(11):839–849, 2004.

[75] M. M. Mueller and N. E. Fusenig. Tumor-associated fibroblasts and their matrix. Chapters 10 and 12. Springer, 2011.

[76] J. D. Murray. Mathematical biology II: spatial models and biomedical applications. 2002. Springer, 3 edition, 2003.

[77] P. A. Netti, D. A. Berk, M. A. Swartz, A. J. Grodzinsky, and R. K. Jain. Role of extracellular matrix assembly in interstitial transport in solid tumors. Cancer Res, 60(9):2479–2503, 2000.

[78] M. Oremland and R. Laubenbacher. Optimization of agent-based models: scaling methods and heuristic algorithms. J Artif Soc Soc Simulat, 17(2):6, 2014.

[79] P. A. Orlando, R. A. Gatenby, and J. S. Brown. Cancer treatment as a game: integrating evolutionary game theory into the optimal control of chemotherapy. Phys Biol, 9(6):065007, 2012.

[80] M. R. Owen, T. Alarcón, P. K. Maini, and H. M. Byrne. Angiogenesis and vascular remodelling in normal and cancerous tissues. J Math Biol, 58(4-5):689–721, 2009.

[81] G. Palmieri, M. Colombino, M. C. Sini, A. Manca, P. A. Ascierto, and A. Cossu. Resistance to targeted therapies in melanoma: new insights. E M J Dermatol, 1:24–37, 2013.

[82] K. H. Paraiso, Y. Xiang, V. W. Rebecca, E. V. Abel, Y. A. Chen, A. C. Munko, E. Wood, I. V. Fedorenko, V. K. Sondak, A. R. Anderson, A. Ribas, M. Dalla Palma, K. L. Nathanson, J. M. Koomen, J. L. Messina, and K. S. M. Smalley. PTEN loss confers BRAF inhibitor resistance to melanoma cells through the suppression of BIM expression. Cancer Res, 71(7):2750–2769, 2011.

[83] A. A. Patel, E. T. Gawlinski, S. K. Lemieux, and R. A. Gatenby. A cellular automaton model of early tumor growth and invasion: the effects of native tissue vascularity and increased anaerobic tumor metabolism. J Theor Biol, 213(3):315–331, 2001.

[84] M. Pennisi. A mathematical model of immune-system-melanoma competition. Comput Math Methods Med, 2012:1–13, 2012.

[85] H. Perfahl, H. M. Byrne, T. Chen, V. Estrella, T. Alarcón, A. Lapin, R. A. Gatenby, R. J. Gillies, M. C. Lloyd, P. K. Maini, M. Reuss, and M. R. Owen. Multiscale modelling of vascular tumour growth in 3D: the roles of domain size and boundary conditions. PLoS one, 6(4):e14790, 2011.

[86] A. J. Perumpanani, J. A. Sherratt, J. Norbury, and H. M. Byrne. Biological inferences from a mathematical model for malignant invasion. Invasion Metastasis, 16(4-5):209–221, 1996.

[87] M. J. Piotrowska and S. D. Angus. A quantitative cellular automaton model of in vitro multicellular spheroid tumour growth. J Theor Biol, 258(2):165–178, 2009.

[88] A. Pluen, Y. Boucher, S. Ramanujan, T. D. McKee, T. Gohongi, E. Di Tomaso, E. B. Brown, Y. Izumi, R. B. Campbell, D. A. Berk, and R. K. Jain. Role of tumor-host interactions in interstitial diffusion of macromolecules: cranial vs. subcutaneous tumors. PNAS, 98(8):4628–4633, 2001.

[89] C. Porta, C. Paglino, and A. Mosca. Targeting PI3K/AKT/mTOR signaling in cancer. Front Oncol, 4(64):1–11, 2014.

[90] P. Poulikakos, C. I. Zhang, G. Bollag, K. M. Shokat, and N. Rosen. RAF inhibitors transactivate RAF dimers and ERK signalling in cells with wild-type BRAF. Nature, 464(427-430), 2010.

[91] G. G. Powathil, M. Swat, and M. A. J. Chaplain. Systems oncology: towards patient-specific treatment regimes informed by multiscale mathematical modelling. Semin Cancer Biol, 30:13–20, 2015.

[92] V. W. Rebecca, R. R. Massaro, I. V. Fedorenko, V. K. Sondak, A. R. A. Anderson, E. Kim, R. K. Amaravadi, S. S. Maria-Engler, J. L. Messina, G. T. Gibney, R. R. Kudchadkar, and K. S. M. Smalley. Inhibition of autophagy enhances the effects of the AKT inhibitor MK-2206 when combined with paclitaxel and carboplatin in BRAF wild-type melanoma. Pigmented Cell Melanoma Res, 27(3):465–478, 2014.

[93] C. Robert and G. Casella. Monte carlo statistical methods. Springer-Verlag New York, 2004.

[94] M. Robertson-Tessi, R. J. Gillies, R. A. Gatenby, and A. R. Anderson. Impact of metabolic heterogeneity on tumor growth, invasion, and treatment outcomes. Cancer Res, 75(8):1567–1579, 2015.

[95] F. Sanz-Rodriguez, A. Hidalgo, and J. Teixidó. Chemokine stromal cell-derived factor-1α modulates VLA-4 integrin-mediated multiple myeloma cell adhesion to CS-1/fibronectin and VCAM-1. Blood, 97(2):346–351, 2001.

[96] K. H. Shain, T. H. Landowski, and W. S. Dalton. Adhesion-mediated intracellular redistribution of c-Fas-associated death domain-like IL-1-converting enzyme-like inhibitory protein-long confers resistance to CD95-induced apoptosis in hematopoietic cancer cell lines. J Immunol, 168(5):2544–2553, 2002.

[97] S. V. Sharma, D. Y. Lee, B. Li, M. P. Quinlan, F. Takahashi, S. Maheswaran, U. McDermott, N. Azizian, L. Zou, M. A. Fischbach, K.-K. Wong, K. Brandstetter, B. Wittner, S. Ramaswamy, M. Classon, and J. Settleman. A chromatin-mediated reversible drug tolerant state in cancer cell subpopulations. Cell, 141(1):69–80, 2010.

[98] K. Smallbone, R. A. Gatenby, R. J. Gillies, P. K. Maini, and G. D. J. Metabolic changes during carcinogenesis: potential impact on invasiveness. J Theor Biol, 244(4):703–713, 2007.

[99] K. S. M. Smalley. Understanding melanoma signaling networks as the basis for molecular targeted therapy. J Invest Dermatol, 130(1):28–37, 2010.

[100] A. C. Society. American Cancer Society. Cancer Facts & Figures 2016, 2016.

[101] J. A. Sosman, K. B. Kim, L. Schuchter, R. Gonzalez, A. C. Pavlick, W. J. S., G. A. McArthur, T. E. Hutson, S. J. Moschos, K. T. Flaherty, P. Hersey, R. Kefford, D. Lawrence, I. Puzanov, K. D. Lewis, R. K. Amaravadi, B. Chmielowski, H. J. Lawrence, Y. Shyr, F. Ye, J. Li, K. B. Nolop, R. J. Lee, A. K. Joe, and A. Ribas. Survival in BRAF V600–mutant advanced melanoma treated with vemurafenib. N Engl J Med, 366(8):707–714, 2012.

[102] G. M. Stella, M. Luisetti, S. Inghilleri, F. Cemmi, R. Scabini, M. Zorzetto, and E. Pozzi. Targeting EGFR in non-small-cell lung cancer: lessons, experiences, strategies. Respir Med, 106(2):173–183, 2012.

[103] S. Sun, M. F. Wheeler, M. Obeyesekerec, and C. W. Patrick Jr. A deterministic model of growth factor-induced angiogenesis. Bull Math Biol, 67(2):313–337, 2005.

[104] A. Swierniak, M. Kimmel, and J. Smieja. Mathematical modeling as a tool for planning anticancer therapy. Eur J Pharmacol, 625(1-3):108–121, 2009.

[105] F. Tas. Metastatic behavior inmelanoma: timing, pattern, survival, and influencing factors. J Oncology, 2012(1-9), 2012.

[106] T. D. Tlsty and L. M. Coussens. Tumor stroma and regulation of cancer development. Annu Rev Pathol Mech Dis, 1:119–150, 2006.

[107] T. Toni, D. Welch, N. Strelkowa, A. Ipsen, and M. P. H. Stumpf. Approximate bayesian computation scheme for parameter inference and model selection in dynamical systems. J R Soc Interface, 2009.

[108] E. M. Van Allen, N. Wagle, A. Sucker, D. J. Treacy, C. M. Johannessen, E. M. Goetz, C. S. Place, A. Taylor-Weiner, S. Whittaker, G. V. Kryukov, E. Hodis, M. Rosenberg, A. McKenna, K. Cibulskis, D. Farlow, L. Zimmer, U. Hillen, R. Gutzmer, S. M. Goldinger, S. Ugurel, H. J. Gogas, F. Egberts, C. Berking, U. Trefzer, C. Loquai, B. Weide, J. C. Hassel, S. B. Gabriel, S. L. Carter, G. Getz, L. A. Garraway, and D. Schadendorf. The genetic landscape of clinical resistance to RAF inhibition in metastatic melanoma. Cancer Discov, 4(1):94–109, 2014.

[109] D. L. Viale, E. G. Cafferata, D. Gould, C. Rotondaro, Y. Chernajovsky, O. L. Podhajcer, and M. V. Lopex. Therapeutic improvement of a stroma-targeted CRAd by incorporating motives responsive to the melanoma microenvironment. J Invest Dermatol, 133(11):2576–2584, 2013.

[110] N. Wagle, C. Emery, M. F. Berger, M. J. Davis, A. Sawyer, P. Pochanard, S. M. Kehoe, C. M. Johannessen, L. E. MacConaill, W. C. Hahn, M. Meyerson, and L. A. Garraway. Dissecting therapeutic resistance to RAF inhibition in melanoma by tumor genomic profiling. J Clin Oncol, 29(22):3085–3096, 2011.

[111] R. A. Weinberg. The biology of cancer. Taylor & Francis, 2006.

[112] D. E. White, J. H. Rayment, and W. J. Muller. Addressing the role of cell adhesion in tumor cell dormancy. Cell Cycle, 5(16):1756–1759, 2006.

[113] N. Yanagisawa, R. Li, D. Rowley, H. Liu, D. Kadmon, B. J. Miles, T. M. Wheeler, and G. E. Ayala. Stromogenic prostatic carcinoma pattern (carcinomas with reactive stromal grade 3) in needle biopsies predicts biochemical recurrence-free survival in patients after radical prostatectomy. Hum Pathol, 2007.

[114] W. Zhihui and T. S. Deisboeck. Computational modeling of brain tumors: discrete, continuum or hybrid? Sci Model Simul, 15(1-3):381–393, 2008.